

MARTIN SCHÄFERLING

CHIRAL PLASMONIC NEAR-FIELD SOURCES

CONTROL OF CHIRAL ELECTROMAGNETIC FIELDS FOR
CHIROPTICAL SPECTROSCOPIES

CHIRAL PLASMONIC NEAR-FIELD SOURCES
CONTROL OF CHIRAL ELECTROMAGNETIC FIELDS FOR
CHIROPTICAL SPECTROSCOPIES

Von der Fakultät Mathematik und Physik
der Universität Stuttgart zur Erlangung der Würde
eines Doktors der Naturwissenschaften (Dr. rer. nat.)
genehmigte Abhandlung

vorgelegt von

Martin Schäferling

aus Donauwörth

Hauptberichter: Prof. Dr. Harald Giessen
Mitberichterin: Jun.-Prof. Dr. Maria Fyta
Tag der Einreichung: 04.02.2015
Tag der mündlichen Prüfung: 27.02.2015

4. Physikalisches Institut der Universität Stuttgart

2016

Martin Schäferling: *Chiral Plasmonic Near-Field Sources: Control of Chiral Electromagnetic Fields for Chiroptical Spectroscopies*, 2016

Für Resi (1921–2014)

We are not to tell nature what she's gotta be.
... She's always got better imagination than we have.

— *Richard P. Feynman*

ABSTRACT

This thesis investigates the chiral near-field response of plasmonic nanostructures. The chiral properties of electromagnetic fields can be quantified by the so-called optical chirality, which is a figure that can be directly calculated from basic field properties. The larger the optical chirality is, the stronger the respective field will interact with chiral molecules.

In principle, electromagnetic fields with high optical chirality enable the detection of the handedness of chiral molecules with enhanced sensitivity. This is of major importance in biochemistry and pharmaceuticals because biological processes essentially depend on the handedness of the involved molecules. We introduce the concept of chiral plasmonic near-field sources to aid the respective chiroptical spectroscopy techniques.

We cover two main topics in our systematic analysis: Firstly, what are the conditions and mechanisms to generate and enhance chiral near-fields? And secondly, which requirements for chiral plasmonic near-field sources exist and how can they be fulfilled? For this, we group the near-field sources regarding the chiral symmetry properties of both the nanostructure as well as the incident light. Both of these constituents influence the properties of the resulting chiral plasmonic near-field sources.

Chiral nanostructures offer the possibility to enhance the optical chirality of the incident light. We show that planar chirality can lead to regions with chiral near-fields of uniform handedness. Regions with opposite handedness are clearly separated by the structure plane. Three-dimensionally chiral structures can exhibit chiral hot-spots where particularly strong optical chirality can be found.

Based on our investigations of chiral structures, we introduce the concept of plasmonic racemates, which are mixtures of both handednesses of the chiral nanostructure. The local interaction with the chiral building blocks allows for the generation of chiral near-fields although the achiral superstructure exhibits no chiroptical far-field response. This enables chiroptical spectroscopy without additional

contributions to the signal due to the presence of a chiral structure. Furthermore, we present a concept for metasurfaces that facilitate plasmonic racemates with particularly high integration density.

The combination of an achiral linear plasmonic nanoantenna with linearly polarized light demonstrates that chiral near-fields can be formed locally in systems without structural chirality. This can be attributed to interference between incident and scattered light, as shown in our analysis. Based on this finding, we propose a chiroptical spectroscopy method that utilizes linearly polarized light instead of the circular polarization that is commonly used.

Furthermore, we demonstrate that the eigenmodes of chiral systems can lead to particularly strong and extended chiral near-fields. The most efficient way to excite these modes is linearly polarized light. We obtained the best results from a design consisting of four intertwined helices. Chiral near-fields have been found in the whole volume surrounded by the structure. In addition, we discuss a configuration of slanted slits on top of a mirror. This design is easy to fabricate and enables chiroptical spectroscopy via reflection measurements.

In summary, we provide fundamental insights into the functioning as well as the properties of chiral plasmonic near-field sources. We show that this concept can be used for highly sensitive enantiomer discrimination and how this can be accomplished. Furthermore, we provide a theoretical basis to optimize chiral plasmonic near-field sources.

ZUSAMMENFASSUNG

Die vorliegende Arbeit untersucht die chirale Nahfeldantwort plasmonischer Nanostrukturen. Die chiralen Eigenschaften elektromagnetischer Felder können über die sogenannte optische Chiralität – ein Wert, der sich direkt aus den bekannten elektromagnetischen Feldgrößen berechnen lässt – quantifiziert werden: Je höher die optische Chiralität, desto stärker interagiert das Feld mit chiralen Molekülen.

Felder mit besonders hoher optischer Chiralität erlauben es prinzipiell, die Händigkeit von chiralen Molekülen mit erhöhter Sensitivität zu bestimmen. Dies hat wichtige Anwendungsbereiche in der Biochemie und der Pharmazie, da biologische Prozesse maßgeblich von der Händigkeit der beteiligten Moleküle abhängen. In der Arbeit wird das Konzept der chiralen plasmonischen Nahfeldquellen eingeführt, um chirale optische Spektroskopiemethoden zu unterstützen.

Durch systematische Untersuchungen wird einerseits die Fragestellung, unter welchen Voraussetzungen und nach welchen Mechanismen chirale Nahfelder erzeugt und verstärkt werden, behandelt. Andererseits wird untersucht, welche Anforderungen an chirale plasmonische Nahfeldquellen gestellt werden müssen und wie diese erfüllt werden können. Dazu werden potentielle Nahfeldquellen an Hand der chiralen Symmetrieeigenschaften von sowohl der Nanostruktur als auch des einfallenden Lichts gruppiert. Beide Konstituenten beeinflussen die Eigenschaften der chiralen plasmonischen Nahfeldquelle.

Eine Möglichkeit, die optische Chiralität des einfallenden Lichts zu erhöhen, ist durch chirale Nanostrukturen gegeben. Es wird gezeigt, dass planare Chiralität zu Gebieten führen kann, die chirale Felder mit einheitlicher Händigkeit beherbergen. Dabei sind unterschiedliche Händigkeiten klar durch die Ebene, in der die Struktur liegt, voneinander abgetrennt. Dreidimensional chirale Strukturen können lokale Hotspots erzeugen, in denen besonders starke optische Chiralität vorherrscht.

Ausgehend von unseren Untersuchungen an chiralen Strukturen wird das Konzept plasmonischer Razemate, die aus einer Mischung beider Händigkeiten der Nanostruktur aufgebaut sind, eingeführt.

Obwohl diese achiralen Superstrukturen keine chirale Fernfeldantwort besitzen, können durch die lokale Interaktion mit den chiralen Konstituenten weiterhin chirale Nahfelder erzeugt werden. Dies erlaubt chirale Spektroskopie ohne Signalbeiträge durch die chirale Struktur. Weiterhin wird ein Konzept für Metaoberflächen vorgestellt, welches plasmonische Razemate mit besonders hoher Integrationsdichte ermöglicht.

Die Kombination einer achiralen linearen plasmonischen Nanoantenne mit linear polarisiertem Licht zeigt, dass auch Systeme ohne geometrische Chiralität lokal chirale Nahfelder erzeugen können. Unsere Analyse zeigt, dass dies durch die Interferenz zwischen einfallendem und gestreutem Licht hervorgerufen wird. Darauf aufbauend wird ein chirales optisches Spektroskopieverfahren, das linear polarisiertes Licht an Stelle der sonst eingesetzten Zirkularpolarisation verwendet, vorgestellt.

Weiterhin wird in der Arbeit demonstriert, dass die Eigenmoden chiraler Strukturen, die am effizientesten mit linear polarisiertem Licht angeregt werden, zu besonders starken und ausgedehnten chiralen Nahfeldern führen. Die besten Ergebnisse wurden hier mit einem Design aus vier ineinander gewundenen Helices erzielt, bei dem das komplette von der Struktur umschlossene Volumen chirale Nahfelder aufweist. Darüber hinaus wird eine Anordnung von schrägen Schlitzten über einem Spiegel, welche besonders einfach herzustellen ist, diskutiert. Diese erlaubt chirale optische Spektroskopie mittels einer Reflexionsmessung.

Zusammenfassend liefert die vorliegende Arbeit grundlegende Einblicke in die Funktionsweise sowie die Eigenschaften chiraler plasmonischer Nahfeldquellen. Es wird gezeigt, dass und wie dieses Konzept für eine hochsensitive Detektion der Händigkeit chiraler Moleküle eingesetzt werden kann. Weiterhin werden theoretische Grundlagen für die Optimierung chiraler plasmonischer Nahfeldquellen bereitgestellt.

KURZFASSUNG

Der Begriff „Chiralität“ bezeichnet eine Symmetrieeigenschaft, bei der die beiden Spiegelbilder eines Objekts nicht deckungsgleich übereinander gelegt werden können. Die Natur zeigt vielfältige Realisierungen dieser geometrischen Eigenschaft. Das bekannteste Beispiel ist die menschliche Hand, aber auch auf mikroskopischer Ebene weisen viele Moleküle Chiralität in der Anordnung ihrer Atome auf.

Die sogenannte Händigkeit chiraler Moleküle hat einen maßgeblichen Einfluss auf chemische und biologische Prozesse. Entsprechend werden für Anwendungsfelder wie die Biochemie oder die Pharmazie Methoden benötigt, diese Händigkeit auch für kleine Stoffkonzentrationen mit hoher Sensitivität zu bestimmen. Allerdings zeigen nur Messgrößen, die auf einer Interaktion mit anderen chiralen Objekten basieren, eine Abhängigkeit von der Händigkeit der Probe.

Das gebräuchlichste Verfahren für die Bestimmung der Händigkeit ist die sogenannte Zirkulardichroismusspektroskopie, bei der der Absorptionsunterschied für links- und rechtszirkular polarisiertes Licht gemessen wird. Stoffe unterschiedlicher Händigkeit zeichnen sich dabei durch entgegengesetzte spektrale Verläufe dieses Absorptionsunterschieds aus. Allerdings ist der Unterschied mehrere Größenordnungen kleiner als die händigkeitsunabhängige Absorption des Lichts.

Plasmonische Nanostrukturen – metallische Objekte mit Strukturgrößen deutlich unter der Wellenlänge von Licht – ermöglichen die Konzentration von Licht weit unterhalb des Beugungslimits. Die in den auftretenden Resonanzen, deren Frequenzen sich über die Geometrie steuern lassen, erhöhten Nahfelder erlauben eine besonders starke Licht-Materie-Interaktion, die zum Beispiel für eine Sensitivitätserhöhung in der Absorptionsspektroskopie eingesetzt wird.

Erste Arbeiten haben gezeigt, dass plasmonische Nanostrukturen ebenfalls eine Verstärkung des Zirkulardichroismussignals nach sich ziehen können. Allerdings wird die Interpretation experimenteller Arbeiten durch die bei diesen Messungen auftretende Sensitivität für geometrische Imperfektionen erschwert. Die größte Verstärkung zeigt sich in Systemen aggregierter Nanopartikel, in denen zwischen

den einzelnen Partikeln starke Hotspots auftreten. Systematische theoretische Untersuchungen beschränken sich bisher auf sehr einfache Strukturen wie Kugeln, die auch in Kombination mit chiralen Molekülen analytisch oder semi-analytisch behandelt werden können. Die theoretisch berechnete Verstärkung wurde auf eine Interaktion mit dem elektrischen Feld zurückgeführt. Sie tritt nur in den sehr kleinen Bereichen maximaler Feldüberhöhung auf.

In einer grundlegenden Arbeit wurde gezeigt, dass der Zirkulardichroismus theoretisch auf eine Eigenschaft des elektromagnetischen Felds – die sogenannte optische Chiralität – zurückgeführt werden kann. Dieser Wert, der sich für monochromatische Felder direkt aus bekannten elektromagnetischen Feldgrößen wie dem elektrischen und magnetischen Feld sowie der Frequenz berechnen lässt, quantifiziert den zu erwartenden Zirkulardichroismus. Insbesondere kann auf diese Weise der Beitrag des Felds vom Beitrag der chiralen Probe separiert werden, so dass beides unabhängig voneinander optimiert werden kann.

Somit besteht eine weitere Möglichkeit, die Sensitivität chiraler optischer Spektroskopiemethoden zu erhöhen, in einer Erhöhung der optischen Chiralität des einfallenden Lichts. Während für ebene Wellen maximale optische Chiralität für Zirkularpolarisation erzielt wird, lassen sich, wie in dieser Arbeit zum ersten Mal systematisch gezeigt wird, Bereiche mit überhöhter optischer Chiralität in den Nahfeldern plasmonischer Nanostrukturen erzeugen. Allerdings erfordert dies andere Designkriterien als die bekannte Erhöhung der elektrischen Feldstärke, da neben dem elektrischen Feld auch das magnetische Feld sowie deren relative Phase kontrolliert werden muss. Diese Anforderungen lassen komplexe Geometrien erwarten, die jedoch mit etablierten numerischen Verfahren analysiert werden können, da die Strukturen unabhängig von den zu untersuchenden chiralen Molekülen optimiert werden können.

Diese grundsätzliche Idee führt zum Konzept der chiralen plasmischen Nahfeldquelle: Eine Nanostruktur, die unter der korrekten Beleuchtung Nahfelder mit hoher optischer Chiralität erzeugt, welche dann für chirale optische Spektroskopiemethoden genutzt werden können. Dieser Nutzungsanspruch erfordert neben hoher optischer Chiralität eine möglichst homogene und weiträumige Verteilung der chiralen Felder, die darüber hinaus einfach für chirale Moleküle zu

erreichen sein müssen. Zusätzliche Einschränkungen für potentielle Nahfeldquellen sind durch Limitierungen der gebräuchlichen Nanofabrikationsmethoden gegeben.

In dieser Arbeit wird eine grundlegende numerische Analyse verschiedener Klassen von Nahfeldquellen vorgenommen. Diese Klassen sind durch die chiralen Symmetrieeigenschaften der Nanostruktur sowie des einfallenden Lichts gegeben. Nur durch die Kombination beider Elemente wird eine chirale Nahfeldquelle beschrieben. Deshalb wurden chirale und achirale Nanostrukturen untersucht, die jeweils mit chiraalem (wobei hier eine Beschränkung auf zirkular polarisiertes Licht stattgefunden hat) und achiraalem Licht beleuchtet werden. Im Folgenden werden die wichtigsten Ergebnisse dieser Klassen zusammengefasst. Gleichzeitig wird die Eignung verschiedener Klassen als chirale plasmonische Nahfeldquelle diskutiert.

Bei der Untersuchung chiraler plasmonischer Nanostrukturen, die mit zirkular polarisiertem Licht beleuchtet werden, muss zunächst zwischen planarer und dreidimensionaler Chiralität unterschieden werden. Alle untersuchten planar chiralen Strukturen resultieren in beiden Händigkeiten von chiralen Nahfeldern, die räumlich getrennt sind, aber vergleichbare Werte aufweisen. Eine besonders gute Trennung kann für eine Spirale erzielt werden: Auf jeder Seite der Struktur herrscht nur eine Händigkeit vor. Weiterhin können auf der jeweiligen Seite der Spirale chirale Nahfelder mit entgegengesetzter Händigkeit durch einen Wechsel der einfallenden Polarisation erzeugt werden. Allerdings unterscheiden sich die Orte stärkster Chiralität für die unterschiedlichen Beleuchtungsszenarien räumlich.

Diese Einschränkung lässt sich durch dreidimensional chirale Nanostrukturen überwinden. Im Gegensatz zu planar chiralen Strukturen wechselwirken diese besonders stark mit einer präferierten zirkularen Polarisation, wie am Beispiel der Helix gezeigt. Die entgegengesetzte Polarisation regt die Struktur weitaus schwächer an, erzeugt dabei aber chirale Nahfelder mit entgegengesetzter Händigkeit an ähnlichen Positionen.

Dieser Effekt führt zu einem ausgeprägten chiralen Hotspot für ein chirales plasmonisches Oligomer, das aus einer chiralen Anordnung von sechs Metallscheiben in zwei Ebenen besteht. In diesem Hotspot kann bei einem Wechsel der einfallenden zirkularen Polarisation lokal ein Chiralitätsunterschied erreicht werden, der den Unterschied

zwischen links- und rechtszirkular polarisiertem Licht um zwei Größenordnungen übersteigt.

Trotz der starken chiralen Nahfeldantwort chiraler plasmonischer Oligomere können diese nicht ohne Weiteres als plasmonische Nahfeldquellen genutzt werden. Der Grund liegt in der bereits beschriebenen asymmetrischen Interaktion mit den unterschiedlichen einfallenden Polarisierungen. Ein reines Zirkulardichroismussignal, das für die spätere Analyse einfach auszuwerten ist, kann nur durch Feldpaare mit entgegengesetzter Händigkeit, aber gleichbleibender Energiedichte erreicht werden. Dies ist für chirale plasmonische Nanostrukturen jedoch nicht gegeben. Deshalb wurden sie zum Konzept der plasmonischen Razemate erweitert.

In solch einem Razemat werden beide Händigkeiten der plasmonischen Struktur kombiniert und simultan beleuchtet. Dadurch entsteht insgesamt eine achirale Struktur, die sich jedoch lokal wie die entsprechende chirale Nanostruktur verhält, solange Nahfeldkopplung durch eine genügend große räumliche Distanz zwischen den einzelnen Strukturen ausgeschlossen werden kann. Insgesamt entsteht auf diese Weise eine symmetrische Anregung, da jede einfallende Polarisation bevorzugt mit der zugehörigen chiralen Nanostruktur interagiert. Damit lässt sich für jeden Punkt im Raum ein korrespondierender Punkt finden, an dem die Nahfelder exakte chirale Symmetrie aufweisen. Weiterhin erzeugt eine solche Anordnung keinen Zirkulardichroismus in Abwesenheit chiraler Moleküle, wie es bei chiralen Nanostrukturen der Fall wäre. Somit dient das Konzept der plasmonischen Razemate auch zur Unterdrückung dieses Hintergrundsignals.

Ein Nachteil plasmonischer Razemate ist die Komplexität der Einheitszelle, die aus einer symmetrischen Kombination beider Händigkeiten der chiralen Struktur besteht und damit die vierfache Größe der ursprünglichen Einheitszelle aufweist. Dieser Nachteil kann über sogenannte lokal chirale plasmonische Metaoberflächen aufgelöst werden. Hierbei wird die Vorstellung einzelner plasmonischer Strukturen aufgegeben und stattdessen ein komplexes Netz aus gekoppelten Einzelstrukturen erzeugt. Dieses ist dergestalt angelegt, dass lokal chirale Formationen auftreten, wobei – abhängig vom Ort – links- oder rechtshändige Strukturen vorherrschen. In einer solchen Struktur regt zirkular polarisiertes Licht bevorzugt eine Händigkeit der lokalen Strukturen an, was sich in der entsprechenden Händigkeit

der lokalen Nahfelder manifestiert. Auf die gleiche Weise wie plasmonische Razemate sind lokal chirale Metaoberflächen global achiral, erlauben dafür aber eine einfachere Einheitszelle sowie eine höhere Packungsdichte.

Für die Eignung als chirale Nahfeldquelle sollten solche Metaoberflächen neben lokaler Chiralität und globaler Achiralität eine vierzählige Rotationssymmetrie sowie eine ausreichende Kopplung zwischen den einzelnen Elementen aufweisen. Besteht die Metaoberfläche aus zwei Lagen, in denen Metallscheiben auf einem periodischen Gitter angeordnet werden, so lässt sich der Parameterraum durch geometrische Überlegungen auf sieben verschiedene Geometrien mit diesen Eigenschaften reduzieren. Alle diese Geometrien weisen Nahfelder auf, die ihre Händigkeit abhängig von der eingestrahnten Polarisation ändern. Zusätzlich konnten in der numerischen Simulation Geometrien ermittelt werden, bei denen für jeweils eine eingestrahlte Polarisation die zugehörige Händigkeit im Nahfeld dominiert. Die optische Chiralität der Nahfelder ist vergleichbar mit der Nahfeldantwort der untersuchten planar chiralen Strukturen. Die Stärke chiraler Hotspots dreidimensionaler Strukturen, die in diesem Konzept bisher noch nicht reproduziert werden konnte, lassen auf weiteres Optimierungspotential für lokal chirale Metaoberflächen schließen.

Grundlegende Einblicke in den Entstehungsmechanismus chiraler Nahfelder können durch die Untersuchung linearer Nanoantennen unter normalem Einfall von linear polarisiertem Licht mit einem parallel zur Antenne ausgerichteten Polarisationsvektor gewonnen werden. Trotz der fehlenden geometrischen Chiralität treten lokal chirale Nahfelder auf, die nur bei räumlicher Mittelung verschwinden. Diese Felder entstehen durch Interferenz zwischen einfallendem und gestreutem Licht. Ein analytisches Modell, das die Antenne durch einen Hertz'schen Dipol beschreibt, führt zu den gleichen qualitativen Ergebnissen. Dies liefert die wichtige Erkenntnis, dass optische Chiralität durch plasmonische Nanostrukturen nicht nur verstärkt wird, sondern dass mit Hilfe der richtigen Konstellation chirale Nahfelder erzeugt werden können.

Weiterhin zeigt sich, dass die Beleuchtung mit zirkular polarisiertem Licht keine signifikante Verstärkung oder sonstige Verbesserung der chiralen Nahfelder nach sich zieht. Sie werden weiterhin durch den Beitrag, der schon bei linearer Polarisation auftritt, dominiert.

Entsprechend sollte die einfallende Polarisation nicht auf Grund ihrer intrinsischen optischen Chiralität ausgewählt werden. Stattdessen muss die Polarisation gesucht werden, die mit der gewählten Struktur optimal interagiert. Im Fall geometrisch achiraler Strukturen ist dabei die Phase zwischen einfallendem und gestreutem Licht essentiell, da sich daraus die Interferenzeigenschaften ableiten.

Eine Abwandlung der sehr einfachen Antennengeometrie erlaubt die grundlegende Demonstration chiraler optischer Spektroskopie mit linear polarisiertem Licht. Dazu wird ein Goldquadrat abwechselnd mit orthogonalen linearen Polarisationen beleuchtet, wodurch sich die Händigkeit der chiralen Nahfelder an jeder Ecke des Quadrats ändert. Ein chirales Medium, das in der numerischen Simulation nur an gegenüberliegenden Ecken positioniert wurde, zeigt deswegen eine unterschiedliche Absorption für die beiden linearen Polarisationen. Diese Absorptionsdifferenz, die analog zum Zirkulardichroismus in konventioneller chiraler optischer Spektroskopie auftritt, demonstriert die generelle Funktionalität des Konzepts chiraler plasmomischer Nahfeldquellen.

Im Vergleich zu achiralen Strukturen unterstützen geometrisch chirale Strukturen Eigenmoden, deren Nahfelder optische Chiralität aufweisen. In diesem Fall vereinfacht sich die Optimierung der einfallenden Polarisation zu derjenigen, welche die stärkste Kopplung an die entsprechende Mode ermöglicht. Eine besonders gute Geometrie stellt unter diesem Gesichtspunkt die Helix dar, da die auftretenden parallelen elektrischen und magnetischen Feldvektoren im Inneren die optische Chiralität maximieren.

Die Kopplung an das einfallende Feld ist maximal für lineare Polarisation entlang der Helixachse. Der maßgebliche Parameter ist das Verhältnis zwischen Radius und Windungsabstand der Helix. Langgezogene Helices haben ein stärkeres Dipolmoment und koppeln besser an das einfallende Feld, eng gewundene Helices erzeugen homogene chirale Nahfelder. Ein Kompromiss kann mit mehreren ineinander gewundenen Helices erreicht werden, welche sehr starke chirale Nahfelder über einen großen räumlichen Bereich – das von den Helices umschlossene Volumen – erzeugen.

Die genauen Optimierungsvorschriften für solche ineinander gewundenen Helices hängen von der Größe des Zieldesigns ab. Während kleine Strukturen im Bereich einiger hundert Nanometer von

einer stärkeren Kopplung an das äußere Feld profitieren, können die stärksten Nahfelder für Strukturgrößen im Mikrometerbereich für engere Windungen und der damit einhergehenden stärkeren Kopplung zwischen den Helices erzielt werden. Für Helices mit einem Durchmesser von $1.2\ \mu\text{m}$ kann auf diese Weise eine um beinahe 200 mal stärkere chirale Nahfeldantwort als für zirkular polarisiertes Licht erreicht werden. Diese beschränkt sich dabei nicht nur auf einzelne Hotspots: Selbst bei einer Mittelung über den gesamten von der Helix umschlossenen Bereich wird ein Faktor von über 50 erzielt.

Der größte Nachteil der vorgeschlagenen Geometrie mit mehreren Helices ist ihre Komplexität und damit einhergehende Fabrikationsschwierigkeiten. Als alternatives Design können zwei übereinander liegende Metallfilme, wobei in den oberen Film schräge Schlitzte eingefügt sind, genutzt werden. Der untere Film dient in dieser Anordnung als Spiegel. Die Fabrikation ist vergleichsweise einfach, da nur eine nanostrukturierte Lage hergestellt werden muss. In diesem Design wird einfallendes linear polarisiertes Licht bei Reflexion in die orthogonale Polarisierung konvertiert. Dies führt zu homogenen chiralen Nahfeldern innerhalb der Löcher. Auf diese Weise wird chirale optische Spektroskopie mit linearer Polarisierung in einer Reflexionsgeometrie ermöglicht, was im Kontrast zu konventionellen chiralen Spektroskopiemethoden, die in Transmission durchgeführt werden, steht.

Zusammenfassend weisen die verschiedenen Klassen chiraler plasmonischer Nahfeldquellen fundamental unterschiedliche Eigenschaften auf. Geometrisch chirale Strukturen, die mit zirkular polarisiertem Licht beleuchtet werden, resultieren in verstärkten chiralen Nahfeldern, die jedoch nicht direkt für die Enantiomerdiskriminierung eingesetzt werden können. Plasmonische Razemate ermöglichen die lokale Nutzung dieser Mechanismen in global achiralen Strukturen. Die Kombination geometrisch achiraler Strukturen mit linear polarisiertem Licht liefert die Erkenntnis, dass chirale Nahfelder selbst in Systemen ohne jegliche geometrische Chiralität erzeugt werden können. In geometrisch chirale Strukturen unter linear polarisiertem Einfall kann eine starke chirale Nahfeldantwort über ein großes Volumen erzielt werden. Damit ist diese Kombination am vielversprechendsten für chirale optische Spektroskopie, wobei das Konzept der plasmonischen Razemate durch seine Einfachheit ebenfalls Vorteile aufweist.

SCIENTIFIC CONTRIBUTIONS

ARTICLES IN PEER-REVIEWED SCIENTIFIC JOURNALS

Articles about chirality in plasmonics:

- [A1] M. Hentschel, **M. Schäferling**, T. Weiss, N. Liu, and H. Giessen: *Three-dimensional Chiral Plasmonic Oligomers*. *Nano Lett.* **12**, 2542–2547 (2012).
DOI 10.1021/nl300769x, cit. on pp. 34, 35, 39.
- [A2] **M. Schäferling**, D. Dregely, M. Hentschel, and H. Giessen: *Tailoring enhanced optical chirality: Design principles for chiral plasmonic nanostructures*. *Phys. Rev. X* **2**, 031010 (2012).
DOI 10.1103/PhysRevX.2.031010, cit. on pp. 4, 160.
- [A3] M. Hentschel, L. Wu, **M. Schäferling**, P. Bai, E. P. Li, and H. Giessen: *Optical Properties of Chiral Three-dimensional Plasmonic Oligomers at the Onset of Charge-transfer Plasmons*. *ACS Nano* **6**, 10355–10365 (2012).
DOI 10.1021/nn304283y, cit. on p. 35.
- [A4] **M. Schäferling**, X. Yin, and H. Giessen: *Formation of chiral fields in a symmetric environment*. *Opt. Express* **20**, 26326–26336 (2012).
DOI 10.1364/OE.20.026326, cit. on pp. 4, 160.
- [A5] M. Hentschel, **M. Schäferling**, B. Metzger, and H. Giessen: *Plasmonic Diastereomers: Adding up Chiral Centers*. *Nano Lett.* **13**, 600–606 (2013).
DOI 10.1021/nl3041355, cit. on p. 36.
- [A6] B. Frank, X. Yin, **M. Schäferling**, J. Zhao, S. M. Hein, P. V. Braun, and H. Giessen: *Large-area 3D chiral plasmonic structures*. *ACS Nano* **7**, 6321–6329 (2013).
DOI 10.1021/nn402370x, cit. on pp. 38, 39.

- [A7] X. Yin, **M. Schäferling**, B. Metzger, and H. Giessen: *Interpreting Chiral Nanophotonic Spectra: The Plasmonic Born-Kuhn Model*. *Nano Lett.* **13**, 6238–6243 (2013).
DOI 10.1021/n1403705k, cit. on pp. 36, 94.
- [A8] **M. Schäferling**, X. Yin, N. Engheta, and H. Giessen: *Helical Plasmonic Nanostructures as Prototypical Chiral Near-Field Sources*. *ACS Photonics* **1**, 530–537 (2014).
This article has been highlighted on the cover.
DOI 10.1021/ph5000743, cit. on pp. 4, 159, 160.
- [A9] X. Yin, **M. Schäferling**, A.-K. U. Michel, A. Tittl, M. Wuttig, T. Taubner, and H. Giessen: *Active Chiral Plasmonics*. *Nano Lett.* **15**, 4255–4260 (2015).
DOI 10.1021/n15042325, cit. on p. 40.

Other articles beyond the topics of this thesis:

- [O1] P. Schau, L. Fu, K. Frenner, **M. Schäferling**, H. Schweizer, H. Giessen, L. M. G. Venancio, and W. Osten: *Polarization scramblers with plasmonic meander-type metamaterials*. *Opt. Express* **20**, 22700–22711 (2012).
DOI 10.1364/OE.20.022700.
- [O2] L. Wollet, B. Frank, **M. Schäferling**, M. Mesch, S. M. Hein, and H. Giessen: *Plasmon hybridization in stacked metallic nanocups*. *Opt. Mater. Express* **2**, 1384–1390 (2012).
DOI 10.1364/OME.2.001384.
- [O3] N. Strohheldt, A. Tittl, **M. Schäferling**, F. Neubrech, U. Kreibitz, R. Griessen, and H. Giessen: *Yttrium Hydride Nanoantennas for Active Plasmonics*. *Nano Lett.* **14**, 1140–1147 (2014).
DOI 10.1021/n1403643v.
- [O4] A. Tittl, M. G. Harats, R. Walter, X. Yin, **M. Schäferling**, N. Liu, R. Rapaport, and H. Giessen: *Quantitative Angle-Resolved Small-Spot Reflectance Measurements on Plasmonic Perfect Absorbers: Impedance Matching and Disorder Effects*. *ACS Nano* **8**, 10885–10892 (2014).
DOI 10.1021/nn504708t.

- [O5] A. Tittl, A.-K. U. Michel, **M. Schäferling**, X. Yin, B. Gholipour, L. Cui, M. Wuttig, T. Taubner, F. Neubrech, and H. Giessen: *Switchable mid-infrared plasmonic perfect absorber with multispectral thermal imaging capability*. *Adv. Mater.* **27**, 4597–4603 (2015).
This article has been highlighted on the front inside cover.
DOI 10.1002/adma.201502023.

CONTRIBUTIONS TO INTERNATIONAL CONFERENCES AND WORKSHOPS

Invited talks and colloquia:

- [I1] P. V. Braun, K. Arpin, S. Gupta, A. Radke, **M. Schäferling**, and H. Giessen: *Electrochemical Fabrication of Chiral Metamaterials*, 3rd International Conference on Metamaterials, Photonic Crystals and Plasmonics (META), Paris (France), 2012.
- [I2] **M. Schäferling**: *Plasmonic Nanostructures as Near-Field Sources for Chiroptical Spectroscopy*, Colloquium of the Engheta Group, University of Pennsylvania, Philadelphia (USA), 2013.
- [I3] H. Giessen, N. Strohfeldt, A. Tittl, F. Neubrech, **M. Schäferling**, R. Griessen, and U. Kreibig: *Novel switchable and reconfigurable active plasmonic materials and devices*, 8th International Congress on Advanced Electromagnetic Materials in Microwaves and Optics (Metamaterials), Copenhagen (Denmark), 2014.

Contributed talks (presenting author):

- [T1] **M. Schäferling**, D. Dregely, T. Weiss, and H. Giessen: *Quantifying Chirality in 2D and 3D Metallic Metamaterials*, DPG Frühjahrstagung der Sektion AMOP (SAMOP) und der Sektion Kondensierte Materie (SKM), Dresden (Germany), 2011.

- [T2] **M. Schäferling**, D. Dregely, M. Hentschel, and H. Giessen: *Spatially resolved enhancement of chirality in planar and 3D chiral metamaterials*, 5th International Congress on Advanced Electromagnetic Materials in Microwaves and Optics (Metamaterials), Barcelona (Spain), 2011.
- [T3] M. Hentschel, **M. Schäferling**, T. Weiss, H.-G. Kuball, N. Liu, and H. Giessen: *Three-dimensional Chiral Plasmonic Oligomers*, DPG Frühjahrstagung der Sektion Kondensierte Materie (SKM), Berlin (Germany), 2012.
- [T4] **M. Schäferling**, M. Hentschel, D. Dregely, and H. Giessen: *Local enhancement of optical chirality in planar and 3D plasmonic nanostructures*, DPG Frühjahrstagung der Sektion Kondensierte Materie (SKM), Berlin (Germany), 2012.
- [T5] **M. Schäferling**, M. Hentschel, D. Dregely, and H. Giessen: *Local Enhancement of Optical Chirality in Plasmonic Nanostructures*, 8th Workshop on Numerical Methods for Optical Nano Structures, Zurich (Switzerland), 2012.
- [T6] **M. Schäferling**, M. Hentschel, D. Dregely, X. Yin, and H. Giessen: *Design of Plasmonic Nanostructures for Chiral Sensing*, Fifth International Workshop on Theoretical and Computational Nano-Photonics (TaCoNa), Bad Honnef (Germany), 2012.
- [T7] **M. Schäferling**, X. Yin, and H. Giessen: *Chiral Fields in Achiral Systems*, DPG Frühjahrstagung der Sektion Kondensierte Materie (SKM), Regensburg (Germany), 2013.
- [T8] M. Hentschel, **M. Schäferling**, B. Metzger, and H. Giessen: *Plasmonic Diastereomers: Adding Up Chiral Centers*, 6th International Conference on Surface Plasmon Photonics (SPP), Ottawa (Canada), 2013.
- [T9] **M. Schäferling**, X. Yin, and H. Giessen: *Chiral Fields in Achiral Systems: Towards Enantiomer Sensing with Linearly Polarized Light*, 6th International Conference on Surface Plasmon Photonics (SPP), Ottawa (Canada), 2013.
- [T10] **M. Schäferling**, X. Yin, and H. Giessen: *Chiral Fields in Achiral Systems: Towards Enantiomer Sensing with Linearly Polarized Light*, 14th International Conference on Chiroptical Spectroscopy, Nashville (USA), 2013.

- [T11] **M. Schäferling**, X. Yin, and H. Giessen: *Chiral Fields in Achiral Systems*, 9th Workshop on Numerical Methods for Optical Nano Structures, Zurich (Switzerland), 2013.
- [T12] **M. Schäferling**, X. Yin, N. Engheta, and H. Giessen: *Helical Plasmonic Nanostructures for Strong Chiral Near-Fields*, DPG Frühjahrstagung der Sektion Kondensierte Materie (SKM), Dresden (Germany), 2014.
- [T13] **M. Schäferling**, X. Yin, N. Engheta, and H. Giessen: *Helical Plasmonic Nanostructures as Prototypical Chiral Near-Field Sources*, 8th International Congress on Advanced Electromagnetic Materials in Microwaves and Optics (Metamaterials), Copenhagen (Denmark), 2014.

Poster contributions (presenting author):

- [P1] **M. Schäferling**, N. Andermahr, C. Fallnich, S. Pricking, P. Kegel, S. Gorlatch, and H. Giessen: *GPU-accelerated Simulation of Linear and Nonlinear Optical Beam Propagation in Waveguides*, International Conference on Simulation Technology (SimTech), Stuttgart (Germany), 2011.
- [P2] **M. Schäferling**, D. Dregely, M. Hentschel, T. Weiss, and H. Giessen: *Spatially resolved enhancement of chirality in planar and 3D chiral plasmonic nanostructures*, Fourth International Workshop on Theoretical and Computational Nano-Photonics (TaCoNa), Bad Honnef (Germany), 2011.
- [P3] **M. Schäferling**, D. Dregely, M. Hentschel, X. Yin, J. Dorfmueller, and H. Giessen: *Local enhancement of optical chirality in plasmonic nanostructures*, 12th International Conference on Near-field Optics and Related Techniques (NFO), San Sebastian (Spain), 2012.
- [P4] **M. Schäferling**, X. Yin, and H. Giessen: *Symmetric Structures Produce Chiral Near Fields: Towards Enantiomer Sensing with Linearly Polarized Light*, 4th International Topical Meeting on Nanophotonics and Metamaterials (Nanometa), Seefeld (Austria), 2013.

- [P5] M. Mesch, B. Frank, M. Hentschel, **M. Schäferling**, X. Yin, C. Zhang, P. V. Braun, and H. Giessen: *Non-invasive Glucose Sensing*, Forschungstag BW Stiftung, Stuttgart (Germany), 2013.
- [P6] **M. Schäferling**, X. Yin, N. Engheta, and H. Giessen: *Helical Plasmonic Nanostructures as Prototypical Chiral Near-Field Sources*, Chirality, Prague (Czech Republic), 2014.

Contributions as co-author:

- [C1] D. Dregely, **M. Schäferling**, and H. Giessen: *Spiral Optical Nanoantenna*. Talk, DPG Frühjahrstagung der Sektion AMOP (SAMOP) und der Sektion Kondensierte Materie (SKM), Dresden (Germany), 2011.
- [C2] M. Hentschel, **M. Schäferling**, T. Weiss, H.-G. Kuball, N. Liu, and H. Giessen: *Three-dimensional Chiral Plasmonic Oligomers*. Talk, 3rd International Conference on Metamaterials, Photonic Crystals and Plasmonics (META), Paris (France), 2012.
- [C3] P. Schau, L. Fu, K. Frenner, H. Schweizer, **M. Schäferling**, H. Giessen, L. M. G. Venancio, S. Hannemann, and W. Osten: *Polarization scrambling with meander structures*. Talk, SPIE Photonics Europe, Brussels (Belgium), 2012.
- [C4] M. Hentschel, **M. Schäferling**, T. Weiss, H.-G. Kuball, N. Liu, and H. Giessen: *Three-dimensional Chiral Plasmonic Oligomers*. Talk, Conference on Lasers and Electro-Optics (CLEO), San José (USA), 2012.
- [C5] B. Frank, J. Zhao, **M. Schäferling**, X. Yin, S. M. Hein, and H. Giessen: *Low-cost large-area fabrication and chiral optical properties of 3D chiral plasmonic nanoantennas*. Poster, 12th International Conference on Near-field Optics and Related Techniques (NFO), San Sebastian (Spain), 2012.
- [C6] M. Hentschel, **M. Schäferling**, T. Weiss, N. Liu, and H. Giessen: *Three-dimensional chiral plasmonic oligomers*. Talk, 12th International Conference on Near-field Optics and Related Techniques (NFO), San Sebastian (Spain), 2012.

- [C7] P. Schau, L. Fu, K. Frenner, H. Schweizer, **M. Schäferling**, T. Weiss, H. Giessen, L. M. G. Venancio, and W. Osten: *Depolarizers for space applications consisting of spatially distributed meander structures with random orientation*. Talk, 6th International Congress on Advanced Electromagnetic Materials in Microwaves and Optics (Metamaterials), St. Petersburg (Russia), 2012.
- [C8] X. Yin, **M. Schäferling**, S. M. Hein, and H. Giessen: *Plasmonic Analog of the Born-Kuhn Model*. Talk, 4th International Topical Meeting on Nanophotonics and Metamaterials (Nanometa), Seefeld (Austria), 2013.
- [C9] B. Frank, X. Yin, **M. Schäferling**, J. Zhao, S. M. Hein, and H. Giessen: *Large-area 3D chiral plasmonic nanostructures fabricated by colloidal hole mask nanolithography*. Talk, DPG Frühjahrstagung der Sektion Kondensierte Materie (SKM), Regensburg (Germany), 2013.
- [C10] M. Hentschel, **M. Schäferling**, B. Metzger, and H. Giessen: *Plasmonic Diastereomers: Adding Up Chiral Centers*. Talk, DPG Frühjahrstagung der Sektion Kondensierte Materie (SKM), Regensburg (Germany), 2013.
- [C11] X. Yin, **M. Schäferling**, and H. Giessen: *Chiral Plasmonic Realization of the Born-Kuhn Mode*. Poster, 6th International Conference on Surface Plasmon Photonics (SPP), Ottawa (Canada), 2013.
- [C12] X. Yin, **M. Schäferling**, and H. Giessen: *Chiral Plasmonic Realization of the Born-Kuhn Mode*. Poster, 14th International Conference on Chiroptical Spectroscopy, Nashville (USA), 2013.
- [C13] B. Frank, X. Yin, **M. Schäferling**, J. Zhao, S. M. Hein, P. V. Braun, and H. Giessen: *Large-area 3D chiral plasmonic structures*. Poster, Advanced Study Institute NATO Nanomaterials and Nanoarchitectures, Cork (Ireland), 2013.
- [C14] N. Strohfeldt, A. Tittl, **M. Schäferling**, F. Neubrech, U. Kreibig, R. Griessen, and H. Giessen: *Yttrium hydride nanoantennas for reconfigurable plasmonics*. Poster, 551. WE-Heraeus-Seminar: Active Nanoplasmonics and Metamaterial Dynamics, Bad Honnef (Germany), 2014.

- [C15] N. Strohfeldt, A. Tittl, **M. Schäferling**, F. Neubrech, U. Kreibig, R. Griessen, and H. Giessen: *Yttrium hydride nanoantennas for reconfigurable plasmonics*. Talk, DPG Frühjahrstagung der Sektion Kondensierte Materie (SKM), Dresden (Germany), 2014.
- [C16] X. Yin, A.-K. U. Michel, **M. Schäferling**, A. Tittl, T. Taubner, and H. Giessen: *Chiral Plasmonic Fano Resonance*. Talk, DPG Frühjahrstagung der Sektion Kondensierte Materie (SKM), Dresden (Germany), 2014.
- [C17] N. Strohfeldt, A. Tittl, **M. Schäferling**, F. Neubrech, U. Kreibig, R. Griessen, and H. Giessen: *Yttrium Hydride Nanoantennas for Active Plasmonics*. Talk, Gordon Research Seminar on Plasmonics, Newry (USA), 2014.
- [C18] X. Yin, **M. Schäferling**, A.-K. U. Michel, A. Tittl, M. Wuttig, T. Taubner, and H. Giessen: *Tunable and Switchable Mid-IR Chiral Metamaterial*. Poster, Gordon Research Conference on Plasmonics, Newry (USA), 2014.
- [C19] N. Strohfeldt, A. Tittl, **M. Schäferling**, F. Neubrech, U. Kreibig, R. Griessen, and H. Giessen: *Yttrium hydride nanoantennas for reconfigurable plasmonics*. Poster, Gordon Research Conference on Plasmonics, Newry (USA), 2014.
- [C20] X. Yin, **M. Schäferling**, A.-K. U. Michel, A. Tittl, M. Wuttig, T. Taubner, and H. Giessen: *Tunable and Switchable Mid-IR Chiral Metamaterial*. Poster, Chirality, Prague (Czech Republic), 2014.
- [C21] T. Weiss, M. Nesterov, X. Yin, **M. Schäferling**, and H. Giessen: *Rigorous numerical analysis of plasmonically enhanced chiroptical response*. Poster, 5th International Topical Meeting on Nanophotonics and Metamaterials (Nanometa), Seefeld (Austria), 2015.
- [C22] X. Yin, A. Tittl, **M. Schäferling**, A.-K. U. Michel, B. Gholipour, L. Cui, M. Wuttig, T. Taubner, F. Neubrech, and H. Giessen: *Active mid-infrared plasmonic metadevices*. Talk, 5th International Topical Meeting on Nanophotonics and Metamaterials (Nanometa), Seefeld (Austria), 2015.

CONTENTS

1	INTRODUCTION	1
2	CHIRALITY IN NATURE AND SCIENCE	5
2.1	Geometrical Chirality	5
2.1.1	Planar Geometrical Chirality	7
2.1.2	Quantification of Chirality and Handedness	8
2.1.3	Physical Manifestation of Geometrical Chirality	11
2.2	Chiral Electrodynamics	12
2.2.1	Electrodynamics of Metallic Nanoparticles	14
2.2.2	Electronic Models of Chiral Materials	22
2.2.3	Chiral Optical Far-Field Responses	29
2.3	Realization of Chiral Materials	31
2.3.1	Chiral Molecules	31
2.3.2	Chiral Plasmonic Nanostructures	33
3	CHIROPTICAL SPECTROSCOPY	41
3.1	Techniques for Optical Enantiomer Discrimination	41
3.1.1	Circular Dichroism Spectroscopy	41
3.1.2	Other Spectroscopic Techniques	43
3.2	Improved Detection Schemes	44
3.3	Plasmonically Enhanced Sensitivity	46
3.3.1	Single Plasmonic Nanoantennas	47
3.3.2	Plasmonic Hot-Spots	51
3.3.3	Observation of Catalytic Reactions	54
3.3.4	Chiral Hot-Spots	56
4	CHIRAL PROPERTIES OF LIGHT	59
4.1	Optical Chirality	59
4.2	Interaction of Chiral Light with Chiral Molecules	61
4.2.1	Handedness-Dependent Absorption	61
4.2.2	Chiral Forces	63
4.3	Optical Chirality beyond Circular Polarization	64
4.4	Chiral Plasmonic Near-Field Sources	67
4.4.1	Design Goals	68
4.4.2	Symmetry Considerations	68
4.4.3	Analysis Method	70

5	ENHANCEMENT OF CHIRAL FIELDS BY GEOMETRICALLY CHIRAL STRUCTURES	73
5.1	Geometrically Planar Chiral Designs	73
5.1.1	Gammadions	73
5.1.2	Two-Armed Nanospirals	76
5.2	Three-dimensional Geometrically Chiral Designs . .	78
5.2.1	Helices	78
5.2.2	Chiral Plasmonic Oligomers	79
5.2.3	Stereometamaterials	81
5.3	Design Principles	81
6	CHIRAL FIELDS OF MACROSCOPICALLY ACHIRAL ARRANGEMENTS	85
6.1	Racemic Mixtures of Chiral Plasmonic Nanostructures	86
6.2	Collective Response of Chiral Molecules near Plasmonic Racemates	89
6.3	Calculated Performance of Plasmonic Racemates . . .	91
6.4	Locally Chiral Plasmonic Metasurfaces	93
6.4.1	Design Conditions	93
6.4.2	Chiroptical Near-Field Response	99
7	FORMATION OF CHIRAL FIELDS NEAR SYMMETRIC STRUCTURES	103
7.1	Optical Chirality Near a Plasmonic Rod Antenna . . .	103
7.2	Dipole Model for the Generation of Chiral Near-Fields	105
7.2.1	Incident Light with Polarization Parallel to the Dipole Axis	106
7.2.2	Incident Light with Circular Polarization . . .	108
7.2.3	Linearly Polarized Incident Light with Arbitrary Polarization Angle	113
7.3	Chiroptical Spectroscopy with Linearly Polarized Light	114
8	CHIRAL EIGENMODES OF GEOMETRICALLY CHIRAL STRUCTURES	119
8.1	Chiral Eigenmodes	119
8.2	Near-Field Response of Multiple Helices	122
8.2.1	Small Four-Helix Design	124
8.2.2	Large Four-Helix Design	126
8.2.3	Enhanced Chiroptical Spectroscopy	130
8.3	Modified Designs for Practical Applications	132

9	CONCLUSIONS AND OUTLOOK	139
A	TECHNICAL DETAILS	145
A.1	Units of Circular Dichroism	145
A.2	Circularly Polarized Light in CST Microwave Studio	147
A.3	Volume Rendering with POV-Ray	149
B	ELECTROMAGNETIC WAVES IN CHIRAL MEDIA	153
B.1	Chiral Wave Equation	153
B.2	Differential Absorbance	154
C	DETAILS OF OPTICAL CHIRALITY	155
C.1	Definition of Optical Chirality	155
C.2	Calculation of Handedness-Dependent Absorption	157
D	ARTWORK	159
	BIBLIOGRAPHY	161

CONSTANTS

c	speed of light in vacuum, $c = 299\,792\,458\text{ m s}^{-1}$
e	elementary charge, $e = 1.602 \times 10^{-19}\text{ C}$
ϵ_0	vacuum permittivity, $\epsilon_0 = 8.854 \times 10^{-12}\text{ F m}^{-1}$
μ_0	vacuum permeability, $\mu_0 = 4\pi \times 10^{-7}\text{ N A}^{-2}$

SYMBOLS

A	absorbance
a	absorption rate of a single molecule
a^*	combined absorption rate of two molecules (see Section 6.2)
α	electric dipole polarizability
B	magnetic field
\mathcal{B}	magnetic field (real part)
β_b, β_e	prefactors of U_b and U_e in the equation for a
χ	magnetic dipole polarizability
C	optical chirality (see Eq. (4.4))
D	electric displacement field
D	propagation distance
d	distance between oscillators in the Born-Kuhn model
E	electric field
\mathcal{E}	electric field (real part)
ϵ	electric permittivity
ϵ	molar extinction coefficient
g	dissymmetry factor (see Eq. (4.13))
g^*	combined dissymmetry factor of two molecules (see Section 6.2)
γ	damping in oscillator models
Γ	chirality parameter of the Drude-Born-Fedorov chiral constitutive equations (see Eq. (2.44))
H	magnetic field strength
J	Jones vector
j	free current

k	wave number
κ	chirality parameter of the standard chiral constitutive equations (see Eqs. (2.48))
\mathbf{m}	magnetic dipole moment
m^*	effective electron mass
μ	magnetic permeability
N	number of particles described by a oscillator model
n	refractive index
ω	angular frequency
ω_0	resonance frequency
ω_c	chiral coupling parameter
ω_p	plasma frequency (see Eq. (2.12))
Ω	abbreviation used in the Born-Kuhn model, $\Omega := \sqrt{\omega_0^2 - \hat{\gamma}\omega - \omega^2}$ (see Eq. (2.36))
\mathbf{P}	macroscopic polarization
\mathbf{p}	electric dipole moment
ϕ	phase
φ	polarization angle
R	reflectance
ϱ	free charge
T	transmittance
\mathbf{u}	displacement of a harmonic oscillator
U_b	time-averaged magnetic energy density (see Eq. (4.9))
U_e	time-averaged electric energy density (see Eq. (4.8))
ξ	mixed electric-magnetic dipole polarizability

Vectors are printed **bold**. Tensorial quantities are typeset with a double bar on top (e. g., $\bar{\bar{x}}$). A circumflex denotes quantities that have been normalized (e. g., $\hat{x} \equiv x/x_{\text{normto}}$). Differential responses are described by Δ . Partial differentiation with respect to the variable x is denoted by ∂_x . The imaginary unit is written as \hat{i} . The real and imaginary part of a variable x are denoted $\Re(x)$ and $\Im(x)$, respectively.

ACRONYMS

ACS	absorption cross section
CD	circular dichroism
CPL	circularly polarized light
CST MWS	CST Microwave Studio
DLW	direct laser writing
DNA	deoxyribonucleic acid
EBL	electron-beam lithography
ECS	extinction cross section
FMM	Fourier modal method
FWHM	full width at half maximum
GLAD	glancing angle deposition
IR	infrared
LCP	left-handed circularly polarized light
LPL	linearly polarized light
NIR	near infrared
OC	optical chirality
ORD	optical rotatory dispersion
PEC	perfect electric conductor
PMMA	Poly(methyl methacrylate)
RCP	right-handed circularly polarized light
SRR	split-ring resonator
STED	stimulated emission depletion
UV	ultraviolet
VCD	vibrational circular dichroism

INTRODUCTION

Chirality—the absence of mirror symmetry—is an integral component of our world. Not only is it ubiquitous in nature, it has inspired people around the world. Figure 1.1 shows some examples of chiral architecture and artwork. In the description of “Twist 1.5”, the wooden spiral installation by Alex Wyse and Ken Guild in Major’s Hill Park in Ottawa (Canada), it says that “it mirrors the spiral motif common in nature”.



FIGURE 1.1. Examples for geometrical chirality in architecture and art. (a) The photograph shows part of the Børsen (old stock exchange) in Copenhagen (Denmark). (b) Geometrically chiral artwork in Ottawa (Canada). The artists emphasized the omnipresence of chirality in nature.

Indeed, chirality is not only omnipresent in nature, but essential for our life. The most well-known example is the double-helix structure of DNA; but most other biomolecules are chiral as well. Louis Pasteur, who was the first to observe chirality in natural molecules, stated that “optical activity is a signature of life”¹ [1].

Nowadays, it is widely believed that chirality is a prerequisite for self-replication. Following this reasoning, it is essential for life [2]. Furthermore, the handedness plays a crucial role. In our chiral world, amino acids are left-handed, while sugars are right-handed. However,

1 The term *optical activity* refers to a measurable physical consequence of the geometrical property “chirality”. It will be explained in detail in Section 2.2.3.

the origin of this so-called *homochirality* is still one of the big open questions in physical chemistry [3].

Different biomolecules “shake hands” when they interact. The complex biochemical processes only work out in the right way when molecules with the correct relative handedness are matched [4]. The wrong handedness can be disastrous. One example is penicillamine, whose right-handed enantiomer is used as a pharmaceutical to treat Wilson’s disease [5]. The left-handed enantiomer, on the other hand, is toxic [6]. Therefore, unambiguous discrimination between the enantiomers is essential.²

However, this discrimination is difficult. Chirality is a geometric property that does not affect most physical effects that are commonly used to distinguish between different substances. Today, one mainly uses the differential absorption of circularly polarized light in chiral materials for this task, but the underlying interactions are weak. Therefore, fast chiral sensing of small quantities is still a challenging task in modern pharmaceutical research.

The problem of highly sensitive enantiomer discrimination should be tackled in this thesis. We will raise the question of how plasmonic nanoparticles—metallic structures much smaller than the wavelength of incident light—can help to increase the obtained signals. Such enhancement has already been demonstrated for conventional absorption spectroscopy [9]. We aim at transferring this concept to chiroptical spectroscopy.

Sub-wavelength plasmonic nanoparticles can strongly confine light. This leads to a strong field-enhancement that can be used for enhanced absorption spectroscopy. In 2010, Tang and Cohen developed a theory for the interaction of light with chiral molecules [10]. They could show that the chiral interaction can be described by an intrinsic quantity of the electromagnetic field, which they termed *optical chirality* (OC). The larger this quantity gets, the stronger the expected interaction will be.

2 Another example commonly referred to is thalidomide, which has been sold as a depressant under the name “Contergan”. Here, only the right-handed enantiomer leads to the desired behavior while the left-handed one is teratogenic [7]. However, both enantiomers are converted into each other without additional external influence. Therefore, even a purified right-handed sample does not prevent negative effects [8].

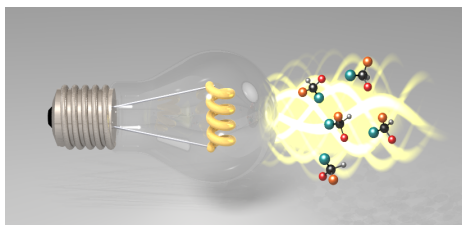


FIGURE 1.2. Artist's view of a chiral plasmonic near-field source. The chiral fields, which are generated by a plasmonic nanostructure, are used to probe the handedness of chiral molecules.

In this thesis, we transfer this concept to plasmonics. We propose plasmonic nanostructures that shape the electromagnetic field in a way that its OC becomes largely enhanced. These fields can then be used to perform chiroptical spectroscopy with higher sensitivity. This means that the nanostructure takes the role of the light source used for enantiomer discrimination (sketched in Fig. 1.2).

We provide, to the best of our knowledge, the first systematic study of plasmonic nanostructures for chiroptical spectroscopies. There are several main questions that have to be addressed. On a fundamental point of view, how are the chiral near-fields generated? What are the mechanisms, and how are they related to the geometry and chiral symmetry of the nanostructure? What do the “best” chiral near-fields look like, and how can we optimize our designs to obtain such a response?

After these questions regarding the near-field generation itself, we can also ask how sensing schemes, which implement such plasmonic enhancement, would look. What additional experimental constraints have to be considered? How could the sensing work in the end?

We tackle these questions by numerical simulations as well as simple analytical models. Analytical considerations help to identify promising designs. The numerical calculations of the chiral near-fields are performed by rigorously solving Maxwell's equations. The resulting chiroptical near-field response is further analyzed to elaborate the working principle behind the respective structures. We do not tend to engineer the best designs possible, but demonstrate several mechanisms to obtain strong chiral near-fields that are shaped in

a way that enantiomer discrimination can be supported. These concepts can then be adapted for real-life applications.

The thesis is structured as follows: In Chapter 2, we provide a detailed introduction to chirality. After discussing the geometrical aspects, we elaborate the electromagnetic behavior of chiral materials and derive their chiroptical responses. In addition, a short theoretical introduction to plasmonic nanoparticles is given.

Chapter 3 deals with chiroptical spectroscopy in more detail. We introduce circular dichroism spectroscopy, the most commonly used technique for chiral sensing, as well as some other spectroscopic techniques. Additionally, recent techniques for enhanced sensitivity (with a strong focus on plasmonic enhancement) are reviewed.

Chapter 4 focuses on the chiral properties of light instead of these of artificial or naturally occurring chiral objects. After a detailed discussion of OC, the concept of chiral near-field sources is introduced.

The following chapters deal with different groups of chiral near-field sources that are separated via their chiral symmetry properties. At first, we demonstrate the enhancement of chiral light in geometrically chiral structures (Chapter 5). In Chapter 6, the structures are modified to become geometrically achiral globally, but maintain their chiral nature locally, to suppress chiroptical far-field responses from the structure itself. After this, we demonstrate in Chapter 7 that even achiral illumination of geometrically achiral structures leads to chiral near-fields locally. The combination of linear polarization with geometrically chiral structures, which leads to strong chiral near-fields of one handedness in an extended volume, is analyzed in Chapter 8.

We discuss the implications for potential sensing applications and novel sensor schemes in addition to the chiroptical near-field response wherever suitable. A comparison of all the different concepts and a short outlook is given in Chapter 9.

Parts of this thesis have already been published in scientific journals. Chapter 5 and parts of Chapter 6 are based on [A2]. Chapter 7 (except for the second part of Section 7.3) is based on [A4]. Chapter 8 (except for Section 8.3) is based on [A8].

CHIRALITY IN NATURE AND SCIENCE

2.1 GEOMETRICAL CHIRALITY

The term *chirality*, which is derived from the Greek word $\chiείρ$ (*cheir*, hand), is used for objects lacking any kind of mirror symmetry. It was introduced in 1884 by Lord Kelvin in his Baltimore Lectures [11]:

“I call any geometrical figure, or group of points, chiral, and say that it has chirality, if its image in a plane mirror, ideally realized, cannot be brought to coincide with itself.”

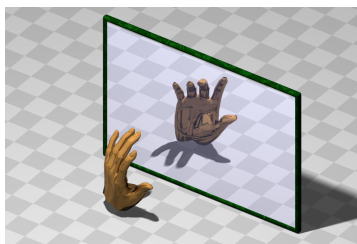


FIGURE 2.1. The human hand is the most prominent example of a geometrically chiral object. The mirror images of a hand cannot be superposed by rotations or translations, leading to two enantiomorphs: The left and the right hand.

The best known example of such a geometrically chiral object is the human hand (cf. Fig. 2.1). The right and the left hand are mirror images of each other, but it is impossible to superpose them. Therefore, chiral objects are referred to as being *handed*. The two versions of geometrically chiral objects, which differ only in their handedness, are called *enantiomorphs* or, in the special case of chiral molecules, *enantiomers*¹ [13].

¹ We will adopt this nomenclature and also speak of enantiomers in case of chiral plasmonic structures. This is common usage in recent literature and also fits to the concept of “plasmonic molecules” [12].

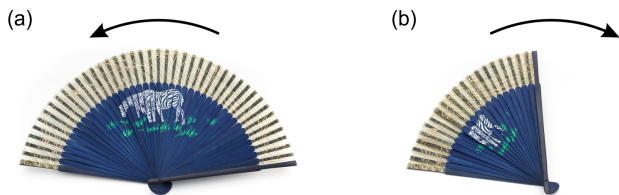


FIGURE 2.2. An opened folding fan is a geometrically chiral object. Its handedness can be defined in two ways. (a) If the relative rotation of the sticks of the opened fan is considered, it is left-handed. (b) If we consider the movement necessary to open the fan, it is right-handed. [Images taken by D. Flöß.]

It is noteworthy that, although there exist two enantiomorphs for every geometrically chiral object, there is no general rule to determine the left-handed or the right-handed one [14]. We show, on one simple example, that this choice is purely arbitrary: Consider the helical arrangement of sticks of a folding fan. The fan clearly is a geometrically chiral object, so we can assign a handedness to it. One might argue that the fan is left-handed because the helix formed by the sticks performs a left-handed rotation in space (cf. Fig. 2.2 (a)). On the other hand, one could define the handedness by the clockwise twist necessary to open the fan (cf. Fig. 2.2 (b)). With this argument, the fan could be labeled “right-handed”.

A more detailed discussion of this problem is given in Section 2.1.2. In this thesis, we will use the first method to define the handedness of geometrically chiral structures whenever possible, because it seems to be more intuitive.

Following Kelvin’s definition, geometrically chiral objects may not exhibit any kind of mirror symmetry. However, rotational symmetry is not forbidden. For example, n multiple intertwined helices (a structure that will be analyzed in detail in Chapter 8) exhibit n -fold rotational symmetry but the structure is still geometrically chiral.

Another important aspect of the definition given by Kelvin is that it is purely mathematical. One can directly decide whether an object is chiral or not just from looking at its geometry. This geometrical property can lead to physical responses that depend on the handedness of the structure. The fundamental properties of such responses are discussed in Section 2.1.3. Their presence implies that a different

definition of chirality can be given by analyzing one specific response. In this case, the object is chiral if and only if the response can be detected.²

It is important to distinguish between these two different definitions. In this thesis, we deal with chiral optical responses that are visible both in the far-field as well as the near-field of plasmonic nanostructures. Hence, we term any object chiral that exhibits such a response. Whenever we refer to the mathematical concept of chirality, the term “geometrical chirality” is used.

2.1.1 Planar Geometrical Chirality

All considerations up to now were made in three-dimensional space. However, the concept of chirality can be also transferred to two dimensions. In this case, all rotations and translations are restricted to a two-dimensional plane. Apart from that, the definition is the same: An object is planar geometrically chiral when its mirror image cannot be brought into coincidence with itself by rotations and translations without lifting the object out of the plane. Some examples are shown in Fig. 2.3. The simplest planar geometrically chiral object would be an asymmetric triangle. The planar analogue of the helix is a spiral. Also, rotational symmetry can occur for planar geometrically chiral structures.

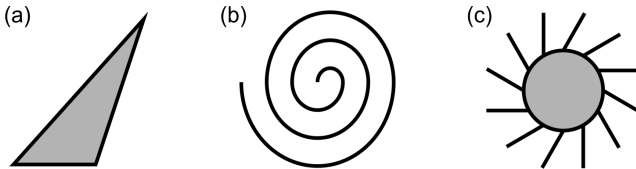


FIGURE 2.3. Different examples of planar geometrically chiral structures. (a) The simplest example is an asymmetric triangle. (b) A spiral is the planar analogue of the helix. (c) Planar chiral objects may possess rotational symmetry such as the sketched blade wheel.

² Note that it is possible to observe chiral responses for structures that are achiral from a geometrical point of view. This can, for example, occur when the combination of structure and incident wave vector form a chiral object. In some literature, such an arrangement is referred to as possessing “extrinsic chirality” [15].

Note that any two-dimensional object, planar geometrically chiral or not, is geometrically achiral in three dimensions because the object plane is a trivial mirror plane in three dimensions: One can easily obtain the enantiomorph of a planar geometrically chiral object by flipping it over. This can be further generalized: Any object that is geometrically chiral in n dimensions will become achiral as soon as an additional dimension is added.

If we do not focus on geometrical chirality but look at chiral responses, it is needless to distinguish between planar and three-dimensional geometrical chirality. The structure might or might not show a specific response, independent of its geometrical chiral properties. However, most responses are defined for isotropically oriented chiral analytes and, therefore, cannot be observed for structures exhibiting only planar geometrical chirality.

2.1.2 *Quantification of Chirality and Handedness*

Kelvin's definition of geometrical chirality is binary: An object is either chiral or achiral. The definition does not allow for any ordering of different geometrically chiral objects. However, one might intuitively argue that, when comparing two helices of the same length, the one that rotates more often is "more chiral" or shows "stronger chirality" than the other.

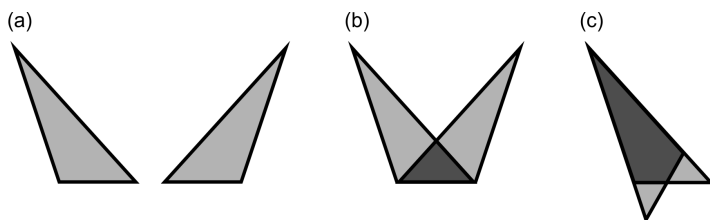


FIGURE 2.4. A simple measure to quantify geometrical chirality. (a) Both enantiomers are taken and (b) overlapped. (c) The maximum overlap defines the degree of geometrical chirality for the structure.

Starting from Kelvin's definition, one can define measures that quantify the chirality of an object by simply looking at its geometry. One possibility is illustrated in Fig. 2.4: We start with the two

enantiomorphs and align them in a way that the maximum overlap between the two structures is obtained. The overlap volume, normalized to the volume of the object, is a measure for the chirality. It results in a value between 0 and 1, where 1 (perfect overlap) describes an achiral object. The smaller the value gets, the higher the chirality of the object is in this measure.

However, there are many more possibilities to define such geometrical measures for chirality [16, 17]. It has been shown that, starting from any chiral tetrahedron, one can construct a measure that leads to highest geometrical chirality for the object initially picked [18, 19]. Therefore, these measures provide no additional benefit from a mathematical point of view.

It becomes even more difficult, if we do not only want to define some degree of geometrical chirality, but try to quantify the handedness of a given structure by a geometrical measure. As already discussed in Section 2.1, there is no straightforward way to determine the handedness of an arbitrary geometrically chiral object.

Let's ask whether a mathematical way of defining the handedness can be found. We consider some measure that describes left-handed structures by positive values and right-handed structures by negative values. Enantiomorphs result in the same absolute value but with opposite sign, geometrically achiral structures result in the value 0. Of course, the measure should be continuous.

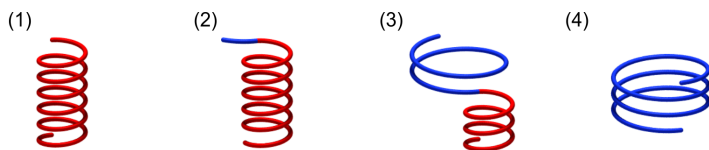


FIGURE 2.5. A helix of one given handedness can be continuously transformed into a helix with opposite handedness by simply pulling at one end and rolling the wire up with a different radius. The different radii of both helices ensure that any intermediate state stays geometrically chiral.

Let's now consider the helix depicted in Fig. 2.5 (1) and compare it to the one in state (4). The handedness of both helices is different. Therefore, the imaginary measure should result in values with opposite sign when analyzing these two structures. However, as shown

in the intermediate sketches, one can continuously transform one helix into the other. This should result in a continuous change of the value of our measure leading to a configuration where the measure is zero. However, due to the different radii of the helices, all intermediate structures are geometrically chiral. Therefore, any such measure will label some geometrically chiral structures as achiral.³ In these cases, the resulting zero value is not due to geometrical achirality but due to the fact that the given measure cannot assign a handedness to this unique structure. This is a general problem of handedness measures, which is referred to as *chiral connectedness* in literature [20].



FIGURE 2.6. If we define handedness by looking at the local deformation of a structure, the handedness of a helix depends on its orientation. (a) If we look along the axis of the helix, the wire bends to the right. (b) If we look perpendicular to the axis, the wire bends to the left. Therefore, opposite handednesses are observed for the different orientations.

Recently, Efrati and Irvine introduced a tensorial measure for the handedness, which is locally defined [21]. In their description, a structure can be, depending on the view, both left- and right-handed at the same time.⁴ For example, the local bending of a helically wound wire depends on the relative orientation of the helix and the observer (cf. Fig. 2.6), which would be reflected in this tensorial measure. This behavior has also been observed in an experiment where the chiroptical response of a helix changed its sign depending on the orientation, which indicates a handedness change [22]. However, this measure is unnecessarily complicated if one only needs to distinguish the two enantiomorphs of a given geometrically chiral structure.

³ One could also argue that, to resort this problem, both helices in the example must have the same handedness. However, it is straightforward to extend the transformation scheme to transform the structure back into the enantiomorph of the initial helix. Those two must have opposite sign in any useful handedness measure.

⁴ Additionally, tensors can change their sign in a continuous transformation without crossing zero.

2.1.3 Physical Manifestation of Geometrical Chirality

So far, we only discussed the geometrical implications of chirality. We will focus on the physical properties of geometrically chiral objects in this section. A physical *response* is a measurable quantity that results from the interaction of at least two different objects. A *chiral response* is a response that depends on the handedness of at least one of the objects. Therefore, chiral responses can be used to quantify the handedness of a given chiral analyte.

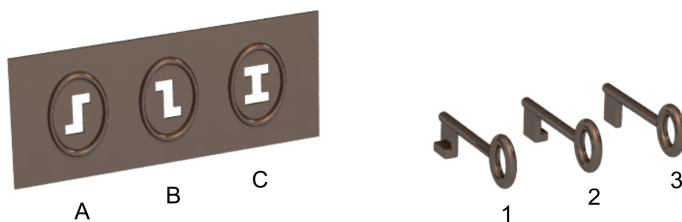


FIGURE 2.7. Illustration of chiral interaction. Only when both the key and the keyhole are geometrically chiral, a different behavior depending on the relative handedness can occur.

At first, we will discuss that both interacting objects must be geometrically chiral to obtain a chiral response. This can be motivated by purely geometrical considerations, as illustrated in Fig. 2.7. The two geometrically chiral keyholes “A” and “B” are enantiomorphs. A geometrically chiral key (“1” or “2”) of one handedness will fit in one of the enantiomorph key-holes, but not in the other.⁵ A geometrically achiral key (“3”), on the other hand, fits or does not fit in both of the key-holes; the response is independent of the handedness. A similar result would be obtained if the keyhole itself is geometrically achiral (“C”). Then, both enantiomorphs of any geometrically chiral key would either fit or not fit. Only the combination of both a geometrically chiral

⁵ Note that the shapes of the keys are not the same as the shapes of the keyholes. This is not necessary to obtain a different response depending on the handedness of the key-hole, only the geometrical chirality is important.

key and a geometrically chiral keyhole leads to responses that depend on the handedness of both of the participants.⁶

This simple example can be extended to all kinds of interactions. Chiral responses can only be found when at least two of the participants are geometrically chiral. All other physical properties that can be analyzed without usage of a geometrically chiral probe do not depend on the handedness of the object.⁷ It is, for example, obvious that the mass of the enantiomorphs must be the same, because a mirror will not change the mass of the mirrored object.

This observation has an important implication: A second chiral object is required to probe the handedness of a given chiral analyte. Also, any chiral measure used to quantify the chirality of an object via its chiral response relies on other chiral objects. This second chiral object should be well-defined in order to be useful as a chiral probe.

Note that such chiral measures still suffer from the limitations discussed in Section 2.1.2. Especially, they respond zero for some geometrically chiral objects. Connections between geometrical and physical chiral measures exist only for a limited number of systems [17].

2.2 CHIRAL ELECTRODYNAMICS

In this section, we will discuss the electromagnetic response of geometrically chiral molecules and plasmonic nanostructures. Classical electrodynamics in matter is based on the macroscopic Maxwell's equations [27]:

$$\nabla \cdot \mathbf{B} = 0, \quad (2.1a)$$

$$\nabla \times \mathbf{E} + \partial_t \mathbf{B} = 0, \quad (2.1b)$$

$$\nabla \cdot \mathbf{D} = \rho, \quad (2.1c)$$

$$\nabla \times \mathbf{H} - \partial_t \mathbf{D} = \mathbf{j}. \quad (2.1d)$$

⁶ Key and keyhole in this example are only planar geometrically chiral. However, it is straight-forward to extend this example to three-dimensional geometrically chiral objects. The planar example has been chosen because it is easier to visualize.

⁷ Strictly speaking, this is not true. Theoretical quantum chemistry predicts a small energy difference between two enantiomers because of the parity violation of the weak interaction [23, 24]. However, this difference is so small that it could not be measured until today [25, 26].

Here, E and H are the electric field and magnetic field strength, respectively, while B denotes the magnetic field and D is the electric displacement field. The free charges ρ and currents j act as sources in the inhomogeneous equations. The material response is described by the linkage of B and D to E and H via the so-called *constitutive equations*, which can be arbitrarily complex in the most general case. In this thesis, we will restrict ourselves to linear materials. If we assume achiral media first, the constitutive equations read [27]

$$D = \varepsilon_0 \bar{\varepsilon} E, \quad (2.2a)$$

$$B = \mu_0 \bar{\mu} H. \quad (2.2b)$$

The response of the material is modeled by the relative permittivity $\bar{\varepsilon}$ and permeability $\bar{\mu}$. In the optical domain, the latter can be approximated as unity for most materials. In the general case of an anisotropic material, both quantities are 3×3 tensors. They reduce to scalars for isotropic media.

Electromagnetic waves in isotropic media must fulfill the wave equation [27]

$$\left(\nabla^2 - \frac{n^2}{c^2} \partial_t^2 \right) E = 0. \quad (2.3)$$

Here, $c = 1/\sqrt{\varepsilon_0 \mu_0}$ is the speed of light in vacuum. $n = \sqrt{\varepsilon \mu}$ denotes the refractive index. A similar equation can be derived for the magnetic field.

A special solution of the wave equation are plain electromagnetic waves given by

$$E = E_0 J e^{i(kz - \omega t)}, \quad (2.4)$$

where J is the Jones vector that describes the polarization state of the light while E_0 is the amplitude of the wave. Special cases of polarization states are linearly polarized light (LPL) with

$$J_{\text{LPL}}^\varphi = \begin{pmatrix} \cos \varphi \\ \sin \varphi \\ 0 \end{pmatrix} \quad (2.5)$$

for a polarization angle φ and circularly polarized light (CPL) with

$$J_{\text{CPL}}^{\pm} = \frac{1}{\sqrt{2}} \begin{pmatrix} 1 \\ \pm i \\ 0 \end{pmatrix}. \quad (2.6)$$

Here, “+” denotes left-handed circularly polarized light (LCP) and “−” right-handed circularly polarized light (RCP).⁸

Although these equations can describe a wide range of materials such as dielectrics, metals, and even more sophisticated materials such as magneto-optically active media, they are not sufficient to describe chiral media. A more general version of the constitutive equations will be derived in Section 2.2.2.3. Before that, we will discuss the properties of achiral metallic nanoparticles.

2.2.1 *Electrodynamics of Metallic Nanoparticles*

2.2.1.1 *Dielectric Function of Metals*

The characteristic optical properties of metals (mainly, the high reflectivity and absorbency) can be attributed to the quasi-free electrons in the metal [28]. These electrons provide the main contribution to the optical response because they oscillate with the incident electric field. In a simple plasma model, this oscillation can be described as a damped harmonic oscillator driven by the external monochromatic field without an additional restoring force [29]:

$$\partial_t^2 \mathbf{u} + \gamma \partial_t \mathbf{u} = -\frac{e}{m^*} \mathbf{E}_0^{\text{ext}} e^{-i\omega t}. \quad (2.7)$$

Here, \mathbf{u} is the displacement of an oscillating electron with charge e and effective mass m^* . The amplitude of the monochromatic external driving field is denoted by E_0^{ext} . The collision frequency γ , which is the inverse of the relaxation time of the free electron gas, quantifies the damping in the system. Note that no term proportional to \mathbf{u} occurs in

⁸ Note that there are several conventions to define the handedness of CPL. We use the so-called *detector’s view* convention, where the handedness is the same as the intuitive handedness of the helix that the electric field vector describes in space at fixed time. A detailed discussion of the different conventions is given in Appendix A.2.

Eq. (2.7) because no restoring force is present. Therefore, no resonance can be found in the system.

Using a time-harmonic ansatz, the solution for \mathbf{u} can be found as

$$\mathbf{u} = \frac{e}{m^*} \frac{1}{\omega^2 + i\gamma\omega} \mathbf{E}_0^{\text{ext}}. \quad (2.8)$$

For N electrons in the unit volume, the polarization \mathbf{P} of the metal can be written as

$$\mathbf{P} = -N e \mathbf{u}. \quad (2.9)$$

The relation

$$\mathbf{D} = \varepsilon_0 \mathbf{E} + \mathbf{P} \quad (2.10)$$

in combination with Eq. (2.2a) leads to the dielectric function of the free electron gas:

$$\varepsilon_D(\omega) = 1 - \frac{\omega_p^2}{\omega^2 + i\gamma\omega}. \quad (2.11)$$

This is the well-known Drude model for isotropic metals. Here, the plasma frequency ω_p has been introduced:

$$\omega_p = \sqrt{\frac{N e^2}{\varepsilon_0 m^*}}. \quad (2.12)$$

The lone parameters necessary to describe the optical response of a given metal in the Drude model are ω_p and γ . Of course, this model is only a rough approximation because all resonances of the material (e. g., due to interband transitions) are ignored. However, it works well in the IR regime far off those resonances.

Figure 2.8 (a) shows the real and imaginary part of the dielectric function of a hypothetical Drude metal close to the plasma frequency. Below the plasma frequency, the metallic behavior is observed: The real part of the permittivity is negative while the imaginary part is non-vanishing, which results in a high absorptance of the material. For frequencies above the plasma frequency, the real part of the permittivity becomes positive. Additionally, the decreasing imaginary

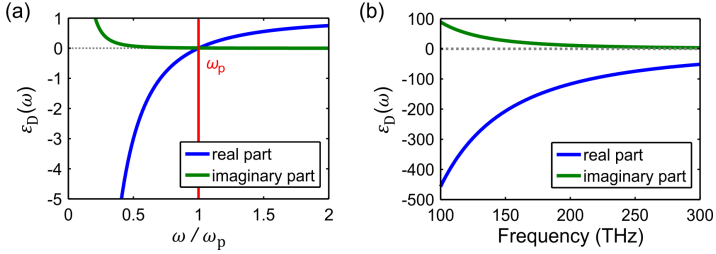


FIGURE 2.8. Dielectric function of a Drude metal. (a) The metal has a negative real permittivity below the plasma frequency, which results in the metallic behavior. Above the plasma frequency, the permittivity becomes positive, resulting in the behavior of a lossy dielectric. The values on the x -axis are given as fractions of the plasma frequency. (b) Gold (modeled with $\omega_p = 1.37 \times 10^{16} \text{ rad s}^{-1}$ and $\gamma = 1.22 \times 10^{14} \text{ rad s}^{-1}$) is purely metallic in the NIR regime. On the x -axis, the frequency $f = \omega/2\pi$ is given.

part results in lower losses of the material. Therefore, the Drude material behaves as a lossy dielectric for frequencies above the plasma frequency. For $\omega \gg \omega_p$, the losses can be neglected and $\epsilon = 1$ is approached. A physical interpretation of this behavior is that, for higher frequencies, the free electrons are not versatile enough to follow the external stimulus.

Figure 2.8 (b) plots the Drude parameters that are used in this thesis to model the response of gold in the NIR region. They have been adopted from [30]:

$$\omega_p = 1.37 \times 10^{16} \text{ rad s}^{-1} \quad (2.13a)$$

and

$$\gamma = 1.22 \times 10^{14} \text{ rad s}^{-1}. \quad (2.13b)$$

It can be seen that the behavior of this “Drude gold” is purely metallic in the complete range below 300 THz ($1 \mu\text{m}$).

Note that the Drude model is a very simple parametrization of the response of metals. Especially the damping parameter γ depends strongly on the frequency. Therefore, one fit that works for all frequencies is not possible. These issues are discussed in detail in [31].

However, these issues are only problematic when we try to qualitatively and quantitatively predict the response of a given metallic

nanostructure. In such cases, tabulated data should be considered. In the plasmonics community, the data of Johnson and Christy is usually used to model the response of gold in the visible spectral region [32]. Recent measurements that span a broad spectral range from 300 nm (1000 THz) to 25 μm (12 THz) have been reported in [33]. An extensive list of tabulated dielectric data for gold and respective Drude fits is given in [31]. An overview of tabulated data for noble metals as well as aluminum, lead, and tungsten with the respective Drude fits can be found in [34].

The Drude model offers a simple and easy parametrization for a fundamental analysis where the behavior of metals (but not the exact response of one specific metal) is needed. Therefore, we use the Drude model with the parameters given in Eqs. (2.13) for the demonstration of different concepts in this thesis. The modeling of the materials should be reconsidered as soon as potential resulting devices should be optimized.

As already discussed, strong deviations from the theoretical behavior of the metal are expected close to interband transitions. These resonances of the bound electrons substantially distort the dielectric function. However, they can be described by a similar model, which includes an additional restoring force. The differential equation of this so-called Lorentz model is given by [35]

$$\partial_t^2 \mathbf{u} + \gamma \partial_t \mathbf{u} + \omega_0^2 \mathbf{u} = -\frac{e}{m^*} \mathbf{E}_0^{\text{ext}} e^{-i\omega t}. \quad (2.14)$$

Here, ω_0 is the resonance frequency of the transition. Note, that m^* is the effective mass of the bound electron in the Lorentz model, while it denoted the effective mass of the free electron in case of the Drude model. The stationary solution is given by

$$\mathbf{u} = -\frac{e}{m^*} \frac{1}{\omega_0^2 - i\gamma\omega - \omega^2} \mathbf{E}_0^{\text{ext}} e^{-i\omega t}. \quad (2.15)$$

Similar considerations as for the Drude model result in the dielectric function

$$\varepsilon_L(\omega) = 1 + \frac{\omega_p^2}{\omega_0^2 - i\gamma\omega - \omega^2}. \quad (2.16)$$

It is important to note that the Lorentz model describes the behavior of the bound electrons for one possible transition, while the Drude

model describes the behavior of the free electrons of the metal. The total dielectric function of the metal with all transitions as well as the contribution of the free electrons can be obtained by summing up the respective terms with the correct weights [36]. Dielectrics can be modeled by ignoring the Drude term.

2.2.1.2 Polarizability of Metallic Nanoparticles

If we do not consider bulk metals but metallic nanoparticles, boundaries due to the finite dimensions of the particle occur. The particle acts as a cavity for the plasma oscillations. This results in non-propagating excitations—the so-called *localized* or *particle plasmons*—at the respective resonance frequency [29].

Let's consider a metallic nanoparticle. The incident electric field E_0 induces a dipole moment \mathbf{p} in the particle. This connection is described by the polarizability $\bar{\alpha}$

$$\mathbf{p} = \bar{\alpha} \mathbf{E}_0, \quad (2.17)$$

which is, in general, a tensorial quantity. For a spherical particle in vacuum with a radius r much smaller than the wavelength of the incident light, where the electrostatic approximation holds, one obtains an isotropic polarizability

$$\bar{\alpha} \equiv \alpha = 4\pi\epsilon_0 r^3 \frac{\epsilon(\omega) - 1}{\epsilon(\omega) + 2}. \quad (2.18)$$

The polarizability diverges for

$$\epsilon(\omega) = -2, \quad (2.19)$$

which is the special case of Fröhlich's condition for a sphere in vacuum [29]. Using the Drude model Eq. (2.11) for the permittivity $\epsilon(\omega)$ of the sphere,⁹ we obtain

$$\alpha = 4\pi\epsilon_0 r^3 \frac{\omega_0^2}{\omega_0^2 - \hat{\gamma}\omega - \omega^2}. \quad (2.20)$$

⁹ It has been shown that the material properties of metal clusters are similar to those of bulk metals down to cluster sizes of a few nanometers [37]. Therefore, the same Drude parameters as for bulk metals can be used.

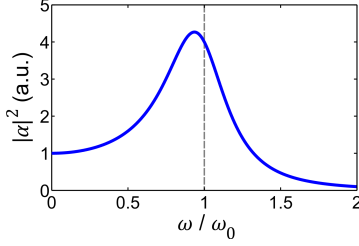


FIGURE 2.9. Polarizability of a metallic sphere with $\gamma = \omega_0/2$. One observes a clear Lorentzian lineshape. Note that the maximum polarizability is red-shifted with respect to ω_0 .

The polarizability shows a resonant behavior with a Lorentzian lineshape. The resonance frequency is given by

$$\omega_0 = \frac{\omega_p}{\sqrt{3}}, \quad (2.21)$$

where ω_p is the plasma frequency of the Drude metal. Note that the polarizability is purely imaginary at resonance indicating a $\pi/2$ phase shift between incident field and the response of the particle, as it is common in resonant systems.

Figure 2.9 shows the resonant behavior of such a particle. $|\alpha|^2$ is plotted for different fractions of the resonance frequency for a strongly damped system with $\gamma = \omega_0/2$. As it can be seen, the spectrum does not peak at ω_0 but is red-shifted. The peak is observed at

$$\omega_{\text{peak}} = \sqrt{\omega_0^2 - \frac{\gamma^2}{2}}. \quad (2.22)$$

Its amplitude is given by

$$|\alpha|_{\text{peak}}^2 = \left(4\pi\epsilon_0 r^3\right)^2 \frac{4\omega_0^4}{4\omega_0^2\gamma^2 - \gamma^4}. \quad (2.23)$$

The resonance frequency is independent of the radius for small spherical Drude metal particles. The response depends on the radius as soon as retardation effects come into play. More complicated particles do have polarizabilities that strongly depend on the geometry.

For example, the resonance position of linear rod antennas depends on the aspect ratio of the antenna [38].

However, the distinct resonances keep the Lorentzian lineshape. Therefore, they can be modeled as a damped harmonic oscillator similar to the Lorentz model. The resulting response has the same functional form as Eq. (2.15). The induced dipole moment can be written as

$$\mathbf{p} = -e\mathbf{u}. \quad (2.24)$$

Comparison with Eq. (2.17) leads to

$$\alpha = -\frac{e^2}{m^*} \frac{1}{\omega_0^2 - i\gamma\omega - \omega^2}. \quad (2.25)$$

Note that γ does not denote the damping of the material but the damping of the plasmonic resonance. Of course, the material damping has an influence on this quantity.

2.2.1.3 Plasmon Hybridization in Coupled Plasmonic Nanoparticles

A special class of complex plasmonic nanostructures are coupled nanoparticles. Several simple particles such as spheres are combined to achieve complex optical responses [39, 40]. It has been suggested already in 1985 that the collective response can be derived from the properties of the single nanoparticles similar to molecular orbital theory [41]. Such an analogous model has been introduced in 2003. In the so-called *plasmon hybridization model*, the plasmons of the coupled nanoparticles hybridize and form new collective resonances [42].

The general idea is the following: Consider two plasmonic particles in vacuum with resonances ω_1 and ω_2 . If the cross-coupling ω_{cc} between the particles is weak (i. e., $\omega_{cc} \ll |\omega_1 - \omega_2|$), the individual resonances are only slightly shifted due to the presence of the second particle. In a simple coupled oscillator model, one obtains

$$\omega'_1 = \omega_1 + \frac{\omega_{cc}}{4(\omega_1 - \omega_2)}, \quad (2.26a)$$

$$\omega'_2 = \omega_2 - \frac{\omega_{cc}}{4(\omega_1 - \omega_2)}. \quad (2.26b)$$

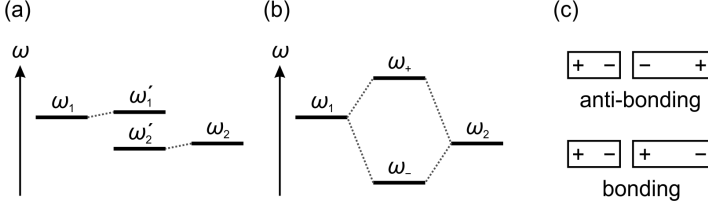


FIGURE 2.10. Hybridization of two plasmonic resonances ω_1 and ω_2 . (a) In a weakly coupled system, both resonances are only slightly shifted. (b) In a strongly coupled system, an energy splitting between the two hybrid modes ω_+ and ω_- is observed. (c) The symmetric mode ω_- is lowered in energy while the anti-symmetric mode ω_+ is increased in energy due to the additional electrostatic interaction.

Both resonances are weakly split by the same amount as shown in Fig. 2.10 (a).

In the case of a strongly coupled system with $\omega_{cc} \gg |\omega_1 - \omega_2|$, new hybrid modes ω_+ and ω_- are formed. Their resonance frequencies can be described by

$$\omega_{\pm} = \frac{\omega_1 + \omega_2}{2} \pm \frac{\omega_{cc}}{2}. \quad (2.27)$$

Those hybrid modes split symmetrically around the mean resonance frequency of the two initial plasmon modes (cf. Fig. 2.10 (b)).

One can also look at this splitting from a fundamental physical view, as sketched in Fig. 2.10 (c). The lower-energy bonding mode is symmetric in its current distribution for both particles: The currents flow in phase. The anti-symmetric anti-bonding mode is higher in energy because additional electrostatic energy is stored in the coupled system due to the charge accumulations.

Note that not all of the hybrid modes are necessarily excitable by an external light source. The bonding mode shows always a strong dipole moment, but the anti-bonding mode results in a charge distribution with lower dipole moment. The dipole moment can vanish in special cases such as two identical particles on the same layer. Such *dark modes* cannot be excited by far-field radiation. Therefore, excitation is not possible by plane waves but may be realized by near-field interaction with other plasmonic nanoparticles.

The plasmon hybridization model not only explains the new hybrid resonances qualitatively, but predicts the resonance energies accurately. However, the coupling between the single plasmons must be quantified, which depends on the specific system. The initial article [42] demonstrated the model for a metallic shell, which can be described as a hybridization of the modes of a sphere and a spherical cavity. The effects of dielectric background media as well as the extraction of polarizabilities for the shell are discussed in [43]. The treatment of dimers consisting of two spherical particles is shown in [44].

2.2.2 *Electronic Models of Chiral Materials*

As shown in Section 2.2.1.2, the response of metals can be described by a harmonic oscillator model. However, a single harmonic oscillator (and, accordingly, a single electron in a harmonic potential) is not sufficient to describe the behavior of chiral systems. Several extensions and alternative models for the description of chiral materials have been proposed over more than the last 100 years. A general overview of electronic theories of chiral materials is given in [45]. A more detailed discussion of selected models can be found in [46].

2.2.2.1 *Overview of Historic Models*

First extensions of the simple oscillator model have been proposed by Drude in 1896, who discussed an electron oscillating on a helical path [47]. However, the model was criticized due to the arbitrary choice of the path [48]. Additionally, Kuhn showed in 1933 that the chiroptical response arising from the model is due to some negligence Drude introduced during his derivation [49].

Condon established a working single-electron model in 1937. Instead of Drude's helical path, the electron is situated in a general chiral potential [50]. This model describes an oscillator in a chiral environment that enforces a helical oscillation. A plasmonic analogue of the Condon model would be a single geometrically chiral nanostructure such as a nanohelix. However, such structures are complicated to fabricate.

As discussed in Section 2.2.1.3, the response of many complex plasmonic systems is obtained because of the coupling between several equally contributing oscillators. In this case, a single-electron model seems to be unnatural.

Chiral plasmonic systems of coupled achiral constituents are well described by the so-called Born-Kuhn model, which uses two coupled orthogonal harmonic oscillators with an external driving force to model the chiral behavior [48, 51–53]. Each damped harmonic oscillator describes an electron performing a linear motion. The chiral response originates from the coupling between the electrons.

2.2.2.2 Details of the Coupled Oscillator Model

The system of coupled equations for the Born-Kuhn model is given by [54]

$$\partial_t^2 u_x + \gamma \partial_t u_x + \omega_0^2 u_x + \omega_c^2 u_y = -\frac{e}{m^*} E_{0,x}^{\text{ext}} e^{i\left(k\left(z_0 + \frac{d}{2}\right) - \omega t\right)}, \quad (2.28a)$$

$$\partial_t^2 u_y + \gamma \partial_t u_y + \omega_0^2 u_y + \omega_c^2 u_x = -\frac{e}{m^*} E_{0,y}^{\text{ext}} e^{i\left(k\left(z_0 - \frac{d}{2}\right) - \omega t\right)} \quad (2.28b)$$

for a molecule located at $\mathbf{r}_0 = (x_0, y_0, z_0)$ illuminated with a plane wave propagating in z -direction. Note that the $\omega_0^2 u_i$ terms are necessary because chiral responses are only present at molecular resonances. Therefore, a model without a restoring force (i. e., coupled Drude-like terms) is not sufficient.

Equations (2.28) are similar to the Lorentz oscillator model for resonant media or nanostructures. The Born-Kuhn model additionally implements a coupling between the two oscillators via the coupling parameter ω_c .

However, the coupling alone will not result in a chiral system. Additionally, there must be a non-zero distance d between the two oscillators. It is introduced by the additional phase terms in the driving field. Note that, although the model accounts for the distance between the oscillators in the driving field, the coupling is still instantaneous.

The description of coupled oscillators is similar to our discussion of plasmon hybridization for the special case of two identical oscillators. Therefore, we expect two hybrid modes that are split in energy.

In the following, we will show how this system can be solved. The system of two coupled equations can be decoupled via the transformation

$$u_{\pm} := \frac{1}{\sqrt{2}} (u_x \pm u_y), \quad (2.29)$$

which leads to

$$\partial_t^2 u_{\pm} + \gamma \partial_t u_{\pm} + (\omega_0^2 \pm \omega_c^2) u_{\pm} = -\frac{e}{m^*} E_{\pm}^{\text{ext}} e^{i(kz_0 - \omega t)} \quad (2.30)$$

with

$$E_{\pm}^{\text{ext}} = \frac{1}{\sqrt{2}} \left(E_{0,x}^{\text{ext}} e^{ik\frac{d}{2}} \pm E_{0,y}^{\text{ext}} e^{-ik\frac{d}{2}} \right). \quad (2.31)$$

As expected, we obtain two uncoupled oscillators that describe the normal modes of the coupled system. The resonance frequency without an external driving force is modified by the coupling constant. The lower energy case u_- corresponds to an in-phase oscillation of the two oscillators, while the u_+ case describes the counter-oscillating mode. The system can now easily be solved and reads

$$u_{\pm} = -\frac{e}{m^*} \frac{1}{(\omega_0^2 \pm \omega_c^2) - i\gamma\omega - \omega^2} E_{\pm}^{\text{ext}} e^{i(kz_0 - \omega t)}. \quad (2.32)$$

We now consider CPL with $\lambda = 4d$ as an external field. This choice leads to

$$e^{\pm ik\frac{d}{2}} = e^{\pm i\frac{\pi}{4}} = \frac{1}{\sqrt{2}} (1 \pm i). \quad (2.33)$$

In this case, we obtain different relations for E_{\pm}^{ext} depending on the handedness. For LCP, we obtain

$$E_+^{\text{ext}} = E_{0,+} e^{i\frac{\pi}{4}}, \quad (2.34a)$$

$$E_-^{\text{ext}} = 0, \quad (2.34b)$$

where E_0 is the amplitude of the incident electromagnetic field. For RCP, the result is opposite:

$$E_+^{\text{ext}} = 0, \quad (2.35a)$$

$$E_-^{\text{ext}} = E_{0,-} e^{i\frac{\pi}{4}}. \quad (2.35b)$$

Each handedness of CPL excites only one specific normal mode of the coupled oscillators when the wavelength is tuned accordingly to the distance between them. The additional phase term can be attributed to the propagation to the center of the molecule, which is separated by $d/2$ from the first resonator. Any other polarization will excite a superposition of both modes.

2.2.2.3 Constitutive Equations

Throughout the derivation of the constitutive equations of a Born-Kuhn type chiral material, we will use the abbreviation

$$\Omega := \sqrt{\omega_0^2 - i\gamma\omega - \omega^2} \quad (2.36)$$

for convenience.

At first, we have to transform the result from Eq. (2.32) back to the Cartesian coordinate system:

$$u_x = -\frac{e}{m^*} \left(\frac{\Omega^2 E_{0,x}^{\text{ext}} e^{ik\frac{d}{2}} - \omega_c^2 E_{0,y}^{\text{ext}} e^{-ik\frac{d}{2}}}{\Omega^4 - \omega_c^4} \right) e^{i(kz_0 - \omega t)}, \quad (2.37a)$$

$$u_y = -\frac{e}{m^*} \left(\frac{\Omega^2 E_{0,y}^{\text{ext}} e^{-ik\frac{d}{2}} - \omega_c^2 E_{0,x}^{\text{ext}} e^{ik\frac{d}{2}}}{\Omega^4 - \omega_c^4} \right) e^{i(kz_0 - \omega t)}. \quad (2.37b)$$

The distance d between the two oscillators leads to a retardation in the excitation between the oscillators for one specific external field E_0^{ext} .

Of course, the radiation emitted from these oscillators will reach an observer at different times as well. Therefore, the optical response of this system can not be obtained as easily as in the Lorentz model. Instead, both electrons and the finite distance d between them must be considered.

The following derivation is based on [54]. Each single electron of the Born-Kuhn molecule adds $-e\mathbf{u}$ to the induced dipole moment. The first electron, which oscillates only in x -direction, is located at $z_0 = d/2$, the second one (oscillating in y -direction) at $z_0 = -d/2$.

Therefore, the polarization of N identically oriented Born-Kuhn molecules can be calculated using Eqs. (2.37) as

$$\mathbf{P} = -\varepsilon_0 \frac{\omega_p^2}{\Omega^4 - \omega_c^4} \begin{pmatrix} \Omega^2 & -\omega_c^2 e^{-ikd} & 0 \\ -\omega_c^2 e^{ikd} & \Omega^2 & 0 \\ 0 & 0 & 0 \end{pmatrix} \mathbf{E}_0^{\text{ext}} e^{-i\omega t}. \quad (2.38)$$

The terms proportional to $e^{\pm ikd}$ stem from the finite distance d between the electrons. In the limit of small molecules compared to the wavelength ($kd \ll 1$), this exponential term can be expanded to

$$e^{\pm ikd} \approx 1 \pm ikd. \quad (2.39)$$

The term linear in k describes optical responses due to first-order spatial dispersion [55].

A plane wave propagating in z -direction has no E_z component. Therefore, the external field fulfills

$$\nabla \times \mathbf{E}_0^{\text{ext}} = \begin{pmatrix} -ikE_{0,y}^{\text{ext}} \\ ikE_{0,x}^{\text{ext}} \\ 0 \end{pmatrix}. \quad (2.40)$$

With this, Eq. (2.38) can be rewritten as

$$\mathbf{P} = -\varepsilon_0 \frac{\omega_p^2}{\Omega^4 - \omega_c^4} \left[\begin{pmatrix} \Omega^2 & -\omega_c^2 & 0 \\ -\omega_c^2 & \Omega^2 & 0 \\ 0 & 0 & 0 \end{pmatrix} - d\omega_c^2 \nabla \times \right] \mathbf{E}_0^{\text{ext}} e^{i-\omega t}. \quad (2.41)$$

After averaging over all orientations of the Born-Kuhn molecules, one finally obtains the constitutive equation

$$\mathbf{D} = \varepsilon_0 \varepsilon_{\text{BK}} \mathbf{E} + \varepsilon_0 \Gamma \nabla \times \mathbf{E} \quad (2.42)$$

with

$$\varepsilon_{\text{BK}} = 1 + \frac{2}{3} \frac{\omega_p^2 \Omega^2}{\Omega^4 - \omega_c^4} \quad (2.43)$$

and

$$\Gamma = -\frac{d}{3} \frac{\omega_p^2 \omega_c^2}{\Omega^4 - \omega_c^4}. \quad (2.44)$$

The factor $2/3$ in the second term of Eq. (2.43) stems from the isotropic averaging because we have only two orthogonal oscillators but three spatial directions. The molecules do not respond to illumination perpendicular to both oscillators. A similar argument explains the factor $1/3$ in Eq. (2.44).

Note that ϵ_{BK} also depends on the coupling parameter ω_c . This means that the presence of a strong chiral response also influences the achiral electrodynamic interaction.

We will now consider the limit of weak chirality, i. e., $\omega_c^4 \ll \Omega^4$. On resonance, this condition reduces to $\omega_c \ll \sqrt{\gamma\omega_0}$. This indicates that any chiral material should be absorptive in this description. After reworking the abbreviation (2.36), we obtain

$$\epsilon_{\text{BK}} \approx 1 + \frac{2}{3} \left(\frac{\omega_p^2}{\omega_0^2 - i\gamma\omega - \omega^2} \right), \quad (2.45)$$

$$\Gamma \approx -\frac{d}{3} \left(\frac{\omega_p^2}{\omega_0^2 - i\gamma\omega - \omega^2} \right) \left(\frac{\omega_c^2}{\omega_0^2 - i\gamma\omega - \omega^2} \right). \quad (2.46)$$

In the weak chirality limit, ϵ_{BK} is very similar to the result of the Lorentz model Eq. (2.16). The difference is again due to the presence of two orthogonal oscillators and the missing oscillator in the third spatial direction. For Γ , an additional Lorentzian is multiplied, but the chirality parameter ω_c replaces the plasma frequency.

Equation (2.42), together with a similar equation for the magnetic field

$$\mathbf{B} = \mu_0 \mu_{\text{BK}} \mathbf{H} + \mu_0 \frac{\mu_{\text{BK}}}{\epsilon_{\text{BK}}} \Gamma \nabla \times \mathbf{H}, \quad (2.47)$$

are the Drude-Born-Fedorov constitutive equations for reciprocal chiral media [56]. We will not give the explicit form of μ_{BK} here, because in most realistic systems the magnetic permeability can be set to unity in the optical domain.

For numerical calculations, the Drude-Born-Fedorov form is difficult to handle because of the curl. However, one can transform it to a simpler set of constitutive equations:

$$\mathbf{D} = \varepsilon_0 \varepsilon \mathbf{E} - \frac{\hat{\mathbf{i}} \kappa}{c} \mathbf{H}, \quad (2.48a)$$

$$\mathbf{B} = \mu_0 \mu \mathbf{H} + \frac{\hat{\mathbf{i}} \kappa}{c} \mathbf{E}. \quad (2.48b)$$

The transformation is given via [57]

$$\varepsilon = \frac{\varepsilon_{\text{BK}}}{1 - \frac{\omega^2}{c^2} \frac{\mu_{\text{BK}}}{\varepsilon_{\text{BK}}} \Gamma^2}, \quad (2.49a)$$

$$\mu = \frac{\mu_{\text{BK}}}{1 - \frac{\omega^2}{c^2} \frac{\mu_{\text{BK}}}{\varepsilon_{\text{BK}}} \Gamma^2}, \quad (2.49b)$$

$$\kappa = \frac{\frac{\omega}{c} \mu_{\text{BK}} \Gamma}{1 - \frac{\omega^2}{c^2} \frac{\mu_{\text{BK}}}{\varepsilon_{\text{BK}}} \Gamma^2}. \quad (2.49c)$$

If we assume that the chirality is weak enough that ε and μ do not depend on the chirality of the material, we can approximate the denominator by unity. With the additional approximation $\mu_{\text{BK}} = 1$, we obtain

$$\varepsilon \approx \varepsilon_{\text{BK}}, \quad (2.50a)$$

$$\mu \approx 1, \quad (2.50b)$$

$$\kappa \approx \frac{\omega}{c} \Gamma. \quad (2.50c)$$

Note that κ —exactly as ε and μ —is a dimensionless parameter in this description, while Γ has the dimension of a length.

All these parameters are scalars because we assume an isotropic chiral medium, i. e., the interaction of incident light is independent on the propagation direction. A thorough theoretical description of the electrodynamics of anisotropic chiral materials can be found in [58].

2.2.3 Chiral Optical Far-Field Responses

For isotropic chiral materials, the homogeneous wave equation can be obtained similarly as in normal linear media (cf. Appendix B.1):

$$\left(\nabla^2 - 2 \frac{i\kappa}{c} \partial_t \nabla \times - \frac{n^2 - \kappa^2}{c^2} \partial_t^2 \right) \mathbf{E} = 0. \quad (2.51)$$

A similar equation can be obtained for the magnetic field.

In isotropic achiral media, the wave equation can be trivially split into three decoupled scalar equations, one for each spatial component (cf. Eq. (2.3)). Therefore, any initial polarization state is preserved for isotropic materials [59].

In case of a chiral medium, the appearing curl term leads to a cross-coupling between the spatial components. Solving this equation for plane waves leads to CPL as eigenpolarizations with a propagation constant [60, 61]

$$k_{\pm}^2 = \frac{\omega^2}{c^2} (n_{\pm})^2, \quad (2.52)$$

where the refractive indices for the two polarizations are given by

$$n_{\pm} = n \pm \kappa. \quad (2.53)$$

Therefore, chiral media are also referred to as a kind of *bi-isotropic media* in literature.¹⁰ The refractive index n can be interpreted as averaged refractive index. It appears for example for unpolarized incident light.

Any non-circular polarization state is altered while propagating through a chiral medium. A special case is obtained for linear polarization. Any linear polarization state can be decomposed into a superposition of LCP and RCP with similar magnitudes. The polarization angle is determined by the relative phase between the circular components. Regarding to Eq. (2.53), both components experience a different phase velocity within the chiral medium due to the difference in the

¹⁰ In general, the term “bi-isotropic medium” comprises a wider class of materials with more general constitutive equations (cf. [56]). They are all characterized by two orthogonal eigenpolarizations with opposite handedness.

real part of the refractive index. This leads to a change of the relative phase of

$$\Delta\phi = 2 \Re(\kappa) D \frac{\omega}{c} \quad (2.54)$$

after a propagation distance D .

Due to this phase change, the polarization angle of the light rotates. The rotation angle Θ is given by

$$\Theta = \frac{\Delta\phi}{2} = \Re(\kappa) D \frac{\omega}{c}. \quad (2.55)$$

Additionally, the imaginary part of κ has further influence on propagating plane waves. It induces a differential absorbance for CPL with opposite handedness. This difference is given by (cf. Appendix B.2)

$$\Delta A := A_+ - A_- = 2(1 - A) \sinh\left(2 \Im(\kappa) D \frac{\omega}{c}\right), \quad (2.56)$$

where A is the absorbance for unpolarized light, which of course depends on D . For small values of κ , which is normally the case, a first-order Taylor expansion of the hyperbolic sine in Eq. (2.56) results in

$$\Delta A \approx 4(1 - A) \Im(\kappa) D \frac{\omega}{c}. \quad (2.57)$$

Equations (2.54) and (2.57) describe the so-called *optical rotatory dispersion (ORD)* (or *natural optical activity*) and the *circular dichroism (CD)*, respectively. Those are the most common chiroptical responses that can be observed.

Note that κ is dispersive, as discussed in Section 2.2.2.3. Its real and imaginary part are Kramers-Kronig related [62]. Figure 2.11 shows typical results obtained from the Born-Kuhn model.¹¹ The CD is five orders of magnitude smaller than the absorbance. ORD would follow exactly the same shape as the real part of κ . Note that the CD curve shows a bisignate lineshape. This is due to the different modes that are selectively excited by the respective circular polarization.

¹¹ The following parameters have been used: $\omega_0 = 500$ THz, $\omega_p = 50$ THz, $\gamma = 5$ THz, $\omega_c = 2.5$ THz and $d = 1$ nm. The propagation distance D has been chosen to obtain strong absorption on resonance, which occurred for these parameters at $D = 2$ μ m. Therefore, the absorption per unit length is much stronger than for most natural chiral materials.

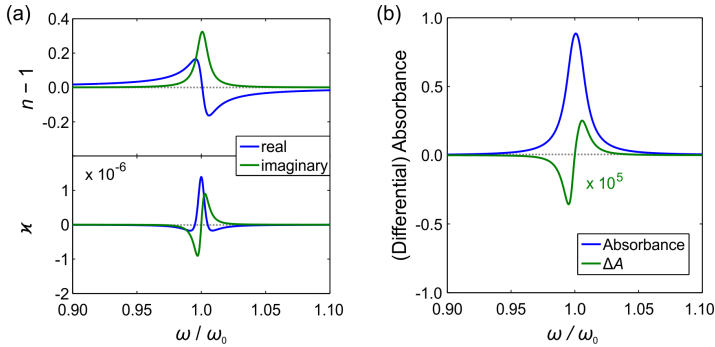


FIGURE 2.11. Results of the Born-Kuhn model for a hypothetical chiral material. (a) Refractive index n and chirality parameter κ . The real part of n has been shifted by -1 . (b) Absorbance and resulting CD. The chiral response is five orders of magnitude smaller than the achiral one. All frequencies are relative to ω_0 .

2.3 REALIZATION OF CHIRAL MATERIALS

After the theoretical considerations in Section 2.2, we will now focus on natural as well as artificial chiral materials, for which the discussed responses can be observed.

2.3.1 Chiral Molecules

A very important example for geometrical chirality in nature can be found in biochemistry. In fact, most biomolecules such as, e. g., all of the essential amino acids, are geometrically chiral [1].

One geometrical origin of chirality in molecules is sketched in Fig. 2.12 (a). It depicts a carbon atom that is bound to four atoms of different sizes. These size differences render the whole configuration geometrically chiral. An intuitive handedness definition is not possible for such an arrangement.

However, one can compare the spatial configurations of molecules via their Fischer projection and, in this way, find a nomenclature where the relative handedness is consistent. Glyceraldehyde has been chosen as a reference molecule to introduce an absolute nomenclature.

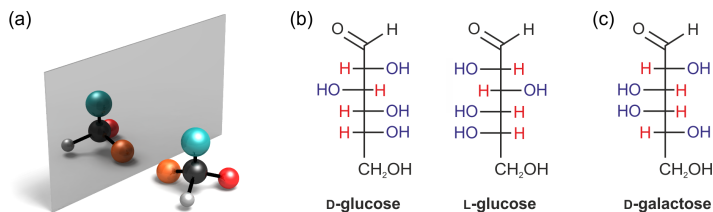


FIGURE 2.12. (a) A carbon atom bound to four differently sized atoms is geometrically chiral. This configuration is the prototypical example of a chiral molecule. (b) Real chiral molecules, such as the glucose molecule, can consist of several chiral centers. (c) If only some of the chiral centers are changed, one obtains a diastereomer.

The two enantiomers are labeled D (*dexter*, right) and L (*laevus*, left) [63]. However, several other naming conventions are used in stereochemistry [64].

Figure 2.12 (b) sketches a more complex example: the glucose molecule, which consists of four carbon atoms with different groups attached. In nature, one commonly finds the right-handed D-glucose. If not all but only few of the chiral centers change their handedness, one speaks of *diastereomers* (cf. Fig. 2.12 (c)).¹²

Figure 2.13 depicts the UV part of the CD spectra of these three sugars.¹³ The values for D-glucose and D-galactose have been measured in [65]. The values for L-glucose have been calculated from those of D-glucose for demonstration purposes. Theory predicts that they must be exactly opposite.

Note that the spectra of the diastereomers differ significantly. While glucose has only one chiroptically active band in the depicted region, one can identify two for galactose. Additionally, the plot shows that it is difficult to extract handedness information from CD measurements. D-glucose and D-galactose are both in their D-form, but exhibit different signs of their CD signal in the same wavelength range. Therefore, one needs substantial knowledge about the analyzed system to extract information from CD studies.

¹² Strictly speaking, only L-glucose and D-galactose are diastereomers. D-glucose and D-galactose, who differ in exactly one chiral center, are called *epimers*.

¹³ In this figure, $\Delta\epsilon$ is the molar differential extinction coefficient. Please refer to Appendix A.1 for an explanation of the different units used in CD spectroscopy.

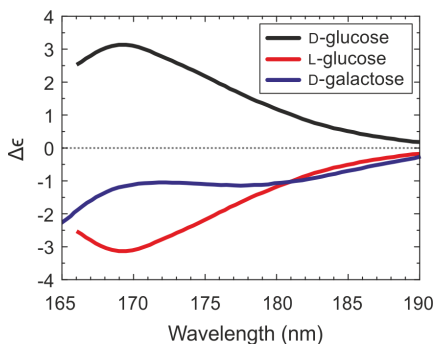


FIGURE 2.13. CD response of the sugars depicted in Fig. 2.12. The data for the D-sugars has been obtained from [65]. The curve for L-glucose has been calculated from D-glucose.

In addition to simple chiral centers around carbon atoms, larger molecules can form geometrically chiral arrangements. The best-known example is DNA with its double-helix, other examples include the secondary structure of proteins or helicene, which is a helical arrangement of benzene rings [66].

2.3.2 Chiral Plasmonic Nanostructures

Metallic nanoparticles can be used to create systems that exhibit much higher chiroptical responses. The induced electric and magnetic dipole moments in plasmonic nanostructures are several orders of magnitude higher than those in any natural molecule because of the large number of electrons involved. Therefore, similar effects as found in natural molecules can be studied in *plasmonic molecules*, but with much stronger responses [12].

The “atoms” of such plasmonic molecules are single nanoparticles, whose collective response is studied. As discussed in Section 2.2.1.3, the response of such complex plasmonic molecules can be obtained by the plasmon hybridization model. Examples for complex collective behavior include artificial aromatic molecules [67], Fano resonances [68], or electromagnetically induced transparency [69, 70] and absorption [71, 72].

Of course, the effects of geometrical chirality can also be studied in such plasmonic molecules [73]. The analogue of the chiral molecule discussed in Fig. 2.12 (a) would be a tetrahedral arrangement of four differently sized plasmonic particles as introduced in [74]. However, the CD response of such an arrangement is rather weak because the single particles are detuned in resonance frequency and oscillator strength. Therefore, they couple only weakly and act more like individual particles.

Stronger coupling is obtained for similar particles. The tetrahedral arrangement of similar spherical particles, however, is geometrically achiral. Therefore, it has been suggested to use similar particles, but arrange them in a way that leads to geometrical chirality. Such structures are called *chiral plasmonic oligomers* [A1].

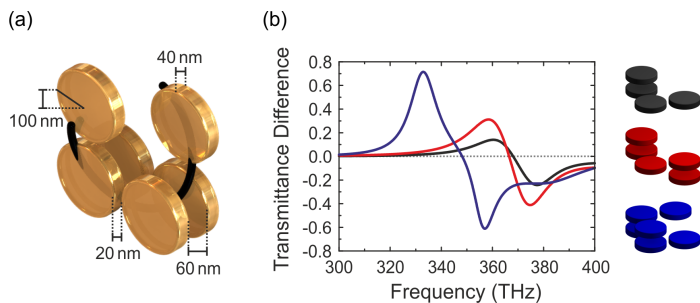


FIGURE 2.14. (a) Sketch of a chiral plasmonic oligomer. The arrangement of the gold disks mimics the geometrically chiral structure of a left-handed helix. (b) Calculated transmittance difference for different chiral plasmonic oligomers. The absolute values increase with the number of gold disks.

The implementation is sketched in Fig. 2.14 (a). The chiral plasmonic oligomer is based on a bi-layer structure. Each layer consists of three gold disks which are arranged in an L-shaped configuration. The second layer is twisted by 90° to emulate the chiral layout of a helix. The dimensions chosen in the sketch lead to a resonance in the near-IR with maximum chiroptical response at 333 THz (900 nm).

Figure 2.14 (b) shows the simulated chiroptical far-field response of the structure aligned in a periodic array with an unit cell of 650 nm.¹⁴ Note that one does not need six disks to obtain geometrical chirality and the subsequent chiroptical response. Four particles, correctly arranged, are sufficient. Therefore, Fig. 2.14 (b) additionally contains the simulated response for chiral plasmonic oligomers with five and four particles. However, by reducing the number of disks, the chiroptical response is weakened.

Additional disks lead to a stronger chiral coupling and, therefore, a stronger chiroptical response. Of course, adding these disks must not destroy the chiral asymmetry of the structure. Therewith, the maximum performance of such designs is limited. Note that the theoretical response of such a monolayer with a thickness well below one micron is several orders of magnitude larger than for natural chiral molecules measured with a path length in the range of millimeters.

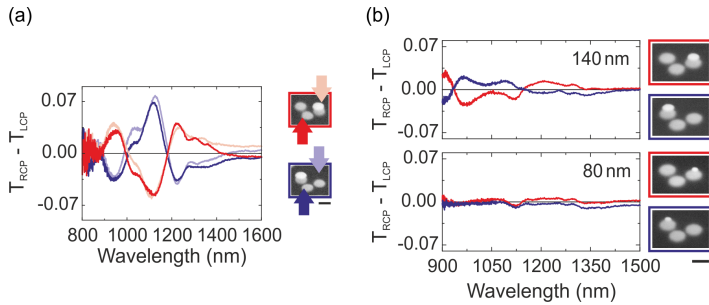


FIGURE 2.15. (a) Differential transmittance of a four-disk chiral plasmonic oligomer illuminated from top and from bottom. (b) The differential signal vanishes when the upper disk becomes smaller. [Measurements by M. Hentschel [A1].]

The simple design with four individual disks (but slightly different dimensions) has been experimentally investigated in [A1], the six-disk structure is discussed in [A3]. Figure 2.15 (a) depicts the obtained

¹⁴ For most plasmonic systems, we show the transmittance difference ΔT instead of ΔA . Both responses contain equivalent information as long as no differential reflectance occurs (cf. Appendix A.1).

transmittance difference of the four-disk oligomer. Both the mirror symmetry of the response of the enantiomers as well as the independence of the response to the orientation of the sample can be clearly seen. The transmittance difference of more than 7 % is much higher than for any natural chiral molecule.

Note that a supercell of four oligomers has been used for the periodic arrangement to ensure C_4 symmetry of the whole array. It can be shown by group theory that only symmetry groups C_3 or higher support CPL as eigenpolarization [75]. For lower symmetries, elliptical birefringence would lead to circular polarization conversion that could be erroneously interpreted as transmittance difference signal [60].

Figure 2.15 (b) demonstrates the importance of resonant coupling: Reducing the size of the disk in the upper layer and, thereby, detuning of the resonance will significantly weaken the chiroptical response. By this means, the chiroptical response vanishes, although the structure stays geometrically chiral. However, from a plasmonic point of view, we obtain several weakly coupled achiral structures instead of one chiral geometry.

The combination of several of these oligomers in one plasmonic molecule leads to a plasmonic analogue of diastereomers [A5]. It could be shown that the chiroptical response of such diastereomers can be decomposed into the sum of the responses of the single chiral centers as long as these centers in the plasmonic molecule are sufficiently decoupled. More details about different combinations of these chiral centers can be found in [76].

The chiroptical response of plasmonic oligomers can in principle be explained by the Born-Kuhn model because it arises due to coupling between similar constituents. The direct plasmonic realization of this model is obtained by two corner-stacked bars [A7].

The simulated response is shown in Fig. 2.16 (a) for the right-handed enantiomer. The length of each rod is 223 nm, the width and thickness 40 nm. The structure has been calculated in a C_4 arrangement with a periodicity of the supercell of 800 nm. The system has been embedded in an environment with a refractive index of $n = 1.5$. We obtained almost perfect selective excitation of the two normal modes (cf. Section 2.2.2.2) due to the matched distance (120 nm) between the rods.

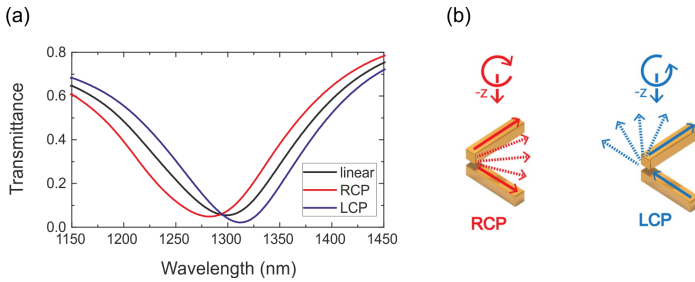


FIGURE 2.16. (a) Simulated response of a right-handed corner-stacked rod structure illuminated with linear polarization and CPL. (b) The two hybrid modes are selectively excited by RCP and LCP if the distance between the rods is chosen accordingly.

An intuitive explanation of this selective excitation can be obtained by analyzing the normal modes of the system via a plasmon hybridization approach. As shown in Fig. 2.16 (b), the anti-bonding and the bonding mode are selectively excited by RCP and LCP, respectively. The electric field vector rotates while traveling the distance between the two rods. Depending on the handedness of the light, either an out-of-phase or an in-phase oscillation of the second rod is induced. Both modes hybridize, with the out-of-phase mode being of higher energy due to the accumulation of charges of the same sign at the corner. Therefore, a strong transmittance difference for the two polarizations is obtained.

The strength of the chiroptical response depends on the coupling strength (and, therefore, the splitting) as well as the width and the modulation of the plasmonic resonance. Note that a reduced distance will lead to a reduced suppression of the second mode for one circular polarization. However, the chiroptical response might still be larger due to the stronger coupling. Additional theoretical insights into chiral plasmonic dimers can be obtained from [77–79].

So far, only coupling of similar geometrically achiral constituents has been discussed. However, complex plasmonic structures can lead to sophisticated responses without coupling. A simple example of such a geometry is the so-called split-ring resonator (SRR), which is depicted in Fig. 2.17 (a). When the structure is excited parallel to the

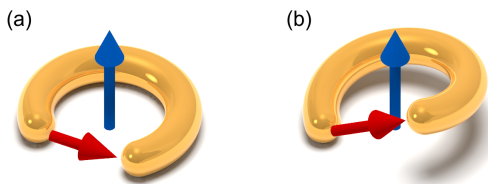


FIGURE 2.17. (a) A SRR exhibits an electric (red) and magnetic (blue) dipole moment. (b) When one of the ends is bent upwards, both dipole moments are not orthogonal anymore. The resulting helical geometry is chiral.

gap, an electric dipole moment is induced in the gap. However, the charge oscillation must follow the bend of the structure. This leads to an induced ring current. Therefore, the structure also exhibits a magnetic dipole moment pointing out of the plane.

The orthogonality of the dipole moments can be eliminated when one of the ends of the SRR is uplifted. In this case, a helical geometry, which is geometrically chiral, is achieved. The magnetic dipole moment will still point along the axis (as in a coil), but the electric dipole moment is rotated to point from one end to the other of the structure. Thus, both dipole moments feature parallel components. Following Rosenfeld's calculations, this will lead to a chiroptical response in case of molecules [80]. Therefore, such structures are also expected to show chiroptical response in the plasmonic case.

One recent realization of this idea is given in [A6], where a gold ramp has been fabricated.¹⁵ Interestingly, even the response of this complex design can be explained qualitatively by the Born-Kuhn model. In this case, higher-order modes are used instead of the hybridized collective modes.

However, the Born-Kuhn model breaks down when the complexity is further increased. Specifically designed helices with two turns can lead to a broadband transmittance dip for one circular polarization, which involves coupling of three plasmonic modes [81, 82]. Theoretical discussions of complex three-dimensional chiral nanostructures such as Möbius strips are given in [83–85].

¹⁵ Note that the fabrication method does not allow for C_3 or C_4 symmetry. However, the structure has been measured from both sides to eliminate the influence of circular conversion dichroism, which exhibits opposite sign for backward illumination.

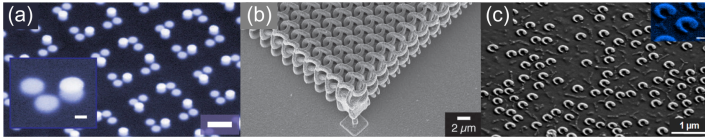


FIGURE 2.18. Different examples for complex geometrically chiral nanostructures fabricated with different methods. (a) Chiral plasmonic oligomer fabricated by two-step EBL. [Fabrication by M. Hentschel [A1].] (b) Bi-chiral plasmonic crystal fabricated by DLW. [Fabrication by A. Radke [86].] (c) Plasmonic ramp fabricated by colloidal lithography with tilted angle evaporation. [Fabrication by B. Frank [A6].]

Fabrication of geometrically chiral plasmonic structures is non-trivial. Figure 2.18 shows some examples of nanostructures fabricated with different methods.

The chiral plasmonic oligomer has been fabricated via electron-beam lithography (EBL) using a stacking procedure first described in [30]. Such two-layer geometrically chiral metamaterials have been extensively studied in literature [87–93]. Additional layers lead to even more sophisticated designs [94, 95]. A special class of lithographically defined chiral metamaterials works without stacking at all. Here, a geometrically planar chiral structure is fabricated on top of a substrate. Therefore, the mirror symmetry is broken in propagation direction [96–100]. This demonstrates that not only the plasmonic structure but also its surrounding play a crucial role for the chiroptical response. However, the interaction of at least two plasmonic modes is necessary to obtain the reported CPL transmittance difference [101].

Although EBL is a powerful and well-established technique, it is restricted to layered geometries. More sophisticated designs are possible by combination with other techniques. For example, lithographic steps [102–104] or asymmetric evaporation [105] on a prestructured template can lead to fully three-dimensional geometrically chiral structures. Other fabrication techniques for such designs include direct laser writing (DLW) [82, 86, 106], glancing angle deposition (GLAD) [107, 108], electron- and ion-beam induced deposition [109–111], anisotropic etching [112] or colloidal lithography with tilted angle evaporation [A6]. GLAD has also been used to fabricate chiral templates,

on which achiral plasmonic nanoparticles can be attached in a subsequent step [113, 114]. An even more exotic technique utilizes the strain in heterostructured films [115]. The chiroptical response of such so-called swiss-roll metamaterials has been analyzed in [116].

In recent years, self-assembly techniques have been adopted to fabricate geometrically chiral nanostructures that are fully three-dimensional. In these methods, small nanoparticles are linked together to a precisely controllable geometry, for example via a DNA template. Both tetrahedral arrangements of differing nanoparticles [74, 117–119] as well as geometrically chiral arrangements of similar building blocks [120–127] have been demonstrated.

Additional complexity can be added to steer the chiral properties of such metamaterials. In the THz region, silicon can be switched into the conducting state under optical illumination. This mechanism has been combined with a sophisticated design to obtain a metamaterial with switchable handedness [128]. Phase change materials, such as germanium antimony telluride, allow for control over the chiroptical response in the NIR [A9]. Geometric reorientation of the chiral structures with respect to the incident light [22], or even reconfiguration of the structure itself [129], is possible with self-assembly techniques.

Much work has been devoted into control and tailoring of the chiroptical far-field response of artificial chiral materials. This is useful to study chirality and influences of the geometry on the resulting chiroptical spectra. Additionally, any application related to circular polarization such as circular polarizers or polarization converters highly benefit from this research. However, the chiroptical response is obtained by the choice of the structure. The problem of enantiomer discrimination needs a method of increasing the response of a specific chiral analyte, which will be discussed in the following chapters.

CHIROPTICAL SPECTROSCOPY

In the last decades, many techniques to distinguish the two enantiomers of a given chiral molecule have been developed. In this chapter, we discuss optical methods that spectrally resolve chiroptical responses. Also, methods to increase the sensitivity of such spectroscopic measurements are reviewed.

3.1 TECHNIQUES FOR OPTICAL ENANTIOMER DISCRIMINATION

3.1.1 *Circular Dichroism Spectroscopy*

The most prominent and well-known chiroptical spectroscopy technique is circular dichroism (CD) spectroscopy. It utilizes the difference in the absorption of LCP and RCP in chiral media (cf. Section 2.1.3). The basic working principle of CD spectrometers is sketched in Fig. 3.1: The chiral analyte is illuminated with LCP and RCP. The transmittance of both incident polarizations is detected. After subtraction, one obtains the CD signal of the sample.

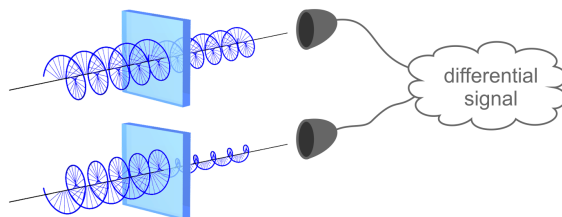


FIGURE 3.1. CD spectroscopy uses the different absorbance of chiral media for left- and right-handed CPL. The spectral differential response is characteristic for a chiral analyte. The signs of the different peaks depend on the handedness of the analyte.

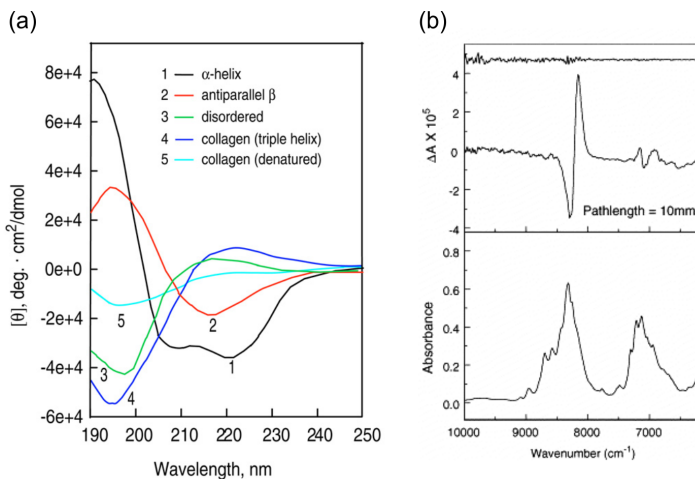


FIGURE 3.2. CD spectra of poly-L-lysine and collagen in different conformations. Please refer to Appendix A.1 for an explanation of the units. [Image reprinted in part by permission from Macmillan Publishers Ltd: Nature Protocols [132], copyright 2007.] (b) VCD spectrum of D- α -pinene. The chiroptical response is five orders of magnitude smaller than the absorbance. The spectrum has been taken in the NIR between 1.0 μm (300 THz) and 1.7 μm (180 THz). [Image reprinted in part with permission from [133]. Copyright 2006 Elsevier.]

Of course, state-of-the-art spectrometers use more subtle methods than direct subtraction of the transmitted intensities to obtain maximum sensitivity. A common method combines switching between the two circular polarizations with a detection scheme using a lock-in amplifier. A more detailed description and overview of recent CD instruments can be found in [130] and [131].

Figure 3.2 (a) shows typical CD spectra of amino acids and proteins. As already discussed in Section 2.3.1, the spectra of the enantiomers would be mirrored with respect to the zero line. Therefore, these signals can be used to detect the handedness of the respective molecules. It can clearly be seen that these samples, similar to most biomolecules, exhibit not only one active CD band. The relative strength of the bands depends strongly on the conformation. Therefore, CD spectroscopy can not only be used for enantiomer discrimination but also for the

conformational analysis of biomolecules, e. g., the secondary structure of proteins [132, 134–136].

The CD bands shown in Fig. 3.2 (a) stem from chiroptically active electronic transitions. For most molecules, these are located in the UV and visible spectral region. In recent years, an extension has been made to the IR regime, where chiroptically active vibrational modes can be probed (cf. Fig. 3.2 (b)). This so-called vibrational circular dichroism (VCD) analysis is a very sensitive technique for probing the absolute configuration of biomolecules, even in cases where electronic CD does not lead to the correct results [137, 138]. One possibility is to calculate the VCD spectra of all conformers and compare them to the measured spectra. However, the VCD signals are even smaller than the responses for electronic CD.

CD measurements suffer from weak signals compared to the absorbance of the molecules. The VCD signal in Fig. 3.2 (b), for example, is five orders of magnitude smaller than the achiral response. To increase the signal, one can increase either the path length or the concentration of the chiral analyte.

However, while an increased path length increases the CD signal, it also decreases the intensities on the detector, which leads to stronger noise. Therefore, one finds an optimum absorbance of the sample for CD measurements that leads to the highest sensitivity. The path lengths and concentrations differ for the different chiral analytes but are typically in the range of millimeter lengths and millimolar concentrations [130]. Difficulties occur, however, when significantly smaller quantities of the chiral analyte should be probed.

3.1.2 *Other Spectroscopic Techniques*

The rotation of linear polarization upon transmission through a chiral material, which is closely related to CD, can also be detected. This ORD signal is weakly visible even further apart from the molecular resonances, while CD can only be observed close to the resonance; the signals drop down rapidly with increased detuning. Therefore, ORD can be detected off-resonant, which is important for molecules whose CD bands are located in spectral regions that are inaccessible by common CD spectrometers. On the other hand, some applications

of CD such as structural analysis are difficult to implement in an ORD scheme because the measured rotations are not induced by only one chiroptically active absorption band but result as a superposition of all nearby bands [139].

The detection scheme for ORD is more complicated than for CD. Instead of small intensity fluctuations, as in the case of CD, small variations of the polarization angle must be detected. Therefore, it is necessary to control and record the full polarization state of the light. Commercial ORD spectrometers with a resolution of about 1 mdeg are available [140].

Other well-known spectroscopic techniques have been extended for chiroptical spectroscopy as well. One example is circularly polarized luminescence spectroscopy, where a difference in the spontaneous emission of left- and right-handed CPL is recorded [141, 142].

Raman optical activity is an extension to classical Raman spectroscopy for the detection of vibrational modes. In such measurements, either the differential scattering intensity for LCP and RCP or a difference in the scattered circular components for a fixed incident polarization is detected [143, 144].

3.2 IMPROVED DETECTION SCHEMES

There are two methods to improve the sensitivity of the discussed spectroscopic techniques. One is to find a system in which the chiroptical interaction is enhanced. Such schemes are reviewed in Section 3.3. Here, we will discuss the second possibility first: Improved detection schemes that are capable of resolving the low signals with high sensitivity. Several possible mechanisms are reviewed in [145].

One possibility is the adaption of quantum-mechanical weak value measurements [146]. After a standard (strong) quantum measurement, the quantum system collapses, i. e., subsequent measurements will all result in the same value. For weak value measurements, the measurement device is a quantum system that is only weakly coupled to the system to be measured.¹ Therefore, only slight perturbations occur and no collapse of the wave function is observed. The measurement

¹ This weak interaction coined the term “weak value measurement”. It does not mean that small values are measured.

device itself can then be probed by a subsequent strong measurement. The so-called weak value V_w of the operator \bar{V} can be described as [147]

$$V_w = \frac{\langle \Psi_f | \bar{V} | \Psi_i \rangle}{\langle \Psi_f | \Psi_i \rangle}, \quad (3.1)$$

where $|\Psi_i\rangle$ and $|\Psi_f\rangle$ are the states before and after the weak measurement, respectively. If one pre- and post-selects the states in such a way that they are almost orthogonal, V_w can reach arbitrarily high values. However, the probability for the measurement to result in the desired final state becomes accordingly small. This can be interpreted in the way that, although the measured values are high (and, therefore, a very high resolution is obtained), the signal drops down. Many of these measurements must be taken to find enough systems that result in the desired state.

Pfeifer and Fischer adopted this scheme for the measurement of ORD [148]. They used the different refraction angles for LPL impinging on a chiral wedge. This difference in refraction is a direct consequence of the different refractive indices for LCP and RCP, which are the source of ORD. Therefore, an incident linearly polarized beam is split. One observes a small angle between the two resulting beams. Most parts of these beams still overlap but can be suppressed by a polarizer orthogonal to the initial linear polarization. This is identical to the post-selection step in the weak value measurement.² Only the non-overlapping wings of the beams are present after the polarizer. Their intensity is a measure for the angle between the beams and, therefore, for the strength of the chiroptical interaction. The handedness of the chiral material can be detected with use of a modulation technique. Using this method, the authors could detect refractive index differences down to 10^{-9} in a volume below $4 \mu\text{L}$.

Other enhancement schemes follow a similar principle. With appropriate detection methods, the huge background of the achiral interaction is suppressed. Although this leads to a small detectable signal compared to the initial illumination, the contrast is enhanced. One

² This post-selection suppresses most of the initial light. The signal drops, but the contrast is enhanced.

development are self-heterodyne techniques, where the signal self-interferes with the incident light. The method uses elliptically polarized light instead of CPL. The ellipticity offers an additional degree of freedom to steer the subsequent self-interference [149]. In active-heterodyne methods, a second external beam is interfered with the signal. The polarization properties of the external beam can be controlled independently, which offers a simpler method to obtain the desired signal enhancement [150].

A resonator-based enhancement approach is reported in [151]. The authors use a bow-tie cavity to magnify the polarization rotation.³ An additional Faraday rotator is used to break the symmetry between the two counter-propagating beams in the cavity. Modulation of the magnetic field of the Faraday rotator suppresses the background from linear birefringence. The authors estimate that a sensitivity down to 3×10^{-14} rad could be achieved. However, the implementation of the cavity and the Faraday medium renders this sensing scheme more complicated than conventional methods.

3.3 PLASMONICALLY ENHANCED SENSITIVITY

We will now ask whether plasmonic systems can increase the chiroptical interaction of chiral molecules placed in their vicinity. It has been shown that the achiral response of a molecule, which is an excitonic system, can be drastically enhanced when coupled to a metallic particle. This has led to novel spectroscopic techniques such as surface-enhanced infrared absorption spectroscopy where a plasmonic antenna enhances the absorbance signal of molecules by several orders of magnitude [9, 152, 153]. Also, strong coupling between excitonic and plasmonic systems has been demonstrated [154]. In such systems, the presence of the exciton leads to a Rabi splitting of the plasmonic resonance.

These observations for achiral spectroscopy techniques motivate the question whether plasmonic nanostructures can increase the sensitivity of chiroptical spectroscopy and, especially, CD spectroscopy as well. However, this question is non-trivial. Although plasmonics

³ Note that only ring cavities can be used for this purpose because polarization rotation in a chiral medium is reversed for opposite propagation directions.

can be used to enhance the absorption of both LCP and RCP, CD spectroscopy requires an enhancement of the differential response.

An early review of the first observations of such enhancement is given in [155]; more recent work has been covered in [156]. In the following, we will review the different approaches for sensitivity enhancement as well as the advances that have been made in recent years both experimentally and theoretically.

We focus on plasmonic enhancement, i. e., results due to electromagnetic near- or far-field interaction either between the nanoparticle and the molecule or between several nanoparticles. Chemical bonds between the molecules and the nanoparticles, which can result in a distortion of the electronic structure that gives rise to additional chiroptical responses, are not in the scope of this thesis. These mechanisms, which result in chiral molecule-nanoparticle clusters, are extensively discussed in chemical literature [157].

3.3.1 *Single Plasmonic Nanoantennas*

We start with the simplest case, where single plasmonic nanoantennas are coupled to chiral molecules. In [158], Lieberman and collaborators reported on one of the first experiments for plasmon enhanced CD spectroscopy. They attached chromophores with chiral centers to small silver particles. The resonances of the chiral transition and the plasmon have been matched. The authors report almost two orders of magnitude enhancement of the CD signal, which they attribute to the presence of the plasmon. However, no further theoretical explanations of the observed behavior are given.

A theoretical description of the chiroptical exciton-plasmon interaction can be found in [159]. There, Govorov and collaborators analyze both resonant and off-resonant coupling via multipolar Coulomb interaction in a quantum-mechanical treatment. They could show that the presence of a metal nanoparticle leads to an enhancement of the natural CD of the molecule (cf. Fig. 3.3). Additionally, the presence of the molecule induces a CD signal at the plasmon resonance. This is attributed to the ORD of the molecule, because its CD signal is vanishing in the off-resonant case. The authors calculate enhancement factors of roughly one order of magnitude in the resonantly coupled

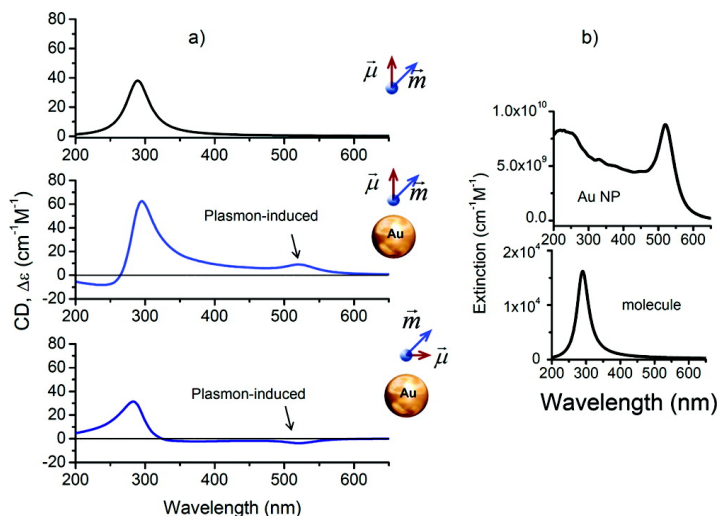


FIGURE 3.3. Theoretical calculations for the combined response of a chiral molecule close to a gold nanoparticle (radius 20 nm). The center-to-center distance has been set to 27 nm. (a) CD of the molecule alone as well as for the complex, plotted for two different orientations of the molecule. Both the enhanced CD of the molecule, as well as the induced CD at the plasmon resonance, are visible. Note that the resulting CD depends crucially on the orientation of the molecule. (b) Molar extinction of the nanoparticle and the molecule. [Image reprinted with permission from [159]. Copyright 2010 American Chemical Society.]

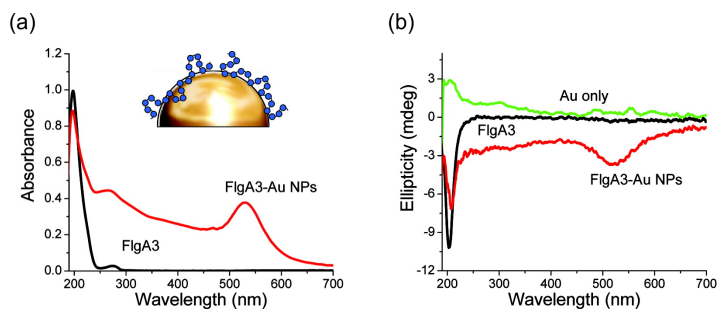


FIGURE 3.4. Induced CD in a gold nanoparticle functionalized with FlgA3 peptides. (a) Absorbance spectra. (b) CD spectra. [Image reprinted in part with permission from [160]. Copyright 2011 American Chemical Society.]

case. The enhancement becomes weaker in the off-resonant case: The induced CD in the nanoparticle scales with the inverse of the detuning, while the plasmonically enhanced CD of the molecule scales with the square of the inverse detuning. However, the off-resonant case is more realistic, because most natural chiral molecules exhibit their CD bands in the UV region, where it is difficult to obtain plasmonic resonances with commonly used materials [161]. A more sophisticated model, where the response of the chiral molecule has been calculated via density functional theory, can be found in [162].

Experimental observation of induced CD has been reported in [160]. In this work, the authors functionalized gold nanoparticles with a radius of 10 nm with chiral peptides (FlgA3). The CD response of this peptide is located in the UV around 200 nm. The authors found an induced CD signal at the plasmon resonance at around 520 nm for the peptide-gold complex (cf. Fig. 3.4).

Similar observations of silver nanoparticles and cysteine, which are consistent with the theoretical model in [159], have been reported in [163]. In [164], the authors attached gold nanoparticles to a tobacco mosaic virus and observed a modification of the electronic CD of the virus in addition to the induced CD at the plasmon resonance. Harada and collaborators reported on enhanced CD and circularly polarized luminescence of a chiral complex in the presence of silver nanoparticles [165].

In [166], Maoz and collaborators could distinguish the plasmonic effect from other enhancement mechanisms. They synthesized silver nanoparticles in a solution of chiral molecules. For similar ratios of silver and molecules, they saw that degradation of the molecules due to high temperatures lowers the chiroptical effect. This indicates a plasmonic enhancement scheme. On the other hand, a dominance of silver in the solution resulted in temperature-independent CD signals indicating the formation of larger silver nanoparticles that are geometrically chiral. The implications of such chiral self-assembly for chiral sensing will be discussed in detail in Section 3.3.3.

For larger distances, retardation effects come into play. The resulting coupling must be described as electromagnetic far-field interaction. In [167], Govorov and Fan discuss a plasmonic particle that is surrounded by a thick shell of chiral molecules. The chiral material is incorporated via the constitutive equations (2.48). Such systems

can be solved analytically by an extension of Mie theory [168]. Similar to the near-field interaction, one observes an induced CD signal at the plasmon resonance. However, the response is very weak for small nanoparticles. For larger particles, the induced CD increases due to additional contributions of differential scattering, which is much stronger than differential absorbance in these systems. However, the response stays well below the CD signal of the molecular resonance.

This far-field coupling mechanism is demonstrated in [169] for gold crosses with lateral dimensions of 400 nm covered with a thick film of flavin mononucleotide. The authors observed induced CD at the plasmon resonance with an enhancement of three orders of magnitude. However, this value is obtained in comparison to the CD of the chiral analyte at the wavelength of the plasmonic resonance, which is negligibly weak. Compared to the molecular CD, the induced CD is roughly one order of magnitude weaker.

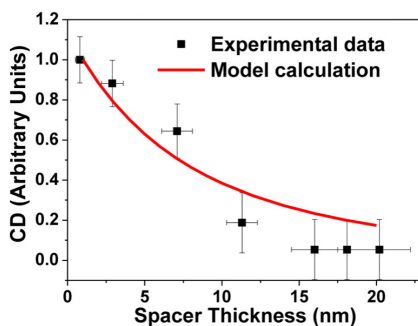


FIGURE 3.5. Induced CD signal on gold islands for various distances of a layer of chiral molecules. The calculated values have been obtained from a dipolar interaction model. [Image reprinted in part with permission from [170]. Copyright 2013 American Chemical Society.]

Maoz and collaborators demonstrated induced CD on gold islands (average radius 16 nm, average height 12 nm) covered with a layer of riboflavin embedded in spin-on glass (PMMA) [170]. They could tune the distance between the nanoparticles and the chiral layer with an achiral spacer layer that has been applied via a layer-by-layer technique [171] and, this way, demonstrate the distance dependence of the induced CD signal (cf. Fig. 3.5). Their results indicate that, for small

nanoparticles, the near-field coupling, which has a polynomial dependence on the distance, is dominant over the far-field coupling, which depends linearly on the distance.

We have shown in this section that single plasmonic nanostructures can enhance the molecular CD. Additionally, they exhibit induced CD at their resonance due to the ORD signal of the molecule. Although this can be used to shift the CD into regions that are better accessible, the enhancement is rather weak. The maximum theoretical enhancement of the CD signal for realistic chiral molecules will not exceed one order of magnitude [172]. Also, this enhancement is only obtained for a very precise distance between plasmonic particle and chiral molecule.

More complex nanoparticles can lead to larger enhancement. Lu and collaborators showed an enhancement of two orders of magnitude for DNA attached on silver nanocubes [173]. The plasmonic resonances around 350 nm are close to the electronic CD signal of DNA at roughly 260 nm. The higher enhancement compared to spheres has been attributed to the stronger field enhancement.

3.3.2 *Plasmonic Hot-Spots*

Another possibility for enhancement beyond the limit of single particles is the enhancement within the gap of a plasmonic dimer. It is important to note that this effect might even arise in experiments that report responses of single nanoparticles: If the nanoparticles are in solution, it is possible that several particles cluster and form small gaps with very high field enhancement. Therefore, such experiments should be checked for possible clustering of the nanoparticles.

An early systematic study of clustering effects is shown in [174]. The authors coated gold spheres (radius 10 nm) with a shell (thickness roughly 25 nm) of chiral oligonucleotide molecules. Compared to previous studies, they found neither enhancement of the natural CD nor induced CD at the plasmon resonance in this system. However, a strong CD response has been observed after washing by centrifugation, which resulted in aggregation of the nanoparticles (cf. Fig. 3.6). The authors confirmed this finding by breaking the aggregates via ultrasonic agitation, which reduced the CD response.

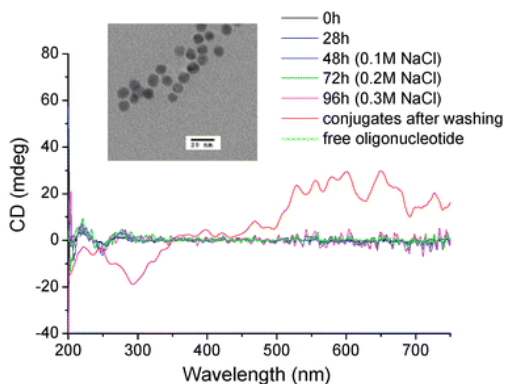


FIGURE 3.6. Conjugation of oligonucleotides to gold spheres alone does not lead to an enhanced CD signal, even after several days. After centrifugation, which leads to aggregation (cf. inset), a strong CD response is observed. [Image reproduced from [174] with permission from The Royal Society of Chemistry.]

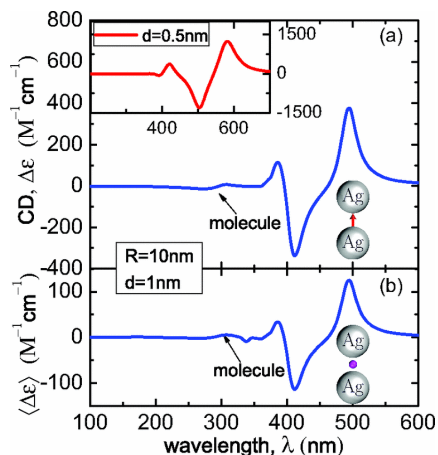


FIGURE 3.7. CD response of a chiral molecule oriented parallel to a dimer of silver nanoparticles for a gap size of 1 nm. The induced CD is significantly stronger than the molecular CD signal. The signal becomes weaker for isotropic orientation of the molecule. [Image reprinted with permission from [175]. Copyright 2013 by the American Physical Society.]

A first theoretical description of this behavior is given in [172], where the authors generalized their work for single plasmonic nanoparticles [159] to arbitrary (but achiral) geometries. They showed that dimers of nanoparticles lead to stronger enhancement than for single spheres both in the resonant as well as the off-resonant case. In [175], the off-resonant case for very small gap sizes has been studied in further detail. The authors demonstrated up to two orders of magnitude enhancement in the gap of a dimer of silver spheres. The enhancement is attributed to the strong near-fields in the gap and scales with the distance of the two nanoparticles. However, it crucially depends on the orientation of the molecule with respect to the dimer (cf. Fig. 3.7).

This theory has been applied to explain the CD spectra of cholate-coated silver nanoparticles [176]. Aggregation of nanoparticles with an average distance of (3 ± 2) nm resulted in a complex induced CD spectrum at the plasmonic resonance in this work. The signal disappeared after a change of the synthesis conditions that led to well-separated single nanoparticles instead of the clusters.

Achiral one-dimensional assemblies of gold nanorods linked by cysteine are reported in [177]. The gold nanorods form gap antennas with cysteine in the gap.

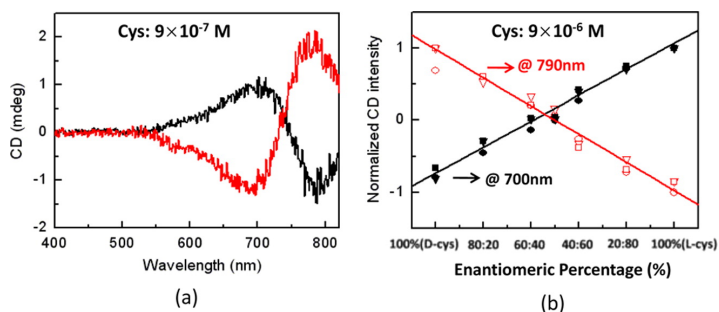


FIGURE 3.8. Enhanced chiroptical response of cysteine placed in a small gap of (1.1 ± 0.6) nm between two gold nanoparticles. (a) CD response for D- (red) and L-cysteine (black). (b) The CD response scales linearly with the percental distribution of the enantiomers. [Image reprinted with permission from [178]. Copyright 2014 American Chemical Society.]

Wang and collaborators reported on two orders of magnitude enhancement of the chiral response of cysteine in a small gap with a size of (1.1 ± 0.6) nm [178]. The electronic CD of the cysteine could not be detected because of the low concentration. The analysis has been performed for both enantiomers of cysteine, the results are mirror symmetric (cf. Fig. 3.8 (a)). Additionally, the CD intensity scales linearly with the enantiomeric purity. Therefore, this system can also be used to determine the distribution of enantiomers in the chiral analyte (cf. Fig. 3.8 (b)).

3.3.3 *Observation of Catalytic Reactions*

The previous sections discussed the coupling between chiral molecules and simple plasmonic nanostructures for CD spectroscopy with enhanced sensitivity. In this section, a different approach is reviewed. It uses the capabilities introduced in Section 2.3.2: Geometrically chiral plasmonic nanostructures exhibit chiroptical responses that are much larger than those of most natural chiral molecules.

These strong responses lead to a different approach for chiral sensing, in which the chiral analyte triggers a self-assembly process that results in a geometrically chiral arrangement of achiral constituents. This is not only useful as a method for structure fabrication, but also for chiral sensing because the resulting chiroptical response of the plasmonic structure can be precisely measured by common CD spectrometers. As long as the concentration of the chiral analyte determines this self-assembly process and, hereby, the CD response, it can be used for very sensitive enantiomer detection. In this method, the chiral analyte is detected indirectly via the much larger response of the assembled chiral nanostructure.

One demonstration of this idea has been reported by Wu and collaborators. They detected a chiral antibody using spherical nanoparticles that were linked to a long chain, which resulted in a sensitivity increase of one order of magnitude [179]. This chain should not be geometrically chiral in theory, but small imperfections in the spheres could result in a geometrically chiral structure. Similar results for the detection of bisphenol A have been reported in [180], silver ions have been detected in [181].

However, the sensitivity enhancement is comparable to the bare interaction with single achiral plasmonic nanoantennas. This can be attributed to the weak chiroptical response of the assembled chiral nanostructures due to the high symmetry of the almost spherical particles.⁴

An arrangement with stronger chiral asymmetry has been reported by Oh and collaborators. They analyzed a combined system of chiral poly(fluorene-alt-benzothiadiazole) and gold nanoparticles where the nanoparticles were arranged on a helical chain. This resulted, together with plasmonic enhancement, in an increase of the CD by three orders of magnitude [182].

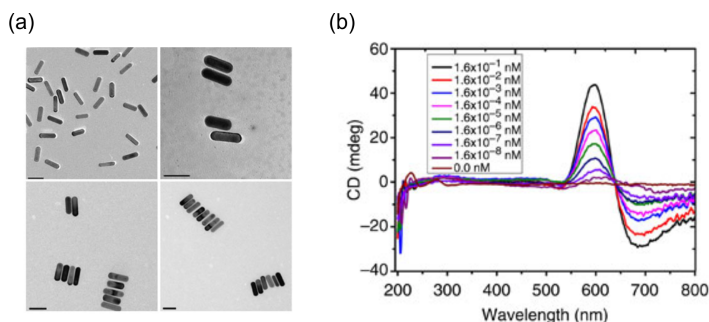


FIGURE 3.9. Indirect sensing of DNA via a self-assembly process. (a) Nanorod chains for increasing numbers of polymerase chain reaction cycles. Neighboring rods are rotated by a small angle with respect to each other. (b) The CD response scales with the DNA concentration. [Image reprinted in part with permission from [183].]

Another approach to reach higher enhancement is the usage of nanoparticles with lower symmetry such as rods. A strong CD signal is observed when several rods on a chain are twisted against each other. This has been demonstrated in [183], where DNA is used to trigger the assembly. The length of the chain depends on the number of polymerase chain reaction cycles, which leads to an increase as well

⁴ Note that also the chiral plasmonic oligomer can be built from perfect spheres. However, these structures utilize a chiral arrangement of the spheres, which cannot be observed in the discussed systems.

as a spectral shift of the CD signal. A change of the DNA concentration results in a change of the CD intensity without noticeable shifts (cf. Fig. 3.9). Monitoring of the CD signal leads to a very sensitive detection scheme for DNA.

Even higher sensitivity up to the zeptomolar scale could be obtained for chiral assemblies that have been coated with an additional metallic shell after the self-assembly process [184]. This surpasses the capabilities of other biosensing tools for the detection of DNA that do not depend on CD.

In principle, these mechanisms should be useful for enantiomer discrimination when the twist and, therefore, the handedness of the plasmonic structure depend on the handedness of the chiral catalyst. However, to the best of our knowledge, no demonstration of enantiomer discrimination by such a catalytic method has been published thus far.

The drawback of these techniques is that they are limited to specific chiral analytes. Only those analytes that trigger the respective self-assembly process can be monitored. The catalytic method offers a very high potential for sensitivity enhancement, but is not applicable as a general tool for arbitrary analytes.

3.3.4 *Chiral Hot-Spots*

The last concept, which we want to discuss here, is the use of chiral hot-spots. Compared to the other methods, complex plasmonic nanoparticles, instead of spheres or rods, are utilized. As such, additional geometrical influences that lead to more sophisticated near-fields can be used.

Pioneering work has been reported by Hendry and collaborators in 2010 [185]. They used a gammadion structure, which is planar geometrically chiral, and covered it with chiral molecules. The gammadion alone exhibits a CD signal due to the presence of the substrate as discussed in Section 2.3.2 (cf. Fig. 3.10 (a)). In the presence of chiral molecules, the authors observe a shift of this CD signal, whose direction depends on the handedness of the gammadion (best visible for β -lactoglobulin in Fig. 3.10 (b)). Any achiral effects should result in shifts in the same direction for both structures. Therefore, the authors attribute this difference in the shift to the chirality of the analyte.

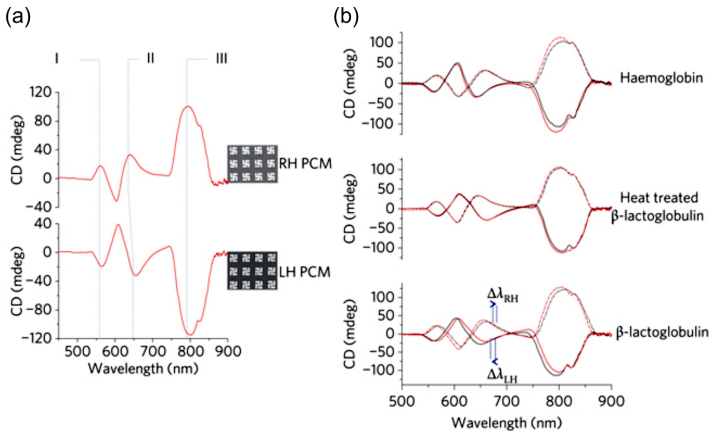


FIGURE 3.10. Enhanced sensitivity for chiral molecules using a plasmonic gam-madion. (a) CD spectrum of the structure in water. (b) The presence of chiral molecules induces opposite shifts for the different handednesses of the gam-madion. [Image reprinted in part by permission from Macmillan Publishers Ltd: Nature Nanotechnology [185], copyright 2010.]

Differences in these shifts of more than 15 nm have been presented. The authors estimate that the chiral interaction is about six orders of magnitude stronger as for measurements with CPL without the nanostructure. Part of this enhancement is dedicated to the enhanced near-fields that are shaped in a way that the interaction with chiral molecules is enhanced. However, no detailed analysis of the origin of these fields and their optimization is given.

Although this theoretical description is not sufficient to explain the experiment completely, it is a strong motivation to specifically analyze complex plasmonic nanostructures in terms of their capability for enhanced chiroptical spectroscopy. This analysis will be performed in the remaining chapters of this thesis.

CHIRAL PROPERTIES OF LIGHT

In Section 3.3, we discussed different approaches to plasmonically enhance the sensitivity of chiroptical spectroscopy techniques. A commonality of these methods is that the combined superstructure of plasmonic particle and chiral analyte is probed by CPL. This means that in the general principle of chiroptical spectroscopy, which is sketched in Fig. 4.1, one alters the chiral object to increase its response. However, the picture offers also a different possibility: We leave the structure unchanged and use some other kind of illumination that interacts stronger with the object to obtain the desired signal enhancement.

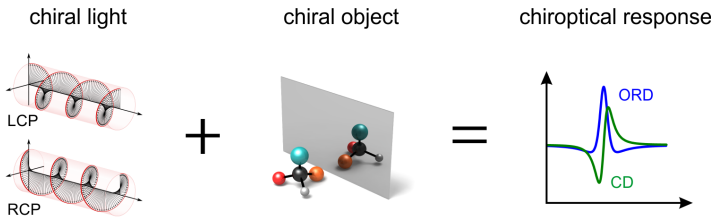


FIGURE 4.1. Sketch of the principle of chiroptical spectroscopy. Chiral light illuminates a chiral object to result in some chiroptical response.

To support this approach, we need to quantify the degree of chirality of electromagnetic waves. Tang and Cohen introduced such a measure and termed it *optical chirality* (OC) [10].¹

4.1 OPTICAL CHIRALITY

The optical chirality C can be directly calculated from the real part of the electric and magnetic fields \mathcal{E} and \mathcal{B} :

$$C := \frac{\epsilon_0}{2} \mathcal{E} \cdot (\nabla \times \mathcal{E}) + \frac{1}{2\mu_0} \mathcal{B} \cdot (\nabla \times \mathcal{B}) . \quad (4.1)$$

¹ In some literature, “optical chirality” is used for chiroptical far-field effects (mostly, CD). In this thesis, it always refers to the quantity defined via Eq. (4.1).

This quantity has already been discussed in 1964 by Lipkin who showed that it is preserved for any given electromagnetic field [186]. However, he was not aware of any physical interpretation of this quantity and, therefore, termed it *zilch*.

The flux Φ_C of OC can be written as

$$\Phi_C := \frac{1}{2} (\mathcal{E} \times (\nabla \times \mathcal{B}) - \mathcal{B} \times (\nabla \times \mathcal{E})) . \quad (4.2)$$

Using this flux, the continuity equation

$$\partial_t C + \frac{1}{\mu_0} \nabla \cdot \Phi_C = -\frac{1}{2} (\mathbf{j} \cdot \nabla \times \mathcal{E} + \mathcal{E} \cdot \nabla \times \mathbf{j}) \quad (4.3)$$

is fulfilled. Equation (4.3) is similar to Poynting's theorem that describes the flux of electromagnetic energy [27]. As it can be seen in the non-zero right hand side of Eq. (4.3), currents \mathbf{j} act as sources and sinks for OC.

An equivalent expression to Eq. (4.1) can be given for monochromatic electromagnetic fields with angular frequency ω :

$$C = -\frac{\varepsilon_0 \omega}{2} \Im \text{m} (\mathbf{E}^* \cdot \mathbf{B}) . \quad (4.4)$$

The derivation of Eq. (4.4) is shown in Appendix C.1. Note that \mathbf{E} and \mathbf{B} in Eq. (4.4) denote the complex electric and magnetic field, respectively, while only the real parts are considered in Eq. (4.1). Equation (4.4) is much simpler to compute than Eq. (4.1) because only the local fields have to be considered.

OC is a local property, i. e., the chiral properties of an electromagnetic field can vary for different spatial locations. It is a time-even pseudoscalar quantity that changes its sign under parity inversion, exactly as a geometrically chiral object changes its handedness when mirrored. Fields with opposite OC (but all other properties, such as, e. g., the energy density, unchanged) are referred to as *enantiomorphic fields*.

A physical interpretation of OC is given as follows: It can be shown that OC is proportional to the averaged helicity of an electromagnetic field while its flux is proportional to the spin angular momentum [187, 188]. However, this only holds true for monochromatic light. In general, the helicity of electromagnetic fields has a more general form, which is not directly proportional to OC [189, 190].

4.2 INTERACTION OF CHIRAL LIGHT WITH CHIRAL MOLECULES

So far, only the symmetry properties of OC have been analyzed. To be a valuable chiral measure, some correlation to chiroptical interactions must be found. We start this analysis by deriving the handedness-dependent absorption, which is directly connected to CD, in chiral fields.

4.2.1 *Handedness-Dependent Absorption*

The absorption characteristics have been theoretically predicted by Tang and Cohen in [10]. Further insight is given by Choi and Cho in [191]. In the following, we will show the key steps of their derivations. A detailed discussion is given in Appendix C.2.

The rate of absorption a of a chiral molecule with electric dipole moment \mathbf{p} and magnetic dipole moment \mathbf{m} in an external electromagnetic field is given as [192]

$$a^\pm = \left\langle \mathcal{E}^\pm \cdot \partial_t \Re(\mathbf{p}) + \mathcal{B} \cdot \partial_t \Re(\mathbf{m}) \right\rangle. \quad (4.5)$$

The superscripts denote the handedness of the incident field. Note that the magnetic field is even under parity, i. e., $\mathbf{B}^+ \equiv \mathbf{B}^- =: \mathbf{B}$. The same holds true for the real part \mathcal{B} . The brackets indicate averaging over time.

The induced dipole moments for a chiral molecule in an electromagnetic field read [13]

$$\mathbf{p} = \alpha \mathbf{E} - i\xi \mathbf{B}, \quad (4.6a)$$

$$\mathbf{m} = \chi \mathbf{B} + i\xi \mathbf{E}. \quad (4.6b)$$

Here, α is the electric, χ the magnetic dipole polarizability. The parameter ξ is the so-called mixed electric-magnetic polarizability [193]. It only appears in chiral systems. Equations (4.6) have a similar form as the constitutive equations for chiral media (cf. Eqs. (2.48)). However, the constitutive equations describe the response of an effective chiral medium, while Eqs. (4.6) describe the local response of a single chiral molecule.

We insert the dipole moments (4.6) into Eq. (4.5) after the time averaging has been performed. Then, we obtain

$$a^\pm = \frac{\omega}{2} \left(\Im \text{m} (\alpha) |\mathbf{E}|^2 + \Im \text{m} (\chi) |\mathbf{B}|^2 \right) + \Im \text{m} (\xi) \omega \Im \text{m} (\mathbf{E}^{\pm,*} \cdot \mathbf{B}) . \quad (4.7)$$

We can directly identify a term proportional to OC (cf. Eq. (4.4)). Now, we introduce the time-averaged electric and magnetic energy densities [27]

$$U_e = \frac{\epsilon_0}{4} |\mathbf{E}|^2 , \quad (4.8)$$

$$U_b = \frac{1}{4\mu_0} |\mathbf{B}|^2 \quad (4.9)$$

and obtain

$$a^\pm = \beta_e U_e + \beta_b U_b - \frac{2}{\epsilon_0} \Im \text{m} (\xi) C^\pm . \quad (4.10)$$

The prefactors β_i are given by

$$\beta_e := \frac{2\omega}{\epsilon_0} \Im \text{m} (\alpha) , \quad (4.11a)$$

$$\beta_b := 2\mu_0 \omega \Im \text{m} (\chi) . \quad (4.11b)$$

They are the same for both enantiomers of a given chiral molecule.

All chiral interaction is described by the product of the imaginary part of the mixed electric-magnetic dipole polarizability ξ and the optical chirality C . The differential response Δa for two incident electromagnetic fields with opposite handedness is given by

$$\Delta a := a^+ - a^- = -\frac{2}{\epsilon_0} \Im \text{m} (\xi) \underbrace{(C^+ - C^-)}_{=:\Delta C} . \quad (4.12)$$

The difference in OC for two enantiomorphous electromagnetic fields determines the differential response that can be theoretically detected in a CD type of measurement.

However, as seen in Eq. (4.10), the absorption also depends on the electric and magnetic energy density. Therefore, these quantities act

as additional background to the detected signal. This might be an issue for the experiment, where the background could be noisy.

Therefore, Tang and Cohen introduced the dissymmetry factor g , which they termed *enantioselectivity*:

$$g := \frac{\Delta a}{\frac{1}{2}(a^+ + a^-)}. \quad (4.13)$$

This equation can be expanded to

$$g = -\frac{2}{\varepsilon_0} \frac{\Im(\xi) \Delta C}{\beta_e U_e + \beta_b U_b} \quad (4.14)$$

for enantiomorphic fields in vacuum. An increase of the enantioselectivity results in a better signal-to-noise ratio for enantiomer discrimination [194]. Experimental evidence has been provided in [195]; the concept of this experiment will be discussed in Section 4.3 in more detail.

Note that the discussion in this section is solely based on electric and magnetic dipole transitions. Similar derivations are possible for higher-order multipole transitions [196]. However, they are not involved in the chiroptical interactions discussed in this theses and are, therefore, not discussed in detail.

4.2.2 Chiral Forces

Beyond absorption, an electromagnetic field that impinges on a molecule exerts optomechanical forces [197]. This is utilized in optical tweezers that trap microscopic dielectric particles in a highly focused laser beam [198]. Recently, Canaguier-Durand and collaborators showed that chiral electromagnetic fields interacting with chiral dipoles introduce additional forces, which depend on the relative handedness [199].

The time-averaged chiral force $\langle F_c \rangle$ can be separated in a reactive (superscript r) and a dissipative (superscript d) component. The reactive chiral force is linked to the gradient of OC :

$$\langle F_c^r \rangle = \frac{c^2}{\omega} \Re(\xi) \nabla C. \quad (4.15)$$

The dissipative component, on the other hand, depends on the flux of OC:

$$\langle F_c^d \rangle = \Im m \left(\xi \right) (2\Phi_C - \nabla \times \langle S \rangle) . \quad (4.16)$$

Here, $S = \Re e \left(\mathbf{E} \times \mathbf{H}^* \right) / 2$ is the Poynting vector. Both forces depend linearly on ξ and, therefore, exhibit opposite sign for the two enantiomers of a chiral molecule. For this reason, they can be used to optomechanically sort chiral molecules. This is beyond enantiomer discrimination, because even racemates are separated into the single enantiomers.

Nevertheless, these forces are small compared to the achiral contributions due to a gradient in the electric energy density. To overcome this issue, one has to engineer fields with homogeneous electric energy density but a gradient in OC. This can be obtained by superpositions of several plane waves [199, 200].

Cameron and collaborators, who performed similar calculations, proposed a scenario for a Stern-Gerlach type of experiment where different enantiomers are deflected into different directions [200]. Ding and collaborators numerically demonstrated an optical pulling force that depends on the relative handedness of the chiral object and the illumination [201].

4.3 OPTICAL CHIRALITY BEYOND CIRCULAR POLARIZATION

It is straightforward to calculate the OC of a plane electromagnetic wave. In the most general form, the complex electric field of such a wave traveling in z -direction is given by (cf. Eq. (2.4)):

$$\mathbf{E} = \begin{pmatrix} E_x e^{i\phi_x} \\ E_y e^{i\phi_y} \\ 0 \end{pmatrix} e^{i(kz - \omega t)} . \quad (4.17a)$$

The according magnetic field reads

$$\mathbf{B} = \frac{1}{c} \left(\hat{e}_z \times \mathbf{E} \right) = \frac{1}{c} \begin{pmatrix} -E_y e^{i\phi_y} \\ E_x e^{i\phi_x} \\ 0 \end{pmatrix} e^{i(kz - \omega t)} . \quad (4.17b)$$

Equation (4.4) finally leads to

$$\begin{aligned} C &= -\frac{\varepsilon_0\omega}{2c} \Im \left(-E_x E_y \left(e^{i(\phi_y - \phi_x)} \right) - e^{i(\phi_x - \phi_y)} \right) \\ &= \frac{\varepsilon_0\omega}{2c} E_x E_y \sin(\Delta\phi) \end{aligned} \quad (4.18)$$

with $\Delta\phi = \phi_x - \phi_y$. Obviously, $\Delta\phi$ is crucial for non-zero OC. LPL with $\Delta\phi = n\pi$ leads to vanishing OC; maximal values are obtained for

$$\Delta\phi = n\pi + \frac{\pi}{2} \quad (4.19)$$

with integral n and $E_x = E_y$. Such plane waves are circularly polarized. One obtains

$$C_{\text{CPL}}^{\pm} = \pm \frac{\varepsilon_0\omega}{2c} |\mathbf{E}|^2 \quad (4.20)$$

for the OC. Positive OC values correspond to left-handed, negative ones to right-handed CPL.

It is an interesting question whether it is possible to exceed these values. This would lead to an increased interaction with chiral molecules and, therefore, to a higher potential sensitivity for enantiomer discrimination.

In Eqs. (4.17), no explicit assumptions for the spatial shape of E_i and ϕ_i were made. Therefore, arbitrary spatial amplitude or phase shaping can change OC locally, but it will not exceed the maximum value that can be reached by CPL with the same local intensity. Even a configuration that looks twisted, such as a doughnut mode with azimuthal polarization, shows no OC because its local polarization is linear everywhere. These findings hold true as long as the field can be described as a traveling plane wave.²

More sophisticated fields, such as Bessel beams, which cannot be described by the general form of Eqs. (4.17), provide additional freedom to create chiral fields. In a focused Bessel beam, OC arises due to the non-zero longitudinal components of the electric and magnetic field [202].

² Similar considerations can be made for spherical waves. In this case, OC additionally scales with the radius r , similar to the intensity of the wave.

Another approach to reach high OC—compared to electric energy density—is given by Tang and Cohen in [10]: They studied the standing wave pattern of a mirror with a reflectivity R below 1 illuminated with CPL. In this case, the electric energy density at the nodes does not completely vanish. It can be shown that the OC is, independent of the spatial location, given by

$$C = \frac{\omega \epsilon_0}{c} (1 - R) |E|^2 \quad (4.21)$$

for incident LCP. The electric energy density, on the other hand, depends on the spatial location:

$$U_e = \frac{\epsilon_0}{2} \left(1 + R - 2\sqrt{R} \cos(2kz) \right) |E|^2. \quad (4.22)$$

This reduces to

$$U_e = \frac{\epsilon_0}{2} \left(1 - \sqrt{R} \right)^2 |E|^2 \quad (4.23)$$

in the nodes of the electric field. There, the maximum value of the dissymmetry factor reads

$$\tilde{g}(R) = \tilde{g}_{\text{CPL}} \frac{1 - \sqrt{R}}{1 + \sqrt{R}}. \quad (4.24)$$

Here, \tilde{g} is the dissymmetry factor when only the absorption due to U_e is considered (i. e., $\beta_b = 0$).

The dissymmetry factor $\tilde{g}(R)$ is strongly enhanced compared to CPL. This is what Tang and Cohen referred to as *superchiral light*. Note that Eq. (4.24) suggests a diverging enantioselectivity for $R \rightarrow 1$. Nevertheless, in this case the signal vanishes as well; the detection becomes more difficult with increasing R .

Additionally, most of the electromagnetic energy is stored in the magnetic field in the nodes of the described standing wave pattern. In this case, the contribution of the magnetic term in equation Eq. (4.10) cannot be ignored any more. This leads to a natural limit of the enhanced enantioselectivity by a factor of approximately [191]

$$\left(\frac{g}{g_{\text{CPL}}} \right)_{\text{max}} \approx \frac{c}{2} \sqrt{\frac{\Im m(\alpha)}{\Im m(\chi)}}, \quad (4.25)$$

which is purely determined by the properties of the chosen chiral analyte.

It is important to note that the areas with enhanced OC or enantioselectivity are always confined to some small spatial regions. The fundamental reason is that, as shown in Eq. (4.18), the OC of traveling plane waves is limited by the value of CPL. Higher values are only possible for superpositions of plane waves.

A different possibility to create strong chiral electromagnetic fields is the near-field region of plasmonic nanostructures, where evanescent waves exist. They can have properties that differ from traveling plane waves. However, the design of such structures is nontrivial because the local electric and magnetic fields must be controlled both in orientation and phase.

4.4 CHIRAL PLASMONIC NEAR-FIELD SOURCES

We term plasmonic nanostructures that are explicitly designed to generate strong chiral near-fields for increased interaction with chiral molecules *chiral plasmonic near-field sources*.

The description of the interaction in Eq. (4.12) offers the advantage that the light source can be completely decoupled from the chiral properties of the molecule as long as the molecules are placed in enantiomorphous fields and only interact weakly with the nanostructure. In this way, the plasmonic structures can be designed and optimized without taking any concrete chiral molecule into account. Additionally, the resulting structures are applicable for enantiomer discrimination in general and are not restricted to some special chiral analytes.

A less general scheme, which does not depend on enantiomorphous fields, could be obtained via Eq. (4.10): The absorption for different enantiomers differs, which could also be monitored. However, this complicates the experiment because a switching of the enantiomers, instead of the illumination conditions, must be applied for any kind of lock-in detection. In addition, the simulation becomes more difficult because ωU_e and ωU_b must be considered together with C .

However, a comparison of Eq. (4.8) with Eq. (4.20) leads to the estimate that ωU_e supersedes C by eight orders of magnitude. Simulations

in free space provide an estimate for the relative numerical error, which is in the order of 10^{-4} . Therefore, it would be necessary to increase the accuracy of the simulations by several digits to calculate the absorption rate via Eq. (4.10). Otherwise, the chiral contribution due to C would be hidden in the numerical noise of the achiral contributions.

The combination of challenges in the numerical simulation and the experimental realization led to the decision that only plasmonic near-field sources with enantiomorphic fields should be considered. For these structures, the calculation of ΔC is sufficient. Additionally, CD type of measurement schemes can be applied.

4.4.1 *Design Goals*

Before we analyze specific structures, we will discuss the design goals that we used for our near-field sources. Of course, the chiral near-fields should be as strong as possible, but this is not sufficient. There are additional requirements for chiral plasmonic near-field sources to be of use for enantiomer discrimination.

It is difficult to place one single chiral molecule in one chiral hot spot in the experiment. Instead, a whole area is covered with the chiral analyte. Therefore, one has to look for a continuous region with uniform handedness where the averaged OC is as high as possible. These regions should be located such that they are easily accessible by the chiral analyte. Regions with opposite OC should be hard to access because they diminish the expected signal.

For fabrication purposes, the dimensions and geometry of the structure must be chosen such that it can be fabricated by modern nanostructuring techniques. Of course, simple and cheap large-area fabrication would be preferable.

4.4.2 *Symmetry Considerations*

There are two main influences for the response of chiral plasmonic near-field sources: The geometry of the nanostructure and the polarization of the incident light that excites the plasmonic resonances. The former determines the plasmonic modes that are supported by the

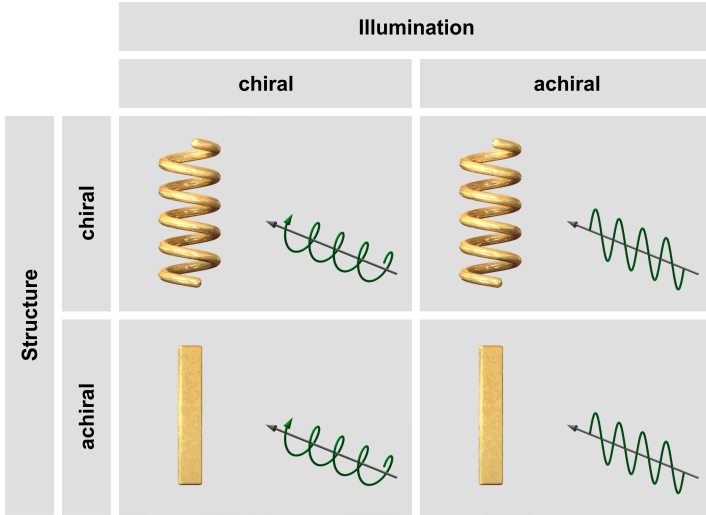


FIGURE 4.2. Plasmonic nanostructures and incident light are grouped by their chiral symmetry. Together, they build chiral plasmonic near-field sources whose properties are analyzed in the next chapters.

structure as well as the near-field patterns of the respective fields. The excitation efficiency of the modes is determined by the incident polarization. Additional near-field effects might arise due to interference between the incident and the scattered fields, which also strongly depends on the incident polarization.

All different combinations of structures and polarizations lead to a plethora of different designs to probe. To simplify the problem, we categorize both the structure and the incident polarization in terms of their chiral symmetry. Both can be either geometrically chiral or achiral. In terms of the incident polarization, we use CPL for the geometrically chiral configuration and LPL for the achiral one.

This categorization leads to four different groups that are sketched in Fig. 4.2. In the following chapters, we will discuss these four groups in detail and analyze the fundamental properties and potential applications for each of these combinations.

4.4.3 *Analysis Method*

We analyze the chiral plasmonic near-field sources by numerical full-field calculations. These calculations are performed by two different tools. Firstly, a commercially available finite element method solver, CST Microwave Studio (CST MWS) [203]. The second tool is an in-house implementation of a scattering matrix approach based on a Fourier basis.

This so-called Fourier modal method (FMM) is well-suited for the simulation of systems with stacked periodic layers. It has been optimized for fast convergence by application of Fourier-factorization rules and adaptive spatial resolution for the interfaces between the nanostructures and the dielectric background [204]. The implementation is very versatile and can be adjusted for specific problems. For instance, the chiral constitutive equations (2.48) have been implemented. Therefore, not only chiral geometries but also effective chiral media can be simulated, which is not possible with most commercial software.

One drawback of the FMM approach is that it is restricted to stacked systems. Fully three-dimensional geometries cannot be tackled with this approach. Additional constraints to the geometry are due to the adaptive spatial resolution that can only be applied to a given set of structures, where the necessary coordinate transformations have been formulated. For all other geometries, the respective transformations must be found first, which might be very time-consuming [205]. Therefore, we use CST MWS for such more complex geometries. The underlying Finite element method meshes the structure with a tetrahedral grid. In principle, it can be applied to arbitrary structures, but computing time and memory consumption increase for complex geometries.

The calculations in Chapters 5 and 6 as well as Section 8.3 have been performed with CST MWS. The FMM has been used for the simulations described in Chapter 7. All these designs have been calculated in a periodic arrangement because most nanofabrication techniques result in a surface patterned with the desired structure. Additionally, single particle experiments are more complicated and we, therefore, expect that experiments on larger samples with many structures will be performed first. We chose the size of the unit cells large enough

that no near-field coupling is observed. As a consequence, the plasmonic modes are localized to single structures. We expect our results to be applicable to single structures as well.

In Section 8.2, single structure calculations have been performed because of the size and the complexity of the suggested design. Such calculations can only be performed with CST MWS because the FMM inherently requires a periodic arrangement.

With both codes, the near-fields of the structures can be calculated. The local OC is obtained using Eq. (4.4). For comparison, we normalize the chiroptical near-field response to the OC obtained for CPL of the same frequency and intensity as the incident light:

$$\hat{C} := \frac{C}{|C_{\text{CPL}}|} = \frac{2c}{\varepsilon_0 \omega} \frac{C}{|\mathbf{E}_{\text{in}}|^2}. \quad (4.26)$$

Please refer to Appendix A.2 for details about the normalization procedure in CST MWS.

For all incident polarizations, the same normalization is performed. Therefore, \hat{C} does not denote the enhancement of OC compared to the incident light. Instead, the light field that is used for the normalization is assumed to be perfectly circular, which leads to the highest OC possible in a plane wave. Therewith, any value above unity describes a near-field pattern that has higher OC than possible for a plane wave with the same intensity and frequency as the incident light. The normalization is necessary to compare different nanostructures that are illuminated at different frequencies because OC is frequency-dependent. The sign of \hat{C} denotes the handedness of the chiral near-fields.

The resulting three-dimensional data is then plotted for analysis. A general overview over the shapes of regions with enhanced chiral near-fields is obtained via three-dimensional OC maps obtained by volume rendering. A detailed description of this plotting technique is given in Appendix A.3. Note that these maps are not optimal to obtain quantitative insights. Quantitative analysis is performed using two-dimensional slice plots.

A rough comparison between different structures can also be obtained by the maximal and minimal values of OC. However, numerical artifacts at the interfaces can lead to unphysical high values in

single points. For a better comparability, we remove these erroneous numbers by a $3 \times 3 \times 3$ median filter.

Nevertheless, we do not recommend to use the obtained values as single parameter for the comparison of different designs. As discussed in Section 4.4.1, several more properties must be taken into account to design good chiral plasmonic near-field sources.

ENHANCEMENT OF CHIRAL FIELDS BY GEOMETRICALLY CHIRAL STRUCTURES

At first, we will discuss the combination of chiral light with geometrically chiral plasmonic nanostructures. CPL exhibits the highest OC of any traveling plane wave (cf. Section 4.3). This section will address the question whether plasmonic nanostructures can locally enhance the OC of the incident light.

It is well-known that such nanostructures can be used to focus and tailor the intensity of an incident beam locally. The lightning-rod effect of sharp nanotips leads to strongly enhanced near-fields that exceed the intensity of the incident light by several orders of magnitude [36]. However, this field enhancement effect destroys the polarization of the incident light because the hot-spots are generated by the scattered fields of the nanostructures. The polarization of these fields is determined by the plasmonic mode excited by the incident light. Therefore, it is not sufficient to use a design with strong field enhancement and illuminate the respective structure with CPL. In this case, only the electromagnetic energy density, but not the OC, is expected to be enhanced.

However, we will show that geometrically chiral nanostructures enhance not only the electromagnetic energy density but can also lead to near-fields with high OC. Interestingly, even geometrically planar chiral structures exhibit promising properties in their near-fields as indicated by earlier work [206, 207]. Therefore, they will be analyzed for their use as chiral plasmonic near-field sources as well.

5.1 GEOMETRICALLY PLANAR CHIRAL DESIGNS

5.1.1 *Gammadions*

We start with an analysis of OC enhancement by the gold gammadion structure introduced in [185] with respect to enantiomer sensing. We

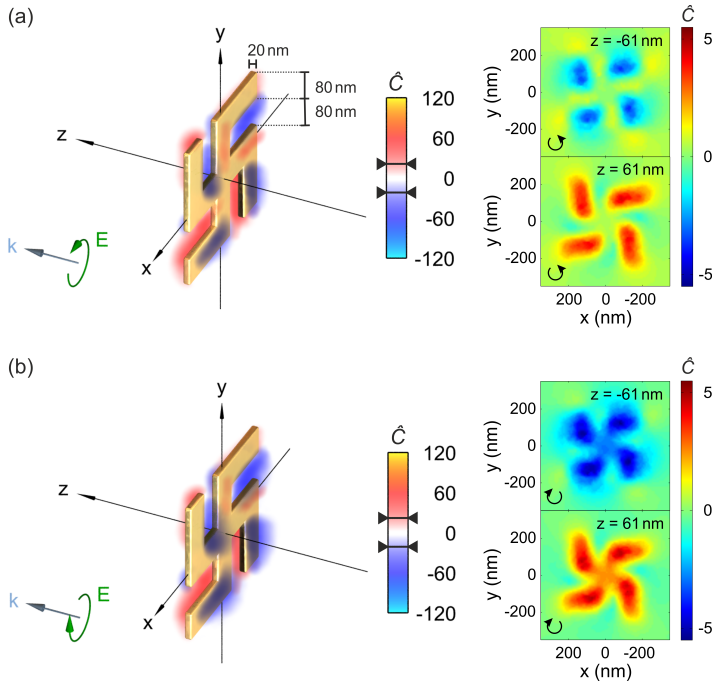


FIGURE 5.1. OC enhancement by planar gammadion structure illuminated with (a) LCP and (b) RCP at a frequency of 149.5 THz ($2.01 \mu\text{m}$). The black horizontal lines in the colorbar denote the maximal and minimal values of OC after filtering (cf. Appendix A.3). The structure exhibits similar shapes of the regions with enhanced chirality for both polarizations, only the values differ (best seen in the two-dimensional slice plots).

used similar dimensions (80 nm both for the width of the arms and the gaps, leading to a total width of 400 nm, but a gold thickness of 20 nm instead of 100 nm; the size of the unit cell was 800 nm). For different sizes of the nanostructure, we expect the OC to scale with the electric dipole moment of the particle plasmon and, therefore, with the volume of the individual nanoparticles. The structure was embedded in air. We calculated the fields at the fundamental plasmon resonance at 149.5 THz ($2.01 \mu\text{m}$).

The gammadion shows a similar behavior for both LCP and RCP as incident polarizations (cf. Fig. 5.1). We calculated maximal enhancement factors for OC in the range of 20. Interestingly, the gammadion shows both positive and negative values of OC with similar absolute values on the different sides of the structure: The regions with negative OC (and, therefore, right-handed near-fields) are located at the front, while left-handed near-fields can be found at the back of the structure. This distribution is independent of the handedness of the incident light.

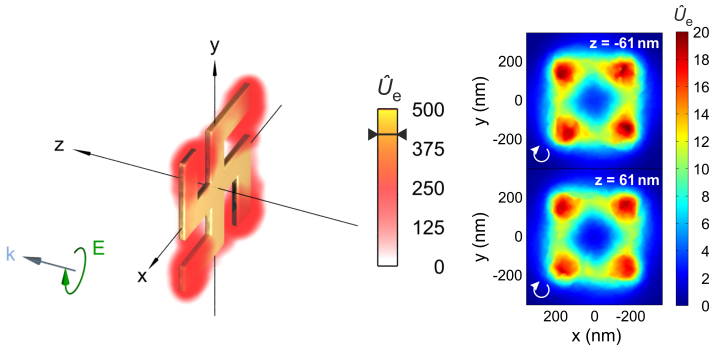


FIGURE 5.2. Enhancement of the electric energy density U_e by planar gammadion structure illuminated with RCP at a frequency of 149.5 THz ($2.01 \mu\text{m}$). Similar to OC, the electric energy density was normalized by the value obtained for RCP without the presence of the nanostructure. Strongest enhancement can be found at the end of each arm and the nearby gaps. For LCP, the enhancement is similar in shape.

The regions with locally enhanced OC are mainly located at the front and the back of the four arms. In contrast, the regions with high-field enhancement can be found at the end of each arm and in the gaps beneath these ends (cf. Fig. 5.2).

Similar to the field enhancement effect, OC is focused on distinct points in space. Nevertheless, the regions with highest enhancements differ for the two quantities. High field enhancement is, therefore, not sufficient to obtain strong OC. The reason is that the polarization of the incident light is not maintained by the field enhancement effect, as already discussed.

5.1.2 *Two-Armed Nanospirals*

A drawback of the gammadion design is that regions with enhanced OC are at the same position and have the same sign for both incident polarizations; only the absolute values differ. Therefore, a change of the incident polarization will result in only a small change of the OC at a certain position, which renders this design impractical for applications such as CD type of spectroscopies that rely on two chiral light fields with opposite handedness. As an additional disadvantage, the enhancement is discontinuous and overall quite small.

In Fig. 5.3, we show a more advanced planar nanostructure, namely, the nanospiral. Compared to the gammadion, the spiral features less sharp corners, which allows for smoother distributions of the regions with enhanced OC. The two-armed design was chosen to operate at 162.5 THz (1.84 μm) with comparable dimensions (80 nm arm width with a gold thickness of 20 nm; the unit cell was 1100 nm). At this frequency, the maximal circular polarization conversion difference is obtained. Each spiral features one and a half rotations, while the gammadion offered only one 90° kink at each arm.

As a result, the two incident polarizations show different behavior, which can be explained by Fig. 5.4. Therein, the induced current distributions for incident LCP and RCP are plotted. The different polarizations excite different modes. LCP excites currents in the outer part of the structure which leads to the ringlike region with enhanced OC, while the enhanced region for RCP is focused on the center. As an additional result, the signs of OC at the front and the back of the spiral along the z -direction change for the different polarizations.

It is important to note that all structures analyzed in this section are geometrically achiral because planar structures cannot possess structural chirality in a three-dimensional space. Nevertheless, the comparison between gammadion and nanospiral shows that stronger OC as well as a more uniform enhancement can be obtained by a structure with a stronger twist. Although the chiral far-field response of such structures occurs only in presence of a substrate, the chiral near-field enhancement is possible even without the substrate, as shown in our simulations.

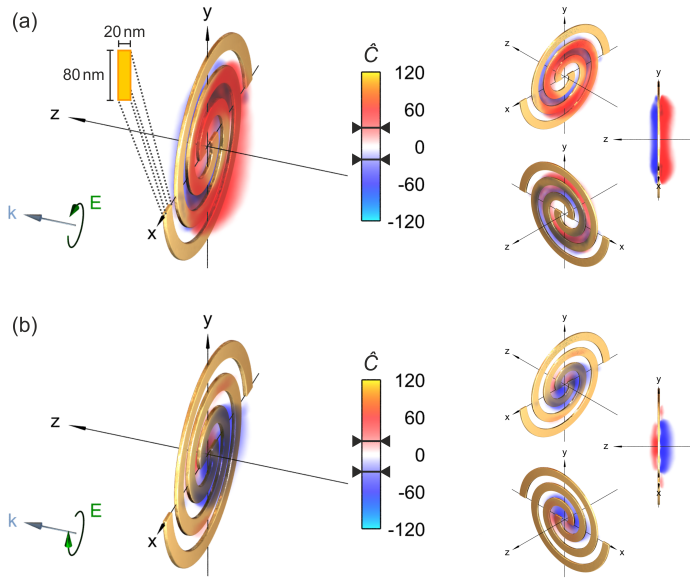


FIGURE 5.3. OC enhancement by a two-armed gold nanospiral with (a) LCP and (b) RCP as incident polarizations at a frequency of 162.5 THz ($1.84 \mu\text{m}$). The two polarizations differ significantly in their near-field response. The smaller pictures on the side show the scenario from different angles. The enhancement of OC is up to 50 % higher than for the gammadion, which can be understood by the fact that the spiral is bent everywhere.

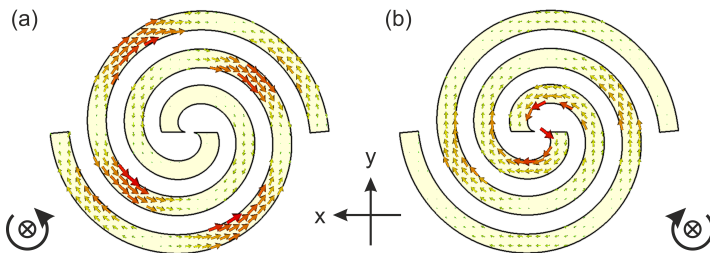


FIGURE 5.4. Current distributions inside the nanospiral for incident (a) LCP and (b) RCP light at 162.5 THz ($1.84 \mu\text{m}$). The two polarizations excite different modes. The current distributions correspond to the regions with enhanced OC identified in Fig. 5.3.

A drawback of structures with only planar geometrical chirality occurs when the response of the two different incident polarizations is compared. Although the absolute values of \hat{C} for the nanospiral are up to 50% higher than those of the gammadion, the contribution of RCP at the spatial points, where the OC enhancement for LCP is strong, is negligibly small and vice versa. This correlation limits the benefit of switching between the two polarizations. To overcome this limitation, one can use three-dimensional structures with intrinsic geometrical chirality.

5.2 THREE-DIMENSIONAL GEOMETRICALLY CHIRAL DESIGNS

5.2.1 Helices

The simplest three-dimensional generalization of the spiral is a helix. It has been shown in detail that such structures exhibit a very strong transmittance difference [81]. However, Fig. 5.5 (a) shows that the OC is enhanced in regions that are quite difficult to access.

The enhancement itself is smaller than the one obtained for the gammadion—even when the handedness of the incident light matches

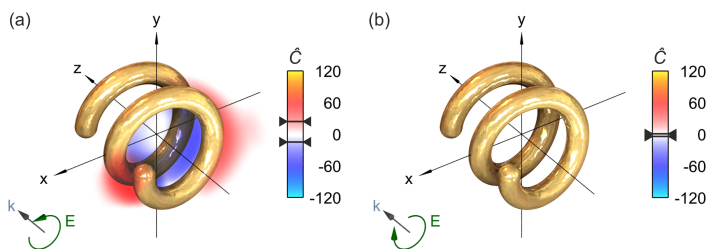


FIGURE 5.5. (a) OC enhancement for a left-handed helix and left-handed CPL at the frequency with maximal transmittance difference (147.5 THz, $\lambda = 2.03 \mu\text{m}$). Diameter and pitch of the helix are 400 nm with a gold thickness of 80 nm (unit cell 750 nm) to match with the dimensions and operation frequencies of the previous structures. The enhancement is even smaller than the values obtained for planar structures. (b) The response is almost vanishing when the incident polarization is right-handed.

the one of the helix. For the opposite circular polarization, the enhancement is too small to be visible in the plot (cf. Fig. 5.5 (b)). However, the locations of the regions with strongest OC enhancement are located at the very same positions, but with different signs for the two polarizations. Thus, three-dimensional chiral structures can lead to an increase of $\Delta\hat{C}$. Unfortunately, the helix offers only small enhancement¹ and is hard to fabricate.

5.2.2 Chiral Plasmonic Oligomers

To overcome the issues with plasmonic nanohelices, we use the six-disk chiral plasmonic oligomer introduced in Section 2.3.2. The stacking of several layers with planar structures is a well-established technique in nanofabrication [30]. Additionally, the usage of small disks as building blocks allows for tuning of the operation frequency to higher values: The resonant operating frequency is governed by the particle plasmon resonance of the individual gold nanodisks, modified by plasmon hybridization due to strong near-field coupling (cf. Section 2.2.1.3). The design exhibits maximal transmittance difference in the NIR at 333.0 THz (900 nm).²

Figure 5.6 shows the OC enhancement induced by the chiral plasmonic oligomer. As in the case of the helix, we obtain a much stronger response when the handednesses of both the structure and the incident light match. Compared to the gammadion, the response of \hat{C} is about five times higher for LCP, while for incident RCP still comparable values occur. The highest absolute values for both polarizations are located at the same spatial positions, which leads to regions with $\Delta\hat{C}$ of more than 100.³ The analysis of the distribution of the regions with enhanced OC reveals that (beside some small areas near the surfaces of the disks) a continuous region with consistent handedness is located around the two disks at the bottom left.

¹ We will show in Section 8.2 that this small enhancement is not an intrinsic problem of the helix but is due to the wrong excitation of its resonance.

² A plot of this chiroptical far-field response can be seen in Fig. 2.14 where the same geometry parameters have been used.

³ This analysis is not shown in Fig. 5.6. However, the design is rediscovered in Section 6.3. A plot of $\Delta\hat{C}$ is shown in Fig. 6.4 in this section.

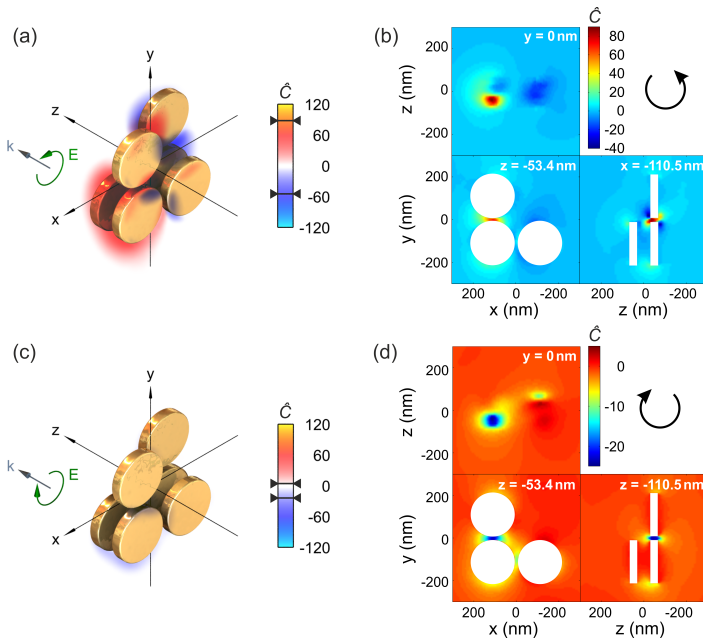


FIGURE 5.6. OC enhancement of the chiral oligomer (disk radius 100 nm, thickness 20 nm, distance 40 nm, unit cell 600 nm) for incident (a), (b) LCP and (c), (d) RCP light at a frequency of 333.0 THz (900 nm). The points with strongest enhancement can be found on similar spatial locations but exhibit different signs. (b), (d) Slices through the central point between the top and bottom left disk of the front layer confirm that the region with strongest enhancement is located in the gap between these two disks.

Subfigures (b) and (d) show slices through the point with highest chirality enhancement, which is located in the center of the gap between the top and the bottom left disk of the front layer. We consider that this particularly strong effect arises because of the near-field enhancement, which is highest in the small gaps between the disks. However, the access to these strongly enhanced chiral near-fields is more challenging than for the discussed planar designs because the structure has to be embedded in a dielectric matrix to enable the stacked fabrication.

5.2.3 *Stereometamaterials*

The third dimension offers many more possibilities for geometrically chiral structures than the two-dimensional case. In Fig. 5.7, we depict the OC for stacked and twisted plasmonic SRRs. The chiral far-field response of these so-called stereometamaterials [92] is well-known [208, 209]. The dimensions were chosen to fit the geometry introduced in [92], which leads to a frequency with highest transmittance difference of 223.5 THz; this corresponds to a wavelength of 1.34 μm .

Interestingly, we find that, for this left-handed structure, the strongest chirality enhancement is obtained not for LCP (Fig. 5.7 (a)) but for RCP incident light (Fig. 5.7 (b)). This behavior can be easily explained: The far-field response of the stereometamaterial shows the typical Born-Kuhn shape with two hybridized modes (cf. Fig. 5.8). We chose the higher-energy mode for the analysis because its transmittance difference was stronger. However, this mode interacts strongest with CPL with a handedness opposite to the intuitive handedness of the structure.⁴

For both polarizations, positive OC values are obtained in the gap, while negative values occur in the surrounding medium. The strength of the enhancement is between the values of the planar structures and the chiral oligomer. The strongest enhancement is not located in the gap of one SRR but in the layer between the two resonators. Additional degrees of freedom, such as the twist angle, could be used to tune this behavior.

5.3 DESIGN PRINCIPLES

Our numerical simulations demonstrate that both planar as well as three-dimensionally geometrically chiral plasmonic structures can drastically change the chiral properties of the incident light. We found that near-field enhancement and twisting should be combined, although highest OC will not automatically occur at regions with highest electric energy density.

⁴ This example shows once more that handedness definitions are rather arbitrary and do not lead to a deeper understanding of the discussed structure. Additional information beyond the handednesses of the constituents is necessary to analyze and describe chiral plasmonic systems properly.

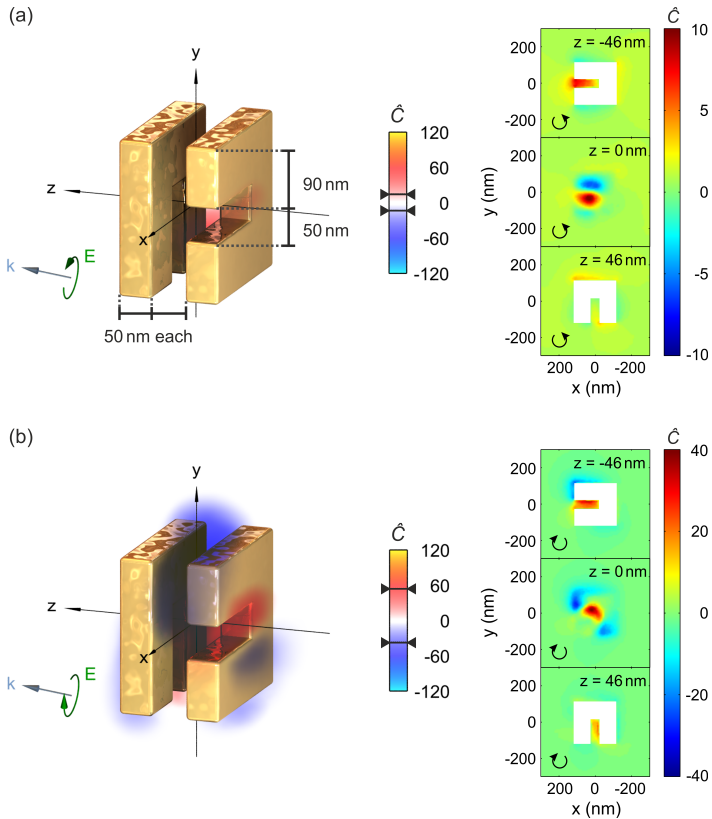


FIGURE 5.7. OC enhancement induced by the stereometamaterial with (a) LCP and (b) RCP as incident polarizations at 223.5 THz ($1.34 \mu\text{m}$). Note that the enhancement is strongest, when the handedness of the light is opposite to the one of the structure. The strongest enhancement can be observed in the middle of the layer between the two SRRs.

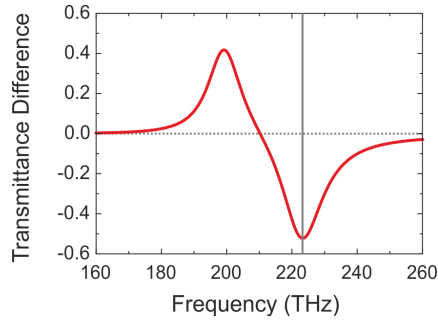


FIGURE 5.8. Chiroptical far-field response of the stereometamaterial. The vertical gray line marks the frequency with strongest transmittance difference. The OC maps in Fig. 5.7 have been calculated at this frequency.

Nevertheless, there is a huge parameter space to explore; the OC enhancement is non-trivial to predict. Therefore, we give some design principles for chiral nanostructures illuminated with CPL that we extracted from our present analysis to match the demands of chiral plasmonic near-field sources. If simple access to a continuous region of enhanced OC is needed, a planar geometrically chiral structure with a strong twist, and ideally without sharp corners, should be used. We recommend three-dimensionally geometrically chiral structures, which should be as compact as possible, to obtain strong chiral near-fields that change their handedness locally upon switching of the incident polarization.

CHIRAL FIELDS OF MACROSCOPICALLY ACHIRAL ARRANGEMENTS

We showed in Chapter 5 how geometrically chiral structures that are illuminated with CPL can lead to areas with strongly enhanced OC. These chiral hot-spots could be used for chiroptical spectroscopy techniques. However, such schemes exhibit two major disadvantages.

The first disadvantage is that they do not provide enantiomorphous fields. Although one chiral hot-spot might change its handedness upon switching of the incident polarization, the absolute values of OC will also change (consider, e. g., the plasmonic oligomer discussed in Section 5.2.2). In addition, the electromagnetic energy density changes. To obtain the enantiomorph of the chiral near-field, incident polarization *and* structure must change their handedness simultaneously.

The second disadvantage results from the chirality of the structure, which leads to a chiroptical far-field response of the nanostructure even without the presence of chiral molecules. As shown in Section 2.3.2, the chiroptical responses of plasmonic nanostructures are several orders of magnitude stronger than those of chiral molecules. Therefore, any measurement suffers from this additional noise.

As a consequence, *achiral* plasmonic nanostructures are preferable. The signal-to-noise ratio is strongly improved because of the missing contribution to the CD signal by the structure itself. Additionally, geometrical achirality ensures enantiomorphous fields: Parity inversion will change the handedness of both the nanostructure and the incident field. If the nanostructure is geometrically achiral, it stays unaltered. Because OC is odd under parity (while the energy density is even), the fields must result in their enantiomorph under parity inversion.

Note that this does not necessarily mean that electromagnetic fields are replaced by their enantiomorph at each point in space when you look at the structure and change the handedness of the illumination. The structure has still been mirrored, although this is not recognized,

because it will look the same after parity inversion. Nevertheless, the enantiomorphic field will be found on the corresponding position of the mirror image.

Recently, Yoo and collaborators have shown that a film of a double fishnet metamaterial locally enhances the OC up to one order of magnitude [210]. Their structure is achiral; switching between enantiomorphic fields can be realized via a change of the incident polarization. Garcia-Etxarri and Dionne showed earlier that enantiomorphic field pairs can be found on top and below spheres illuminated with CPL [211].

However, the values of OC found for these designs are rather low compared to the results we obtained in Chapter 5. In this chapter, we will demonstrate how to use our previous findings to design near-field sources that combine the advantages of geometrical achirality with the strong chiroptical near-field response gained by geometrically chiral structures.

6.1 RACEMIC MIXTURES OF CHIRAL PLASMONIC NANOSTRUCTURES

The key idea, which we used to accomplish the goal of combining the strong response of chiral structures with the benefits of geometrical achirality, is the so-called *racemic mixture*. In chemistry, a racemic mixture (or *racemate*) is an equal mixture of both enantiomers of a given chiral substance. Each of the single molecules is still chiral, but the total chiroptical response, which is given as the averaged response of all the individual molecules, vanishes. Therefore, the racemate is effectively achiral.¹

We realize plasmonic racemates by using a supercell that combines both enantiomers of a given geometrically chiral plasmonic nanostructure. Figure 6.1 demonstrates this concept for the example of a helix. Each individual helix is geometrically chiral, but the supercell

¹ This is even true from a geometric point of view: For each left-handed molecule, there is also a right-handed one in the mixture. Each individual molecule changes its handedness after parity inversion, but the collective superstructure of all molecules looks still the same.

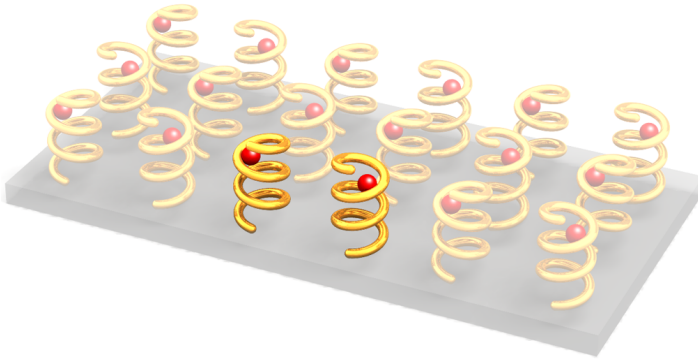


FIGURE 6.1. A plasmonic racemate is built by the combination of both enantiomers of a geometrically chiral plasmonic structure in one supercell. Each individual structure is chiral, but the whole array is achiral due to the presence of both enantiomers. The red spheres indicate regions where enantiomorphous electromagnetic fields are expected when the incident polarization is switched.

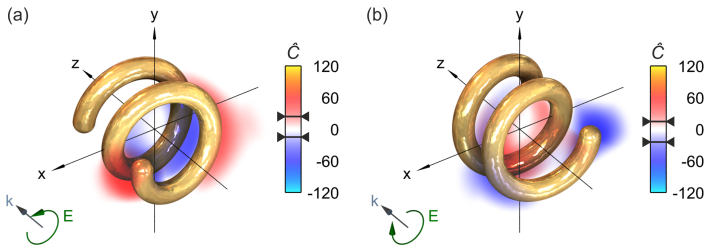


FIGURE 6.2. (a) A left-handed helix illuminated with LCP at 147.5 THz ($2.03 \mu\text{m}$) leads to strong chiral near-fields. (b) Enantiomorphous fields are generated when the handednesses of both the helix as well as the incident polarization are switched.

is geometrically achiral. Therefore, no chiroptical far-field response is obtained for the periodic arrangement of this supercell.²

As long as there is a sufficient gap between the single helices, their near-fields are effectively decoupled. This means that the near-field response is similar for an arrangement of helices with only one handedness. Such an arrangement has been discussed in Section 5.2.1. Figure 6.2 (a) is a reproduction of Fig. 5.5 (a): A left-handed helix illuminated with left-handed CPL. If only the incident polarization is switched, the coupling of the external field to the helix is strongly reduced and, therefore, the OC almost vanishes (cf. Fig. 5.5 (b)). To obtain enantiomorphic fields, the handedness of the helix must be switched as well (cf. Fig. 6.2 (b)). Then, the local chiral near-fields change their handedness as expected.

Note that the regions with strongest OC also change with respect to the parity inversion: The left-handed fields, which are located left to the front of the left-handed helix, find their counterpart right to the front of the right-handed one.³ Therefore, it is impossible to illuminate a single molecule by enantiomorphic fields in this configuration. However, two molecules located at corresponding positions (as indicated by the red spheres in Fig. 6.1) will be illuminated by enantiomorphic fields after the handedness of the incident polarization is switched.

The general idea can be described like this: One incident polarization excites the corresponding enantiomers of the plasmonic nanostructure, which will lead to chiral near-fields. Then, the incident polarization is switched. The second polarization interacts stronger with the other enantiomer of the structure. Therefore, the second molecule is excited by a chiral field that is the enantiomorph of the field exciting the first one. As long as the molecules are chiral (and possess the same handedness), the difference in the simultaneous response of both molecules upon a change of the incident polarization can be detected.

² Recently, Larsen and collaborators used a GLAD technique to fabricate a chiral racemate. The resulting film consisted of patches with opposite handedness [212].

³ This is a fact that is simply understood because the helix itself is geometrically chiral. In Chapter 7, where we will discuss highly symmetric and geometrically achiral nanoantennas, the same effect occurs. However, this behavior is much more confusing in the corresponding discussion due to the high symmetry of the system.

6.2 COLLECTIVE RESPONSE OF CHIRAL MOLECULES NEAR PLASMONIC RACEMATES

We consider two molecules located at the positions \mathbf{r} and \mathbf{r}' where enantiomorphic fields are generated (cf. Fig. 6.3). These fields fulfill the conditions

$$U_e^\pm(\mathbf{r}) = U_e^\mp(\mathbf{r}') , \quad (6.1a)$$

$$U_b^\pm(\mathbf{r}) = U_b^\mp(\mathbf{r}') , \quad (6.1b)$$

$$C^\pm(\mathbf{r}) = -C^\mp(\mathbf{r}') . \quad (6.1c)$$

The superscripts denote the two different incident polarizations that generate the chiral near-fields. Note that they are not necessarily circular polarizations with opposite handedness, any pair of polarizations that is connected via mirror symmetry can be used. For consistency, we will use the superscripts with respect to the handedness of the chiral near-fields generated. The polarization that generates predominantly left-handed chiral near-fields in the region of interest is labeled “+”, the other “-”.

Note that the fields of both incident polarizations must be evaluated at both spatial locations. Although the incident polarization might excite one enantiomer of the plasmonic nanostructure more strongly,

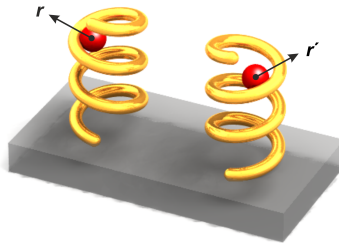


FIGURE 6.3. The unit cell of a plasmonic racemate consists of the two enantiomers of one geometrically chiral plasmonic nanostructure. Enantiomorphic near-fields are generated at the positions \mathbf{r} and \mathbf{r}' . These two positions are related by the same mirror operation that translates the two enantiomorphic nanoobjects one into another.

it still generates chiral fields at the location of the other molecule. Of course, this excitation—albeit weaker—is also detected in the proposed measurement scheme.

The combined absorption rate a^* of both molecules under mirror-symmetric illumination is given by (cf. Eq. (4.10))

$$\begin{aligned} a^{*,\pm} &:= a_r^\pm + a_{r'}^\pm \\ &= \beta_e \left(U_e^\pm(\mathbf{r}) + U_e^\pm(\mathbf{r}') \right) + \beta_b \left(U_b^\pm(\mathbf{r}) + U_b^\pm(\mathbf{r}') \right) \\ &\quad - \frac{2}{\varepsilon_0} \Im \text{m} \left(\xi \right) \left(C^\pm(\mathbf{r}) + C^\pm(\mathbf{r}') \right). \end{aligned} \quad (6.2)$$

Here, the subscript of a denotes the respective molecule. Using the conditions in Eqs. (6.1), this reduces to

$$\begin{aligned} a^{*,\pm} &= \beta_e \left(U_e^\pm(\mathbf{r}) + U_e^\mp(\mathbf{r}) \right) + \beta_b \left(U_b^\pm(\mathbf{r}) + U_b^\mp(\mathbf{r}) \right) \\ &\quad - \frac{2}{\varepsilon_0} \Im \text{m} \left(\xi \right) \left(C^\pm(\mathbf{r}) - C^\mp(\mathbf{r}) \right). \end{aligned} \quad (6.3)$$

Only the near-fields at location \mathbf{r} are necessary to obtain the collective response. Therefore, it is sufficient to calculate the near-field response of only one enantiomer as long as the two structures in the supercell do not couple. This simplifies the calculations because the simulation domain is effectively cut in half.⁴ Near-field coupling, of course, would distort the fields.

Using Eq. (6.3), the differential absorption rate of the whole system illuminated with altering polarizations + and – can be calculated as

$$\Delta a^* = -\frac{2}{\varepsilon_0} \Im \text{m} \left(\xi \right) \left(2C^+ - 2C^- \right) = -\frac{4}{\varepsilon_0} \Im \text{m} \left(\xi \right) \Delta C \equiv 2\Delta a. \quad (6.4)$$

The additional factor of 2 compared to Eq. (4.12) is obtained because the response of two molecules is considered. The enhancement of the differential response compared to illumination with CPL is given by

$$\Delta \hat{a}^* = \Delta \hat{C}. \quad (6.5)$$

Therefore, $\Delta \hat{C}$ can be used to estimate the usefulness of a given plasmonic nanostructure as a sensing device when the proposed measurement method is used.

⁴ It is divided by four if the more isotropic unit cell from Fig. 6.1 is assumed.

6.3 CALCULATED PERFORMANCE OF PLASMONIC RACEMATES

When we evaluate the enhanced combined absorption rate for the helix structure already discussed, we find a similar picture as Fig. 6.2 (a). Plots for $\Delta\hat{C}$ are almost identical to the respective \hat{C} maps because the responses for LCP illumination of the right-handed enantiomer as well as RCP illumination of the left-handed enantiomer are very small. The maximum OC enhancement for both configurations is 4; at most spatial locations, the enhancement is smaller.

The chiral plasmonic oligomer, which we already discussed in Section 5.2.2, offers much higher OC. In addition, the regions with highest enhancement are the same for both incident polarizations, but the

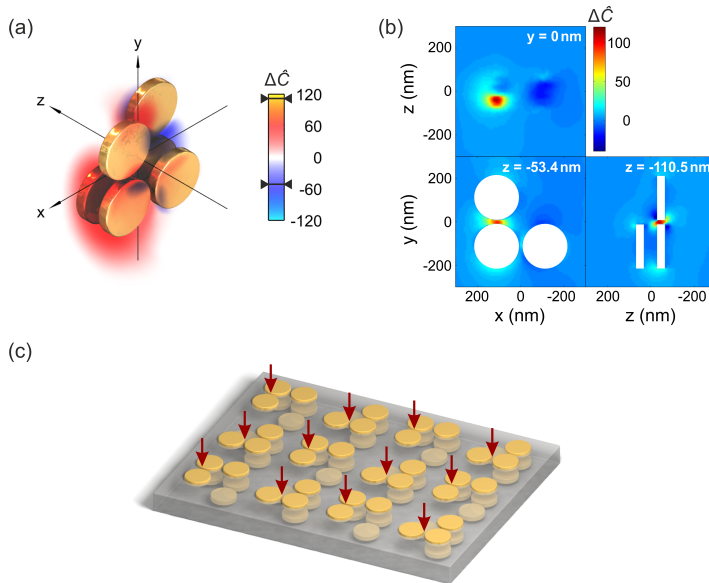


FIGURE 6.4. (a) Differential chiral near-field response $\Delta\hat{C}$ of the chiral plasmonic oligomer at 333.0 THz (900 nm). Overall, a strong chiroptical near-field response is obtained. (b) The slice plots confirm the hot-spot between two disks of the upper layer. (c) Schematic view of the according plasmonic racemate. The red arrows mark the positions with strongest differential chiral near-field response, where the chiral analyte should be placed.

handedness of the respective chiral near-fields differs. Therefore, we obtain high values for $\Delta\hat{C}$ (cf. Fig. 6.4 (a)). Enhancement factors that exceed 100 could be obtained in the hot-spot between two disks of the first layer (cf. Fig. 6.4 (b)).

However, small hot-spots are a disadvantage for the general performance of chiral near-field sources. Although some enhancement is expected in the surrounding as well, the structure works best if the chiral analyte is located only at the hot-spots. This is sketched in Fig. 6.4 (c), where we construct a racemate from chiral plasmonic oligomers. We used a supercell with four single oligomers where the next neighbors in each direction are enantiomers. Note that this supercell offers no intrinsic C_4 symmetry. Therefore, the device should be checked carefully for circular polarization conversion. The positions, at which the chiral analyte should be placed, have been marked with red arrows. This leads to a non-trivial pattern that might be difficult to realize in the experiment.

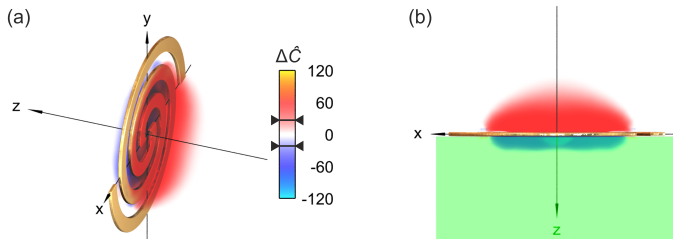


FIGURE 6.5. Enhancement difference $\Delta\hat{C}$ of the nanospiral at 162.5 THz ($1.84\ \mu\text{m}$). (a) The distribution of the regions with enhanced OC is continuous, while the structure separates the parts with different signs. (b) The access is limited to one polarity in presence of a substrate. Note that this picture is only a sketch; the calculation has been performed without the substrate.

A simpler access scheme can be realized in the nanospiral, whose response to CPL has been discussed in Section 5.1.2. Most importantly, the regions with opposite handedness of the chiral near-fields are separated by the structure in this design: One handedness appears at the front, the other at the back. The signs flip when the incident polarization is changed. Therefore, we obtain uniform signs for the differential OC enhancement, as shown in Fig. 6.5 (a). Although the regions with

enhanced OC are different for the two incident polarizations, they add up nicely when the differential response is considered.

Again, the regions with different polarity are clearly divided by the structure. This offers a straightforward way to ensure that only regions with the same polarity are accessed: When the plasmonic racemate from nanospirals is fabricated on top of a substrate, which is normally the case for lithographically defined structures, access to the back of the structure is prevented (cf. Fig. 6.5 (b)). Therefore, this design can be directly used as chiral plasmonic near-field source without further modifications.

6.4 LOCALLY CHIRAL PLASMONIC METASURFACES

The big gap between the structures, which is necessary to prevent near-field interaction, is a disadvantage of the plasmonic racemates discussed thus far. If we think of a surface covered with plasmonic nanostructures that should act as a sensing device, only small parts of this surface enhance the chiroptical response. Most of the chiral analyte is located at regions with no nanostructure and, therefore, no benefits for enantiomer discrimination.

In addition, fabrication is more complex when a supercell consisting of both enantiomers must be considered. This is no constraint for EBL or comparable methods, but many low-cost large-area methods cannot fabricate arbitrarily complex patterns.

In this section, we will loosen the constraint of the big gap between the single structures and discuss designs where both enantiomers are combined in one continuous unit cell. The advantages are a higher density of chiral near-fields as well as simpler designs for fabrication.

6.4.1 *Design Conditions*

We start with an analysis of the simplest chiral plasmonic oligomer consisting of four disks in a periodic arrangement (cf. Fig. 6.6). Here, only the right-handed enantiomer is considered. Obviously, the arrangement of the four disks renders the oligomer geometrically chiral. If the neighbor-to-neighbor distance is three times the gap between the disks in the lower layer, the superstructure obtained from

the periodic arrangement is geometrically chiral as well. However, the latter is only true because of the special choice of the periodicity.

The superstructure, albeit being built up by a geometrically chiral unit cell, becomes geometrically achiral when the distance between two neighboring array cells equals the distance between the disks of one structure. This is clear because a mirror plane (indicated by the shaded half space in Fig. 6.6) can be drawn for the structure. Using this image, one can directly explain why the periodic arrangement is achiral: Any 2×2 array of four neighboring disks can act as a unit cell that results in the same structure after periodic repetition. By picking the right disks, also the enantiomorph (blue) of the initial unit cell (red) can be selected. The resulting array can be seen as a plasmonic racemate that locally consists of geometrically chiral constituents, but is geometrically achiral globally.⁵

This behavior is a major disadvantage when searching for chiral plasmonic structures with strong chiroptical far-field response: The far-field response is expected to be stronger for smaller periodicity because the integration density becomes larger. However, the geometrical chirality that is necessary for a chiroptical far-field response vanishes at some point. Therefore, one expects to find an optimal parameter for the periodicity.⁶

The chiroptical near-field response, on the other hand, is not restricted to geometrically chiral structures, as we have already seen in Section 5.1. However, we still expect each local enantiomer to interact stronger with the corresponding handedness of CPL.

The design in Fig. 6.6 can as easily be simulated and fabricated as the original chiral plasmonic oligomer. However, CPL is not the eigenpolarization, which will lead to circular polarization conversion. This might be a drawback for applications because it can lead to additional noise, especially when fabrication imperfections distort the perfect alignment.

⁵ Similar observations for gammadion-shaped planar chiral geometries have been reported in [213].

⁶ The optimization is even more complicated due to Rayleigh anomalies, which arise from the periodic arrangement. It has been shown that they can have a strong influence on the magnitude of recorded chiroptical responses [A7]. However, a detailed analysis of the influence of Rayleigh anomalies on chiral plasmonics has, to the best of our knowledge, not been carried out yet.

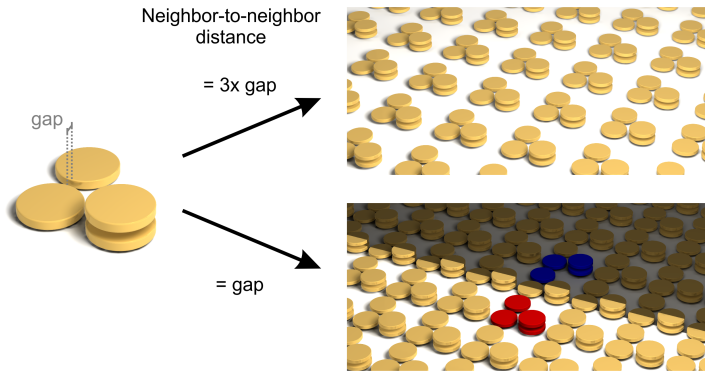


FIGURE 6.6. A chiral plasmonic oligomer consisting of four disks is placed in a periodic arrangement. The unit cell is geometrically chiral. The symmetry properties of the periodic arrangement depend on the periodicity: If the neighbor-to-neighbor distance is different from the gap between single disks, the resulting superstructure is geometrically chiral. However, if both distances are the same, a geometrically achiral arrangement is obtained. This can be seen by the mirror plane that connects the bright and the shaded area in the respective sketch. Both enantiomers of the initial unit cell (red and blue) can be used to build the array by periodic displacement.

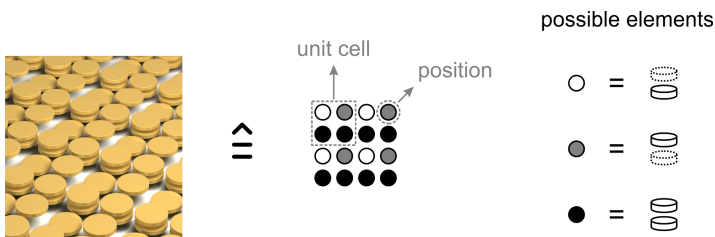


FIGURE 6.7. Chiral plasmonic metasurfaces can be described by unit cells consisting of several positions where different elements can be placed. In case of two-layered plasmonic oligomers as building blocks, four different elements (the three depicted and a hole) are possible.

Therefore, we consider metasurfaces that are built by more sophisticated unit cells. For a convenient description, we look at these unit cells from top. Then, we have several positions in each unit cell where we can place different elements.

In case of two-layered plasmonic oligomers, four different elements are possible: One disk at the bottom or the top layer, disks in both layers, or no disk at all (cf. Fig. 6.7). However, the concept is not restricted to these elements. The only condition is the discrete placement of different elements; additionally, the gaps between two neighboring unit cells must equal the gaps between two elements within the unit cell.

We will, at first, discuss the constraints for unit cells that result in metasurfaces with all desired properties: local geometrical chirality, global geometrical achirality, and circular eigenpolarizations. Note that this discussion is independent of the actual elements that can be placed on the single positions. However, we assume elements with rotational symmetry⁷ and square unit cells for convenience.

The array must be at least C_3 symmetric to support circular eigenpolarizations. C_3 symmetry is impossible due to the two-dimensional periodicity with a rectangular unit cell. Therefore, we have to enforce C_4 symmetry. Simple geometric considerations show that a geometrically chiral unit cell, which leads to a C_4 symmetric array, must consist of at least 4×4 positions with the center for the rotational symmetry located in the center of the unit cell, i. e., the unit cell itself is C_4 symmetric (cf. Fig. 6.8).

If we allow n different elements at each position, this leads to n^{16} possible unit cells. However, this can be efficiently reduced due to different constraints. Firstly, only a 2×2 subcell must be considered; the full cell is then defined by enforcing the C_4 symmetry. This results in n^4 different subcells. For the following, we will consider the upper left part of the full 4×4 cell.

The full unit cell must be geometrically chiral. Therefore, the off-diagonal elements of the subcell must not be the same. Otherwise, the diagonals of the full unit cell would be an axis of mirror symmetry (cf. Fig. 6.9 (a)). The diagonal elements of the subcell, on the other

⁷ Although full rotational symmetry is considered (and provided by the disks), C_4 symmetry would be sufficient. Our considerations do not hold for elements that are neither C_4 nor C_∞ .

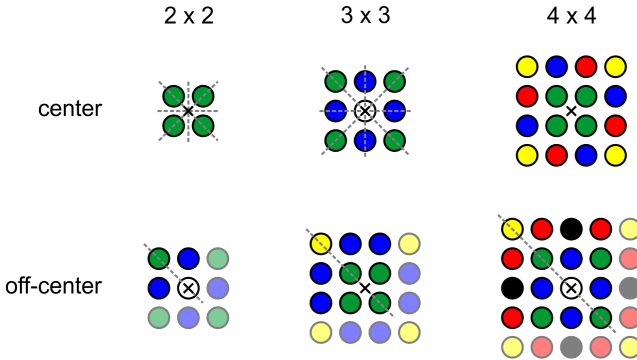


FIGURE 6.8. Some elements in unit cells of different size must be the same to obtain C_4 symmetry. If the center of rotation (marked by a cross) is not the center of the unit cell, neighboring positions must be taken into account as well (shaded). The assumed periodicity introduces additional constraints. Positions with the same color must host the same elements to ensure both periodicity and rotational symmetry. Only the 4×4 unit cell with rotation around the center has no axis of mirror symmetry (dashed gray lines) and can therefore be geometrically chiral. Smaller unit cells have four axis of symmetry; all unit cells with a rotation center that does not coincide with the center of the unit cell have one axis of mirror symmetry along the diagonal.

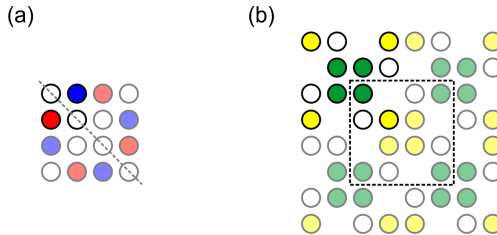


FIGURE 6.9. (a) The off-diagonal elements of the upper left 2×2 subcell determine the geometrical chirality of the whole unit cell. If they are the same, the diagonal is an axis of mirror symmetry (dashed line). (b) The diagonal elements of the subcell control the geometrical chirality of the whole surface. The dashed rectangle marks an alternative 4×4 unit cell. If the two diagonal elements (green and yellow) of the subcell are the same, this alternative unit cell is the enantiomorph of the initial cell. If not, the whole surface is geometrically chiral.

hand, must be the same. Otherwise, the whole array would be geometrically chiral as well, as shown in Fig. 6.9 (b). This leads to a total of $n^2 (n - 1)$ geometries.

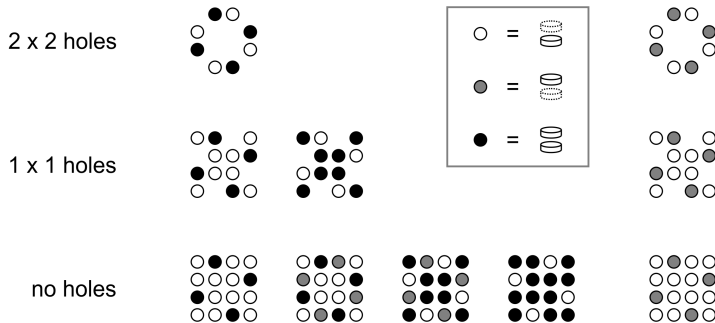


FIGURE 6.10. Ten different locally chiral metasurfaces with C_4 symmetry can be identified. They can be grouped by the maximum size of the holes in the surface. The two layers are only weakly coupled in case of the three geometries on the right.

We now consider the special case of two-layered chiral plasmonic oligomers with four different elements, i. e., $n = 4$. For these oligomers, the number of 24 possible unit cells can be further reduced.

Firstly, geometrical chirality can be broken if the structure is symmetric in z -direction. This is the case when only one layer is present. Six different combinations, which were allowed by the general constraints for locally chiral metasurfaces, result in only one layer and must, therefore, be forbidden. Additionally, we find that some combinations describe the same structure, only flipped around. In the end, we find the ten different geometries shown in Fig. 6.10, which can be grouped by the maximum block size of positions without any disks attached.

The last entry in each group has a maximum of one disk at each position. Therefore, the two layers are expected to be effectively decoupled. This leaves us with seven different geometries that are locally geometrically chiral, C_4 symmetric, and globally geometrically achiral.

6.4.2 *Chiroptical Near-Field Response*

The proposed structures are complex because they consist of many individual particles that are coupled via their near-fields. Therefore, each structure exhibits a multitude of plasmonic resonances that can be excited. The higher the frequency, the more complex the expected current distributions and, accordingly, the chiral near-fields of the mode are expected to be. For the sake of simplicity, we restrict the analysis to the lowest energy transmittance dip.

We chose disks with a radius of 70 nm and a thickness of 20 nm as the fundamental building block for our calculations. The gap between the disks as well as the distance in z -direction is 20 nm as well.

Figure 6.11 shows the chiral near-field response of selected structures for incident CPL. We directly see that switching of the handedness of incident CPL results in enantiomorphic fields. The locations of these fields depend on the local handedness of the metasurface. All designs result in comparable values for the OC enhancement.

The strongest response is obtained for the design with 2×2 holes. Additionally, the handedness of the chiral near-fields is homogeneous in the upper layer. However, the OC decays rapidly in lateral direction because of the single outstanding disks.

Chiral near-fields with only one handedness in the upper layer could not be obtained for designs with 1×1 holes. These designs apparently offer regions that are similar enough to be excited by either polarization but generate near-fields of opposite handedness. Therefore, they are not suitable as chiral near-field sources.

Homogeneous handedness in the upper layer is obtained for all designs with no holes. For the lower layer, this criterion is only fulfilled if not every position in this layer is occupied. A response over a larger area is obtained if several neighboring positions are occupied in both layers. This allows for interlayer coupling, which induces chiral hot spots.

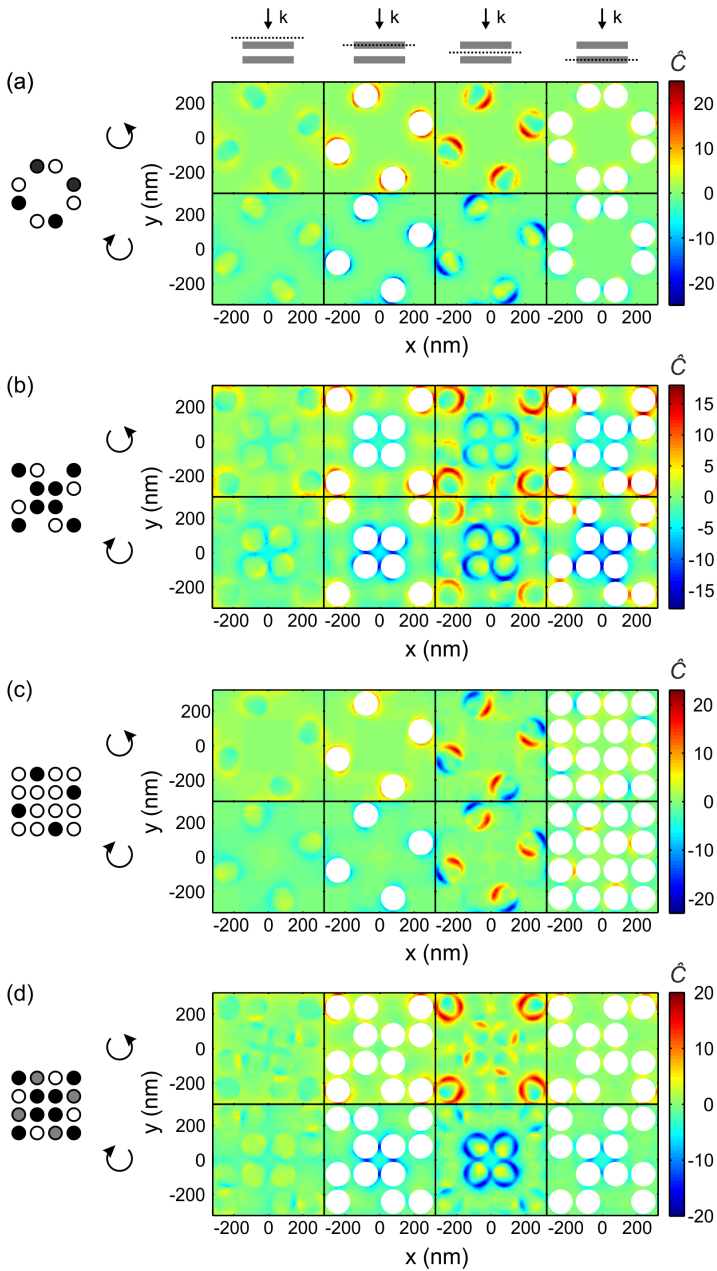
It can be seen that the response of these structures is strongly dependent on the coupling and cannot be predicted from the geometry in a straight-forward way. Things become even more complicated when higher order resonances are considered. Those might result in stronger chiral near-fields, but no conditions have been found where homogeneous handedness could be achieved. However, we

believe that an optimized excitation frequency might improve our results.

Compared to our designs in Chapter 5, these locally geometrically chiral metasurfaces create weaker chiral hot-spots. However, they are simpler to fabricate and provide higher integration density. Note that no structural optimization has been performed because we aimed at the fundamental demonstration of the principle.

Elements different from disks provide another degree of freedom for optimization. Therefore, we believe that our concept of locally geometrically chiral metasurfaces will be a valuable tool for the design of chiral near-field sources.

FIGURE 6.11 (*FACING PAGE*). Chiral near-fields of selected locally geometrically chiral metasurfaces illuminated with LCP (top rows) and RCP (bottom rows) on the lowest transmittance dip. Cuts have been made 10 nm above the upper layer, in the middle of each layer, and in between the two layers (indicated by the pictograms on the top of the figure). (a) Design with 2×2 holes at 450 THz (666 nm). (b) Design with 1×1 holes and no position with disks only in the upper layer at 368.6 THz (813 nm). (c) Design with no holes and no neighboring disks in the upper layer at 450 THz (666 nm). (d) Design with no holes, maximum connection between neighboring particles, and positions with no disks in the lower layer at 435 THz (689 nm).



FORMATION OF CHIRAL FIELDS NEAR SYMMETRIC STRUCTURES

We have seen in Chapter 5 that the OC of circularly polarized (and, therefore, chiral) electromagnetic fields can be locally enhanced by geometrically chiral plasmonic nanostructures. However, we could demonstrate that this is not just due to the field enhancement effect, because the polarization of the incident light (and, therefore, its OC) is not preserved in the resulting near-field of the structure.

In a different interpretation, chiral near-fields are formed due to an interplay between the incident field and the near-fields of the structure. From this perspective, the analyzed combination of chiral light with chiral structures to obtain chiral near-fields is the most complex scheme that could be considered. We will discuss much simpler schemes in this chapter to obtain better insights how the formation of chiral near-fields in the presence of plasmonic nanostructures works.

Until now, to the best of our knowledge, no chiroptical far-field response has been reported for systems without geometrical chirality. Chiral near-fields, on the other hand, have been found in the vicinity of planar and three-dimensional geometrically achiral structures [214]. In this work, the phase difference between resonant and off-resonant antennas has been utilized.

In this section, we demonstrate, on a fundamental theoretical basis, how chiral near-fields can be formed under conditions without any geometrical chirality at all. Compared to [214], we use only a single plasmonic nanoantenna.

7.1 OPTICAL CHIRALITY NEAR A PLASMONIC ROD ANTENNA

We consider a linear plasmonic gold nanoantenna that exhibits neither three-dimensional nor planar geometrical chirality. The structure is illuminated with LPL where the electric field vector is parallel to the antenna axis. The combination of structure and incident polarization

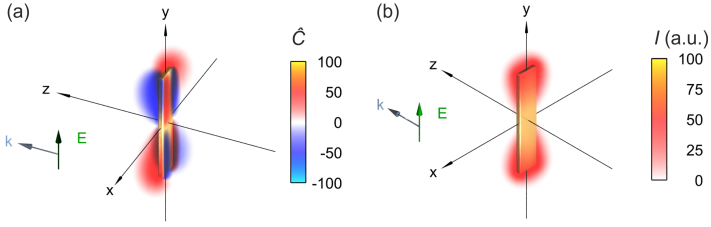


FIGURE 7.1. (a) OC induced by a linear plasmonic nanoantenna illuminated with light polarized parallel to the antenna axis under normal incidence at resonance ($1.38 \mu\text{m}$). (b) The fundamental antenna mode exhibits strongest intensity of the electric field at the ends of the rod. The distribution differs significantly from the regions with strongest OC.

exhibits no geometrical chirality. Therefore, the system exhibits neither intrinsic nor extrinsic geometrical chirality; no chiroptical far-field response can be obtained. Also, influences from spatial dispersion [215] can be excluded because all calculations were carried out at normal incidence.

The chiroptical near-field response of this configuration can be seen in Fig. 7.1 (a), which depicts the OC near the nanoantenna. Local chiral fields, which arise from this geometrically achiral system, are clearly visible. The dimensions of the antenna are 400 nm in length and 80 nm in width with a thickness of 20 nm (unit cell 800 nm) which leads to a resonance at 217 THz ($1.38 \mu\text{m}$).

The regions with strong OC form four main lobes originating from the sides of the antenna with alternating handedness of the chiral fields. At the front of the structure, four smaller regions with opposite handedness than the corresponding main lobes occur in addition. Due to the symmetry of the configuration, the integral over OC in each slice normal to the propagation direction of the incident light vanishes. This is a big difference to the different configurations discussed in Chapter 5 where such integrals do not necessarily vanish.

Compared to the distribution of electric field enhancement shown in Fig. 7.1 (b), the shapes of the respective fields are different. Once again, we find that the formation and enhancement of chiral fields are no direct consequence of electric field enhancement alone. Furthermore, the chiral near-fields can not be explained by just the scattered

field of the antenna. Analysis of the fields of the fundamental mode of the antenna calculated without an external stimulus [216] yields vanishing OC because the respective electric and magnetic fields are orthogonal. For a proper explanation, the incident field has to be taken into account. The generated OC is a result of the interference between incident and scattered fields.

7.2 DIPOLE MODEL FOR THE GENERATION OF CHIRAL NEAR-FIELDS

To demonstrate the underlying mechanism, we replace the nanoantenna with a point dipole. A Hertzian dipole directly supports one of the prerequisites for chiral fields because the electric and magnetic fields feature a perfect phase difference of $\pi/2$ in the near-field (cf. Eq. (4.4)). Nevertheless, the field lines are orthogonal at each point in space, leading to no OC at all. In the presence of an external driving field, however, the lines can become distorted in a way such that OC occurs.

We model the incident electromagnetic field as an arbitrarily polarized plane wave propagating in z -direction (see Eq. (2.4)):

$$\mathbf{E}_{\text{in}} = E_0 \mathbf{J} e^{i(kz - \omega t)}, \quad (7.1a)$$

$$\mathbf{B}_{\text{in}} = \frac{1}{c} (\hat{\mathbf{e}}_z \times \mathbf{E}_{\text{in}}). \quad (7.1b)$$

Close to the antenna, one is situated in the near-field regime of the dipole. Therefore, the fields can be approximated as [27]

$$\mathbf{E}_{\text{d}}(\mathbf{r}) \approx \frac{1}{4\pi\epsilon_0} \frac{3\mathbf{n}(\mathbf{p} \cdot \mathbf{n}) - \mathbf{p}}{r^3}, \quad (7.2a)$$

$$\mathbf{B}_{\text{d}}(\mathbf{r}) \approx \frac{\mu_0}{4\pi} ik \frac{c}{r^2} (\mathbf{r} \times \mathbf{p}). \quad (7.2b)$$

The electric dipole moment \mathbf{p} depends on the polarizability of the antenna and the incident electric field \mathbf{E}_{in} (cf. Eq. (2.17)). Because we are only interested in qualitative results, we use a very simple model to calculate $\bar{\alpha}$:

$$\bar{\alpha} = \alpha \text{diag}(\hat{\mathbf{p}}) e^{i\frac{\pi}{2}}. \quad (7.3)$$

The normalized dipole moment $\hat{\boldsymbol{p}}$ describes the orientation of the antenna in space: Only electric field components parallel to the dipole axis can excite the dipole. The last term introduces a phase shift of $\pi/2$ between the incident electric field and the electric field of the dipole according to theoretical predictions for plasmonic antennas driven at resonance frequency [217]. Of course, this phase shift is of major importance because the phase difference of the different fields plays an important role (cf. Eq. (4.4)). No further assumptions about α (except that it is real) have been made because it only scales the resulting field. A correct quantitative analysis is not necessary to understand the formation of chiral near-fields.

Within this simple model, the OC of a driven Hertzian dipole can be calculated as

$$\begin{aligned} C_d &= -\frac{\varepsilon_0\omega}{2} \Im\text{m} \left[(\mathbf{E}_{\text{in}} + \mathbf{E}_d)^* \cdot (\mathbf{B}_{\text{in}} + \mathbf{B}_d) \right] \\ &= C_{\text{in}} - \frac{\varepsilon_0\omega}{2} \left[\Im\text{m} (\mathbf{E}_{\text{in}}^* \cdot \mathbf{B}_d) + \Im\text{m} (\mathbf{E}_d^* \cdot \mathbf{B}_{\text{in}}) \right]. \end{aligned} \quad (7.4)$$

Here, C_{in} is the OC of the incident electromagnetic field. The term $\mathbf{E}_d^* \cdot \mathbf{B}_d$ vanishes because the electric and magnetic field lines of the undistorted dipole are orthogonal. Therefore, the electromagnetic near-field of the dipole alone is achiral at every point in space.

This simple model cannot be used for a quantitative analysis because important aspects such as the exact polarizability of the antenna or the absorption in the gold are not taken into account. Nevertheless, it is useful to obtain more general insights into the principles behind generation and enhancement of fields with nonzero OC.

7.2.1 Incident Light with Polarization Parallel to the Dipole Axis

Figure 7.2 shows the calculated OC for a Hertzian dipole oriented in y -direction. The obtained values have been plotted in a logarithmic scale for better contrast. The incident light was y -polarized. This corresponds to the situation in Fig. 7.1(a) where a linear antenna was driven by LPL. In both the simulation and the dipole model one recognizes the four main lobes with alternating sign of OC (and, therefore, alternating handedness of the chiral fields) around the scatterer. In

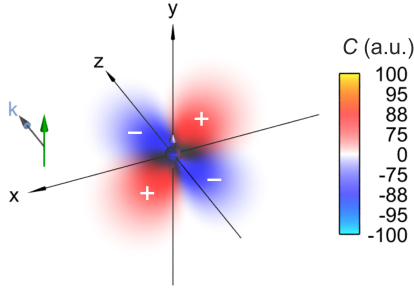


FIGURE 7.2. Distribution of OC near a Hertzian dipole driven by an external field. A highly symmetric pattern is formed. The plot uses a nonlinear color scale to obtain better contrast.

this way, the simple Hertzian dipole is a good model for the plasmonic nanoantenna.

To understand the fundamental behavior behind the generation of chiral fields by a linear antenna, we evaluate Eq. (7.4) using the Jones vector of LPL (see Eq. (2.5)). The term $\Im \mathfrak{m} (\mathbf{E}_{\text{in}}^* \cdot \mathbf{B}_{\text{d}})$ vanishes because the magnetic field component parallel to the dipole axis is zero. Because LPL features no OC, one obtains

$$C_{\text{d}}^{\text{lin}} = -\frac{\epsilon_0 \omega}{2} \Im \mathfrak{m} (\mathbf{E}_{\text{d},x}^* \cdot \mathbf{B}_{\text{in},x}) . \quad (7.5)$$

This equation shows that the induced OC is due to an interaction of the magnetic field of the incident light, which is only present in x -direction, with the scattered electric field of the dipole.

Because the incident magnetic field of the incoming plane wave is uniform, the four lobes and their alternating signs are a result of the distribution of the x -component of the dipole field. It changes indeed sign between the quadrants of the x, y -plane. The sign is independent of z for each point in such a quadrant. Additionally, strongest values of E_x occur at lines with an angle of 45° with respect to the coordinate axis, while this component vanishes at the x - and y -axis. Therefore, the shape of the chiral fields can be explained just by geometric considerations.

Nevertheless, the additional distortions at the front of the structure are not accounted for in the model. They arise due to the finite dimensions of the antenna, which allow non-zero x -components of

the induced currents. However, these contributions are beyond the fundamental analysis performed in this chapter.

Note that one of the quantities determining the values of OC is the field enhancement due to the dependence of C_d^{lin} on the scattered electric field (cf. Eq. (7.5)). Therefore, one way to increase the OC would be to alter the design in a way that the field enhancement is increased. Nevertheless, the dipolar character of the scattered fields must be maintained to keep our simple model applicable.

7.2.2 Incident Light with Circular Polarization

For incident CPL, which already exhibits non-vanishing OC itself, the Jones vector reads (see Eq. (2.6))

$$J_{\text{CPL}}^{\pm} = \frac{1}{\sqrt{2}} \begin{pmatrix} 1 \\ \pm i \\ 0 \end{pmatrix}. \quad (7.6)$$

We start the evaluation of Eq. (7.4) with a discussion of the cross term $\Im\text{m}(\mathbf{E}_d^* \cdot \mathbf{B}_{\text{in}})$. Because the x - and y -component of the incident magnetic field are $\pi/2$ out of phase while all components of the electric field of the dipole are in phase, only one of the two terms obtained in the scalar product can contribute to OC. Careful examination yields that this is indeed the x -component as in the case of incident LPL.

We get an additional contribution from $\Im\text{m}(\mathbf{E}_{\text{in}}^* \cdot \mathbf{B}_d)$ due to the non-vanishing x -component of the incident electric field. Because $B_{d,y}$ is still zero, the OC of the Hertzian dipole driven by CPL can be written as

$$C_d^{\text{CPL}} = C_d^{\text{lin}} + C_{\text{in}}^{\text{CPL}} - \frac{\varepsilon_0 \omega}{2} \Im\text{m}(E_{\text{in},x}^* \cdot B_{d,x}). \quad (7.7)$$

Here, $C_{\text{in}}^{\text{CPL}}$ denotes the intrinsic OC of CPL while C_d^{lin} is the distribution of OC obtained for incident LPL (cf. Eq. (7.5)). Therefore, switching from linear to circular polarization only adds additional terms to the response for LPL.

The three terms in Eq. (7.7) behave differently when the handedness of the incident CPL is changed. Firstly, C_d^{lin} does not depend on

the handedness of the incident field because it occurs already for linear polarization. The sign of $C_{\text{in}}^{\text{CPL}}$, which originates from the incident field alone, differs for the two different polarizations.

The third term requires more detailed analysis: In our description, the x -component of the scattered magnetic field of the dipole exhibits a sign flip when the handedness of the incident polarization is switched, while the sign of $E_{\text{in},x}$ stays the same (cf. Eq. (7.6)). Therefore, the third term also flips its sign when the incident polarization changes. One can deduce from the symmetry of the x -component of the induced magnetic field that the third term additionally changes its sign between the two half spaces defined by the x, y -plane.

Due to this sign flip, the volume integral over the third term in Eq. (7.7) vanishes. Therefore, the volume integral of the OC in this configuration is determined by the OC of the incident light. This finding is consistent with the intuitive imagination that the presence of an achiral structure should only induce local changes to the OC that vanish when integrated over all space. This behavior is also confirmed by the continuity equation (4.3).

Figure 7.3 shows the behavior of a linear plasmonic nanoantenna at its fundamental plasmon resonance for CPL in both simulation as well as the dipole model. Slices normal to the propagation direction 30 nm before and behind the structure are shown to obtain a better comparison of the different scenarios. The equivalent distance in wavelength units has been used for the z -distance in the dipole model. Note that the x - and y -axis do not correspond to the scales used to plot the simulations. As explained, the discrepancies in the lateral dimensions can be related to the finite dimensions of the plasmonic antenna, which cannot be taken into account using our model.

One can clearly identify the four main lobes that already occurred for incident LPL. As discussed, these lobes experience no sign flip when the handedness of the incident polarization is switched. Due to the CPL, two opposing lobes are slightly connected. The pair of lobes forming this connection changes depending on the handedness of the incident light as well as the z -position. The change of the response, which depends on the relative z -position with respect to the structure, is a clear indication that the third term in Eq. (7.7) dominates over the OC of the incident CPL that only adds a constant value independent of the spatial position.

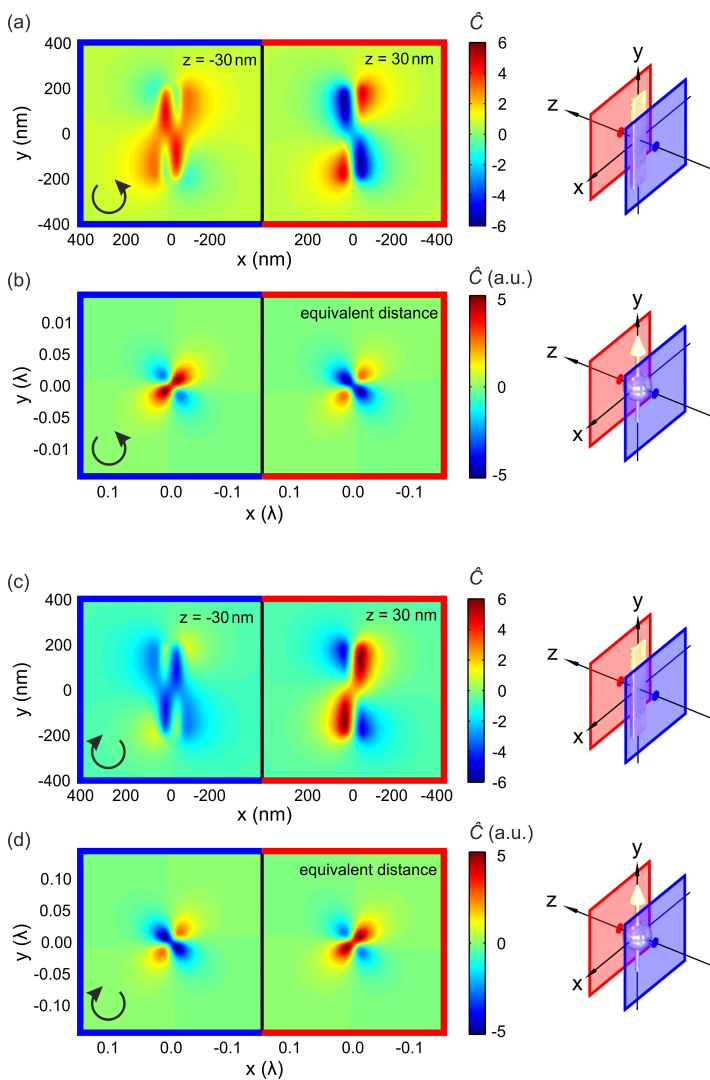
Furthermore, Figure 7.3 demonstrates that the influence of C_d^{lin} is indeed strong because it determines the general shape of the chiral near-fields. Close to the structure, where OC is strongest, the second and third term in Eq. (7.7) induce only minor changes to the chiral field distributions. For larger distances, however, the difference between the two excitations becomes more pronounced, as shown in Fig. 7.4 for a distance of 50 nm. Nevertheless, the absolute values of OC decrease with increasing distance.

This behavior can also be understood using our dipole model because C_d^{lin} is determined by the electric field of the dipole, while the magnetic field enters the third term of Eq. (7.7). The electric near-field is stronger but decays faster than the magnetic field of the Hertzian dipole, as it can be seen from Eqs. (7.2).

This distance-dependent difference of the single contributions to OC leads to the interesting effect that three-dimensional maps of OC for circularly polarized incidence look similar as the one shown in Fig. 7.1 (a) for LPL. Close to the structure, the contribution of C_d^{lin} dominates, while for larger distances OC becomes too small to be visible in the map.

The field plots obtained from the dipole model in Figs. 7.3 and 7.4 resemble the simulated results with good agreement. The general behavior of the plasmonic antenna illuminated with CPL can be explained qualitatively; only the distortions at the front cannot be found in the model, which was also the case for incident LPL.

FIGURE 7.3 (FACING PAGE). OC induced by CPL near (a, c) a linear plasmonic nanoantenna compared to (b, d) the dipole model. Slices were taken 30 nm before (blue border) and behind (red border) the structure. The distribution of OC is similar to the case of incident LPL (cf. Fig. 7.1 (a) and Fig. 7.2) with some of the lobes being stronger for CPL. The selection of the strengthened lobes depends on the handedness of the incident polarization as well as the position of the cut in z -direction. The dipole model resembles the qualitative distribution of OC very well. Nevertheless, some additional distortions, which cannot be explained by this simple model, occur at the front of the structure. Note that these distortions are also visible for incident LPL (cf. Fig. 7.1 (a)).



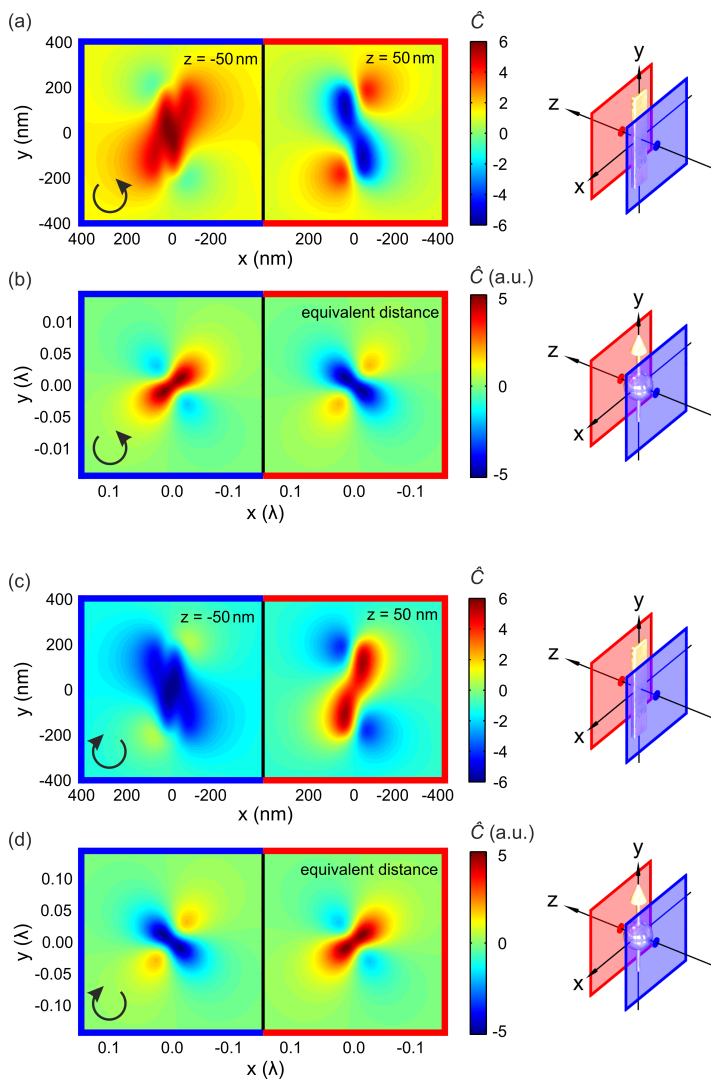


FIGURE 7.4. The same situation as in Fig. 7.3, but at larger distances of 50 nm. The changes due to the circular polarization compared to LPL (visible in the connection of two opposing lobes) are clearer than for smaller distances. Nevertheless, the overall values of OC drop down due to the larger distance.

7.2.3 *Linearly Polarized Incident Light with Arbitrary Polarization Angle*

A third configuration, which differs from both illumination schemes discussed thus far, is LPL with a nonzero angle φ between the electric field and the dipole axis. As in the case of CPL, both the x - and y -component of the incident fields are present.

The difference is the absence of the $\pi/2$ phase shift for the single components of each field. Therefore, E_{in} and B_{d} are in phase and the corresponding term in Eq. (7.4) vanishes. In exchange, the y -component of the incident magnetic field and the electric field of the dipole are out of phase and, therefore, contribute to OC. As a result, we obtain

$$C_{\text{d}}^{\varphi} = C_{\text{d}}^{\text{lin}} - \frac{\varepsilon_0 \omega}{2} \Im \left(E_{\text{d},y}^* \cdot B_{\text{in},y} \right), \quad (7.8)$$

This equation might look similar to the results that we analyzed before. Nevertheless, there is a crucial difference: For the first time, also the y -component of the fields, which is the component parallel to the dipole axis, contributes to OC. Additionally, both contributing terms are of the same magnitude at each distance.

For the case of CPL, one could still interpret the plots as a superposition of $C_{\text{d}}^{\text{lin}}$ and some additional components. This picture becomes more complicated for LPL with arbitrary polarization angles (cf. Fig. 7.5): We do still find connected lobes as in the case of CPL. However, for incident LPL, whose polarization is not parallel to the dipole axis, the whole pattern is rotated.

The absolute values of OC increase with increasing polarization angle (up to a maximum at $\varphi = 45^\circ$). The values decrease for larger angles, because the excitation of the dipole decreases as well. The OC vanishes for $\varphi = 90^\circ$ because, in this case, the incident light is orthogonal to the dipole. Note that, in a realistic system, the angle with maximum OC depends on the polarizability of the dipole which is not explicitly taken into account in our simple model.

As a result, we find that CPL leads to distributions of OC that are quite similar to light polarized parallel to the dipole axis. However, the picture becomes more complicated as soon as the polarization angle is rotated.

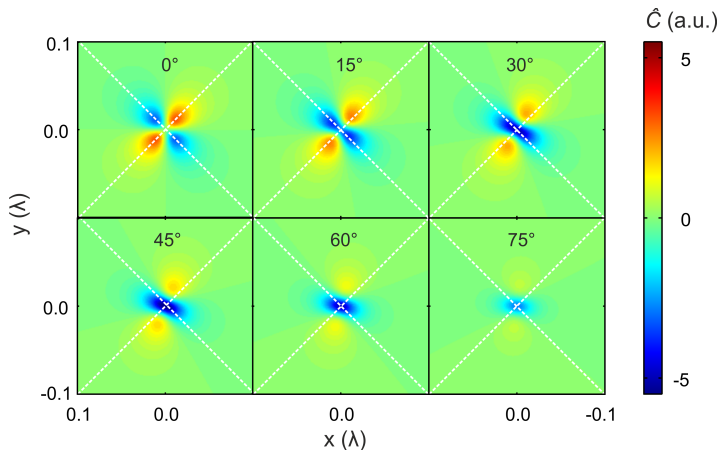


FIGURE 7.5. OC of a Hertzian dipole illuminated with LPL at a distance of 0.02λ behind the dipole. The pattern changes with increasing polarization angle. The white dashed lines are guides to the eye to depict the rotation of the initial lobes of OC.

7.3 CHIROPTICAL SPECTROSCOPY WITH LINEARLY POLARIZED LIGHT

Based on our theoretical findings, we propose the following measurement scheme: We consider a gold square instead of the linear antenna previously analyzed. For incident light with linear polarization in y -direction, essentially the same distribution of OC as for the linear antenna shown in Fig. 7.1(a) occurs; only minor differences due to the different dimensions are visible (cf. Fig. 7.6(a)). In contrast to the antenna, the incident light is in resonance with the structure for the orthogonal polarization as well. In this case, the pattern of OC is just rotated by 90° as shown in Fig. 7.6(b). The sign of OC changes for the two different linear polarizations at each position in space.

Therefore, enantiomorphic fields are generated at the corners of the nanosquare. The mirror plane that connects the two enantiomorphic configurations of structure and incident light is determined by

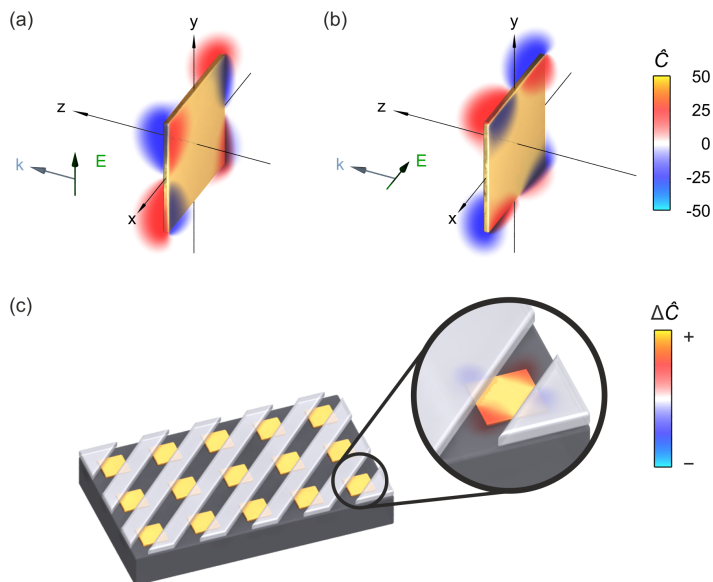


FIGURE 7.6. (a) A metallic nanosquare, illuminated with y -polarized light at a frequency of 268 THz ($1.12\ \mu\text{m}$), yields chiral near-fields that are similar to those of the linear antenna discussed in Section 7.1. (b) When the orthogonal polarization is used, the incident light is still in resonance with the square which leads to the same pattern of OC but rotated by 90° . Note that the scale of the color bar is only half as large as for the linear antenna analyzed in Fig. 7.1 (a). (c) The nanosquare can be used for CD type of measurements with LPL when only opposing corners can be accessed by the chiral analyte. This can be realized by an additional layer of diagonal stripes that blocks the access to one handedness of chiral near-fields.

the diagonal of the square and the z -axis. The positions for two chiral molecules for a description similar to Section 6.2 are situated at mirror-symmetric locations with respect to this mirror plane.

Nevertheless, it is important to deposit molecules only onto regions with the same sign of OC. If the complete square would be covered homogeneously with molecules, the difference in absorption would be expected to vanish when averaged over a large area.

To grant access to only one handedness, we suggest a design as shown in Fig. 7.6 (c): Starting from an array of gold nanosquares,

an additional layer is added. In this layer, diagonal stripes block the access to two opposing corners of the square. Therefore, only one handedness of the generated chiral near-field is accessible for molecules. One can get rid of the distortions at the front of the structure by illuminating the sample from the back. In this case, the substrate prevents accessing these areas.

This geometry should, in principle, allow for CD type of measurements with LPL. Chiral molecules placed in the grooves interact with only one polarity of the resulting difference in OC as depicted in the close-up in Fig. 7.6 (c). We suggest to match the refractive index of the chiral medium to that of the the top layer to suppress contributions from a refractive index grating.

We further investigated the properties of our proposed design by numerical simulations using the FMM code. However, the exact design is difficult to simulate using our current implementation due to the non-rectangular polygons that would be necessary. Therefore, we decided to investigate a simplified design with similar features. At first, the gold square is placed on top of a 100 nm thick slab of a chiral medium. We have chosen constant values $\varepsilon = 0.75 + 1\hat{i}$ and $\kappa = 0.2\hat{i}$ over the whole simulated frequency range. This results in a chiral medium with a refractive index of $n = 1 + 0.5\hat{i}$.¹

As expected, the configuration with the continuous chiral slab shows no difference in the response for the two incident linear polarizations (cf. Fig. 7.7 (a)). However, if the slab is quartered and two opposing quarters are changed to an achiral medium with the same refractive index (by setting $\kappa = 0$), one clearly sees the proposed difference signal. It is strongest at resonance.

We also see that signals with opposite signs occur at the edge of the resonance. This can be attributed to the change in the phase between incident and scattered light due to the detuning. A more detailed discussion of the detuned case is given in [218].

Figure 7.7 (b) depicts the differential response (vertically minus horizontally polarized light) for the two enantiomers of the chiral analyte, which are described by $\kappa = \pm 0.2\hat{i}$. The respective responses are perfectly mirror-symmetric. Therefore, their nature is purely chiroptical.

¹ Note that any chiral medium must be absorptive. Otherwise, artificial gain would be introduced for one polarization because $n^\pm = n \pm \kappa$ (see Eq. (2.53)).

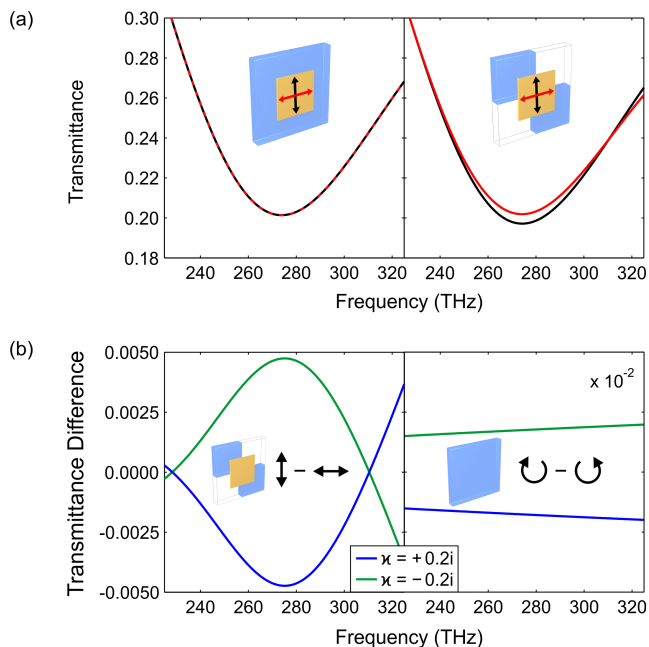


FIGURE 7.7. Numerical calculations of a gold nanosquare on top of a chiral slab. (a) Transmittance for vertically (black) and horizontally (red) polarized incident light for a homogeneous slab. The response is independent on the incident polarization. If only two opposing corners cover the chiral analyte, a clear difference in the transmittance for the two incident polarizations can be obtained. (b) The transmittance difference signal changes its sign for opposite handedness of the chiral analyte. For comparison, the response of incident CPL in absence of the gold square is given. Note that this response is two orders of magnitude stronger than the response for the squares with incident LPL.

For comparison, the figure also shows the response of a chiral film with a thickness of 50 nm illuminated with CPL without the nanostructure.² This is the response that a conventional CD spectrometer would detect for an equivalent amount of chiral analyte.

The response obtained for the CD spectroscopy scheme is roughly two orders of magnitude stronger than for our proposed design. However, this is due to the simulated geometry, which places a significant

2 Please refer to Section 2.2.3 for details about the frequency dependence of this response.

amount of the chiral analyte in regions where the chiral near-fields have already vanished. Better performance can be obtained when the chiral analyte is placed only close to the corners, where the fields are strongest. However, we have not performed the respective analysis because no additional insights would be gained.

Note that the chirality parameter κ of our chosen artificial material is several orders of magnitude higher than for all natural chiral materials. Additionally, we used a purely imaginary value to specifically demonstrate the proposed behavior of the nanosquare and theoretically prove the viability of CD type of responses with LPL. The real part of κ must be taken into account to model realistic chiral materials. One possibility to perform this modeling is the Born-Kuhn model discussed in Section 2.2.2.2.

However, this will lead to a difference in the real part of the refractive index for the surrounding medium for both incident polarizations and, therefore, to a slight shift of the plasmon resonance. For this reason, the realistic performance of our proposed device is even more complicated because the differential response due to this shift has to be taken into account as well. It can be expected that the presence of chiral near-fields will influence this resonance shift. Additional theoretical investigations are necessary to link these two effects.

Nevertheless, we demonstrated the possibility of CD type of measurements with LPL to detect the handedness of chiral molecules. Spectroscopic measurements employing LPL are simpler than those using CPL because no broadband circular polarizer is needed. Based on the demonstrated principle, one can engineer structures that allow not only the use of linear polarization states, but will also show an enhanced response compared to conventional CD spectroscopy. However, full numerical analysis with realistic parameters is necessary to analyze such designs.

CHIRAL EIGENMODES OF GEOMETRICALLY CHIRAL STRUCTURES

After discussing the enhancement of chiral light by geometrically chiral structures in Chapter 5, we showed in Chapter 7 that chiral near-fields can also occur in geometrically achiral systems illuminated with LPL. In these cases, interference between the incident and the scattered fields is crucial for the OC of the near-fields.

In this section, we will return to the case of geometrically chiral structures and demonstrate that the electromagnetic fields of their modes exhibit nonzero OC on their own. This is what we term the *chiral eigenmodes* of a plasmonic structure. Compared to the examples in Chapter 7, the incident polarization is only necessary to excite the respective modes. Interference (and, therefore, the phase difference) between incident and scattered fields must not necessarily be controlled. Therefore, the resulting designs are expected to be more reliable.

Additionally, we can control the background signal of such systems. If we choose the plasmonic near-field source, which generates enantiomorphic fields, such that no birefringence occurs for the incident polarizations, the detected differential response stems purely from the chiral analyte.

8.1 CHIRAL EIGENMODES

As it can be inferred from Eq. (4.4), the electric and magnetic fields must have parallel components that are out of phase for non-zero OC. A prototypical design that fulfills these conditions is a helical structure, as shown in Fig. 8.1. Its fundamental mode has a dipolar character, which leads to an electric field vector pointing from one end to the other. A magnetic field in the same direction is generated due to the coiled wire. Furthermore, the phase condition between the electric and the magnetic field is automatically fulfilled because the magnetic

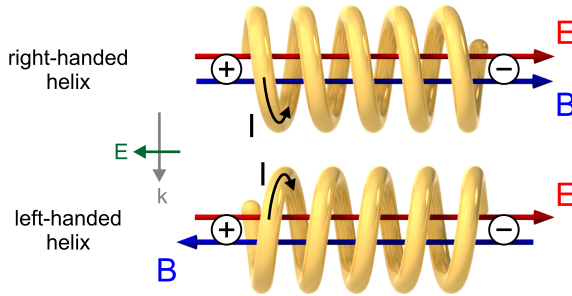


FIGURE 8.1. The fundamental mode of a helical plasmonic nanoantenna exhibits non-orthogonal electric and magnetic dipole moments. Within the structure, the electric (red) and magnetic (blue) field vectors are mainly parallel, leading to non-zero OC. Changing the handedness of the structure flips the relative orientation of the field vectors and, therefore, the handedness of the chiral near-fields. Thus, such helical antennas are prototypes of a plasmonic nanostructure with strong chiral eigenmodes.

field scales with the current, while the electric field is maximal when the carriers are accumulated at the ends of the wire. Therefore, strong chiral near-fields are expected in the region surrounded by the wire. Changing the handedness of the helix will change the relative orientation of the two fields and will, therefore, change the handedness of the respective near-fields.

Because the fundamental mode of the helix will generate chiral near-fields by itself, the incident field is only needed to excite this mode. This can be carried out most efficiently by illuminating the helix from the top with LPL, as indicated in Fig. 8.1. In this configuration, the external field couples to the electric dipole moment of the helix.

Note that this scheme differs from the usage of the helix as circular polarizer where the helix is illuminated axially, i.e., the wave vector of the incident light is parallel to the axis of the helix. This illumination leads to different excitation for left- and right-handed CPL [81, 82]. This configuration has also been discussed in Section 5.2.1 (Fig. 5.5) for incident CPL.

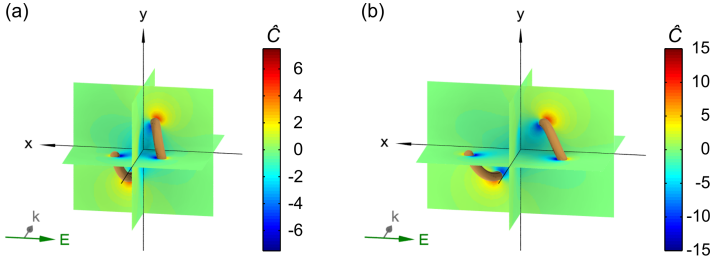


FIGURE 8.2. (a) A single helix with a small pitch of 50 nm exhibits well confined chiral near-fields (156 THz, $\lambda = 1.92 \mu\text{m}$). (b) The absolute values of OC increase with increasing pitch (100 nm), but the confinement becomes weaker (152 THz, $\lambda = 1.97 \mu\text{m}$).

Figure 8.2 depicts the OC near a small gold helix with one turn for different pitch values on resonance. The radius of the helix is 30 nm, the wire diameter 10 nm. The plot shows that non-zero OC is not only found close to the metal, but also inside the helix, as expected. Moreover, the chiral near-fields are predominantly right-handed.

Left-handed fields occur outside the helix, but the right-handed fields are stronger and cover a larger area. Therefore, integration over the whole volume would lead to a non-zero result. This is different to the case of achiral structures and is a clear sign that the scattered fields of the structure are chiral. This is only possible due to the geometrical chirality of the helix. Otherwise, parity inversion would change the net handedness of the near-field after averaging, but leave the structure itself unaltered. As a result, the structure and its generated chiral fields can be used as chiral plasmonic near-field sources without any additional adjustments.

Note that the resulting chiral near-field distribution is much simpler than for the helix discussed in Section 5.2.1 (Fig. 5.5). The difference is that, here, the illumination is LPL, while the response in Fig. 5.5 stems from CPL, which exhibits non-zero OC itself. Therefore, the local interference between incident and scattered fields is expected to have a stronger influence on the total response. Additionally, the excitation and, therefore, the resulting mode is different: The helix discussed in

Section 5.2.1 is much larger, but is operated at a comparable wavelength as the small helix discussed in this section. Therefore, higher order modes are excited.

The chiral near-fields of the helix under linear illumination are mostly confined to its interior region. The confinement is best when the pitch of the helix is small. Figure 8.2 (a) depicts the response of a helix with a pitch of 50 nm. A larger pitch increases the dipole moment of the structure and, therefore, improves the coupling to the external field. This can lead to an increase of the absolute values of OC, as seen in Fig. 8.2 (b) for a pitch of 100 nm, but with weaker confinement of the fields. The ultimate limit is a straight rod antenna as discussed in Chapter 7.

This leads to a trade-off between strength, confinement, and net chirality of the generated fields. An optimal design should feature strong chiral near-fields of one handedness over a large volume, as discussed in Section 4.4.1.

8.2 NEAR-FIELD RESPONSE OF MULTIPLE HELICES

The initial design of a single helix must be adjusted to fulfill the design goals for chiral plasmonic near-field sources. Figure 8.3 sketches

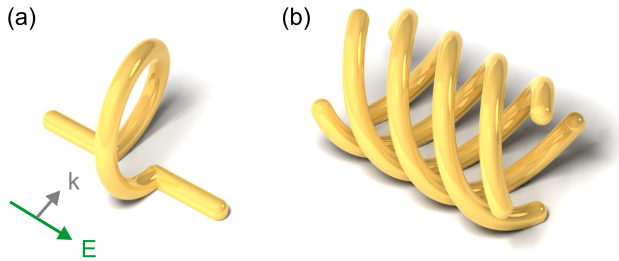


FIGURE 8.3. Modified designs that are expected to feature simultaneously strong chiral near-fields and good coupling to the external field. (a) The dipole moment of the loop-wire structure is enlarged due to the linear antennas at each side of the loop. (b) Designs with multiple helices couple well to the external field because the pitch of each single helix can be enlarged. Simultaneously, the wires surround a larger volume.

two different approaches. The first one (Fig. 8.3 (a)) starts from a helix with a small pitch and adds additional antennas at each end to increase the coupling to the external field. This so-called loop-wire structure has already been discussed as prototype for plasmonic structures with strong chiroptical far-field response [85, 219], but should also feature promising near-field characteristics. However, the volume that is possibly filled with chiral near-fields is limited due to the small pitch.

Therefore, we will focus on the second approach that is sketched in Fig. 8.3 (b): We start with a helix with a large pitch, which automatically leads to a larger volume that is enclosed by gold wires. To obtain a better confinement of the fields, additional helices are added. A similar approach has been utilized for circular polarizers, where superstructures of multiple helices have been used to improve the circular polarization extinction ratio [220–223].

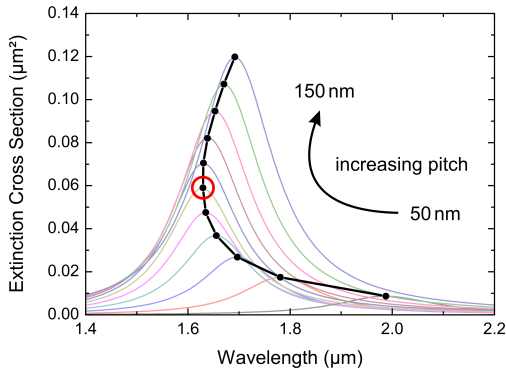


FIGURE 8.4. The ECS of the four-helix structure increases with increasing pitch. A strong blueshift occurs when starting from small pitch values. This switches to the expected redshift when the pitch is further increased. The switching point occurs for a pitch of 100 nm (red circle). The pitch is changed by 10 nm for neighboring plots.

8.2.1 *Small Four-Helix Design*

Additional helices lead to a more complex behavior of the whole design because the single helices can interact with one another. Figure 8.4 shows the extinction cross section (ECS) of four intertwined helices for pitch values varying from 50 nm to 150 nm. The pitch is varied by 10 nm for neighboring plots. All other dimensions are the same as for the single helix calculated in Fig. 8.2.

As expected, the ECS increases with increasing pitch because the structure couples stronger to the external field. However, for small pitch values, an increase of the pitch leads to a blueshift of the fundamental resonance. This is in contrast to the expectation because an increasing pitch leads to longer wires and should, therefore, result in a redshift.

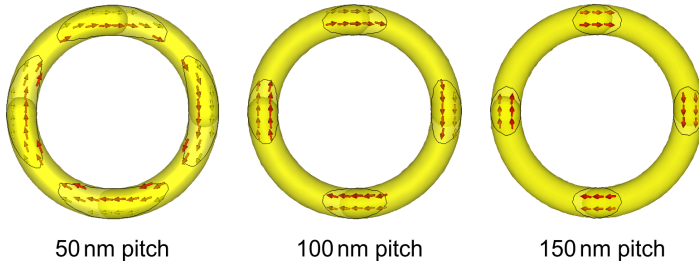


FIGURE 8.5. For the fundamental mode, the currents in all wires flow into the same direction. This leads to the lowest possible energy in terms of plasmon hybridization of the different wires. The coupling between the wires is decreased with increasing pitch because the distance between the wires becomes larger. The plots show a cut through the center of the structure perpendicular to the axis of the helix.

The unexpected blue-shift can be explained by analyzing the mode hybridization in the four-helix structure. Only the lowest energy mode is excited by the external dipolar field (cf. Fig. 8.5). This mode exhibits a strong blue-shift when the coupling is reduced due to an enlargement of the pitch. In the case of small pitches, where the initial coupling is sufficiently strong, this blueshift can supersede the intrinsic redshift resulting from the elongation of the wires. The redshift dominates the observed behavior for pitches larger than 100 nm.

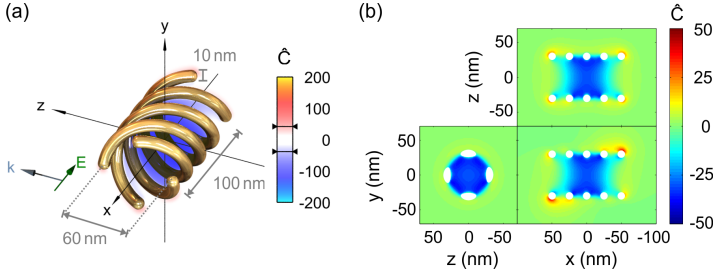


FIGURE 8.6. (a) Strongly confined chiral near-fields are generated within the four-helix design for a pitch of 100 nm (red circle in Fig. 8.4). (b) The slice plots confirm the confinement to the interior region.

Figure 8.6 (a) shows a three-dimensional map of the OC around a four-helix structure with a pitch of 100 nm on resonance (red circle in Fig. 8.4). The resonance position is located in the NIR wavelength regime at 184 THz (1.63 μm). The chiral near-fields are mainly located inside the design and are enclosed by the wires. The slice plots in Fig. 8.6 (b) confirm this observation. Note that the fields are right-handed in the whole interior of the structure. Left-handed fields also occur (mainly, at the ends of the wires) but, when averaging over the whole volume, the right-handed characteristic dominates.

The structure also performs well regarding the absolute values of normalized OC. The design shown in Fig. 8.6 reaches -38 for the minimal OC. In Section 5.2.2, higher values have been found for the chiral oligomer, but only in some hot spots. The four-helix structure, on the other hand, features near-fields with significantly higher OC than CPL of the same frequency over an extended volume.

When the pitch is further increased to 150 nm, the maximum and minimum values of OC stay almost the same, although the ECS roughly doubles. Additionally, the confinement of the fields becomes weaker, as already discussed for the single helix. Therefore, we attribute the characteristics of the four-helix structure to the coupling between the single wires. Increasing the pitch further than 100 nm, where the resonance position starts to shift red with further increasing pitch, seems to have no benefit for the generation of chiral near-fields.

Note that the dimensions of the design are very small, which could pose challenges for fabrication. Recently, Mark and collaborators have fabricated single helices with comparable dimensions by a GLAD technique [108]. However, especially the ratio between helix diameter and wire thickness is substantially smaller than in our calculations, which leads to a narrowing of the accessible volume inside the helix.

DNA nanoassembly with subsequent metal coating might offer an alternative route, but the DNA scaffolds prevent the analyte from reaching the interior region [124]. Helices with feature sizes below 100 nm have been fabricated by electron-beam induced deposition, but the metal is incorporated in a carbon matrix, which is expected to weaken the near-field response [111]. Improvements have been reported in [110].

All of these techniques have been used to fabricate single helices thus far. The step to the suggested four-helix design seems to be non-trivial.

8.2.2 *Large Four-Helix Design*

A technique that could in principle be used to fabricate the proposed design is 3D DLW because it is very versatile in terms of possible geometries. However, the laser wavelength limits the minimal feature size. Additionally, the smallest voxels that can be written are elliptical due to a difference between the axial and the longitudinal resolution. Recent developments such as STED DLW [224, 225], utilization of the diffusion of quencher molecules [226], or the combination of DLW with spatial light modulators [227] significantly improved both the resolution as well as the voxel aspect ratio. However, the dimensions of the small design discussed in the previous section are still out of reach for DLW with present techniques.

Therefore, we analyze the behavior of a 20 times larger version of our four-helix design. Now, the pitch of the structure is $2.0\ \mu\text{m}$, the helix radius is $0.6\ \mu\text{m}$, and the diameter of the wire is $0.2\ \mu\text{m}$. Such dimensions are, in principle, feasible for a 3D DLW approach. However, the obtained OC is reduced by a factor of roughly 1.7 compared to the original design (cf. Fig. 8.7). The scales of both the three-dimensional map and the slice plots are the same as in Fig. 8.6, which depicts the

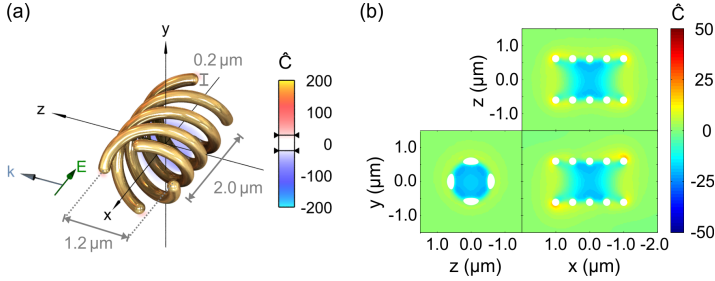


FIGURE 8.7. (a) The optimal small design is enlarged by a factor of 20 to enable fabrication by 3D DLW. After this upscaling process, the obtained normalized OC is decreased. (b) The slice plots demonstrate a drop by a factor of 1.7 compared to the small design shown in Fig. 8.6.

small version of the design. This is even more striking because the dipole moment of the structure is strongly increased due to the up-scaling. Therefore, higher values of OC were expected.

We additionally calculated the far-field response depending on the pitch as already done for the small four-helix structure to obtain further insights in the behavior of the enlarged design. The results are shown in Fig. 8.8 for pitch values between $1.0\ \mu\text{m}$ and $2.0\ \mu\text{m}$. Neighboring plots differ by $0.1\ \mu\text{m}$ in pitch. As for the small design, these values are in the range where we obtain a blueshift when increasing the pitch. Furthermore, the ECS increases with the structure, as expected.

Interestingly, the absorption cross section (ACS) behaves differently for the enlarged structure compared to the small design. One obtains a decreasing ACS with increasing pitch. This behavior is opposite to the small four-helix structure, where the absorption and scattering cross sections exhibit the same scaling behavior: They both increase with increasing pitch.

The enhanced OC around the large four-helix structure with the smallest pitch calculated ($1.0\ \mu\text{m}$, red circle in Fig. 8.8) is roughly eight times higher compared to the $2.0\ \mu\text{m}$ pitch (cf. Fig. 8.9 (a)). The resulting chiral near-fields reach values down to -179 , which even exceeds the best design of the small four-helix structure and is, to the best of our knowledge, the highest value reported in literature thus far.

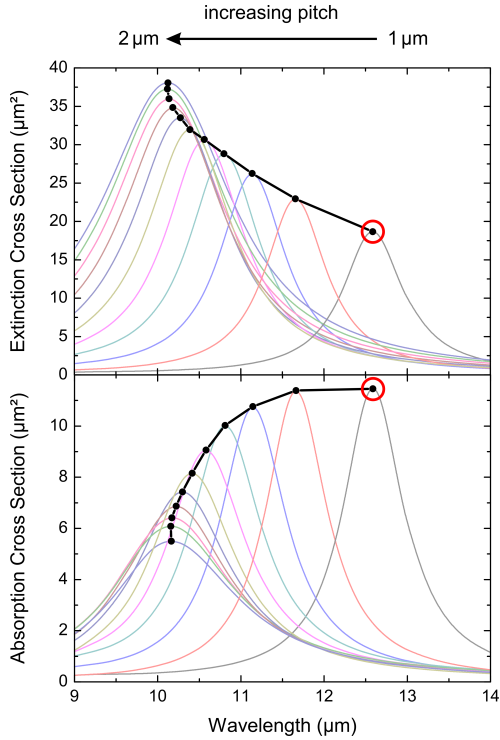


FIGURE 8.8. Extinction and absorption cross section of the upscaled four-helix structure. The pitch is changed by $0.1 \mu\text{m}$ for neighboring plots. Maximum absorption is obtained for the smallest pitch ($1.0 \mu\text{m}$, red circle).

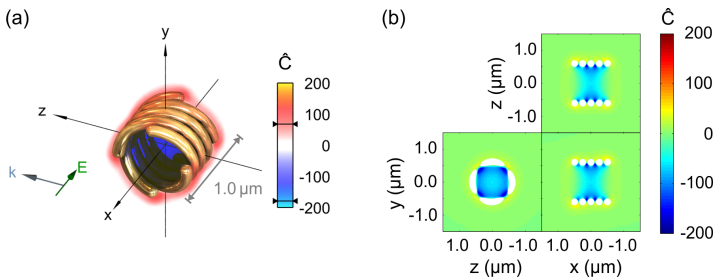


FIGURE 8.9. (a) The OC map of the large four-helix design with a pitch of $1.0 \mu\text{m}$ shows strong chiral near-fields of one handedness in the region enclosed by the structure. (b) The slice plots confirm the confinement to the inner region.

The slice plots (Fig. 8.9 (b)) confirm that we still obtain predominantly right-handed near-fields that are confined to the interior of the structure.

Compared to the small four-helix design, the values decrease faster when we move away from the wires towards the center of the structure. This can be explained by the stronger coupling between the single wires in case of smaller pitches, which leads to higher field enhancement in the gap and, therefore, higher values of OC at the respective positions. Nevertheless, we still find substantial chiral near-fields in the center that exceed the response of the small four-helix design.

Note that a decrease of the pitch in the small design does not lead to the same effect. In contrast, the OC is weakened because the influence of the weaker coupling to the external field is stronger than the benefits from the stronger coupling between the wires.

It should also be mentioned that this design is more difficult to fabricate because of the small gaps between the wires when compared to designs with larger pitch values. Additionally, the enlarged version shifts the operating wavelength to the mid IR wavelength regime, which might be a drawback for some applications. However, it might be explicitly favorable for applications such as VCD spectroscopy, which operate in this spectral regime (cf. Section 3.1.1).

The resonance frequency is very sensitive to the actual pitch due to the coupling between the wires, which is also challenging for fabrication. A balance between performance and fabrication demands should be found for real applications.

Of course, the details of this optimization depend crucially on the fabrication technique that is used. The chosen technique might introduce additional imperfections, such as grainy surfaces or deviations from the assumed perfectly round shape of the wires. The former influences the near-fields only very close to the surface [228]; the latter might modify the coupling between the helices. While our findings provide fundamental insights into the working principle and general characteristics of the proposed design, more specialized calculations are necessary for realistic modeling of definite experiments.

8.2.3 *Enhanced Chiroptical Spectroscopy*

When the four-helix design is used for chiroptical spectroscopy, it is not sufficient to only consider single spatial points. Rather, one obtains the response that is of interest by averaging over a specific volume that is filled with a chiral analyte.

As discussed in Section 4.2, we need enantiomorphic fields to perform CD type of measurements. To obtain such field pairs, both enantiomers of the nanostructure can be used to create fields with opposite handedness for incident LPL. In this case, corresponding locations, where the near-fields are interchangeable by parity, can be found and the treatment introduced in Section 6.2 is applicable. For convenience, we repeat the main result that was given in Eq. (6.5):

$$\Delta\hat{a}^* = \Delta\hat{C}. \quad (8.1)$$

In contrast to plasmonic racemates, the scheme described here uses only one illumination for each of the enantiomers. The differential response must be detected by two independent measurements with both helices. Therefore, $\Delta\hat{C}$ reduces to the single response of the enantiomer that is used for the analysis.

In our right-handed helix, we find predominantly right-handed near-fields that are described by

$$\hat{C}_{\text{Helix}} := \hat{C}^-. \quad (8.2)$$

Therefore, Eq. (8.1) results in

$$\Delta\hat{a}^* = -\hat{C}_{\text{Helix}}. \quad (8.3)$$

The value $\Delta\hat{a}^*$ describes the expected enhancement factor due to the presence of the nanostructure (and the described measurement scheme) for every point in space compared to a CD measurement. Averaging over a specific volume V via numerical integration [229] finally leads to

$$\langle\Delta\hat{a}\rangle_V := -\frac{1}{V} \int_V \hat{C}_{\text{Helix}} dV, \quad (8.4)$$

which quantifies the expected enhancement of the response when V is filled with a chiral analyte.

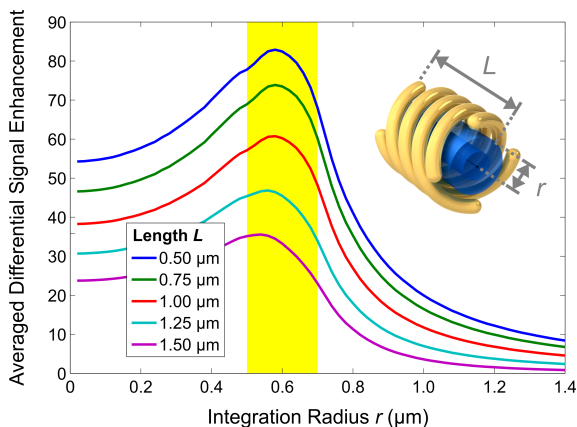


FIGURE 8.10. The averaged normalized OC is a measure of the possible enhancement of chiroptical responses compared to a CD measurement when the integration area is filled with a chiral analyte. The integration has been performed for cylindrical areas with varying radius r (cf. inset). The results are plotted for several cylinder lengths L . All evaluations have been performed for the large four-helix structure with a pitch of $1.00 \mu\text{m}$, as discussed in Section 8.2.2, at its fundamental resonance (23.8 THz , $\lambda = 12.6 \mu\text{m}$). The yellow stripe depicts the area where the gold wires are located.

We evaluated Eq. (8.4) for the large four-helix structure with a pitch of $1.0 \mu\text{m}$, which featured the strongest chiral near-fields. The integration volume V has been chosen as the volume of a cylinder with radius r and length L that is collinear with the helix.

Figure 8.10 shows the value of $\langle \Delta \hat{a} \rangle_V$ depending on r . The different plots correspond to different lengths L . The yellow vertical area depicts the location of the wires. When r reaches this area, the integration volume penetrates into the metal. The respective points have been excluded from the volume calculation because they cannot be accessed by the chiral analyte.

Significant enhancement of the response is expected for all values of L as long as the chiral analyte is restricted to the interior of the helix. As soon as the analyte reaches the exterior parts, the signal drops. This is due to the increasing volume with chiral near-fields with opposite or vanishing OC.

Because $\langle \Delta \hat{a} \rangle_V$ describes the enhancement compared to the whole volume being analyzed by CD spectroscopy, its value is obviously maximal when V is confined to the region with highest OC. For an infinite radius, $\langle \Delta \hat{a} \rangle_V$ approaches zero. Small radii, on the other hand, also lower the response because the strongest chiral near-fields are located closer to the gold wires. Therefore, the maximal signal enhancement is obtained when r equals the radius of the four-helix structure.

The OC is longitudinally confined to the center of the structure: Larger values of L lead to a smaller averaged chiral response. When L exceeds the pitch of the structure, the maximal enhancement shifts to lower radii because the exterior of the structure possesses near-fields with a handedness opposite to its interior (cf. Fig. 8.8 (c)). Largest enhancement is obtained for small values of L . For a cylinder length that equals half of the pitch, enhancement factors of more than 80 have been calculated.

8.3 MODIFIED DESIGNS FOR PRACTICAL APPLICATIONS

In the last section, we demonstrated that plasmonic nanostructures consisting of multiple helices generate near-fields with high OC over an extended region. The incident field is only used to excite the resonance of the structure. We have shown that we can expect an almost two orders of magnitude enhanced chiroptical response compared to conventional CD measurements. However, the geometry of the design is complicated, which hampers fabrication. Nevertheless, our designs aid as prototypes for chiral near-field sources with strong OC.

Chiral eigenmodes lead to chiral near-fields of one handedness inside the structure. We will now discuss how this principle can be used for modified designs with a stronger focus on practical applications. The principal idea starts from the helix and modifies the structure to achieve the properties for optimal chiral near-field sources discussed in Section 4.4.1.

Figure 8.11 visualizes the modification process. Firstly, the helix is replaced by a two-layered design that consists of diagonal stripes.

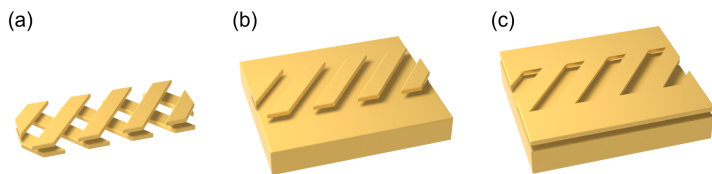


FIGURE 8.11. Steps to optimize the initial helix design for practical applications. (a) The structure is replaced by a two-layer design of diagonal stripes that mimics the current distribution of a helix. (b) The lower layer is replaced by a mirror to achieve better coupling between the layers. (c) Babinet's principle is used to simplify the access of the chiral analyte to the areas with highest OC.

These stripes mimic the current distribution within the helix. However, coupling between these layers is a critical issue. It is non-trivial to design the structure in a way that the resulting mode looks similar to the fundamental plasmon mode in the helix. Therefore, as a second step, the lower layer is replaced by a simple mirror (cf. Fig. 8.11 (b)). Therewith, coupling between the layers only depends on their distance. Of course, this will not exactly mimic the current distribution obtained in the layered structure. However, the induced mirror plasmons still result in a circular current distribution and, therefore, an effective magnetic dipole moment of the design. As a last step, the upper layer is replaced by its inverse structure. Babinet's principle shows that the device still exhibits chiroptical near-field response [27, 230]. The usage of diagonal slits instead of stripes offers a natural way of adding the chiral analyte: It should be filled in the holes of the upper gold layer. Additionally, the structure is simple to fabricate because only one nanostructured layer is present.

It should be mentioned that a concept that looks similar has been already discussed in literature. Hendry and collaborators investigated an arrangement of two slits where the end of one slit is located near the center of the second slit to overlap the generated electric and magnetic near-fields (cf. Fig. 8.12) [231]. However, their structure exhibits only planar geometrical chirality and is achiral in three dimensions. Therefore, one obtains regions with left- and right-handed chiral near-fields, similar to our observations in Section 5.1.

Our diagonal slit structure is geometrically chiral due to the mirror. Therefore, it is expected to support chiral eigenmodes that result in strong chiral near-fields of one handedness. However, we do not expect to be able to explain the behavior of the diagonal slit structure by the same intuitive description that we could use for the four-helix structure because the eigenmodes are expected to be more complicated.

To obtain first insights, we model the structure with a perfect electric conductor (PEC).¹ The design parameters are shown in Fig. 8.13 (a). Figure 8.13 (b) shows the obtained reflectance spectra for different distances d_z between the slit layer and the mirror. The spectra have been calculated for incident vertically polarized light; only light with the same polarization has been recorded for calculating the reflectance. At resonance, most of the incident light is converted to the horizontally polarized state by the structure. The same spectrum is obtained for incident horizontally polarized light. As a consequence of the PEC, the resonance position has only a slight dependance on d_z , but the resonance width as well as the conversion efficiency are influenced.

The electric field vector must twist to perform the observed transformation of the polarization state. Therefore, we expect the near-fields to exhibit non-zero OC. This expectation can be confirmed in Fig. 8.14 (a). Here, we illuminated the structure for $d_z = 20$ nm, where the strongest resonance has been found. In this case, also the strongest chiral near-fields can be observed. Right-handed fields have been found above, below and in the center of the slit layer. Therefore, the whole interior of the slits down to the mirror can be used as a chiral near-field source.

Figure 8.14 (b) demonstrates that the behavior of the diagonal slit structure depends crucially on the mirror. As soon as it is removed, the handednesses above and below the slits are opposite, while the OC within the slit layer is almost vanishing. Additionally, the absolute values drop down by a factor of more than 50. As a benefit from the PEC material, the resonance frequency shifts only slightly from 488.74 THz to 483.82 THz when the mirror is removed. Therefore, we can safely

¹ The benefits of the PEC compared to real metals are explained later.

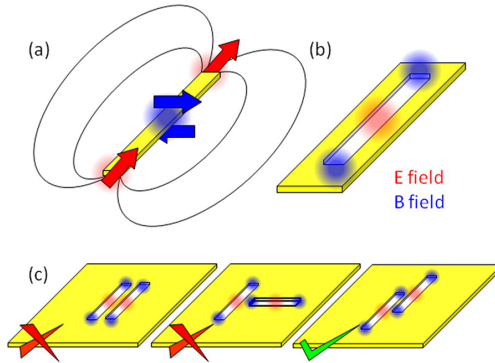


FIGURE 8.12. (a) Electric and magnetic fields of a rod antenna. (b) The fields are interchanged in case of a slit. (c) The correct combination of two slits results in chiral near-fields in the center. [Image reprinted with permission from [231]. Copyright 2012 American Chemical Society.]

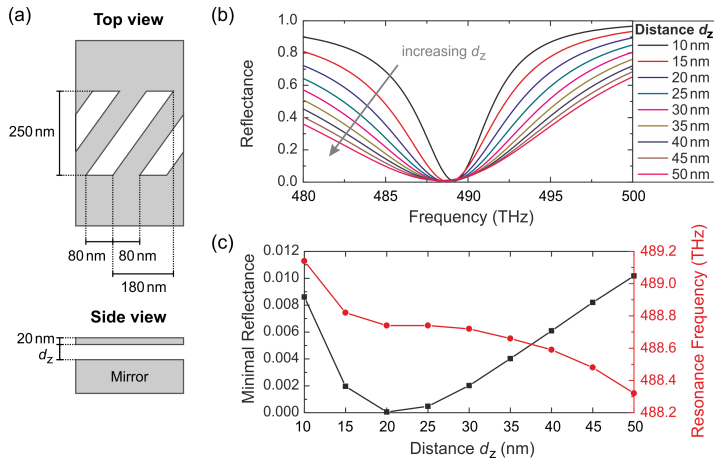


FIGURE 8.13. (a) Dimensions of the diagonal slit structure that have been used for the calculations. The distance between two slit rows was 300 nm. (b) Reflectance spectra for different distances d_z . (c) For a PEC, only the minimal reflectance changes. The resonance frequency is only slightly altered.

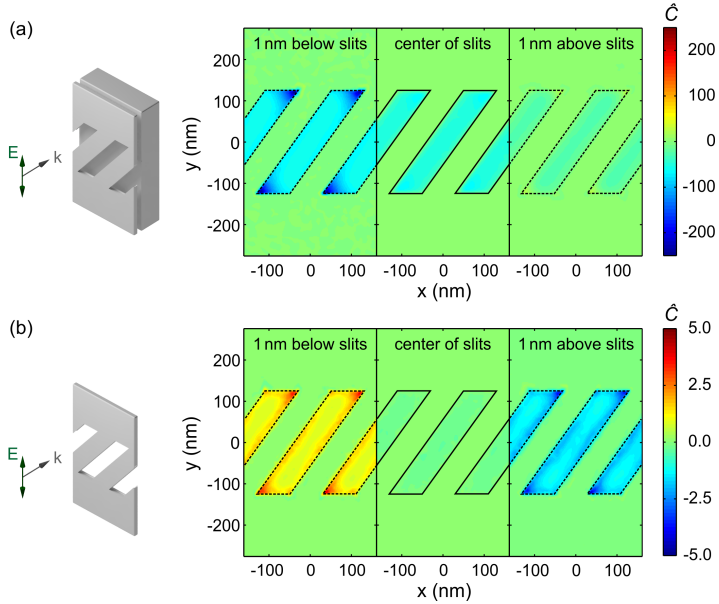


FIGURE 8.14. (a) Chiral near-fields obtained from the PEC diagonal slit structure with a distance $d_z = 20$ nm illuminated with vertically polarized light at resonance (488.74 THz, $\lambda = 613.4$ nm). Strong fields of one handedness are obtained in the whole slit. (b) Fields with opposite handedness above and below the slits are obtained when the mirror is removed. The resonance frequency changed to 483.82 THz (619.6 nm). The dashed lines indicate the positions of the slits in the close-by slit layer.

compare these two scenarios. For any realistic metal, a strong resonance shift would be expected, which might induce additional effects. This is why we chose a PEC for these first investigations.

Although the absolute values of OC are very strong for the diagonal slit structure, and even exceed those of the best four-helix design, they cannot be directly compared due to the PEC. Therefore, we simulated the structure with the same geometry for gold. The far-field behavior for different distances d_z can be seen in Fig. 8.15. Again, we obtain a dip in the reflectance spectrum for incident LPL. However, absorption must be taken into account as loss mechanism in addition to polarization conversion. Therefore, the response is different for the two

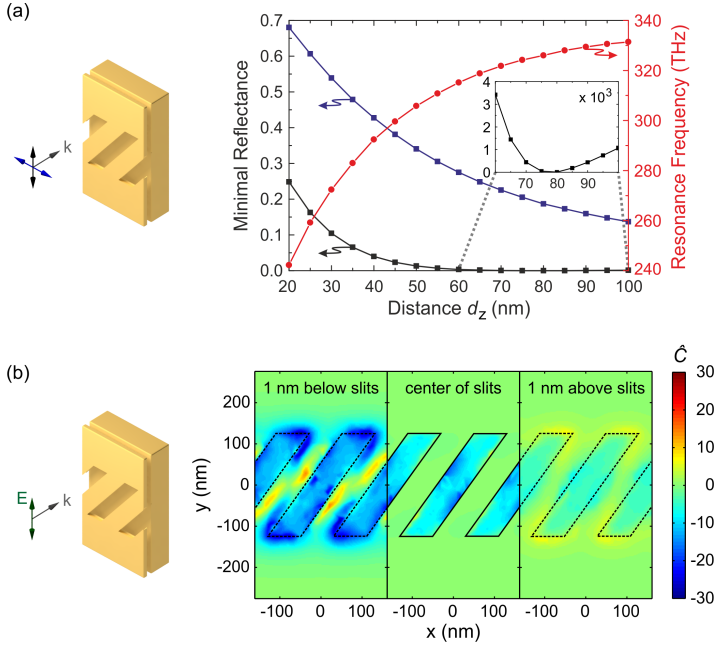


FIGURE 8.15. (a) Minimal reflectance and resonance positions for the diagonal slit structure made from gold. There is a strong difference in reflectance for vertically (black) and horizontally (blue) polarized incident light. The inset is a magnification for larger distances. (b) For a distance of $d_z = 30$ nm (resonance frequency 272.4 THz, $\lambda = 1100.6$ nm), predominantly right-handed fields are observed within the slits. The dashed lines indicate the positions of the slits in the close-by slit layer.

distinct incident polarizations. The strongest interaction could be obtained for vertically polarized light. As expected, a strong dependence of the resonance frequency on d_z is observed.

The lowest reflectance can be observed for $d_z = 80$ nm. However, the minimal reflectance cannot be used to optimize the chiral near-field response. It maximizes the absolute values of the chiral near-fields, but the handedness uniformity is reduced due to the weaker coupling to the mirror. To obtain near-fields of one handedness, the distance d_z must be reduced. We manually determined $d_z = 30$ nm as a good trade-off between strength and handedness preservation.

The results for this distance are depicted in Fig. 8.15 (b). The values are significantly lower than for the PEC, but we still obtain one order of magnitude of enhancement compared to CPL of the same frequency in the whole slit area. Although we additionally find regions with left-handed chiral near-fields, those are well outside of this area. Therefore, they cannot be accessed by any chiral analyte filled only in the slits.

Note that these chiral near-fields are generated in a reflection geometry. Therefore, the chiroptical response of some chiral analyte placed in the slits would also be recorded in reflection. This is in contrast to common CD spectroscopy that works in transmission. Classical CD spectroscopy cannot be applied in reflection because the incident CPL changes its handedness upon reflection. Therefore, no differential signal is expected for the two incident circular polarizations [60].² Our scheme does not have these limitations. In fact, reflection mode is not only possible but necessary for the creation of the chiral near-fields.

Note that the diagonal slit structures that we discussed here have not been optimized for strongest response. As we have shown in Section 8.2, even the design with four intertwined helices is non-trivial to optimize. Depending on the dimensions of the helices, different approaches are necessary to maximize the obtained OC: Small structures need a sufficiently large pitch to obtain good coupling to the external field, whereas large structures benefit from small pitches and the resulting stronger coupling between the single wires.

Therefore, it is expected that the modified two-layered system is non-trivial to optimize as well. Additional theoretical investigations, for example by an adaption of the dipole model discussed in Chapter 7, are necessary to obtain a better understanding of the working principle of this design. However, we could demonstrate that the concept of chiral eigenmodes in geometrically chiral systems can be used for strong chiral near-field sources, which can additionally be optimized for simple fabrication.

² There is some special method called “diffuse reflectance CD”, which probes the chirality of surfaces. However, it uses diffuse reflection and not the specular reflection as in the method we propose [232].

CONCLUSIONS AND OUTLOOK

In this thesis, we explored for the first time the chiral near-field response of plasmonic nanostructures in a systematic manner. First and foremost, we could demonstrate that such structures can be used to obtain fields with significantly higher OC than CPL of the same frequency and intensity. Furthermore, we showed that local OC is a new way to look at chiral nanostructures. A structure with a strong chiroptical far-field response will not automatically exhibit the strongest chiral near-fields.

The chiroptical near-field response is more complicated than the well-understood field enhancement effect, because the relative orientation and phase of both the electric and the magnetic field must be controlled simultaneously. Not only is the geometry of the structure crucial, but also the choice of the illumination is important.

In Section 4.4.1, we grouped the whole set of possible designs, which in principle consists of all plasmonic structures illuminated under any polarization, in terms of the chiral symmetry of both the structure and the illumination. Figure 9.1 depicts the most important concepts and designs that we elaborated for the different combinations.

We were able to answer several fundamental questions about the generation and amplification of chiral near-fields. The illumination of an achiral rod antenna with achiral light revealed that geometrical chirality is not necessary to obtain non-zero OC locally. Although neither the structure nor the light exhibit chiral near-fields on their own, their combination leads to non-zero OC due to interference effects. Globally, the integrated OC vanishes, which is in consistence with the continuity equation for OC. However, the effects of the chiral near-fields can be experienced locally.

A similar observation has been made for the plasmonic racemate illuminated with chiral light. Although this structure is geometrically achiral globally, we find geometrically chiral substructures locally. These small parts of our locally chiral metasurfaces interact preferably with the appropriate handedness of the incident light; their

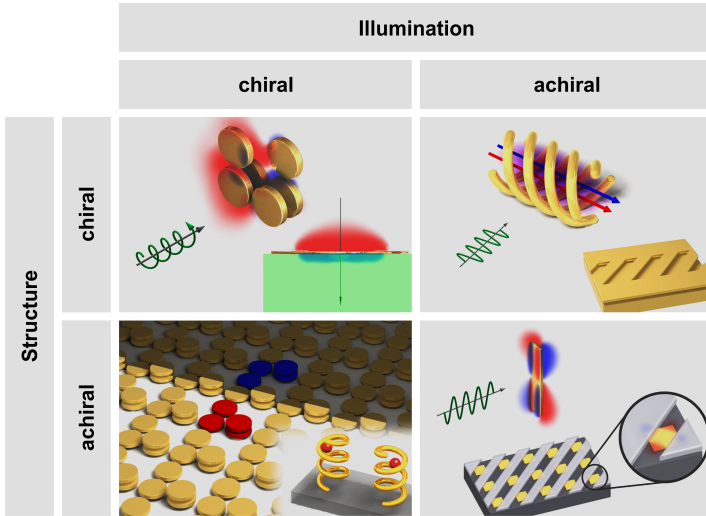


FIGURE 9.1. Possible combinations of plasmonic nanostructures and incident polarizations are grouped by their chiral symmetry. Each cell sketches the major results that we found for the respective combination.

modes result in near-fields with the respective handedness. In this way, the predominant handedness of the near-fields can be controlled by the handedness of the illumination.

The concept of chiral eigenmodes leads to a different mechanism for the generation of chiral near-fields: The geometry of the structure enforces electric and magnetic field vectors that are partially parallel and, therefore, lead to non-zero OC without the need for interference with the external field. Because of that, the illumination should not be optimized for its intrinsic OC, but shaped such, that the respective eigenmodes of the structure are excited most efficiently. A beneficial configuration for such schemes is the combination of geometrically chiral structures with LPL because linear polarizations excite dipolar plasmonic resonances most efficiently.¹

¹ The helix, which generated strong OC for linear polarization, featured much weaker response under CPL illumination parallel to its axis even for matching handedness. This underlines the critical importance of the correct illumination of chiral plasmonic near-field sources.

For geometrically chiral structures that are illuminated with chiral light, a strong difference in the excitation efficiency depending on the handedness of the incident light can be observed. The non-zero OC of the light allows for an additional degree of freedom in the design: The handedness of the fields close to properly designed three-dimensional or planar geometrically chiral nanostructures can be locally steered by the handedness of the incident light.

The plasmonic nanospiral, which is a planar geometrically chiral structure, is a good example that the concept of chiral plasmonic near-field sources works. In this concept, a nanostructure provides fields with strong OC for chiroptical spectroscopy with enhanced sensitivity. The nanospiral can shape its surrounding chiral fields in such a way that regions with opposite handedness are located on different sides of the structure. Therefore, the nanospiral fulfills most of the design goals that we elaborated for chiral plasmonic near-field sources: It provides fields with uniform handedness, which feature significantly stronger OC than CPL and are easily accessible; furthermore, these fields can be found in an extended area. Three-dimensionally geometrically chiral structures can lead to strong chiral hot-spots with enhancement factors of more than 80. However, both of these designs do not provide enantiomorphic fields. Additionally, the combination of chiral structures with chiral light leads to chiroptical far-field responses that are significantly stronger than those of the chiral analyte, which is a drawback for chiroptical spectroscopy because it adds an additional background signal.

Both issues can be overcome in plasmonic racemates. These structures are geometrically achiral. Therefore, no chiroptical far-field response is expected. Additionally, enantiomorphic fields can be obtained by switching the handedness of the incident CPL due to the local interaction with substructures of the appropriate handedness. If the distance between these substructures is large enough, the designs for geometrically chiral structures can be used as a blueprint. Our concept of locally chiral plasmonic metasurfaces, on the other hand, offers a high integration density while maintaining the advantages of plasmonic racemates. Plasmonic racemates are especially powerful because conventional CD spectroscopy techniques can still be used, but with enhanced signals. However, the expected enhancement is weak because OC is either small or highly localized.

Strong OC in a large volume could be obtained by the illumination of intertwined helices with LPL. However, these structures are not optimal for use as chiral plasmonic near-field sources because of their complex geometry, which is challenging for fabrication. Additionally, filling the chiral analyte into the helices is non-trivial. Therefore, we proposed a design with diagonal slits on top of a mirror, which offers simple fabrication and straightforward access to chiral near-fields with an OC enhancement of up to a factor of 30.

Usage of this diagonal-slit structure as a chiral plasmonic near-field source for chiroptical spectroscopy would ask for novel measurement schemes. Not only is LPL used, but the detection of differential reflectance instead of transmittance would be needed. Although this demands further development, it could be advantageous for remote sensing devices because illumination and detection do not need to be spatially separated, as in the case of a transmission measurement.

The general possibility of CD type of chiroptical spectroscopy with LPL has been theoretically demonstrated with the nanosquare. However, this design is not the optimum for real-life applications because of its weak response. Nevertheless, it might be a good candidate for first experimental verifications of our proposed concepts because of its simplicity.

Our results indicate that the most promising concepts for chiroptical spectroscopy with enhanced sensitivity are plasmonic racemates and chiral eigenmodes. Plasmonic racemates allow for simple integration in conventional CD measurement schemes, but only moderate enhancement could be demonstrated thus far. Chiral eigenmodes offer the possibility of very high enhancement, but modified sensing schemes must be applied. Depending on the problem, one or the other concept might be superior.

For future work, the experimental verification of our concepts is highly desirable. Until today, only one experiment, which probed the chiral fields near plasmonic nanostructures, has been reported [233]. Additional experimental work is necessary to verify the capabilities of chiral plasmonic near-field sources for enhanced chiroptical spectroscopy. Furthermore, direct mapping of the OC might be possible by an extension of existing techniques used to map the electric near-field of plasmonic nanostructures [234].

In addition, our investigations open up several perspectives for future theoretical studies. As shown for the linear rod antenna, dipole models are a powerful tool to predict the shapes of chiral near-fields. An extension that uses several dipoles located at positions, which match the plasmonic mode of the structure, might offer a fast initial optimization step for more complex geometries [235].

Our designs should only demonstrate the more fundamental underlying concepts. For applications in spectroscopy, these designs can be further optimized. A good start is our locally chiral metasurface. Higher enhancement factors might be possible by changing the geometry or using other building blocks than disks. The diagonal-slit structure should be further investigated to reveal whether a design, where the handedness of the generated near-fields switches with a rotation of the incident linear polarization, can be found.

Novel designs are not restricted to variations of our demonstrated concepts. Besides novel geometries, they could incorporate novel materials. One possibility could be magneto-optically active materials, which can strongly influence the polarization state of the transmitted light [236]. The additional influence of the external magnetic field might offer unique control over the chiral near-fields [237].

An analysis similar to ours could be performed for a sensor for the magneto-electric effect, which is closely related to chirality, but nonreciprocal.² It has been shown recently that this effect can be probed with high sensitivity via electromagnetic fields whose real part of $\mathbf{E}^* \cdot \mathbf{B}$ (in contrast to the imaginary part of this quantity, which has been utilized to quantify the chiral interaction in this thesis) is large [238]. This real part is zero for any traveling plane wave, independent of its polarization. However, we expect that plasmonic nanostructures can be designed to provide appropriate near-fields.

We believe that we only started to explore the possibilities of plasmonic nanostructures to tailor and shape electromagnetic fields with

² Magneto-electrically active media can be described by similar constitutive equations as chiral media with the difference that the coupling parameter, which links \mathbf{D} to \mathbf{B} and \mathbf{H} to \mathbf{E} , has the same sign in both constitutive equations. This difference gives rise to the non-reciprocity. However, such media are still isotropic, which is a major difference to a magneto-optically active medium, where the external magnetic field introduces an anisotropy to the system. Magneto-optically active media can be described by the standard linear constitutive equations with tensorial $\bar{\epsilon}$.

complex properties. Furthermore, we expect exciting research in the young field of plasmonically enhanced chiroptical spectroscopy in the next years. We believe that our concept of chiral plasmonic near-field sources will benefit these studies. Although we cannot propose one single perfect design that is the optimum for all possible challenges, we provide fundamental insights that might aid experimentalists to identify the best design for their specific needs.

A.1 UNITS OF CIRCULAR DICHROISM

In Section 2.2.3, the absorbance A is defined via the attenuation of the incident light beam. All the intensity of the incident beam is either transmitted, reflected, or absorbed. Therefore, one can write

$$1 = T + R + A \quad (\text{A.1})$$

with T being the transmittance and R the reflectance of the illuminated system. The differential absorbance is related to the differential transmittance via

$$\Delta A = -\Delta T - \Delta R. \quad (\text{A.2})$$

For an isotropic chiral material described by the constitutive equations (2.48), ΔR vanishes [87]. This is the common case for chiral liquids with isotropic orientation of the chiral molecules. For such systems, a measurement of ΔT is sufficient to obtain information about ΔA .

Artificial chiral materials, such as chiral plasmonic nanostructures, cannot be described by absorption alone; scattering might play an important role as well [168].¹ Their response is, in general, anisotropic. Non-zero ΔR can occur when the eigenpolarizations differ from CPL.² One must be careful when such anisotropic materials are analyzed regarding their CD response via transmission measurements.³

¹ There exist several techniques to describe chiral metamaterials via effective constitutive parameters [239–241]. This allows, in principle, to predict the chiroptical response without a full-field calculation of the underlying structure. However, a thorough optical characterization of the metamaterial is necessary for the parameter retrieval.

² This is the main mechanism of the helix-based circular polarizer discussed in [82].

³ Circular eigenpolarizations can be ensured via the arrangement. They are supported by structures with C_3 , C_4 , or C_6 rotational symmetry under normal incidence [75]. For all other symmetries, one should carefully check for differential reflectance.

In some chemical literature, CD is not defined via the differential absorbance ΔA . Instead, they use Beer's law (in base 10 notation), which describes the attenuation of the light intensity I in the system:

$$I = I_0 10^{-\epsilon l c_{\text{mol}}}, \quad (\text{A.3})$$

where ϵ is the molar extinction coefficient, l is the path length, and c_{mol} is the concentration of the chiral analyte in moles per liter. Then, one can identify the absorptivity \mathcal{A} as

$$\mathcal{A} := \epsilon l c = \log \left(\frac{I_0}{I} \right). \quad (\text{A.4})$$

CD is then defined as the differential absorptivity:

$$\Delta \mathcal{A} := \mathcal{A}^+ - \mathcal{A}^- = \log \left(\frac{I^-}{I^+} \right). \quad (\text{A.5})$$

This definition has the advantage that no reference beam is needed for the measurement [242].

Sometimes, also the difference of the extinction coefficients is given, because it is independent on path length and concentration. A transformation between the two definitions can be obtained by

$$\Delta \epsilon = \frac{1}{l c_{\text{mol}}} \Delta \mathcal{A}. \quad (\text{A.6})$$

In some chemical literature, the measured CD spectra do not report $\Delta \mathcal{A}$ or $\Delta \epsilon$ but ellipticity θ (sometimes also Ψ), which is defined as

$$\theta \text{ (rad)} = \frac{\sqrt{I^-} - \sqrt{I^+}}{\sqrt{I^-} + \sqrt{I^+}}. \quad (\text{A.7})$$

Comparison with Beer's law leads to

$$\theta \text{ (rad)} \approx \Delta \mathcal{A} \frac{\ln 10}{4} \quad (\text{A.8})$$

for small values of $\Delta \mathcal{A}$. Here, θ is given in radians. A conversion to millidegrees results in

$$\theta \text{ (mdeg)} \approx 32982 \cdot \Delta \mathcal{A}, \quad (\text{A.9})$$

which is a commonly used unit for CD spectra. The molar ellipticity $[\theta]$ is given as

$$[\theta] = \frac{0.1 \cdot \theta \text{ (mdeg)}}{l c_{\text{mol}}} \approx 3298.2 \cdot \Delta \epsilon. \quad (\text{A.10})$$

A.2 CIRCULARLY POLARIZED LIGHT IN CST MICROWAVE STUDIO

As discussed in Section 2.1, the definition of the handedness of a given geometrically chiral object is purely arbitrary. This has led to two distinct definitions for the handedness of CPL [60].

In this thesis, we use the *detector's view* convention: The observer stands in the detector plane and looks in the direction of the *in-going* beam. The direction of rotation of the electric field vector in this plane defines the handedness of the light: Clockwise rotation belongs to RCP, counterclockwise rotation to LCP. If we freeze time, the intuitive handedness of the helix of the electric field vector in space matches the one of the circular polarization. This convention is used in most optics textbooks.

A different interpretation is made by the *source view* convention: Instead of the detector plane, the observer stands in the source plane and looks in the direction of the *out-going* beam. Again, the rotation of the electric field vector in this plane defines the handedness. However, the handedness of CPL in these two conventions is exactly opposite.⁴ This convention is commonly used in quantum optics and engineering.

While we use the detector's view convention, CST MWS uses the source view convention. Additionally, CST MWS uses the following time dependence for monochromatic plane waves

$$E \propto e^{i(\omega t - kz)} \quad (\text{A.11})$$

instead of Eq. (2.4). Therefore, the intuitive handedness of the helix of the electric field vector in space does not coincide with the nominal handedness of the light in CST MWS. However, the intuitive handedness is of major importance for our qualitative analysis of the behavior of geometrically chiral plasmonic nanostructures, e. g., the discussion of selectively excited modes in Born-Kuhn type structures. We give a mapping of the modes to the respective helices for Floquet ports⁵ as well as plane wave incidence in Table A.1.

⁴ This can be intuitively understood as follows: The rotation in a plane is a planar geometrically chiral system. Depending on the convention, we look from opposite sides on this system, which changes its handedness.

⁵ These ports are used by the frequency domain solver with unit cell boundary conditions.

PORT	HELIX	OC
Zmin(1)	right	+
Zmin(2)	left	-
Zmax(1)	left	-
Zmax(2)	right	+
LCP (+z)	right	+
RCP (+z)	left	-
LCP (-z)	right	+
RCP (-z)	left	-

TABLE A.1. Intuitive handedness of the helix of the electric field vector in space and sign of OC (calculated via Eq. (4.4)) for the different port modes in CST MWS. The second part of the table covers plane wave incidence for propagation in positive and negative z -direction.

In addition, the difference in the time dependence results in a sign flip of the calculated values of OC compared to the values obtained in Eq. (4.20) for CPL. Table A.1 shows the signs of OC obtained for the different ports. To be consistent with the conventions used in this thesis, the signs of OC values obtained from CST MWS must be inverted.

The calculation of \hat{C} requires the values of $|C_{\text{CPL}}|$ for the normalization. With Eq. (4.20), one obtains

$$\hat{C} = \frac{\Im \left(\mathbf{E}^* \cdot \mathbf{B} \right)}{\frac{1}{c} |\mathbf{E}|^2} = \frac{\mu_0 c \Im \left(\mathbf{E}^* \cdot \mathbf{H} \right)}{|\mathbf{E}|^2}. \quad (\text{A.12})$$

Here, the sign flip has already been included. The second step is necessary because CST MWS calculates the magnetic field strength \mathbf{H} instead of the magnetic field \mathbf{B} .

For plane wave excitation, the amplitude of the electric field vector can be configured. Therefore, calculation of the normalized values is straightforward. For the default value of $|\mathbf{E}| = 1 / \sqrt{2} \text{ V m}^{-1}$, one obtains

$$\hat{C} = \frac{\mu_0 c}{2} \Im \left(\mathbf{E}^* \cdot \mathbf{H} \right) \approx 188.365 \cdot \Im \left(\mathbf{E}^* \cdot \mathbf{H} \right). \quad (\text{A.13})$$

For Floquet ports, the whole port provides an input peak power of 1 W. Therefore, the absolute value of the Poynting vector \mathbf{S} is given as

$$|\mathbf{S}| = \sqrt{\frac{\mu_0}{\varepsilon_0}} |\mathbf{E}|^2 = \frac{1 \text{ W}}{A_p}, \quad (\text{A.14})$$

where A_p is the area of the port in meter. Solving for $|\mathbf{E}|^2$ and inserting in Eq. (A.12) yields

$$\hat{C} = \frac{\Im \mathfrak{m}(\mathbf{E}^* \cdot \mathbf{H})}{A_p}. \quad (\text{A.15})$$

A.3 VOLUME RENDERING WITH POV-RAY

We used POV-Ray (version 3.6.1 with MegaPOV 1.2.1) to visualize our results. We followed the guide given in [243]. The volume rendering was obtained by a transparent medium whose density and color was influenced by the local value of the OC as shown in Listing A.1.

At first, a cube with unity side length is created. This is necessary because media statements fill only this region, independent of the dimensions of the object. The box is rescaled afterwards to fit the dimensions of the exported fields.

The values are given via `df3` files. These are binary files with a simple file format [244]: At first, a header of three 16 bit unsigned integers describing the length of the three dimensions of the data set is needed. After this header, the data is expected as stream of unsigned integers in column major order, i. e., the first dimension varies the fastest. The size of the single integers is determined by the total size of the file. Note that all values are expected in big-endian byte order, while most Intel systems normally use little-endian encoding.⁶ Therefore, the encoding must be set manually.

The simplified MATLAB code in Listing A.2 stores the negative values of a three-dimensional array in a `df3` file. A similar script can be used for the positive values. The values are rescaled to the maximum absolute value occurring in the initial data set. Of course, this can be

⁶ Big-endian and little-endian refer to different orderings of the bytes in multibyte values. More details can be found in [245].

```

1  box {
2      <0,0,0>, <1,1,1>
3      pigment { rgbt 1 }
4      interior {
5          media {
6              intervals 100
7              samples 1,20
8              emission 1/50
9              absorption 1/10
10             density {
11                 density_file df3 "values-negative.df3"
12                 interpolate 1
13                 color_map { CMAP_NEGATIVE }
14             } }
15         media {
16             /* same statement, but with
17              values-positive.df3 and CMAP_POSITIVE */
18         } }
19     hollow
20     translate <-0.5,-0.5,-0.5>
21     /* sizes must be set to the dimensions
22      of the exported data in the df3 files */
23     scale <SIZE_X, SIZE_Y, SIZE_Z>
24 }

```

LISTING A.1. POV-Ray statements to render transparent media with color and density controlled by numerical values.

changed to scale several data sets to the same value for comparison. Note that MATLAB stores arrays in column major order as well. Therefore, the array can be written to the file without further treatment.

For the scaling, values that exceed the absolute value of OC in all data sets that should be compared have been used. However, numerical noise can lead to extraordinary high values. Those unphysical responses would destroy the scaling. Therefore, we filtered all data with a $3 \times 3 \times 3$ median filter. This is a nonlinear filter that is used for noise reduction in image processing. It is the optimal filtering technique to remove single outstanding values.

```

1  %% assumes values to save given in 'Data'
2
3  % prepare output file
4  out = fopen('values-negative.df3', 'w', 'ieee-be');
5
6  % header
7  fwrite(out, size(Data), 'uint16', 0, 'ieee-be');
8
9  % rescale values
10 Data_df3 = uint32((2^32-1)*abs(Data)/max(abs(Data)
11     (:))));
12
13 % delete positive values
14 Data_df3(Data > 0) = 0;
15
16 % output
17 fwrite(out, Data_df3, 'uint32', 0, 'ieee-be');
18 fclose(out);

```

LISTING A.2. MATLAB code to save a given array in a df3 file for use in POV-Ray.

```

1  #declare CMAP_NEGATIVE = color_map {
2    [0 rgb 0]
3    [0.025 rgb 0]
4    [0.5 rgb <1,1,0 >]
5    [1 rgb <3,0,0 >]
6  }
7
8  #declare CMAP_POSITIVE = color_map {
9    [0 rgb 0]
10   [0.025 rgb 0]
11   [0.5 rgb <0,1,1 >]
12   [1 rgb <0,0,3 >]
13  }

```

LISTING A.3. POV-Ray color maps to obtain the color scheme used for volume rendering.

We use two media statements in the POV-Ray code because `df3` files can only contain unsigned values. Therefore, we separated positive and negative values into different files. It would be possible to rescale the whole range to positive values. However, the density is lowest for the value 0, resulting in minimal medium density for the strongest negative OC.

The color of each pixel is controlled by the respective color map. We used the maps in Listing A.3. Note that, due to the `absorption` keyword, the colors given in the color map have to be inverted. `<1, 1, 0>`, for example, absorbs red and green resulting in the blue color for negative values. The second entry in each color map controls the value up to which the OC is not shown at all. This is necessary because the incident light can also carry non-zero OC, which should not be visualized. Otherwise, the whole domain would be colored. Dismissing these values results in no loss of information because we are only interested in enhanced values above the OC of CPL. We used different cutting values depending on the normalization.

For most plots displaying OC, the value 0.025 has been used. This allows for a simple comparison of the respective designs. However, the plots in Chapter 8 have been rendered with 0.075; additionally, a value of 0.6 instead of 0.5 was used in the third line of the color maps. Figure 7.2 was rendered using a very small value of 0.003 due to the logarithmic scale used in this plot. The plots of the electric energy density enhancement were rendered with 0.05 (Fig. 5.2) and 0.01 (Fig. 7.1 (b)).

Due to the transparency, the color of one distinct point depends not only on the actual OC value at this point but also on the color of the region behind. Therefore, the plots should not be used for quantitative analysis. However, this is a general problem of all volume rendering tools. The resulting plots are only useful to obtain information about the general shape and location of the chiral near-fields, which is important for the general design of chiral near-field sources. We provide slice plots for quantitative analysis wherever necessary.

In this appendix, we derive the equations for electromagnetic waves propagating in chiral media that are discussed in Section 2.2.3.

B.1 CHIRAL WAVE EQUATION

As for the classical linear wave equation, we evaluate $\nabla \times \nabla \times \mathbf{E}$. Maxwell's curl equation (2.1b) in combination with the constitutive equation for \mathbf{B} (2.48b) leads to

$$\nabla \times \mathbf{E} = -\partial_t \mathbf{B} = -\mu_0 \mu \partial_t \mathbf{H} - \frac{\hat{\kappa}}{c} \partial_t \mathbf{E}. \quad (\text{B.1})$$

Then, we can derive

$$\nabla \times \nabla \times \mathbf{E} = -\mu_0 \mu \partial_t \underbrace{\nabla \times \mathbf{H}}_{=\partial_t \mathbf{D}} - \frac{\hat{\kappa}}{c} \partial_t \nabla \times \mathbf{E}. \quad (\text{B.2})$$

Here, the second curl equation (2.1d) has been used. Applying the constitutive equation for \mathbf{D} (2.48a) results in

$$\nabla \times \nabla \times \mathbf{E} = -\frac{n^2}{c^2} \partial_t^2 \mathbf{E} + \mu_0 \mu \frac{\hat{\kappa}}{c} \partial_t^2 \mathbf{H} - \frac{\hat{\kappa}}{c} \partial_t \nabla \times \mathbf{E}. \quad (\text{B.3})$$

Using

$$\partial_t^2 \mathbf{H} = \frac{1}{\mu_0 \mu} \partial_t \left(\underbrace{\partial_t \mathbf{B}}_{=-\nabla \times \mathbf{E}} - \frac{\hat{\kappa}}{c} \partial_t \mathbf{E} \right), \quad (\text{B.4})$$

which is obtained from Eqs. (2.1b) and (2.48b), one arrives at

$$\nabla \times \nabla \times \mathbf{E} = -\frac{n^2 - \kappa^2}{c^2} \partial_t^2 \mathbf{E} - 2 \frac{\hat{\kappa}}{c} \partial_t \nabla \times \mathbf{E} \quad (\text{B.5})$$

after some sorting.

Similar to the standard wave equation for achiral media, one can write

$$\nabla \times \nabla \times \mathbf{E} = \nabla (\nabla \cdot \mathbf{E}) - \nabla^2 \mathbf{E}. \quad (\text{B.6})$$

The electric field \mathbf{E} can be written as sum of terms proportional to D and \mathbf{B} . Therefore, $\nabla \cdot \mathbf{E} = 0$ and

$$\nabla \times \nabla \times \mathbf{E} = -\nabla^2 \mathbf{E}. \quad (\text{B.7})$$

A comparison of Eqs. (B.5) and (B.7) leads to the chiral wave equation (2.51).

B.2 DIFFERENTIAL ABSORBANCE

Absorbance in a medium with thickness D and complex refractive index n_{\pm} can be written as

$$A_{\pm} = 1 - e^{-2\Im m(n_{\pm})D\frac{\omega}{c}}. \quad (\text{B.8})$$

This assumes that all attenuation of the intensity is due to absorption; no scattering is observed. Then, the differential absorbance is given by

$$\Delta A = -e^{-2\Im m(n)D\frac{\omega}{c}} \left(\underbrace{e^{-2\Im m(\kappa)D\frac{\omega}{c}} - e^{2\Im m(\kappa)D\frac{\omega}{c}}}_{=-2\sinh(2\Im m(\kappa)D\frac{\omega}{c})} \right). \quad (\text{B.9})$$

Compared to Eq. (B.8), the first exponential is connected to the averaged absorbance in the material:

$$e^{-2\Im m(n)D\frac{\omega}{c}} = 1 - A. \quad (\text{B.10})$$

After this simplification, we arrive at Eq. (2.56).

DETAILS OF OPTICAL CHIRALITY

In this appendix, we derive the main equations (4.4) and (4.10) of the manuscript in more detail. Equation (4.4) describes how to calculate OC from the electric and magnetic field, while Eq. (4.10) quantifies the dependence of the handedness-dependent absorption rate of a chiral molecule on OC.

C.1 DEFINITION OF OPTICAL CHIRALITY

For historical reasons, OC is defined by Eq. (4.1), which we repeat for convenience:

$$C := \frac{\epsilon_0}{2} \mathcal{E} \cdot (\nabla \times \mathcal{E}) + \frac{1}{2\mu_0} \mathcal{B} \cdot (\nabla \times \mathcal{B}) . \quad (\text{C.1})$$

However, for *physical* reasons,

$$C \propto -\Im \left(\mathbf{E}^* \cdot \mathbf{B} \right) \quad (\text{C.2})$$

should be used instead: This quantity determines the handedness-dependent absorption rate of a chiral molecule in an electromagnetic field (cf. Eq. (4.7)). The negative sign in Eq. (C.2) leads to positive values for LCP, which is consistent with the sign convention of the Jones vector for CPL in the detector's view convention (cf. Eq. (2.6) and the discussion in Appendix A.2).

We will now show the equivalency of these two equations for monochromatic electromagnetic fields, i. e.,

$$\mathcal{E} \equiv \Re (\mathbf{E}) = \Re \left(\mathbf{E}_0 e^{-i\omega t} \right) , \quad (\text{C.3a})$$

$$\mathcal{B} \equiv \Re (\mathbf{B}) = \Re \left(\mathbf{B}_0 e^{-i\omega t} \right) . \quad (\text{C.3b})$$

Starting from Eq. (C.1), we apply Maxwell's curl equations (2.1b) and (2.1d). Note, that these calculations are performed in vacuum; therefore, the relations

$$\mathcal{D} = \varepsilon_0 \mathcal{E}, \quad (\text{C.4a})$$

$$\mathcal{B} = \mu_0 \mathcal{H} \quad (\text{C.4b})$$

hold true. With this, we obtain

$$C = -\frac{\varepsilon}{2} \left(\mathcal{E} \cdot \partial_t \mathcal{B} - \mathcal{B} \cdot \partial_t \mathcal{E} \right). \quad (\text{C.5})$$

For monochromatic electromagnetic waves, the time derivatives in Eq. (C.5) can easily be calculated if we use complex-valued electric and magnetic fields.

We make use of the identities

$$\Re(z) = \frac{1}{2} (z + z^*), \quad (\text{C.6a})$$

$$\Im(z) = \frac{1}{2i} (z - z^*), \quad (\text{C.6b})$$

which hold true for any complex number z . One obtains

$$\begin{aligned} & \mathcal{E} \cdot \partial_t \mathcal{B} - \mathcal{B} \cdot \partial_t \mathcal{E} \\ &= \frac{-i\omega}{4} \left[(E + E^*) \cdot (B - B^*) - (B + B^*) \cdot (E - E^*) \right] \\ &= \frac{-i\omega}{2} \underbrace{(E^* \cdot B - E \cdot B^*)}_{=2i \Im(E^* \cdot B)} = \omega \Im(E^* \cdot B). \quad (\text{C.7}) \end{aligned}$$

With this result, Eq. (C.5) reduces to

$$C = -\frac{\varepsilon_0 \omega}{2} \Im(E^* \cdot B), \quad (\text{C.8})$$

which is the equation for OC used in this thesis. The prefactors are determined by the historical definition Eq. (C.1).

C.2 CALCULATION OF HANDEDNESS-DEPENDENT ABSORPTION

We start with the absorption rate of a chiral molecule in an arbitrary electromagnetic field as given in Eq. (4.5):

$$a = \left\langle \mathcal{E} \cdot \partial_t \Re(\mathbf{p}) + \mathcal{B} \cdot \partial_t \Re(\mathbf{m}) \right\rangle. \quad (\text{C.9})$$

The induced magnetic and electric dipole moments are harmonic in time because of the monochromatic external stimulus. Therefore, they can be written as

$$\mathbf{p} = \mathbf{p}_0 e^{-i\omega t}, \quad (\text{C.10a})$$

$$\mathbf{m} = \mathbf{m}_0 e^{-i\omega t}. \quad (\text{C.10b})$$

Using the identities (C.6), the calculation of the time derivative is similar to the derivation in Eq. (C.7):

$$\begin{aligned} a &= \frac{-\hat{i}\omega}{4} \left\langle (\mathbf{E} + \mathbf{E}^*) \cdot (\mathbf{p} - \mathbf{p}^*) + (\mathbf{B} + \mathbf{B}^*) \cdot (\mathbf{m} - \mathbf{m}^*) \right\rangle \\ &= \frac{-\hat{i}\omega}{4} \left\langle (\mathbf{E}_0 e^{-i\omega t} + \mathbf{E}_0^* e^{i\omega t}) \cdot (\mathbf{p}_0 e^{-i\omega t} - \mathbf{p}_0^* e^{i\omega t}) \right. \\ &\quad \left. + (\mathbf{B}_0 e^{-i\omega t} + \mathbf{B}_0^* e^{i\omega t}) \cdot (\mathbf{m}_0 e^{-i\omega t} - \mathbf{m}_0^* e^{i\omega t}) \right\rangle. \quad (\text{C.11}) \end{aligned}$$

In the second step, we explicitly included the harmonic time dependence.

All terms that keep the harmonic time dependence after multiplication vanish during the time averaging process. Therefore, only terms with one complex conjugated contribution persist:

$$\begin{aligned} a &= \frac{-\hat{i}\omega}{4} \left(\mathbf{E}^* \cdot \mathbf{p} - \mathbf{E} \cdot \mathbf{p}^* + \mathbf{B}^* \cdot \mathbf{m} - \mathbf{B} \cdot \mathbf{m}^* \right) \\ &= \frac{\omega}{2} \Im \left(\mathbf{E}^* \cdot \mathbf{p} + \mathbf{B}^* \cdot \mathbf{m} \right). \quad (\text{C.12}) \end{aligned}$$

We now insert the explicit relations for the dipole moments given in Eqs. (4.6). Then,

$$\begin{aligned} \Im(\mathbf{E}^* \cdot \mathbf{p}) &= \Im(\alpha |\mathbf{E}|^2 - i\xi \mathbf{E}^* \cdot \mathbf{B}) \\ &= \Im(\alpha) |\mathbf{E}|^2 - \Im(i\xi \mathbf{E}^* \cdot \mathbf{B}) \end{aligned} \quad (\text{C.13a})$$

and, similarly,

$$\Im(\mathbf{B}^* \cdot \mathbf{m}) = \Im(\chi) |\mathbf{B}|^2 + \Im(i\xi \mathbf{E} \cdot \mathbf{B}^*) . \quad (\text{C.13b})$$

Therefore, Eq. (C.12) can be simplified to

$$\begin{aligned} a &= \frac{\omega}{2} \left(\Im(\alpha) |\mathbf{E}|^2 + \Im(\chi) |\mathbf{B}|^2 \right) \\ &\quad + \frac{\omega}{2} \Im \left(i\xi \underbrace{(\mathbf{E} \cdot \mathbf{B}^* - \mathbf{E}^* \cdot \mathbf{B})}_{=-2i \Im(\mathbf{E}^* \cdot \mathbf{B})} \right) . \end{aligned} \quad (\text{C.14})$$

Because $\Im(\mathbf{E}^* \cdot \mathbf{B})$ is a real number, one finds

$$2 \Im \left(\xi \Im(\mathbf{E}^* \cdot \mathbf{B}) \right) = 2 \Im(\xi) \Im(\mathbf{E}^* \cdot \mathbf{B}) . \quad (\text{C.15})$$

With this, we arrive at Eq. (4.7).

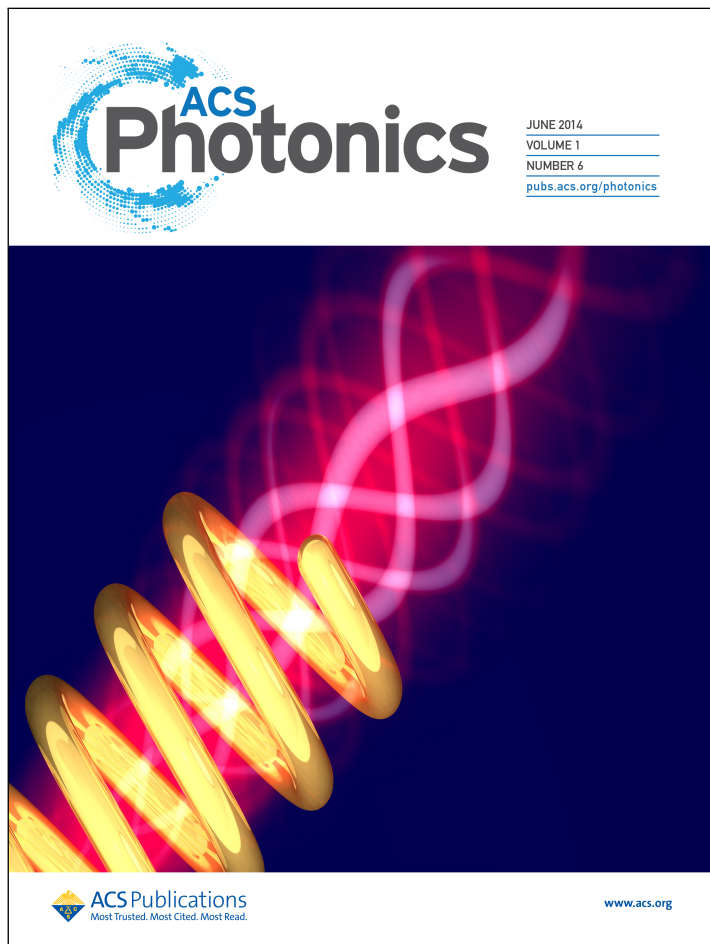


FIGURE D.1. Cover of the June 2014 issue of ACS Photonics highlighting [A8].

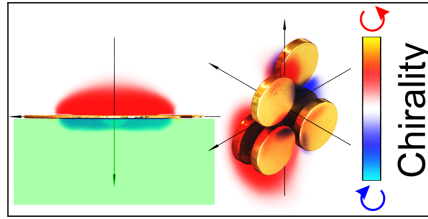


FIGURE D.2. Table of contents figure of [A2].

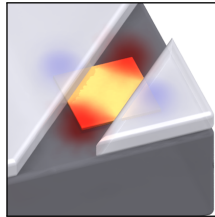


FIGURE D.3. Table of contents figure of [A4].

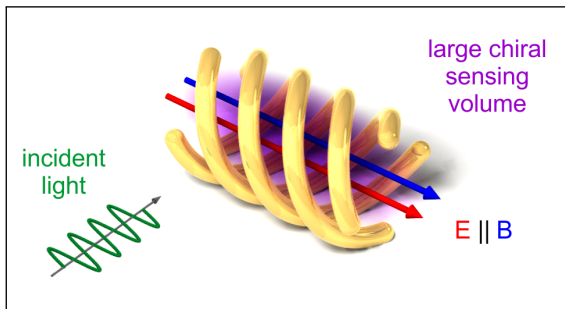


FIGURE D.4. Table of contents figure of [A8].

BIBLIOGRAPHY

- [1] U. Meierhenrich: *Amino Acids and the Asymmetry of Life*, Springer (Berlin), 2008.
ISBN 978-3-540-76886-9, cit. on pp. 1, 31.
- [2] L. D. Barron: *Chirality and Life*. *Space Sci. Rev.* **135**, 187–201 (2008).
DOI 10.1007/s11214-007-9254-7, cit. on p. 1.
- [3] American Association for the Advancement of Science: *So much more to know*. *Science* **309**, 78–102 (2005).
DOI 10.1126/science.309.5731.78b, cit. on p. 2.
- [4] J. S. Siegel: *Biochemistry. Single-handed cooperation*. *Nature* **409**, 777–778 (2001).
DOI 10.1038/35057421, cit. on p. 2.
- [5] P. Ferenci: *Diagnosis and current therapy of Wilson’s disease*. *Aliment. Pharmacol. Ther.* **19**, 157–165 (2004).
DOI 10.1046/j.1365-2036.2003.01813.x, cit. on p. 2.
- [6] M. Quack: *Structure and Dynamics of Chiral Molecules*. *Angew. Chemie Int. Ed.* **28**, 571–586 (1989).
DOI 10.1002/anie.198905711, cit. on p. 2.
- [7] R. W. Smithells and C. G. Newman: *Recognition of thalidomide defects*. *J. Med. Genet.* **29**, 716–723 (1992).
PMID 1433232, cit. on p. 2.
- [8] T. Eriksson, S. Björkman, B. Roth, A. Fyge, and P. Höglund: *Stereospecific determination, chiral inversion in vitro and pharmacokinetics in humans of the enantiomers of thalidomide*. *Chirality* **7**, 44–52 (1995).
DOI 10.1002/chir.530070109, cit. on p. 2.
- [9] F. Neubrech, A. Pucci, T. Cornelius, S. Karim, A. García-Etxarri, and J. Aizpurua: *Resonant Plasmonic and Vibrational Coupling in a Tailored Nanoantenna for Infrared Detection*. *Phys. Rev. Lett.* **101**, 157403 (2008).
DOI 10.1103/PhysRevLett.101.157403, cit. on pp. 2, 46.

- [10] Y. Tang and A. E. Cohen: *Optical Chirality and Its Interaction with Matter*. Phys. Rev. Lett. **104**, 163901 (2010).
DOI 10.1103/PhysRevLett.104.163901, cit. on pp. 2, 59, 61, 66.
- [11] W. T. Kelvin: *Baltimore Lectures on Molecular Dynamics and the Wave Theory of Light*, CJ Clay and Sons (London), 1904.
Cit. on p. 5.
- [12] H. Wang, D. W. Brandl, P. Nordlander, and N. J. Halas: *Plasmonic nanostructures: artificial molecules*. Acc. Chem. Res. **40**, 53–62 (2007).
DOI 10.1021/ar0401045, cit. on pp. 5, 33.
- [13] L. D. Barron: *Molecular Light Scattering and Optical Activity*, 2nd edition, Cambridge University Press (Cambridge), 2004.
ISBN 978-0-521-12137-8, cit. on pp. 5, 61.
- [14] E. Ruch: *Algebraic aspects of the chirality phenomenon in chemistry*. Acc. Chem. Res. **5**, 49–56 (1972).
DOI 10.1021/ar50050a002, cit. on p. 6.
- [15] E. Plum, V. A. Fedotov, and N. I. Zheludev: *Extrinsic electromagnetic chirality in metamaterials*. J. Opt. A Pure Appl. Opt. **11**, 074009 (2009).
DOI doi:10.1088/1464-4258/11/7/074009, cit. on p. 7.
- [16] P. W. Fowler: *Quantification of Chirality: Attempting the Impossible*. Symmetry Cult. Sci. **16**, 321–334 (2005).
Cit. on p. 9.
- [17] M. Petitjean: *Chirality and Symmetry Measures: A Transdisciplinary Review*. Entropy **5**, 271–312 (2003).
DOI 10.3390/e5030271, cit. on pp. 9, 12.
- [18] A. Rassat and P. W. Fowler: *Any Scalene Triangle Is the Most Chiral Triangle*. Helv. Chim. Acta **86**, 1728–1740 (2003).
DOI 10.1002/hlca.200390143, cit. on p. 9.
- [19] A. Rassat and P. W. Fowler: *Is there a “most chiral tetrahedron”?* Chemistry **10**, 6575–6580 (2004).
DOI 10.1002/chem.200400869, cit. on p. 9.
- [20] P. G. Mezey: *Rules on chiral and achiral molecular transformations. II*. J. Math. Chem. **18**, 133–139 (1995).
DOI 10.1007/BF01164654, cit. on p. 10.

- [21] E. Efrati and W. Irvine: *Orientation-Dependent Handedness and Chiral Design*. Phys. Rev. X **4**, 011003 (2014). DOI 10.1103/PhysRevX.4.011003, cit. on p. 10.
- [22] R. Schreiber, N. Luong, Z. Fan, A. Kuzyk, P. C. Nickels, T. Zhang, D. M. Smith, B. Yurke, W. Kuang, A. O. Govorov, and T. Liedl: *Chiral plasmonic DNA nanostructures with switchable circular dichroism*. Nat. Commun. **4**, 2948 (2013). DOI 10.1038/ncomms3948, cit. on pp. 10, 40.
- [23] S. L. Nahrwold: *Electroweak quantum chemistry: Parity violation in spectra of chiral molecules containing heavy atoms*. PhD thesis, Johann Wolfgang Goethe-Universität Frankfurt, 2010. URN urn:nbn:de:hebis:30:3-257101, cit. on p. 12.
- [24] C. S. Wu: *Experimental Test of Parity Conservation in Beta Decay*. Phys. Rev. **105**, 1413–1415 (1957). DOI 10.1103/PhysRev.105.1413, cit. on p. 12.
- [25] B. Darquié, C. Stoeffler, A. Shelkownikov, C. Daussy, A. Amy-Klein, C. Chardonnet, S. Zrig, L. Guy, J. Crassous, P. Soulard, P. Asselin, T. R. Huet, P. Schwerdtfeger, R. Bast, and T. Saue: *Progress toward the first observation of parity violation in chiral molecules by high-resolution laser spectroscopy*. Chirality **22**, 870–884 (2010). DOI 10.1002/chir.20911, cit. on p. 12.
- [26] M. Quack, J. Stohner, and M. Willeke: *High-resolution spectroscopic studies and theory of parity violation in chiral molecules*. Annu. Rev. Phys. Chem. **59**, 741–769 (2008). DOI 10.1146/annurev.physchem.58.032806.104511, cit. on p. 12.
- [27] J. D. Jackson: *Classical Electrodynamics*, 3rd edition, Wiley-VCH (New York), 1998. ISBN 0-471-30932-X, cit. on pp. 12, 13, 60, 62, 105, 133.
- [28] N. W. Ashcroft and N. D. Mermin: *Solid State Physics*, Thomson Learning (Boston), 1976. ISBN 978-0-03-083993-1, cit. on p. 14.

- [29] S. A. Maier: *Plasmonics: Fundamentals and Applications*, Springer (New York), 2007.
ISBN 978-0-387-33150-8, cit. on pp. 14, 18.
- [30] N. Liu, H. Guo, L. Fu, S. Kaiser, H. Schweizer, and H. Giessen: *Three-dimensional photonic metamaterials at optical frequencies*. *Nat. Mater.* **7**, 31–37 (2008).
DOI 10.1038/nmat2072, cit. on pp. 16, 39, 79.
- [31] R. Taubert: *From Near-Field to Far-Field: Plasmonic Coupling in Three-Dimensional Nanostructures*. PhD thesis, Universität Stuttgart, 2012.
URN urn:nbn:de:bsz:93-opus-77795, cit. on pp. 16, 17.
- [32] P. B. Johnson and R. W. Christy: *Optical Constants of the Noble Metals*. *Phys. Rev. B* **6**, 4370–4379 (1972).
DOI 10.1103/PhysRevB.6.4370, cit. on p. 17.
- [33] R. L. Olmon, B. Slovick, T. W. Johnson, D. Shelton, S.-H. Oh, G. D. Boreman, and M. B. Raschke: *Optical dielectric function of gold*. *Phys. Rev. B* **86**, 235147 (2012).
DOI 10.1103/PhysRevB.86.235147, cit. on p. 17.
- [34] M. A. Ordal, L. L. Long, R. J. Bell, S. E. Bell, R. R. Bell, R. W. Alexander, Jr., and C. A. Ward: *Optical properties of the metals Al, Co, Cu, Au, Fe, Pb, Ni, Pd, Pt, Ag, Ti, and W in the infrared and far infrared*. *Appl. Opt.* **22**, 1099–1119 (1983).
DOI 10.1364/AO.22.001099, cit. on p. 17.
- [35] M. Dressel and G. Grüner: *Electrodynamics of Solids: Optical Properties of Electrons in Matter*, Cambridge University Press (Cambridge), 2002.
ISBN 0-521-59726-9, cit. on p. 17.
- [36] L. Novotny and B. Hecht: *Principles of Nano-Optics*, 2nd edition, Cambridge University Press (Cambridge), 2012.
ISBN 978-1-107-00546-4, cit. on pp. 18, 73.
- [37] U. Kreibig and M. Vollmer: *Optical Properties of Metal Clusters*. Springer Series in Materials Science, vol. 25, Springer (Berlin), 1995.
ISBN 978-3-662-09109-8, cit. on p. 18.

- [38] L. Novotny: *Effective Wavelength Scaling for Optical Antennas*. Phys. Rev. Lett. **98**, 266802 (2007).
DOI 10.1103/PhysRevLett.98.266802, cit. on p. 20.
- [39] N. J. Halas, S. Lal, W.-S. Chang, S. Link, and P. Nordlander: *Plasmons in strongly coupled metallic nanostructures*. Chem. Rev. **111**, 3913–3961 (2011).
DOI 10.1021/cr200061k, cit. on p. 20.
- [40] N. Liu and H. Giessen: *Coupling effects in optical metamaterials*. Angew. Chemie Int. Ed. **49**, 9838–9852 (2010).
DOI 10.1002/anie.200906211, cit. on p. 20.
- [41] J. I. Gersten and A. Nitzan: *Photophysics and photochemistry near surfaces and small particles*. Surf. Sci. **158**, 165–189 (1985).
DOI 10.1016/0039-6028(85)90293-6, cit. on p. 20.
- [42] E. Prodan, C. Radloff, N. J. Halas, and P. Nordlander: *A hybridization model for the plasmon response of complex nanostructures*. Science **302**, 419–422 (2003).
DOI 10.1126/science.1089171, cit. on pp. 20, 22.
- [43] E. Prodan and P. Nordlander: *Plasmon hybridization in spherical nanoparticles*. J. Chem. Phys. **120**, 5444–5454 (2004).
DOI 10.1063/1.1647518, cit. on p. 22.
- [44] P. Nordlander, C. Oubre, E. Prodan, K. Li, and M. I. Stockman: *Plasmon Hybridization in Nanoparticle Dimers*. Nano Lett. **4**, 899–903 (2004).
DOI 10.1021/nl049681c, cit. on p. 22.
- [45] T. M. Lowry: *Optical Rotatory Power*, Longmans, Green & Co. (London), 1935.
Cit. on p. 22.
- [46] R. Weindl: *Chiralität und Chaos*. PhD thesis, Universität Regensburg, 2002.
URN urn:nbn:de:bvb:355-opus-1042, cit. on p. 22.
- [47] P. Drude: *Lehrbuch der Optik*, 2nd edition, S. Hirzel (Leipzig), 1906.
Cit. on p. 22.

- [48] M. Born: *Elektronentheorie des natürlichen optischen Drehungsvermögens isotroper und anisotroper Flüssigkeiten*. Ann. Phys. **360**, 177–240 (1918).
DOI 10.1002/andp.19183600302, cit. on pp. 22, 23.
- [49] W. Kuhn: *Über die Drudesche Theorie der optischen Aktivität*. Z. Phys. Chem. Abt. B **20**, 325–332 (1933).
Cit. on p. 22.
- [50] E. U. Condon, W. Altar, and H. Eyring: *One-Electron Rotatory Power*. J. Chem. Phys. **5**, 753–775 (1937).
DOI 10.1063/1.1749938, cit. on p. 22.
- [51] M. Born: *The natural optical activity of liquids and gases*. Phys. Z. **16**, 251–258 (1915).
Cit. on p. 23.
- [52] C. W. Oseen: *Über die Wechselwirkung zwischen zwei elektrischen Dipolen und über die Drehung der Polarisationsebene in Kristallen und Flüssigkeiten*. Ann. Phys. **353**, 1–56 (1915).
DOI 10.1002/andp.19153531702, cit. on p. 23.
- [53] W. Kuhn: *Quantitative Verhältnisse und Beziehungen bei der natürlichen optischen Aktivität*. Z. Phys. Chem. B **4**, 14–36 (1929).
Cit. on p. 23.
- [54] Y. P. Svirko and N. I. Zheludev: *Polarization of Light in Nonlinear Optics*, Wiley-VCH (New York), 1998.
ISBN 978-0-471-97640-0, cit. on pp. 23, 25.
- [55] L. D. Landau, E. M. Lifshitz, and L. P. Pitaevskii: *Electrodynamics of Continuous Media*. Course of Theoretical Physics, vol. 8, 2nd edition, trans. by J. B. Sykes, J. S. Bell, and M. J. Kearsley, Butterworth-Heinemann (Oxford), 1984.
ISBN 978-0-7506-2634-7, cit. on p. 26.
- [56] I. V. Lindell, A. H. Sihvola, S. Tretyakov, and A. J. Viitanen: *Electromagnetic Waves in Chiral and Bi-Isotropic Media*, Artech House (London), 1994.
ISBN 978-0-89006-684-3, cit. on pp. 27, 29.

- [57] A. H. Sihvola and I. V. Lindell: *Bi-isotropic constitutive relations*. *Microw. Opt. Technol. Lett.* **4**, 295–297 (1991). DOI 10.1002/mop.4650040805, cit. on p. 28.
- [58] A. Serdyukov, I. Semchenko, S. Tretyakov, and A. H. Sihvola: *Electromagnetics of Bi-Anisotropic Materials: Theory and Applications*. *Electrocomponent Science Monographs*, vol. 11, Gordon and Breach (Amsterdam), 2001. ISBN 978-90-5699-327-6, cit. on p. 28.
- [59] E. Hecht: *Optics*, 4th edition, Pearson Education (Harlow), 2013. ISBN 978-1-292-02157-7, cit. on p. 29.
- [60] M. Decker: *New Light on Optical Activity: Interaction of Electromagnetic Waves with Chiral Photonic Metamaterials*. PhD thesis, Karlsruher Institut für Technologie, 2010. URN urn:nbn:de:swb:90-190605, cit. on pp. 29, 36, 138, 147.
- [61] N. Engheta and D. Jaggard: *Electromagnetic chirality and its applications*. *IEEE Antennas Propag. Soc. Newsl.* **30**, 6–12 (1988). DOI 10.1109/MAP.1988.6086107, cit. on p. 29.
- [62] A. Moscovitz: *Theoretical Aspects of Optical Activity Part One: Small Molecules*. *Adv. Chem. Phys.* **4**, 67–112 (1962). DOI 10.1002/9780470143506.ch2, cit. on p. 30.
- [63] F. A. Carey and R. J. Sundberg: *Advanced Organic Chemistry Part A: Structure and Mechanisms*, 5th edition, Springer (New York), 2007. ISBN 978-0-387-68346-1, cit. on p. 32.
- [64] G. P. Moss: *Basic terminology of stereochemistry (IUPAC Recommendations 1996)*. *Pure Appl. Chem.* **68**, 2193–2222 (1996). DOI 10.1351/pac199668122193, cit. on p. 32.
- [65] R. G. Nelson and W. C. Johnson: *Optical properties of sugars. I. Circular dichroism of monomers at equilibrium*. *J. Am. Chem. Soc.* **94**, 3343–3345 (1972). DOI 10.1021/ja00765a013, cit. on pp. 32, 33.

- [66] M. Gingras: *One hundred years of helicene chemistry. Part 3: applications and properties of carbohelicenes*. Chem. Soc. Rev. **42**, 1051–1095 (2013).
DOI 10.1039/c2cs35134j, cit. on p. 33.
- [67] N. Liu, S. Mukherjee, K. Bao, L. V. Brown, J. Dorfmüller, P. Nordlander, and N. J. Halas: *Magnetic plasmon formation and propagation in artificial aromatic molecules*. Nano Lett. **12**, 364–369 (2012).
DOI 10.1021/nl203641z, cit. on p. 33.
- [68] B. Luk'yanchuk, N. I. Zheludev, S. A. Maier, N. J. Halas, P. Nordlander, H. Giessen, and C. T. Chong: *The Fano resonance in plasmonic nanostructures and metamaterials*. Nat. Mater. **9**, 707–715 (2010).
DOI 10.1038/nmat2810, cit. on p. 33.
- [69] N. Liu, L. Langguth, T. Weiss, J. Kästel, M. Fleischhauer, T. Pfau, and H. Giessen: *Plasmonic analogue of electromagnetically induced transparency at the Drude damping limit*. Nat. Mater. **8**, 758–762 (2009).
DOI 10.1038/nmat2495, cit. on p. 33.
- [70] N. Liu, T. Weiss, M. Mesch, L. Langguth, U. Eigenthaler, M. Hirscher, C. Sönnichsen, and H. Giessen: *Planar metamaterial analogue of electromagnetically induced transparency for plasmonic sensing*. Nano Lett. **10**, 1103–1107 (2010).
DOI 10.1021/nl902621d, cit. on p. 33.
- [71] R. Taubert, M. Hentschel, and H. Giessen: *Plasmonic analog of electromagnetically induced absorption: simulations, experiments, and coupled oscillator analysis*. J. Opt. Soc. Am. B **30**, 3123–3134 (2013).
DOI 10.1364/JOSAB.30.003123, cit. on p. 33.
- [72] R. Taubert, M. Hentschel, J. Kästel, and H. Giessen: *Classical analog of electromagnetically induced absorption in plasmonics*. Nano Lett. **12**, 1367–1371 (2012).
DOI 10.1021/nl2039748, cit. on p. 33.

- [73] V. K. Valev, J. J. Baumberg, C. Sibilia, and T. Verbiest: *Chirality and Chiroptical Effects in Plasmonic Nanostructures: Fundamentals, Recent Progress, and Outlook*. Adv. Mater., 2517–2534 (2013).
DOI 10.1002/adma.201205178, cit. on p. 34.
- [74] A. J. Mastroianni, S. A. Claridge, and A. P. Alivisatos: *Pyramidal and chiral groupings of gold nanocrystals assembled using DNA scaffolds*. J. Am. Chem. Soc. **131**, 8455–8459 (2009).
DOI 10.1021/ja808570g, cit. on pp. 34, 40.
- [75] B. Bai, K. Ventola, J. Tervo, and Y. Zhang: *Determination of the eigenpolarizations in arbitrary diffraction orders of planar periodic structures under arbitrary incidence*. Phys. Rev. A **85**, 053808 (2012).
DOI 10.1103/PhysRevA.85.053808, cit. on pp. 36, 145.
- [76] M. Hentschel: *Complex 2D & 3D Plasmonic Nanostructures: Fano Resonances, Chirality, and Nonlinearities*. PhD thesis, Universität Stuttgart, 2013.
URN urn:nbn:de:bsz:93-opus-83062, cit. on p. 36.
- [77] S. V. Zhukovsky, C. Kremers, and D. N. Chigrin: *Plasmonic rod dimers as elementary planar chiral meta-atoms*. Opt. Lett. **36**, 2278–2280 (2011).
DOI 10.1364/OL.36.002278, cit. on p. 37.
- [78] D. N. Chigrin, C. Kremers, and S. V. Zhukovsky: *Plasmonic nanoparticle monomers and dimers: from nanoantennas to chiral metamaterials*. Appl. Phys. B **105**, 81–97 (2011).
DOI 10.1007/s00340-011-4733-7, cit. on p. 37.
- [79] B. Auguie, J. L. Alonso-Gómez, A. Guerrero-Martínez, and L. M. Liz-Marzán: *Fingers Crossed: Optical Activity of a Chiral Dimer of Plasmonic Nanorods*. J. Phys. Chem. Lett. **2**, 846–851 (2011).
DOI 10.1021/jz200279x, cit. on p. 37.
- [80] L. Rosenfeld: *Quantenmechanische Theorie der natürlichen optischen Aktivität von Flüssigkeiten und Gasen*. Z. Phys. **52**, 161–174 (1929).
DOI 10.1007/BF01342393, cit. on p. 38.

- [81] J. K. Gansel, M. Wegener, S. Burger, and S. Linden: *Gold helix photonic metamaterials: A numerical parameter study*. *Opt. Express* **18**, 1059–1069 (2010).
DOI 10.1364/OE.18.001059, cit. on pp. 38, 78, 120.
- [82] J. K. Gansel, M. Thiel, M. S. Rill, M. Decker, K. Bade, V. Saile, G. von Freymann, S. Linden, and M. Wegener: *Gold helix photonic metamaterial as broadband circular polarizer*. *Science* **325**, 1513–1515 (2009).
DOI 10.1126/science.1177031, cit. on pp. 38, 39, 120, 145.
- [83] Z. Fan and A. O. Govorov: *Plasmonic circular dichroism of chiral metal nanoparticle assemblies*. *Nano Lett.* **10**, 2580–2587 (2010).
DOI 10.1021/n1101231b, cit. on p. 38.
- [84] Z. Fan and A. O. Govorov: *Chiral nanocrystals: plasmonic spectra and circular dichroism*. *Nano Lett.* **12**, 3283–3289 (2012).
DOI 10.1021/n13013715, cit. on p. 38.
- [85] C. Rockstuhl, C. Menzel, T. Paul, and F. Lederer: *Optical activity in chiral media composed of three-dimensional metallic meta-atoms*. *Phys. Rev. B* **79**, 035321 (2009).
DOI 10.1103/PhysRevB.79.035321, cit. on pp. 38, 123.
- [86] A. Radke, T. Gissibl, T. Klotzbücher, P. V. Braun, and H. Giessen: *Three-Dimensional Bichiral Plasmonic Crystals Fabricated by Direct Laser Writing and Electroless Silver Plating*. *Adv. Mater.* **23**, 3018–3021 (2011).
DOI 10.1002/adma.201100543, cit. on p. 39.
- [87] M. Decker, R. Zhao, C. M. Soukoulis, S. Linden, and M. Wegener: *Twisted split-ring-resonator photonic metamaterial with huge optical activity*. *Opt. Lett.* **35**, 1593–1595 (2010).
DOI 10.1364/OL.35.001593, cit. on pp. 39, 145.
- [88] M. Decker, M. W. Klein, M. Wegener, and S. Linden: *Circular dichroism of planar chiral magnetic metamaterials*. *Opt. Lett.* **32**, 856–858 (2007).
DOI 10.1364/OL.32.000856, cit. on p. 39.

- [89] R. Zhao, L. Zhang, J. Zhou, T. Koschny, and C. Soukoulis: *Conjugated gammadion chiral metamaterial with uniaxial optical activity and negative refractive index*. Phys. Rev. B **83**, 035105 (2011).
DOI 10.1103/PhysRevB.83.035105, cit. on p. 39.
- [90] C. Menzel, C. Helgert, C. Rockstuhl, E.-B. Kley, A. Tünnermann, T. Pertsch, and F. Lederer: *Asymmetric Transmission of Linearly Polarized Light at Optical Metamaterials*. Phys. Rev. Lett. **104**, 253902 (2010).
DOI 10.1103/PhysRevLett.104.253902, cit. on p. 39.
- [91] M. Decker, M. Ruther, C. E. Kriegler, J. Zhou, C. M. Soukoulis, S. Linden, and M. Wegener: *Strong optical activity from twisted-cross photonic metamaterials*. Opt. Lett. **34**, 2501–2503 (2009).
DOI 10.1364/OL.34.002501, cit. on p. 39.
- [92] N. Liu, H. Liu, S. Zhu, and H. Giessen: *Stereometamaterials*. Nat. Photonics **3**, 157–162 (2009).
DOI 10.1038/nphoton.2009.4, cit. on pp. 39, 81.
- [93] A. V. Rogacheva, V. A. Fedotov, A. S. Schwanecke, and N. I. Zheludev: *Giant Gyrotropy due to Electromagnetic-Field Coupling in a Bilayered Chiral Structure*. Phys. Rev. Lett. **97**, 177401 (2006).
DOI 10.1103/PhysRevLett.97.177401, cit. on p. 39.
- [94] C. Helgert, E. Pshenay-Severin, M. Falkner, C. Menzel, C. Rockstuhl, E. B. Kley, A. Tünnermann, F. Lederer, and T. Pertsch: *Chiral metamaterial composed of three-dimensional plasmonic nanostructures*. Nano Lett. **11**, 4400–4404 (2011).
DOI 10.1021/nl202565e, cit. on p. 39.
- [95] Y. Zhao, M. A. Belkin, and A. Alù: *Twisted optical metamaterials for planarized ultrathin broadband circular polarizers*. Nat. Commun. **3**, 870 (2012).
DOI 10.1038/ncomms1877, cit. on p. 39.

- [96] K. Konishi, T. Sugimoto, B. Bai, Y. Svirko, and M. Kuwata-Gonokami: *Effect of surface plasmon resonance on the optical activity of chiral metal nanogratings*. *Opt. Express* **15**, 9575–9583 (2007). DOI 10.1364/OE.15.009575, cit. on p. 39.
- [97] V. K. Valev, N. Smisdom, A. V. Silhanek, B. De Clercq, W. Gillijns, M. Ameloot, V. V. Moshchalkov, and T. Verbiest: *Plasmonic ratchet wheels: switching circular dichroism by arranging chiral nanostructures*. *Nano Lett.* **9**, 3945–3948 (2009). DOI 10.1021/nl9021623, cit. on p. 39.
- [98] E. Plum, X.-X. Liu, V. Fedotov, Y. Chen, D. Tsai, and N. Zheludev: *Metamaterials: Optical Activity without Chirality*. *Phys. Rev. Lett.* **102**, 113902 (2009). DOI 10.1103/PhysRevLett.102.113902, cit. on p. 39.
- [99] A. Papakostas, A. Potts, D. Bagnall, S. Prosvirnin, H. Coles, and N. Zheludev: *Optical Manifestations of Planar Chirality*. *Phys. Rev. Lett.* **90**, 107404 (2003). DOI 10.1103/PhysRevLett.90.107404, cit. on p. 39.
- [100] M. Kuwata-Gonokami, N. Saito, Y. Ino, M. Kauranen, K. Jefimovs, T. Vallius, J. Turunen, and Y. Svirko: *Giant Optical Activity in Quasi-Two-Dimensional Planar Nanostructures*. *Phys. Rev. Lett.* **95**, 227401 (2005). DOI 10.1103/PhysRevLett.95.227401, cit. on p. 39.
- [101] F. Eftekhari and T. Davis: *Strong chiral optical response from planar arrays of subwavelength metallic structures supporting surface plasmon resonances*. *Phys. Rev. B* **86**, 075428 (2012). DOI 10.1103/PhysRevB.86.075428, cit. on p. 39.
- [102] K. Dietrich, D. Lehr, C. Helgert, A. Tünnermann, and E.-B. Kley: *Circular dichroism from chiral nanomaterial fabricated by on-edge lithography*. *Adv. Mater.* **24**, OP321–OP325 (2012). DOI 10.1002/adma.201203424, cit. on p. 39.

- [103] K. Dietrich, C. Menzel, D. Lehr, O. Puffky, U. Hübner, T. Pertsch, A. Tünnermann, and E.-B. Kley: *Elevating optical activity: Efficient on-edge lithography of three-dimensional starfish metamaterial*. *Appl. Phys. Lett.* **104**, 193107 (2014). DOI 10.1063/1.4876964, cit. on p. 39.
- [104] C. Han and W. Y. Tam: *Chirality from shadowing deposited metallic nanostructures*. *Photonics Nanostruct. Fundam. Appl.* **13**, 50–57 (2014). DOI 10.1016/j.photonics.2014.10.002, cit. on p. 39.
- [105] B. Yeom, H. Zhang, H. Zhang, J. I. Park, K. Kim, A. O. Govorov, and N. A. Kotov: *Chiral Plasmonic Nanostructures on Achiral Nanopillars*. *Nano Lett.* **13**, 5277–5283 (2013). DOI 10.1021/nl402782d, cit. on p. 39.
- [106] J. K. Gansel, M. Latzel, A. Frölich, J. Kaschke, M. Thiel, and M. Wegener: *Tapered gold-helix metamaterials as improved circular polarizers*. *Appl. Phys. Lett.* **100**, 101109 (2012). DOI 10.1063/1.3693181, cit. on p. 39.
- [107] J. G. Gibbs, A. G. Mark, S. Eslami, and P. Fischer: *Plasmonic nanohelix metamaterials with tailorable giant circular dichroism*. *Appl. Phys. Lett.* **103**, 213101 (2013). DOI 10.1063/1.4829740, cit. on p. 39.
- [108] A. G. Mark, J. G. Gibbs, T.-C. Lee, and P. Fischer: *Hybrid nanocolloids with programmed three-dimensional shape and material composition*. *Nat. Mater.* **12**, 802–807 (2013). DOI 10.1038/nmat3685, cit. on pp. 39, 126.
- [109] M. Esposito, V. Tasco, F. Todisco, A. Benedetti, D. Sanvitto, and A. Passaseo: *Three Dimensional Chiral Metamaterial Nanospirals in the Visible Range by Vertically Compensated Focused Ion Beam Induced Deposition*. *Adv. Opt. Mater.* **2**, 154–161 (2013). DOI 10.1002/adom.201300323, cit. on p. 39.

- [110] M. Esposito, V. Tasco, M. Cuscunà, F. Todisco, A. Benedetti, I. Tarantini, M. D. Giorgi, D. Sanvitto, and A. Passaseo: *Nanoscale 3D Chiral Plasmonic Helices with Circular Dichroism at Visible Frequencies*. ACS Photonics **2**, 105–114 (2015).
DOI 10.1021/ph500318p, cit. on pp. 39, 126.
- [111] K. Höflich, R. B. Yang, A. Berger, G. Leuchs, and S. Christiansen: *The direct writing of plasmonic gold nanostructures by electron-beam-induced deposition*. Adv. Mater. **23**, 2657–2661 (2011).
DOI 10.1002/adma.201004114, cit. on pp. 39, 126.
- [112] K. M. McPeak, C. D. van Engers, M. Blome, J. H. Park, S. Burger, M. A. Gosálvez, A. Faridi, Y. R. Ries, A. Sahu, and D. J. Norris: *Complex chiral colloids and surfaces via high-index off-cut silicon*. Nano Lett. **14**, 2934–2940 (2014).
DOI 10.1021/nl501032j, cit. on p. 39.
- [113] G. Nair, H. J. Singh, D. Paria, M. Venkatapathi, and A. Ghosh: *Plasmonic Interactions at Close Proximity in Chiral Geometries: Route toward Broadband Chiroptical Response and Giant Enantiomeric Sensitivity*. J. Phys. Chem. C **118**, 4991–4997 (2014).
DOI 10.1021/jp4117535, cit. on p. 40.
- [114] J. H. Singh, G. Nair, A. Ghosh, and A. Ghosh: *Wafer scale fabrication of porous three-dimensional plasmonic metamaterials for the visible region: chiral and beyond*. Nanoscale **5**, 7224–7228 (2013).
DOI 10.1039/c3nr02666c, cit. on p. 40.
- [115] L. Zhang, E. Deckhardt, A. Weber, C. Schönenberger, and D. Grützmacher: *Controllable fabrication of SiGe/Si and SiGe/Si/Cr helical nanobelts*. Nanotechnology **16**, 655–663 (2005).
DOI 10.1088/0957-4484/16/6/006, cit. on p. 40.
- [116] A. Demetriadou and J. B. Pendry: *Extreme chirality in Swiss roll metamaterials*. J. Phys. Condens. Matter **21**, 376003 (2009).
DOI 10.1088/0953-8984/21/37/376003, cit. on p. 40.

- [117] W. Yan, L. Xu, C. Xu, W. Ma, H. Kuang, L. Wang, and N. A. Kotov: *Self-assembly of chiral nanoparticle pyramids with strong R/S optical activity*. *J. Am. Chem. Soc.* **134**, 15114–15121 (2012).
DOI 10.1021/ja3066336, cit. on p. 40.
- [118] W. Chen, A. Bian, A. Agarwal, L. Liu, H. Shen, L. Wang, C. Xu, and N. A. Kotov: *Nanoparticle superstructures made by polymerase chain reaction: collective interactions of nanoparticles and a new principle for chiral materials*. *Nano Lett.* **9**, 2153–2159 (2009).
DOI 10.1021/nl900726s, cit. on p. 40.
- [119] V. E. Ferry, J. M. Smith, and A. P. Alivisatos: *Symmetry breaking in tetrahedral chiral plasmonic nanoparticle assemblies*. *ACS Photonics* **1**, 1189–1196 (2014).
DOI 10.1021/ph5002632, cit. on p. 40.
- [120] A. Guerrero-Martínez, J. L. Alonso-Gómez, B. Auguie, M. M. Cid, and L. M. Liz-Marzán: *From individual to collective chirality in metal nanoparticles*. *Nano Today* **6**, 381–400 (2011).
DOI 10.1016/j.nantod.2011.06.003, cit. on p. 40.
- [121] X. Shen, A. Asenjo-Garcia, Q. Liu, Q. Jiang, F. J. García de Abajo, N. Liu, and B. Ding: *Three-dimensional plasmonic chiral tetramers assembled by DNA origami*. *Nano Lett.* **13**, 2128–2133 (2013).
DOI 10.1021/nl400538y, cit. on p. 40.
- [122] A. Guerrero-Martínez, B. Auguie, J. L. Alonso-Gómez, Z. Džolić, S. Gómez-Graña, M. Žinić, M. M. Cid, and L. M. Liz-Marzán: *Intense Optical Activity from Three-Dimensional Chiral Ordering of Plasmonic Nanoantennas*. *Angew. Chemie Int. Ed.* **123**, 5613–5617 (2011).
DOI 10.1002/ange.201007536, cit. on p. 40.
- [123] X. Shen, C. Song, J. Wang, D. Shi, Z. Wang, N. Liu, and B. Ding: *Rolling up gold nanoparticle-dressed DNA origami into three-dimensional plasmonic chiral nanostructures*. *J. Am. Chem. Soc.* **134**, 146–149 (2012).
DOI 10.1021/ja209861x, cit. on p. 40.

- [124] A. Kuzyk, R. Schreiber, Z. Fan, G. Pardatscher, E.-M. Roller, A. Högele, F. C. Simmel, A. O. Govorov, and T. Liedl: *DNA-based self-assembly of chiral plasmonic nanostructures with tailored optical response*. *Nature* **483**, 311–314 (2012). DOI 10.1038/nature10889, cit. on pp. 40, 126.
- [125] X. Lan, X. Lu, C. Shen, Y. Ke, W. Ni, and Q. Wang: *Au Nanorod Helical Superstructures with Designed Chirality*. *J. Am. Chem. Soc.* **137**, 457–462 (2015). DOI 10.1021/ja511333q, cit. on p. 40.
- [126] W. Ma, H. Kuang, L. Wang, L. Xu, W.-S. Chang, H. Zhang, M. Sun, Y. Zhu, Y. Zhao, L. Liu, C. Xu, S. Link, and N. A. Kotov: *Chiral plasmonics of self-assembled nanorod dimers*. *Sci. Rep.* **3**, 1934 (2013). DOI 10.1038/srep01934, cit. on p. 40.
- [127] D. Zerrouki, J. Baudry, D. Pine, P. Chaikin, and J. Bibette: *Chiral colloidal clusters*. *Nature* **455**, 380–382 (2008). DOI 10.1038/nature07237, cit. on p. 40.
- [128] S. Zhang, J. Zhou, Y.-S. Park, J. Rho, R. Singh, S. Nam, A. K. Azad, H.-T. Chen, X. Yin, A. J. Taylor, and X. Zhang: *Photoinduced handedness switching in terahertz chiral metamolecules*. *Nat. Commun.* **3**, 942 (2012). DOI 10.1038/ncomms1908, cit. on p. 40.
- [129] A. Kuzyk, R. Schreiber, H. Zhang, A. O. Govorov, T. Liedl, and N. Liu: *Reconfigurable 3D plasmonic metamolecules*. *Nat. Mater.* **13**, 862–866 (2014). DOI 10.1038/nmat4031, cit. on p. 40.
- [130] W. C. Johnson Jr.: *Circular Dichroism Instrumentation*. In: *Circular Dichroism and the Conformational Analysis of Biomolecules*, ed. by G. D. Fasman, Plenum Press (New York), 1996. ISBN 978-0-306-45142-3, cit. on pp. 42, 43.

- [131] J. C. Sutherland: *Measurement of the Circular Dichroism of Electronic Transitions*. In: *Comprehensive Chiroptical Spectroscopy: Volume 1 – Instrumentation, Methodologies, and Theoretical Simulations*, ed. by N. Berova, P. L. Polavarapu, K. Nakanishi, and R. W. Woody, John Wiley & Sons (Hoboken), 2012. ISBN 978-1-118-01293-2, cit. on p. 42.
- [132] N. J. Greenfield: *Using circular dichroism spectra to estimate protein secondary structure*. *Nat. Protoc.* **1**, 2876–2890 (2006). DOI 10.1038/nprot.2006.202, cit. on pp. 42, 43.
- [133] C. Guo, R. D. Shah, R. K. Dukor, T. B. Freedman, X. Cao, and L. A. Nafie: *Fourier transform vibrational circular dichroism from 800 to 10,000 cm⁻¹: Near-IR-VCD spectral standards for terpenes and related molecules*. *Vib. Spectrosc.* **42**, 254–272 (2006). DOI 10.1016/j.vibspec.2006.05.013, cit. on p. 42.
- [134] W. C. Johnson: *Protein secondary structure and circular dichroism: a practical guide*. *Proteins* **7**, 205–214 (1990). DOI 10.1002/prot.340070302, cit. on p. 43.
- [135] W. C. Johnson: *Secondary structure of proteins through circular dichroism spectroscopy*. *Annu. Rev. Biophys. Biophys. Chem.* **17**, 145–166 (1988). DOI 10.1146/annurev.bb.17.060188.001045, cit. on p. 43.
- [136] S. M. Kelly, T. J. Jess, and N. C. Price: *How to study proteins by circular dichroism*. *Biochim. Biophys. Acta* **1751**, 119–139 (2005). DOI 10.1016/j.bbapap.2005.06.005, cit. on p. 43.
- [137] L. A. Nafie: *Vibrational Optical Activity: Principles and Applications*, Wiley-VCH (New York), 2011. ISBN 978-0-470-03248-0, cit. on p. 43.
- [138] P. L. Polavarapu: *Renaissance in chiroptical spectroscopic methods for molecular structure determination*. *Chem. Rec.* **7**, 125–136 (2007). DOI 10.1002/tcr.20117, cit. on p. 43.

- [139] K.-P. Wong: *Optical rotary dispersion and circular dichroism*. J. Chem. Educ. **51**, A573–A578 (1974).
DOI 10.1021/ed051pA573, cit. on p. 44.
- [140] P. H. Vaccaro: *Optical Rotation and Intrinsic Optical Activity*. In: *Comprehensive Chiroptical Spectroscopy: Volume 1 – Instrumentation, Methodologies, and Theoretical Simulations*, ed. by N. Berova, P. L. Polavarapu, K. Nakanishi, and R. W. Woody, John Wiley & Sons (Hoboken), 2012.
ISBN 978-1-118-01293-2, cit. on p. 44.
- [141] J. P. Riehl and G. Muller: *Circularly Polarized Luminescence Spectroscopy and Emission-Detected Circular Dichroism*. In: *Comprehensive Chiroptical Spectroscopy: Volume 1 – Instrumentation, Methodologies, and Theoretical Simulations*, ed. by N. Berova, P. L. Polavarapu, K. Nakanishi, and R. W. Woody, John Wiley & Sons (Hoboken), 2012.
ISBN 978-1-118-01293-2, cit. on p. 44.
- [142] J. P. Riehl and F. S. Richardson: *Circularly polarized luminescence spectroscopy*. Chem. Rev. **86**, 1–16 (1986).
DOI 10.1021/cr00071a001, cit. on p. 44.
- [143] W. Hug: *Measurement of Raman Optical Activity*. In: *Comprehensive Chiroptical Spectroscopy: Volume 1 – Instrumentation, Methodologies, and Theoretical Simulations*, ed. by N. Berova, P. L. Polavarapu, K. Nakanishi, and R. W. Woody, John Wiley & Sons (Hoboken), 2012.
ISBN 978-1-118-01293-2, cit. on p. 44.
- [144] L. D. Barron, F. Zhu, L. Hecht, G. E. Tranter, and N. W. Isaacs: *Raman optical activity: An incisive probe of molecular chirality and biomolecular structure*. J. Mol. Struct. **834–836**, 7–16 (2007).
DOI 10.1016/j.molstruc.2006.10.033, cit. on p. 44.
- [145] H. Rhee, J. S. Choi, D. J. Starling, J. C. Howell, and M. Cho: *Amplifications in chiroptical spectroscopy, optical enantioselectivity, and weak value measurement*. Chem. Sci. **4**, 4107–4114 (2013).
DOI 10.1039/c3sc51255j, cit. on p. 44.

- [146] Y. Aharonov, D. Albert, and L. Vaidman: *How the result of a measurement of a component of the spin of a spin-1/2 particle can turn out to be 100*. Phys. Rev. Lett. **60**, 1351–1354 (1988). DOI 10.1103/PhysRevLett.60.1351, cit. on p. 44.
- [147] B. Tamir and E. Cohen: *Introduction to Weak Measurements and Weak Values*. Quanta **2**, 7–17 (2013). DOI 10.12743/quantum.v2i1.14, cit. on p. 45.
- [148] M. Pfeifer and P. Fischer: *Weak value amplified optical activity measurements*. Opt. Express **19**, 16508–16517 (2011). DOI 10.1364/OE.19.016508, cit. on p. 45.
- [149] R. A. Goldbeck, D. B. Kim-Shapiro, and D. S. Kliger: *Fast natural and magnetic circular dichroism spectroscopy*. Annu. Rev. Phys. Chem. **48**, 453–479 (1997). DOI 10.1146/annurev.physchem.48.1.453, cit. on p. 46.
- [150] H. Rhee, Y.-G. June, J.-S. Lee, K.-K. Lee, J.-H. Ha, Z. H. Kim, S.-J. Jeon, and M. Cho: *Femtosecond characterization of vibrational optical activity of chiral molecules*. Nature **458**, 310–313 (2009). DOI 10.1038/nature07846, cit. on p. 46.
- [151] D. Sofikitis, L. Bougas, G. E. Katsoprinakis, A. K. Spiliotis, B. Loppinet, and T. P. Rakitzis: *Evanescence-wave and ambient chiral sensing by signal-reversing cavity ringdown polarimetry*. Nature **514**, 76–79 (2014). DOI 10.1038/nature13680, cit. on p. 46.
- [152] J. Aizpurua, G. W. Bryant, L. J. Richter, and F. J. García de Abajo: *Optical properties of coupled metallic nanorods for field-enhanced spectroscopy*. Phys. Rev. B **71**, 235420 (2005). DOI 10.1103/PhysRevB.71.235420, cit. on p. 46.
- [153] A. Pucci, F. Neubrech, J. Aizpurua, T. Cornelius, and M. Lamy de la Chapelle: *Electromagnetic nanowire resonances for field-enhanced spectroscopies*. In: One-Dimensional Nanostructures, Lecture Notes in Nanoscale Science and Technology, vol. 3, ed. by Z. M. Wang, Springer (New York), 2008. ISBN 978-0-387-74131-4, cit. on p. 46.

- [154] A. E. Schlather, N. Large, A. S. Urban, P. Nordlander, and N. J. Halas: *Near-field mediated plexcitonic coupling and giant Rabi splitting in individual metallic dimers*. Nano Lett. **13**, 3281–3286 (2013).
DOI 10.1021/nl4014887, cit. on p. 46.
- [155] A. O. Govorov, Y. K. Gun'ko, J. M. Slocik, V. A. Gérard, Z. Fan, and R. R. Naik: *Chiral nanoparticle assemblies: circular dichroism, plasmonic interactions, and exciton effects*. J. Mater. Chem. **21**, 16806–16818 (2011).
DOI 10.1039/c1jm12345a, cit. on p. 47.
- [156] A. Ben-Moshe, B. M. Maoz, A. O. Govorov, and G. Markovich: *Chirality and chiroptical effects in inorganic nanocrystal systems with plasmon and exciton resonances*. Chem. Soc. Rev. **42**, 7028–7041 (2013).
DOI 10.1039/c3cs60139k, cit. on p. 47.
- [157] C. Noguez and I. L. Garzón: *Optically active metal nanoparticles*. Chem. Soc. Rev. **38**, 757–771 (2009).
DOI 10.1039/b800404h, cit. on p. 47.
- [158] I. Lieberman, G. Shemer, T. Fried, E. M. Kosower, and G. Markovich: *Plasmon-resonance-enhanced absorption and circular dichroism*. Angew. Chemie Int. Ed. **47**, 4855–4857 (2008).
DOI 10.1002/anie.200800231, cit. on p. 47.
- [159] A. O. Govorov, Z. Fan, P. Hernandez, J. M. Slocik, and R. R. Naik: *Theory of circular dichroism of nanomaterials comprising chiral molecules and nanocrystals: plasmon enhancement, dipole interactions, and dielectric effects*. Nano Lett. **10**, 1374–1382 (2010).
DOI 10.1021/nl100010v, cit. on pp. 47–49, 53.
- [160] J. M. Slocik, A. O. Govorov, and R. R. Naik: *Plasmonic circular dichroism of Peptide-functionalized gold nanoparticles*. Nano Lett. **11**, 701–705 (2011).
DOI 10.1021/nl1038242, cit. on pp. 48, 49.

- [161] J. M. Sanz, D. Ortiz, R. Alcaraz de la Osa, J. M. Saiz, F. González, A. S. Brown, M. Losurdo, H. O. Everitt, and F. Moreno: *UV Plasmonic Behavior of Various Metal Nanoparticles in the Near- and Far-Field Regimes: Geometry and Substrate Effects*. J. Phys. Chem. C **117**, 19606–19615 (2013).
DOI 10.1021/jp405773p, cit. on p. 49.
- [162] D. V. Chulhai and L. Jensen: *Plasmonic Circular Dichroism of β - and α -Helix Using a Discrete Interaction Model/Quantum Mechanics Method*. J. Phys. Chem. A **119**, 5218–5223 (2014).
DOI 10.1021/jp5099188, cit. on p. 49.
- [163] P. Řezanka, K. Záruba, and V. Král: *Supramolecular chirality of cysteine modified silver nanoparticles*. Colloids Surfaces A Physicochem. Eng. Asp. **374**, 77–83 (2011).
DOI 10.1016/j.colsurfa.2010.11.015, cit. on p. 49.
- [164] M. Kobayashi, S. Tomita, K. Sawada, K. Shiba, H. Yanagi, I. Yamashita, and Y. Uraoka: *Chiral meta-molecules consisting of gold nanoparticles and genetically engineered tobacco mosaic virus*. Opt. Express **20**, 24856–24863 (2012).
DOI 10.1364/OE.20.024856, cit. on p. 49.
- [165] T. Harada, N. Kajiyama, K. Ishizaka, R. Toyofuku, K. Izumi, K. Umemura, Y. IMAI, N. Taniguchi, and K. Mishima: *Plasmon Resonance-Enhanced Circularly Polarized Luminescence of Self-Assembled Meso-tetrakis(4-sulfonatophenyl)porphyrin-Surfactant Complexes in Interaction with Ag Nanoparticles*. Chem. Commun. **50**, 11169–11172 (2014).
DOI 10.1039/C4CC04477K, cit. on p. 49.
- [166] B. M. Maoz, R. van der Weegen, Z. Fan, A. O. Govorov, G. Ellestad, N. Berova, E. W. Meijer, and G. Markovich: *Plasmonic chiroptical response of silver nanoparticles interacting with chiral supramolecular assemblies*. J. Am. Chem. Soc. **134**, 17807–17813 (2012).
DOI 10.1021/ja309016k, cit. on p. 49.

- [167] A. O. Govorov and Z. Fan: *Theory of chiral plasmonic nanostructures comprising metal nanocrystals and chiral molecular media*. Chem. Phys. Chem. **13**, 2551–2560 (2012). DOI 10.1002/cphc.201100958, cit. on p. 49.
- [168] C. F. Bohren and D. R. Huffman: *Absorption and Scattering of Light by Small Particles*, John Wiley & Sons (New York), 1998. ISBN 047105772X, cit. on pp. 50, 145.
- [169] N. Abdulrahman, Z. Fan, T. Tonooka, S. Kelly, N. Gadegaard, E. Hendry, A. O. Govorov, and M. Kadodwala: *Induced chirality through electromagnetic coupling between chiral molecular layers and plasmonic nanostructures*. Nano Lett. **12**, 977–983 (2012). DOI 10.1021/nl204055r, cit. on p. 50.
- [170] B. M. Maoz, Y. Chaikin, A. B. Tesler, O. Bar Elli, Z. Fan, A. O. Govorov, and G. Markovich: *Amplification of chiroptical activity of chiral biomolecules by surface plasmons*. Nano Lett. **13**, 1203–1209 (2013). DOI 10.1021/nl304638a, cit. on p. 50.
- [171] G. Decher: *Fuzzy Nanoassemblies: Toward Layered Polymeric Multicomposites*. Science **277**, 1232–1237 (1997). DOI 10.1126/science.277.5330.1232, cit. on p. 50.
- [172] A. O. Govorov: *Plasmon-Induced Circular Dichroism of a Chiral Molecule in the Vicinity of Metal Nanocrystals. Application to Various Geometries*. J. Phys. Chem. C **115**, 7914–7923 (2011). DOI 10.1021/jp1121432, cit. on pp. 51, 53.
- [173] F. Lu, Y. Tian, M. Liu, D. Su, H. Zhang, A. O. Govorov, and O. Gang: *Discrete nanocubes as plasmonic reporters of molecular chirality*. Nano Lett. **13**, 3145–3151 (2013). DOI 10.1021/nl401107g, cit. on p. 51.
- [174] V. A. Gérard, Y. K. Gun'ko, E. Defrancq, and A. O. Govorov: *Plasmon-induced CD response of oligonucleotide-conjugated metal nanoparticles*. Chem. Commun. **47**, 7383–7385 (2011). DOI 10.1039/c1cc11083g, cit. on pp. 51, 52.

- [175] H. Zhang and A. O. Govorov: *Giant circular dichroism of a molecule in a region of strong plasmon resonances between two neighboring gold nanocrystals*. Phys. Rev. B **87**, 075410 (2013). DOI 10.1103/PhysRevB.87.075410, cit. on pp. 52, 53.
- [176] M. E. Layani, A. Ben Moshe, M. Varenik, O. Regev, H. Zhang, A. O. Govorov, and G. Markovich: *Chiroptical Activity in Silver Cholate Nanostructures Induced by the Formation of Nanoparticle Assemblies*. J. Phys. Chem. C **117**, 22240–22244 (2013). DOI 10.1021/jp400993j, cit. on p. 53.
- [177] Z. Zhu, W. Liu, Z. Li, B. Han, Y. Zhou, Y. Gao, and Z. Tang: *Manipulation of collective optical activity in one-dimensional plasmonic assembly*. ACS Nano **6**, 2326–2332 (2012). DOI 10.1021/nn2044802, cit. on p. 53.
- [178] R.-Y. Wang, P. Wang, Y. Liu, W. Zhao, D. Zhai, X. Hong, Y. Ji, X. Wu, F. Wang, D. Zhang, W. Zhang, R. Liu, and X. Zhang: *Experimental Observation of Giant Chiroptical Amplification of Small Chiral Molecules by Gold Nanosphere Clusters*. J. Phys. Chem. C **118**, 9690–9695 (2014). DOI 10.1021/jp5025813, cit. on pp. 53, 54.
- [179] X. Wu, L. Xu, L. Liu, W. Ma, H. Yin, H. Kuang, L. Wang, C. Xu, and N. A. Kotov: *Unexpected chirality of nanoparticle dimers and ultrasensitive chiroplasmonic bioanalysis*. J. Am. Chem. Soc. **135**, 18629–18636 (2013). DOI 10.1021/ja4095445, cit. on p. 54.
- [180] Z. Xu, L. Xu, Y. Zhu, W. Ma, H. Kuang, L. Wang, and C. Xu: *Chirality based sensor for bisphenol A detection*. Chem. Commun. **48**, 5760–5762 (2012). DOI 10.1039/c2cc31327h, cit. on p. 54.
- [181] Z. Xu, L. Xu, L. M. Liz-Marzán, W. Ma, N. A. Kotov, L. Wang, H. Kuang, and C. Xu: *Sensitive Detection of Silver Ions Based on Chiroplasmonic Assemblies of Nanoparticles*. Adv. Opt. Mater. **1**, 626–630 (2013). DOI 10.1002/adom.201300148, cit. on p. 54.

- [182] H. S. Oh, S. Liu, H. Jee, A. Baev, M. T. Swihart, and P. N. Prasad: *Chiral poly(fluorene-alt-benzothiadiazole) (PFBT) and nanocomposites with gold nanoparticles: plasmonically and structurally enhanced chirality*. J. Am. Chem. Soc. **132**, 17346–17348 (2010).
DOI 10.1021/ja107064a, cit. on p. 55.
- [183] W. Ma, H. Kuang, L. Xu, L. Ding, C. Xu, L. Wang, and N. A. Kotov: *Attomolar DNA detection with chiral nanorod assemblies*. Nat. Commun. **4**, 2689 (2013).
DOI 10.1038/ncomms3689, cit. on p. 55.
- [184] Y. Zhao, L. Xu, W. Ma, L. Wang, H. Kuang, C. Xu, and N. A. Kotov: *Shell-Engineered Chiroplasmonic Assemblies of Nanoparticles for Zeptomolar DNA Detection*. Nano Lett. **14**, 3908–3913 (2014).
DOI 10.1021/n1501166m, cit. on p. 56.
- [185] E. Hendry, T. Carpy, J. Johnston, M. Popland, R. V. Mikhaylovskiy, A. J. Laphorn, S. M. Kelly, L. D. Barron, N. Gadegaard, and M. Kadodwala: *Ultrasensitive detection and characterization of biomolecules using superchiral fields*. Nat. Nanotechnol. **5**, 783–787 (2010).
DOI 10.1038/nnano.2010.209, cit. on pp. 56, 57, 73.
- [186] D. M. Lipkin: *Existence of a New Conservation Law in Electromagnetic Theory*. J. Math. Phys. **5**, 696–700 (1964).
DOI 10.1063/1.1704165, cit. on p. 60.
- [187] M. M. Coles and D. L. Andrews: *Chirality and angular momentum in optical radiation*. Phys. Rev. A **85**, 063810 (2012).
DOI 10.1103/PhysRevA.85.063810, cit. on p. 60.
- [188] K. Bliokh and F. Nori: *Characterizing optical chirality*. Phys. Rev. A **83**, 021803 (2011).
DOI 10.1103/PhysRevA.83.021803, cit. on p. 60.
- [189] R. P. Cameron, S. M. Barnett, and A. M. Yao: *Optical helicity of interfering waves*. J. Mod. Opt. **61**, 25–31 (2013).
DOI 10.1080/09500340.2013.829874, cit. on p. 60.

- [190] S. M. Barnett, R. P. Cameron, and A. M. Yao: *Duplex symmetry and its relation to the conservation of optical helicity*. Phys. Rev. A **86**, 013845 (2012).
DOI 10.1103/PhysRevA.86.013845, cit. on p. 60.
- [191] J. S. Choi and M. Cho: *Limitations of a superchiral field*. Phys. Rev. A **86**, 063834 (2012).
DOI 10.1103/PhysRevA.86.063834, cit. on pp. 61, 66.
- [192] R. A. Harris: *On the Optical Rotary Dispersion of Polymers*. J. Chem. Phys. **43**, 959–970 (1965).
DOI 10.1063/1.1696878, cit. on p. 61.
- [193] D. P. Craig and T. Thirunamachandran: *New approaches to chiral discrimination in coupling between molecules*. Theor. Chem. Acc. **102**, 112–120 (1999).
DOI 10.1007/s002140050480, cit. on p. 61.
- [194] A. G. Smart: *A mirror gives light an extra twist*. Phys. Today **64**, 16–17 (2011).
DOI 10.1063/1.3603909, cit. on p. 63.
- [195] Y. Tang and A. E. Cohen: *Enhanced enantioselectivity in excitation of chiral molecules by superchiral light*. Science **332**, 333–336 (2011).
DOI 10.1126/science.1202817, cit. on p. 63.
- [196] N. Yang and A. E. Cohen: *Local geometry of electromagnetic fields and its role in molecular multipole transitions*. J. Phys. Chem. B **115**, 5304–5311 (2011).
DOI 10.1021/jp1092898, cit. on p. 63.
- [197] A. Ashkin: *Acceleration and Trapping of Particles by Radiation Pressure*. Phys. Rev. Lett. **24**, 156–159 (1970).
DOI 10.1103/PhysRevLett.24.156, cit. on p. 63.
- [198] A. Ashkin, J. M. Dziedzic, J. E. Bjorkholm, and S. Chu: *Observation of a single-beam gradient force optical trap for dielectric particles*. Opt. Lett. **11**, 288–290 (1986).
DOI 10.1364/OL.11.000288, cit. on p. 63.
- [199] A. Canaguier-Durand, J. A. Hutchison, C. Genet, and T. W. Ebbesen: *Mechanical separation of chiral dipoles by chiral light*. New J. Phys. **15**, 123037 (2013).
DOI 10.1088/1367-2630/15/12/123037, cit. on pp. 63, 64.

- [200] R. P. Cameron, S. M. Barnett, and A. M. Yao: *Discriminatory optical force for chiral molecules*. New J. Phys. **16**, 013020 (2014).
DOI 10.1088/1367-2630/16/1/013020, cit. on p. 64.
- [201] K. Ding, J. Ng, L. Zhou, and C. T. Chan: *Realization of optical pulling forces using chirality*. Phys. Rev. A **89**, 063825 (2014).
DOI 10.1103/PhysRevA.89.063825, cit. on p. 64.
- [202] C. Rosales-Guzmán, K. Volke-Sepulveda, and J. P. Torres: *Light with enhanced optical chirality*. Opt. Lett. **37**, 3486–3488 (2012).
DOI 10.1364/OL.37.003486, cit. on p. 65.
- [203] CST Computer Simulation Technology AG: *CST MICROWAVE STUDIO*,
<http://www.cst.com/Products/CSTMWS> (visited on Dec. 15, 2014).
Cit. on p. 70.
- [204] T. Weiss, G. Granet, N. A. Gippius, S. G. Tikhodeev, and H. Giessen: *Matched coordinates and adaptive spatial resolution in the Fourier modal method*. Opt. Express **17**, 8051–8061 (2009).
DOI 10.1364/OE.17.008051, cit. on p. 70.
- [205] S. Essig and K. Busch: *Generation of adaptive coordinates and their use in the Fourier Modal Method*. Opt. Express **18**, 23258–23274 (2010).
DOI 10.1364/OE.18.023258, cit. on p. 70.
- [206] K. Konishi, M. Nomura, N. Kumagai, S. Iwamoto, Y. Arakawa, and M. Kuwata-Gonokami: *Circularly Polarized Light Emission from Semiconductor Planar Chiral Nanostructures*. Phys. Rev. Lett. **106**, 057402 (2011).
DOI 10.1103/PhysRevLett.106.057402, cit. on p. 73.
- [207] S. Takahashi, A. Potts, D. Bagnall, N. Zheludev, and A. Zayats: *Near-field polarization conversion in planar chiral nanostructures*. Opt. Commun. **255**, 91–96 (2005).
DOI 10.1016/j.optcom.2005.06.001, cit. on p. 73.

- [208] H. Liu, J. X. Cao, S. N. Zhu, N. Liu, R. Ameling, and H. Giessen: *Lagrange model for the chiral optical properties of stereometamaterials*. Phys. Rev. B **81**, 241403 (2010). DOI 10.1103/PhysRevB.81.241403, cit. on p. 81.
- [209] D. A. Powell, K. Hannam, I. V. Shadrivov, and Y. S. Kivshar: *Near-field interaction of twisted split-ring resonators*. Phys. Rev. B **83**, 235420 (2011). DOI 10.1103/PhysRevB.83.235420, cit. on p. 81.
- [210] S. Yoo, M. Cho, and Q.-H. Park: *Globally enhanced chiral field generation by negative-index metamaterials*. Phys. Rev. B **89**, 161405 (2014). DOI 10.1103/PhysRevB.89.161405, cit. on p. 86.
- [211] A. García-Etxarri and J. A. Dionne: *Surface-enhanced circular dichroism spectroscopy mediated by nonchiral nanoantennas*. Phys. Rev. B **87**, 235409 (2013). DOI 10.1103/PhysRevB.87.235409, cit. on p. 86.
- [212] G. K. Larsen, Y. He, W. Ingram, and Y. Zhao: *Hidden chirality in superficially racemic patchy silver films*. Nano Lett. **13**, 6228–6232 (2013). DOI 10.1021/nl4036687, cit. on p. 88.
- [213] V. K. Valev, J. J. Baumberg, B. De Clercq, N. Braz, X. Zheng, E. J. Osley, S. Vandendriessche, M. Hojeij, C. Blejean, J. Mertens, C. G. Biris, V. Volskiy, M. Ameloot, Y. Ekinici, G. A. E. Vandenbosch, P. A. Warburton, V. V. Moshchalkov, N. C. Panoiu, and T. Verbiest: *Nonlinear superchiral meta-surfaces: tuning chirality and disentangling non-reciprocity at the nanoscale*. Adv. Mater. **26**, 4074–4081 (2014). DOI 10.1002/adma.201401021, cit. on p. 94.
- [214] P. Biagioni, M. Savoini, J.-S. Huang, L. Duò, M. Finazzi, and B. Hecht: *Near-field polarization shaping by a near-resonant plasmonic cross antenna*. Phys. Rev. B **80**, 153409 (2009). Cit. on p. 103.
- [215] B. Gompf, J. Braun, T. Weiss, H. Giessen, M. Dressel, and U. Hübner: *Periodic Nanostructures: Spatial Dispersion Mimics Chirality*. Phys. Rev. Lett. **106**, 185501 (2011). DOI 10.1103/PhysRevLett.106.185501, cit. on p. 104.

- [216] T. Weiss, N. A. Gippius, S. G. Tikhodeev, G. Granet, and H. Giessen: *Derivation of plasmonic resonances in the Fourier modal method with adaptive spatial resolution and matched coordinates*. J. Opt. Soc. Am. A **28**, 238–244 (2011).
DOI 10.1364/JOSAA.28.000238, cit. on p. 105.
- [217] J. Dorfmüller, R. Vogelgesang, W. Khunsin, C. Rockstuhl, C. Etrich, and K. Kern: *Plasmonic nanowire antennas: experiment, simulation, and theory*. Nano Lett. **10**, 3596–3603 (2010).
DOI 10.1021/nl101921y, cit. on p. 106.
- [218] T. J. Davis and E. Hendry: *Superchiral electromagnetic fields created by surface plasmons in nonchiral metallic nanostructures*. Phys. Rev. B **87**, 085405 (2013).
DOI 10.1103/PhysRevB.87.085405, cit. on p. 116.
- [219] S. Tretyakov, F. Mariotte, C. Simovski, T. Kharina, and J.-P. Heliot: *Analytical antenna model for chiral scatterers: comparison with numerical and experimental data*. IEEE Trans. Antennas Propag. **44**, 1006–1014 (1996).
DOI 10.1109/8.504309, cit. on p. 123.
- [220] Z. Yang, M. Zhao, and P. Lu: *How to improve the signal-to-noise ratio for circular polarizers consisting of helical metamaterials?* Opt. Express **19**, 4255–4260 (2011).
DOI 10.1364/OE.19.004255, cit. on p. 123.
- [221] Y. Yu, Z. Yang, S. Li, and M. Zhao: *Higher extinction ratio circular polarizers with hetero-structured double-helical metamaterials*. Opt. Express **19**, 10886–10894 (2011).
DOI 10.1364/OE.19.010886, cit. on p. 123.
- [222] J. Kaschke, J. K. Gansel, and M. Wegener: *On metamaterial circular polarizers based on metal N-helices*. Opt. Express **20**, 26012–26020 (2012).
DOI 10.1364/OE.20.026012, cit. on p. 123.
- [223] Z. Y. Yang, M. Zhao, P. X. Lu, and Y. F. Lu: *Ultrabroadband optical circular polarizers consisting of double-helical nanowire structures*. Opt. Lett. **35**, 2588–2590 (2010).
DOI 10.1364/OL.35.002588, cit. on p. 123.

- [224] J. Fischer, J. B. Mueller, A. S. Quick, J. Kaschke, C. Barner-Kowollik, and M. Wegener: *Exploring the Mechanisms in STED-Enhanced Direct Laser Writing*. Adv. Opt. Mater. **3**, 221–232 (2014). DOI 10.1002/adom.201400413, cit. on p. 126.
- [225] J. Fischer and M. Wegener: *Three-dimensional optical laser lithography beyond the diffraction limit*. Laser Photon. Rev. **7**, 22–44 (2013). DOI 10.1002/lpor.201100046, cit. on p. 126.
- [226] I. Sakellari, E. Kabouraki, D. Gray, V. Purlys, C. Fotakis, A. Pikulin, N. Bityurin, M. Vamvakaki, and M. Farsari: *Diffusion-assisted high-resolution direct femtosecond laser writing*. ACS Nano **6**, 2302–2311 (2012). DOI 10.1021/nn204454c, cit. on p. 126.
- [227] E. H. Waller, M. Renner, and G. von Freymann: *Active aberration- and point-spread-function control in direct laser writing*. Opt. Express **20**, 24949–24956 (2012). DOI 10.1364/OE.20.024949, cit. on p. 126.
- [228] A. M. Kern and O. J. F. Martin: *Excitation and reemission of molecules near realistic plasmonic nanostructures*. Nano Lett. **11**, 482–487 (2011). DOI 10.1021/nl1032588, cit. on p. 129.
- [229] M. M. Tai: *A mathematical model for the determination of total area under glucose tolerance and other metabolic curves*. Diabetes Care **17**, 152–154 (1994). DOI 10.2337/diacare.17.2.152, cit. on p. 130.
- [230] D. Rossouw and G. A. Botton: *Resonant optical excitations in complementary plasmonic nanostructures*. Opt. Express **20**, 6968–6973 (2012). DOI 10.1364/OE.20.006968, cit. on p. 133.
- [231] E. Hendry, R. V. Mikhaylovskiy, L. D. Barron, M. Kadodwala, and T. J. Davis: *Chiral electromagnetic fields generated by arrays of nanoslits*. Nano Lett. **12**, 3640–3644 (2012). DOI 10.1021/nl3012787, cit. on pp. 133, 135.

- [232] I. Bilotti, P. Biscarini, E. Castiglioni, F. Ferranti, and R. Kuroda: *Reflectance circular dichroism of solid-state chiral coordination compounds*. *Chirality* **14**, 750–756 (2002). DOI 10.1002/chir.10136, cit. on p. 138.
- [233] N. Meinzer, E. Hendry, and W. L. Barnes: *Probing the chiral nature of electromagnetic fields surrounding plasmonic nanostructures*. *Phys. Rev. B* **88**, 041407 (2013). DOI 10.1103/PhysRevB.88.041407, cit. on p. 142.
- [234] D. Dregely, F. Neubrech, H. Duan, R. Vogelgesang, and H. Giessen: *Vibrational near-field mapping of planar and buried three-dimensional plasmonic nanostructures*. *Nat. Commun.* **4**, 2237 (2013). DOI 10.1038/ncomms3237, cit. on p. 142.
- [235] L. Langguth and H. Giessen: *Coupling strength of complex plasmonic structures in the multiple dipole approximation*. *Opt. Express* **19**, 22156–22166 (2011). DOI 10.1364/OE.19.022156, cit. on p. 143.
- [236] V. I. Belotelov, I. A. Akimov, M. Pohl, V. A. Kotov, S. Kasture, A. S. Vengurlekar, A. V. Gopal, D. R. Yakovlev, A. K. Zvezdin, and M. Bayer: *Enhanced magneto-optical effects in magnetoplasmonic crystals*. *Nat. Nanotechnol.* **6**, 370–376 (2011). DOI 10.1038/nnano.2011.54, cit. on p. 143.
- [237] G. Armelles, B. Caballero, P. Prieto, F. García, A. Cebollada, M. U. González, and A. García-Martin: *Magnetic field modulation of chiroptical effects in magnetoplasmonic structures*. *Nanoscale* **6**, 3737–3741 (2014). DOI 10.1039/c3nr05889a, cit. on p. 143.
- [238] K. Y. Bliokh, Y. S. Kivshar, and F. Nori: *Magnetolectric Effects in Local Light-Matter Interactions*. *Phys. Rev. Lett.* **113**, 033601 (2014). DOI 10.1103/PhysRevLett.113.033601, cit. on p. 143.
- [239] D. Zarifi, M. Soleimani, and A. Abdolali: *Parameter retrieval of chiral metamaterials based on the state-space approach*. *Phys. Rev. E* **88**, 023204 (2013). DOI 10.1103/PhysRevE.88.023204, cit. on p. 145.

- [240] D.-H. Kwon, D. H. Werner, A. V. Kildishev, and V. M. Shalaev: *Material parameter retrieval procedure for general bi-isotropic metamaterials and its application to optical chiral negative-index metamaterial design*. *Opt. Express* **16**, 11822–11829 (2008).
DOI 10.1364/OE.16.011822, cit. on p. 145.
- [241] R. Zhao, T. Koschny, and C. M. Soukoulis: *Chiral metamaterials: retrieval of the effective parameters with and without substrate*. *Opt. Express* **18**, 14553–14567 (2010).
DOI 10.1364/OE.18.014553, cit. on p. 145.
- [242] G. Snatzke: *Circular Dichroism: An Introduction*. In: *Circular Dichroism Principles and Applications*, ed. by N. Berova, K. Nakanishi, and R. W. Woody, Wiley-VCH (New York), 2000.
ISBN 978-0-471-33003-5, cit. on p. 146.
- [243] P. Bourke: *POVRay density (DF3) files*,
<http://paulbourke.net/miscellaneous/povexamples/#df3>
(visited on Aug. 21, 2014).
Cit. on p. 149.
- [244] Persistence of Vision Raytracer Pty. Ltd.: *POV-Ray 3.6 Documentation: 2.5.11.11 Density_File*,
<http://www.povray.org/documentation/view/3.6.1/374/>
(visited on Aug. 21, 2014).
Cit. on p. 149.
- [245] A. S. Tanenbaum and T. Austin: *Structured Computer Organization*, 6th edition, Pearson (Harlow), 2012.
ISBN 978-0-273-76924-8, cit. on p. 149.

DANKSAGUNG

Theoretische Forschungen haben den Vorteil, dass sie – zumindest theoretisch – alleine durchgeführt werden können. In der Praxis wäre diese Arbeit jedoch ohne Unterstützung so nicht möglich gewesen. Deshalb möchte ich mich hier bei allen Unterstützern bedanken.

Hierbei danke ich zunächst Prof. Dr. Harald Giessen für die Möglichkeit, diese Arbeit in seiner Gruppe anzufertigen. Besonders positiv empfand ich die vielen Freiheiten, die ich bei meiner Forschung hatte. Dabei fehlte es jedoch nicht an Unterstützung, sei es durch Diskussionen oder die Herstellung von Kontakten. Ich bin auch sehr dankbar dafür, dass ich meine Ergebnisse auf so vielen Konferenzen im In- und Ausland vorstellen konnte. Weiterhin danke ich meiner Mitberichterin, Jun.-Prof. Dr. Maria Fyta, sowie Prof. Dr. Martin Dressel, der den Vorsitz der Prüfungskommission übernommen hat.

Allen, die mich in Diskussionen inspiriert und weitergebildet haben, bin ich sehr dankbar. Allen voran möchte ich mich hier bei meinen „chiralen“ Kollegen Xinghui Yin, Dr. Mario Hentschel und Jun.-Prof. Dr. Thomas Weiss bedanken. Prof. Dr. Nader Engheta danke ich für die Möglichkeit, seine Gruppe zu besuchen, sowie die daraus entstandenen Ideen. Weiterhin danke ich Dr. Jens Dorfmueller und Dr. Richard Taubert für viele spannende physikalische (und nicht so physikalische) Diskussionen. Vielen Dank auch an Dr. Christine von Rekowski für die immerwährende Unterstützung bei der Vermeidung bürokratischer Fallstricke. Selbstverständlich bin ich auch allen anderen aktuellen und ehemaligen Mitgliedern des 4. Physikalischen Instituts dankbar für die gute Zusammenarbeit.

Nicht nur die Arbeitsatmosphäre, auch das allgemeine Institutsklima war und ist herausragend. Ich danke allen regelmäßigen Besuchern der Kaffeeecke für viele innovative Theorien und niveauvolle Diskussionen am Rande und abseits der Physik. Stefano Cataldo, Larissa Wollet, Dominik Flöß und Shahin Bagheri danke ich für die angenehme Büroatmosphäre selbst unter eingeschränkten Platzverhältnissen. Weiterhin danke ich Martin Mesch für die gute Zusammenarbeit, wenn der Institutsserver eben diese eingestellt hat.

Korrekturgelesen wurde diese Arbeit von Dr. Mario Hentschel, Xinghui Yin und Jun.-Prof. Dr. Thomas Weiss, denen ich für ihre fachlichen Ratschläge sehr dankbar bin. Mein besonderer Dank gilt John Williamson, der als Nichtphysiker Grammatik und Rechtschreibung großer Teile der Arbeit verbessert hat. Eva Grimme und Michèle Neumann danke ich für wertvolle Ratschläge in Bezug auf Gestaltung, Layout und Typographie. Für die Adaption der 3D-Datenvisualisierung in POV-Ray sowie darüber hinausgehende Unterstützung bei meinen Versuchen, schöne Grafiken zu erstellen, bin ich Sven M. Hein sehr dankbar. Dr. Richard Taubert danke ich dafür, dass er mir André Miedes CLASSICTHESIS-Vorlage nähergebracht hat.

Schließlich – aber nicht zuletzt – danke ich meinen Eltern Helga und Hans-Peter sowie meinem Bruder Sebastian mit seiner Frau Saskia für ihre ebenso umfassende wie bedingungslose Unterstützung. Ohne meine Familie wäre diese Arbeit nicht entstanden. Der letzte Eintrag gebührt jedoch Michèle: Danke, für alles!

CURRICULUM VITÆ

NAME	Martin Schäferling
BORN	05.07.1984 in Donauwörth
CITIZENSHIP	German
EMAIL	m.schaeferling@pi4.uni-stuttgart.de
2010–2015	Ph.D. thesis: “Chiral Plasmonic Near-Field Sources: Control of Chiral Electromagnetic Fields for Chiroptical Spectroscopies”, Universität Stuttgart; advisor: Prof. Dr. Harald Giessen.
2010–2015	Research assistant, group of Prof. Dr. Harald Giessen, Universität Stuttgart.
2010	Research assistant, group of Prof. Dr. Carsten Fallnich, Universität Münster.
2008–2010	Diploma thesis: “GPU-gestützte Simulation der Wechselwirkung transversaler Moden in Wellenleitern (GPU-Based Simulation of the Interaction of Transverse Modes in Waveguides)”, Universität Münster; advisors: Prof. Dr. Carsten Fallnich and Prof. Dr. Sergei Gorlatch; awarded as best interdisciplinary diploma thesis by the “Förderkreis der Angewandten Informatik an der WWU e. V.”.
2006–2010	Tutor for computer science courses, Universität Münster.
2005–2010	Studies of physics, Universität Münster; Dipl.-Phys. (1.0) on 15.06.2010.
2004–2010	Studies of computer science, Universität Münster; Dipl.-Inform. (1.0) on 29.06.2010.
1991–2004	Gymnasium Donauwörth; Abitur (1.7) on 25.06.2010.

COLOPHON

This thesis was typeset with $\text{\LaTeX} 2_{\epsilon}$ using the free Linux Libertine font. The style was inspired by Robert Bringhurst's "*The Elements of Typographic Style*". It is available for \LaTeX via CTAN as CLASSICTHESIS.